

PROBING THE FREEZEOUT MECHANISMS
AND ISOSPIN EFFECTS IN
MULTIFRAGMENTATION

By

Wanpeng Tan

A DISSERTATION

Submitted to
Michigan State University
in partial fulfillment of the requirements
for the Degree of

DOCTOR OF PHILOSOPHY

Department of Physics and Astronomy

2002

ABSTRACT

**PROBING THE FREEZEOUT MECHANISMS AND ISOSPIN
EFFECTS IN MULTIFRAGMENTATION**

By

Wanpeng Tan

Multifragmentation processes have been studied by measuring $^{129}\text{Xe}+^{197}\text{Au}$ collisions at 50A MeV with a large area silicon-strip/CsI detector array (LASSA). The LASSA was designed and constructed to provide excellent energy, angular and isotope resolution for the detection of charged particles. Each of nine LASSA telescopes consists of two silicon strip detectors ($65\mu\text{m}$ and $500\mu\text{m}$ thick, respectively) and four CsI(Tl) crystals. A non-uniformity in light output of the CsI(Tl) crystals better than 1% was obtained via the crystal selection and quality control procedure. Isotopically resolved particles from hydrogen to oxygen were detected in polar angles of $12^\circ < \theta < 62^\circ$ with an angular resolution of $\pm 0.43^\circ$.

Experimental correlation functions for particles detected in LASSA are analyzed using the Koonin-Pratt formalism and by making an assumption of thermal equilibrium. A method of probing the breakup density is demonstrated and the results from the equilibrium approach are compared with those from the Koonin-Pratt formalism for light particle correlations. The extracted values of the free volume are about 2.5 (10% uncertainty) times the volume of the total system at saturation density, which corresponds to a freezeout density of 1/5-1/3 times the nuclear saturation density.

A new technique of spin determination from particle correlation functions is proposed utilizing the same equilibrium assumption. A few examples of correlation

functions are studied to demonstrate the promising sensitivity of this new technique. In particular, the spin of the first excited state of ${}^8\text{B}$ at 0.774 MeV is determined as $J=1$ via the p - ${}^7\text{Be}$ correlation function.

To better understand the isospin effects and to further confront calculations with experimental data, an empirically modified statistical multifragmentation model (SMM) was developed. This model treats the properties and decay of nuclear excited states self-consistently and calculates the secondary decay using the empirical information about the excited states. The importance of using empirical binding energies and experimental level densities is shown in detailed comparisons. Nuclear thermometry is studied and compared with data to demonstrate that the corrections for secondary decay can be modelled accurately within this approach.

From the isotopic composition of particles emitted during an energetic nucleus-nucleus collision, we can test the isospin dependence of the nuclear equation of state (EOS). Hybrid calculations were performed using isospin dependent BUU transport model and the improved SMM. Comparisons between measured isotopic yield ratios and theoretical predictions in the equilibrium limit are used to assess the sensitivity to the density dependence of the asymmetry term of the EOS. This analysis suggests preference for a stiff density dependence and indicates that such comparisons may provide an opportunity to constrain this important property of nuclear matter.

To

my wife - *Lihui Zhai*

and

my parents - *Guoyang Tan & Fengqin Wang.*

ACKNOWLEDGEMENTS

First of all, I would like to express my deepest gratitude to my thesis advisor, Dr. William G. Lynch. His invaluable support and guidance are indispensable for the completion of my thesis. In the past years, I have learned much from his deep understanding of nuclear physics on both experimental and theoretical aspects, his attitude and patience of doing physics research without omitting any details, and his strong leadership and enthusiastic stamina of completing research projects successfully. I would also like to thank Dr. S. Billinge, Dr. P. Danielewicz, Dr. C. Schmidt, and Dr. B. Sherrill for reading my dissertation and also serving on my guidance committee.

I am deeply indebted to the LASSA collaboration. Without the productive collaboration of the groups at Michigan State University (MSU), Indiana University (IU) and Washington University (WU), the LASSA project would not have been completed in such a great success. I would like to thank the MSU group of C.K. Gelbke, T.X. Liu, X.D. Liu, W.G. Lynch, M.B. Tsang, A. Vander Molen, G. Verde, A. Wagner, H.F. Xi and H.S. Xu, the IU group of L. Beaulieu, B. Davin, Y. Laroche, T. Lefort, R.T. de Souza, R. Yanez and V.E. Viola, and the WU group of R.J. Charity and L.G. Sobotka.

I am also very grateful to my collaborators on model calculations. I own my sincere thanks to Dr. Sergio Souza and Dr. Raul Donangelo from Brazil for their great help on SMM calculations. Dr. Bao-An Li from Arkansas State University offered valuable discussions and BUU calculations for the collaboration on studying the isospin dependence of the equation of state. I would also greatly appreciate the help of Dr. Bob Charity from Washington University for incorporating his GEMINI model into our statistical calculations. In the later stage of my thesis, Dr. G. Verde kindly offered a great amount of help on the imaging analysis and model simulations

of collective effects and I owe great thanks to him.

Special thanks go to Dr. Betty Tsang who has been very helpful throughout my thesis experiment and later data analysis. I have also benefited much from various discussions with Dr. Pawel Danielewicz, Dr. Konrad Gelbke and Dr. Scott Pratt. I want to thank Dr. Aaron Galonsky, Dr. Pawel Danielewicz and Dr. Betty Tsang for their kindness of providing me letters of references. I will cherish the friendship and various helps during my stay at NSCL from Michael Famiano, Marc-Jan van Goethem, Paul Hosmer, Patrick Lofy, Michal Mocho, Lijun Shi, Richard Shomin, Mark Wallace, besides people mentioned above.

I would like to acknowledge the excellent support of the staff at the National Superconducting Cyclotron Laboratory of Michigan State University. I appreciate the help from John Yurkon of the detector lab, Len Morris of the design group, Jim Vincent of electronics group, Ron Fox of the computer group and Mathias Steiner of the operations group.

Last but not the least, I would thank the love and patience of my wife and my parents, and the understanding and support of my sisters and brothers.

Contents

LISI OF TABLES	x
LIST OF FIGURES	xii
1 Introduction	1
1.1 Freeze-out Conditions of Multifragmentation	7
1.2 Fragmentation and Isospin Effects	9
1.3 Organization of the Thesis	10
2 Experimental Setup	12
2.1 Mechanical Setup	12
2.2 Electronic Scheme	14
2.3 Miniball/Miniwall	15
3 LASSA Telescopes	18
3.1 Silicon Detectors	20
3.1.1 Specifications	20
3.1.2 Energy Calibration	22
3.2 CsI(Tl) Detectors	23
3.2.1 Pre-selecting and Scanning CsI(Tl) Crystals	24
3.2.2 Testing Wrapping Materials	28
3.2.3 Other Effects and Assembly	31
3.2.4 Energy Calibration	34
4 Data Reduction and Analysis	39
4.1 Overview of the Analysis	39
4.2 Pixelation Technique	41
4.3 CsI Crosstalk	44
4.4 Uniformity Correction	46

4.5	Isotope Resolutions and PID	52
5	Particle Correlations	55
5.1	Selecting the Impact Parameters	56
5.2	Two Particle Correlations and the Koonin-Pratt Formalism	59
5.3	Influence of Collective Motion	69
5.4	Equilibrium Correlation Functions	84
5.5	Interpretations of Correlation Functions Using the Equilibrium Correlation Approximation	88
5.6	Spin Determination of Particle Unstable States	103
5.7	Multiple Particle Correlations	114
6	Statistical Multifragmentation Model with Empirical Modifications	120
6.1	Microcanonical Statistical Multifragmentation Model (SMM)	121
6.1.1	Underlying Formalism	121
6.1.2	Temperature Distributions	125
6.1.3	Effects of Temperature Variations	130
6.1.4	Chemical Potentials	135
6.2	Empirically Improved Model	140
6.2.1	Ground State Energies	140
6.2.2	Internal free energy	144
6.2.3	Empirical Sequential Decay	155
6.3	Model Predictions and Comparisons	158
6.3.1	Caloric Curve	158
6.3.2	Elemental and Mass Distributions	162
6.3.3	Isotope Thermometry	167
7	Isospin Dependence of the EOS	177
7.1	Density Dependence of Asymmetric EOS	178
7.2	Hybrid Model Calculations	181
7.3	Isotopic Composition and Isospin Dependence	184
7.3.1	Relative Free n/p Densities and Mirror Nuclei Ratios	186
7.3.2	Mirror Nuclei Ratios	190
7.4	Remarks	190
8	Summary	193

List of Tables

2.1	List of the original number of detectors in a ring of Miniball/Miniwall, the solid angle of a detector in that ring, and the numbers of mounted and removed detectors in that ring, respectively.	17
3.1	List of fragmentation products used in the energy calibration of the LASSA CsI(Tl) crystals.	35
5.1	List of quantities are shown for the p-p correlations (Figs. 5.3-5.6) for inclusive and three different c.m. energy gates. The λ that relevant to the fraction of protons contributed to the fitted source and the rms radius r_{rms} of the two proton source are extracted from the fitted source distribution. The λ' values are calculated from the integral of the source functions for $r \leq 7$ fm in Eq. 5.5. The density ρ/ρ_0 is estimated by taking into account collective effects in Eq. 5.9.	66
5.2	List of quantities are shown for the d- α correlations (Figs. 5.12-5.13) for inclusive data and three different c.m. energy gates. The λ that relevant to the fraction of the involved particles contributed to the fitted source and the rms radius r_{rms} of the two proton source are extracted from the fitted source distribution. The density ρ/ρ_0 is estimated by taking into account collective effects in Eq. 5.9.	78
5.3	Relevant spectroscopic information of ${}^6\text{Li}$, ${}^7\text{Li}$, ${}^7\text{Be}$ and ${}^8\text{Be}$ which is adopted from ref. [98] is listed for the correlation functions discussed in this section.	93
5.4	List of quantities are shown for the d- α , t- α , ${}^3\text{He}$ - α and α - α correlations (Figs. 5.16-5.19). The values of V_f/V_0 are obtained from the corresponding experimental correlation functions. F_{dec} is the correction factor in Eq. 5.26 calculated from secondary decay contributions in the SMM. The density ρ/ρ_0 is estimated in Eq. 5.28 using the secondary decay correction factor F_{dec} from the SMM while $\rho/\rho_0(\text{KP})$ is obtained using $F_{dec}(\text{KP})$ (see text). The corresponding ρ_f/ρ_0 and $\rho_f/\rho_0(\text{KP})$ are calculated in Eq. 5.29 without considering excluded volumes. . . .	102
5.5	Spectroscopic information of ${}^{10}\text{B}^* \rightarrow \alpha + {}^6\text{Li}$ adopted from ref. [98]. The state at the 6.56 MeV is assigned tentatively with J=4 and only alpha decay is confirmed. The last three states contribute very little to the fitting. For details see text.	112

6.1	Best fit parameters to the LDM formula of ref. [105]-[106]. All the values are given in MeV, except for k which is unitless.	142
6.2	List of isotopic thermometers with $\Delta B > 10$ MeV. The left column shows the IMF thermometers involving isotopes of $3 \leq Z \leq 8$. The right column lists the He thermometers involving the isotope pair of ${}^3,4\text{He}$	170
7.1	The first two columns provide the N/Z ratio and number of nucleons in the prefragments produced in the calculations for an elapsed time of 100 fm/c and density cutoff of $\rho_0/8$. The next two columns provide corresponding information for the same cutoff density but a shorter elapsed time of 80 fm/c. All calculations were performed at an impact parameter of 1 fm.	183

List of Figures

2.1	Schematic drawing of Miniball/Miniwall + LASSA setup in the vertical plane.	13
2.2	Miniball/Miniwall + LASSA setup housed in the 92" chamber.	14
2.3	Miniball/Miniwall + LASSA detector setup viewed inside from the beam direction.	15
2.4	Schematic diagram of electronics setup for LASSA.	16
3.1	One of the nine identical LASSA telescopes.	19
3.2	Picture of one 500 μm thick double-sided silicon strip detector.	20
3.3	Pulsar calibration for three dynamic ranges.	23
3.4	Energy calibration for a typical silicon strip.	24
3.5	CsI crystal scanning setup with alpha source.	25
3.6	Uniformity results of accepted and rejected CsI crystals.	27
3.7	Comparisons of different wrapping materials used for CsI crystals.	29
3.8	CsI preamplifiers and their housing.	32
3.9	CsI packing in one telescope.	33
3.10	Calibration curves for ^{11}C , ^{12}C , ^{13}C and ^{14}C for the CsI (Tl) crystals obtained using direct fragmentation beams listed in Table 3.1. The curves are the best fit according to Eq. 3.1.	37
4.1	Flow chart of data analysis for the LASSA.	40
4.2	EB-EF fine-tuning calibration for pixelation. On the left panel discrepancy between EB and EF calibrated from the precision pulser is shown. After the EB-EF flattening routine is applied, the good agreement between EB and EF is shown on the right panel.	42
4.3	layout of CsI crystals within one telescope and typical crosstalk shown for light leakage from CsI X to CsI Y in Telescope 2. Similar results for CsI Y \rightarrow CsI X are not shown. Units are in raw channel numbers.	45
4.4	Non-uniformity of one typical 65 μm thick silicon detector.	47
4.5	Non-uniformity of one typical 500 μm thick silicon detector.	48
4.6	PID lines of Li and C isotopes before and after uniformity correction.	49

4.7	Isotopically resolved PID lines from H to O are shown for particles stopped in Silicon Detectors	50
4.8	Isotopically resolved PID lines from H to O are shown for particles stopped in CsI crystals	51
4.9	One-dimensional PID lines from H to O are shown for particles stopped in Si detectors	52
4.10	One-dimensional PID lines from H to O are shown for particles stopped in CsI crystals	53
4.11	Mass resolution is illustrated from one-dimensional PID plots of Carbon isotopes. Left panel is for Carbons stopped in the second layer of Silicon detectors. Right panel is for Carbons stopped in the CsI crystals.	54
5.1	reduced impact parameter as function of total charged particle multiplicity.	57
5.2	Differential multiplicites of hydrogen and helium isotopes at angles of 17° , 27° , 37° , 47° and 57°	58
5.3	Inclusive p-p correlation function in central $^{129}\text{Xe}+^{197}\text{Au}$ collisions at $E/A = 50$ MeV is shown. The black points are experimental data and the grey line is the best fit by the imaging technique. See table 5.1 for specific parameters.	61
5.4	The p-p correlation functions are shown for three c.m. energy gates of $0 < E_{cm} < 15$ MeV, $15 < E_{cm} < 30$ MeV, and $E_{cm} > 30$ MeV. For the middle and high energy gates, the image technique is used. The simple Gaussian source parametrization in Eq. 5.6 is applied for the low energy gate. See table 5.1 for specific parameters.	62
5.5	The imaged source function is shown by inverting the p-p correlation in Fig. 5.3. See table 5.1 for the extracted source radius.	63
5.6	The source functions are shown for the p-p correlation functions in Fig. 5.4 for three c.m. energy gates of $0 < E_{cm} < 15$ MeV, $15 < E_{cm} < 30$ MeV, and $E_{cm} > 30$ MeV. For the middle and high energy gates, the image technique is used. The simple Gaussian source parametrization in Eq. 5.6 is applied for the low energy gate. See table 5.1 for extracted source radii.	65
5.7	The inclusive d- α correlation function for the central collision gate is shown as a function of relative momentum by the black points. The solid line is the fit by the simple Gaussian source parametrization in Eq. 5.6 without corrections for collective motion. The blown-up in the top right shows the poor quality of the fit to the second peak of the d- α correlation.	68
5.8	A source with only thermal motion (open arrows) is shown on the left. The collective velocity field (solid arrows) is drawn on the right and results in a grey area of the source where emission into the right half plane is improbable.	69

5.9	The source reduction factor, f_{coll} , obtained from the ratio of the rms radius to the system radius for the two particle sources with collective motion, are shown by the solid line as a function of the mass number. The ratio without collective motion is denoted by the dashed line. The solid line is calculated for a uniform spherical system with a radius of 11 fm while the three symbols denote the corresponding calculations for a system with a radius of 7 fm.	72
5.10	The solid line shows a simulation of the resonant distribution as a function of relative energy for the d-alpha correlation. The dashed line denotes the simulation for non-resonant background while the dotted line demonstrates the relative energy distribution for mixed event background. All the distributions are normalized to one for comparisons. .	74
5.11	The ratios of the resonant yield over the mixed event distribution for the d-alpha correlation are shown in three panels for maximum, 80% and zero of the collective motion, respectively. The corresponding values of T_{eff} are extracted from the fits (dashed lines).	75
5.12	The inclusive d-alpha correlation function for the central collision gate is shown as a function of relative momentum by the black points. The solid line is the best fit by the simple Gaussian source parametrization in Eq. 5.6 with T_{eff} corrections for collective motion. The blown-up in the top right shows the good reproduction of the second peak of the d-alpha correlation after T_{eff} corrections. The extracted source radius is $r_0 = 3.3$ fm (see Table 5.2 for the rms value). The dashed and dotted lines are the fits assuming that the source radius is $r_0 = 2.0$ fm and $r_0 = 5.0$ fm, respectively.	77
5.13	The d-alpha correlation functions are shown for three c.m. energy gates of $0 < E_{d,cm} < 20$ MeV and $0 < E_{\alpha,cm} < 25$ MeV, $20 < E_{d,cm} < 40$ MeV and $25 < E_{\alpha,cm} < 45$ MeV, and $E_{d,cm} > 40$ MeV and $E_{\alpha,cm} > 45$ MeV. Fits by the simple Gaussian source parametrization in Eq. 5.6 are shown by the solid lines after T_{eff} corrections for collective motion. See table 5.1 for extracted source radii and λ values.	79
5.14	The ratios of the resonant yield over the mixed event distribution for the p-p correlation are shown in three panels for maximum, 50% and zero of the collective motion, respectively. The corresponding values of T_{eff} are extracted from the fits (dashed lines).	80
5.15	The experimental d-alpha correlation function is shown. The smooth solid line is the empirical background used for the analysis. The dashed and dotted lines are the Coulomb correlation calculated from Eq. 5.21 for sharp sphere radii of $R=12.4$ and 15.6 fm, respectively.	89
5.16	The left panel shows the experimental d-alpha correlation function. The solid, dashed and dotted lines are the different backgrounds used for the estimation of uncertainty. The right panel exhibits the fit of the first resonance peak after subtracting the background (solid line in the left panel).	92

5.17	The experimental t- α correlation function is shown in the left panel. The solid, dashed and dotted lines are the different backgrounds used for the estimation of uncertainty. The right panel exhibits the fit of the first resonance peak after subtracting the background (solid line in the left panel).	94
5.18	The left panel shows the experimental ^3He - α correlation function. The solid, dashed and dotted lines are the different backgrounds used for the estimation of uncertainty. The right panel exhibits the fit of the first resonance peak after subtracting the background (solid line in the left panel)	95
5.19	The experimental α - α correlation function is shown in the left panel. The solid, dashed and dotted lines are the different backgrounds used for the estimation of uncertainty. The right panel exhibits the fit of the first resonance peak after subtracting the background (solid line in the left panel).	95
5.20	The densities of the resonance states from d- α , t- α , ^3He - α and α - α correlations are fitted after subtracting the backgrounds carefully selected by the solid lines in Figures 5.16-5.19.	97
5.21	The proton- ^7Li correlation function is plotted. The dashed line is the selected background. See text for details.	104
5.22	The density profile of the resonances of ^8Be is shown in the p- ^7Li correlation after subtracting the background selected in Figure 5.21.	106
5.23	The best fit (solid line) is performed for the p- ^7Li correlation by varying the background and the spin value of the 17.64 MeV state. The dashed line is the fitted background. Two calculations are shown as the dotted lines assuming that the spin of the 17.64 MeV state is 0 and 2, respectively and keeping the other parameters the same.	107
5.24	The p- ^7Be correlation function is fitted by the solid line assuming only two states at 0.774 MeV and 2.32 MeV. The dashed line is the fitted background.	109
5.25	The p- ^7Be correlation function is fitted by the solid line assuming the existence of an additional state at 1.4 MeV. The dashed line is the fitted background.	110
5.26	The α - ^6Li correlation function is fitted by taking into account all the spectroscopic information shown in Table 5.5 except for the 6.56 MeV state. By varying the spin of the 6.56 MeV state from 1 to 4 and assuming the decay branching ratio is 100%, one obtains the dashed, solid, dotted and dot-dashed fitting lines, respectively. If a branching ratio of 55% is assumed, the solid line represents a fit of J=4.	111
5.27	The α - α - α correlation function is shown. Resonances from the excited states of ^{12}C are labelled with the first peak seen more clearly in the inner upright panel.	116
5.28	The p-p- α correlation function is shown.	117
5.29	The p- α - α correlation function is plotted. The resonances from the decay of ^9B are shown.	118

5.30	The d- α - α correlation function is shown. The resonance states of ^{10}B that contribute this decay are listed. See detailed discussions in text.	119
6.1	The points denote distributions of temperatures calculated with the SMM approach for the decay of a ^{112}Sn nucleus at three different excitation energies. The lines denote gaussian fits to the calculated distributions.	126
6.2	The points denote temperature distributions calculated with the SMM approach for the different isotopes considered in the carbon thermometer for an excitation energy of $E_0^*/A = 6\text{MeV}$. The lines denote gaussian fits to the calculated distributions.	127
6.3	Comparisons of various primary temperatures T_{MIC} , T_{IMF} and T_{iso}^{smm} from the SMM and T_{iso}^{cal} from the analytical calculation in the grand canonical limit. For details see the text. One point is missing for T_{iso}^{cal} with $\sigma_T = 0.8\text{MeV}$ because the calculated value for p for the correction term in Eq.(6.17) becomes negative at $E_0^*/A = 3\text{MeV}$, i.e. the expansion breaks down in this case.	129
6.4	The solid squares and circles denote the free proton and neutron yields, respectively, calculated via the SMM approach. The solid and dashed lines denote fits to the calculated yields following Eq. (6.23).	134
6.5	The squares, circles and triangles denote neutron chemical potentials derived from Eq. (6.24) using SMM predictions for Carbon and Lithium isotopic yields at various initial excitation energies for the decay of the nucleus ^{112}Sn . The stars and the dot-dashed line denote approximate values calculated from Eq.(6.28) for $T=0$ and 4.58 MeV , respectively. The error bars denote the statistical errors in the calculation, which in many cases are too small to be observed in the figure.	137
6.6	Difference between the <i>total</i> binding energies predicted by the LDM and those recommended in ref. [104]. Plot A corresponds to the parameter set adopted in standard SMM [103], whereas Plot B is obtained using the parameters presented in this work.	142
6.7	Total binding energies for different nuclei. The full lines correspond to the corrected LDM formula, whereas the symbols represent the experimental data of ref. [104]. The dashed lines correspond to the predictions given by Eq. (6.30). For details see text.	143
6.8	Internal free energies for $A = 20$ (upper panel) and $A = 200$ (lower panel). The standard SMM expression [Eq. (6.34)] is represented by the full line whereas the dashed lines stand for the results obtained with the Taylor expansion [Eq. (6.36)]. The Free energy calculated through the level density given by Eq. (6.38) is depicted by the symbols.	147

6.9	Level densities as a function of excitation energy for ^{20}Ne and ^{31}P . Two energy ranges are plotted to show the behaviors of level densities at both low and high energy ends. The density of experimentally known levels is shown as bars in the low energy region. The dashed lines are the extrapolations of the empirical values according to Eq. 6.43. The dotted lines are the level density (Eq. 6.38) parametrized from the standard SMM. The solid lines are the level density adopted in this work (Eqs. 6.49-6.52).	150
6.10	Comparison between $F^*(E)$ calculated through Eqs. (6.35) and (6.49)-(6.52), symbols, and the approximation given by Eq. (6.53), full line. To illustrate the influence of quantum effects at low temperatures, the dashed line represents the free energy used in standard SMM calculations Eq. (6.34). For details see text.	154
6.11	Best fit values of T_0 for different nuclei (symbols). The dashed line corresponding to Eq. 6.54 is used for $Z > 15$	155
6.12	Caloric curves are shown for calculations of the system of $A=168$ and $Z=75$ at fixed breakup density and multiplicity-dependent density. The dotted lines are calculated from the standard SMM. The dashed lines are calculated as empirical binding energies are taken into account. The solid lines are obtained from the improved model with empirical modifications of both binding energies and free energies.	160
6.13	Pressure curves due to kinetic motion and Coulomb interaction (see Eq. 6.58) are plotted for the system of $A=168$ and $Z=75$ at fixed breakup density and multiplicity-dependent density. The dotted lines are calculated from the standard SMM while the improved SMM presents the solid lines.	161
6.14	Average breakup multiplicities are shown for the system of $A=168$ and $Z=75$ at fixed breakup density and multiplicity-dependent density. The dotted lines are calculated from the standard SMM while the improved SMM presents the solid lines.	162
6.15	Dependences of temperature on excitation energy and breakup density are shown for the system of $A=168$ and $Z=75$. Calculations as function of excitation energy at fixed density of $1/6$ normal density are shown as solid circles. Calculations as function of density at fixed excitation energy are shown as open squares.	163
6.16	Mass and charge distributions are shown for the system of $A=186$ and $Z=75$. The dashed lines are the calculations from the standard SMM. The solid lines are calculated using the improved model.	164
6.17	Final mass and charge distributions after applying the empirical secondary decay procedure discussed in Sect. 6.2.3. The dashed lines are calculated from the primary results of the standard SMM while the solid lines are from the improved model.	166
6.18	Final mass and charge distributions from the present model (solid lines) and the Botvina version (dashed lines) are shown. For reference, some measured data is plotted as solid circles.	167

6.19	Primary isotopic distributions are shown for Be, C, O and Ne nuclei. The dashed lines correspond to the calculations of the Botvina code while the solid lines represent the results of the improved model. . . .	168
6.20	Isotopic distributions are shown for isotopes from Li to O. Experimental data is shown as the solid circles. The dashed lines denote the Botvina calculations and the solid lines are the final distributions after decaying the hot primary fragment via the empirical secondary decay procedure discussed in Sect. 6.2.3.	169
6.21	Isotopic temperatures are extracted from 18 IMF thermometers (see table 6.2) with $3 \leq Z \leq 8$ and $\Delta B > 10$ MeV. Experimental data is shown as the solid circles. The open squares are the calculations from the improved model. For reference, the primary temperature calculated from the present model is shown as the dashed line.	171
6.22	Isotopic temperatures are extracted from 18 IMF thermometers (see table 6.2) with $3 \leq Z \leq 8$ and $\Delta B > 10$ MeV. Experimental data is shown as the solid circles. The open triangles are the calculations from the Botvina model. For reference, the primary temperature calculated from the present model is shown as the dashed line.	172
6.23	Isotopic temperatures are extracted from 12 light thermometers (see table 6.2) satisfying $\Delta B > 10$ MeV and involving the isotope pair of ${}^3,{}^4\text{He}$. Experimental data is shown as the solid circles. The open circles are the calculations from the present model without corrections of nonequilibrium emissions. For reference, the primary temperature calculated from the present model is shown as the dashed line.	174
6.24	Isotopic temperatures are extracted from 12 light thermometers (see table 6.2) satisfying $\Delta B > 10$ MeV and involving the isotope pair of ${}^3,{}^4\text{He}$. Experimental data is shown as the solid circles. The open squares are the calculations from the present model with corrections of nonequilibrium emissions of ${}^3\text{He}$. For reference, the primary temperature calculated from the present model is shown as the dashed line.	175
6.25	Isotopic temperatures are extracted from 12 light thermometers (see table 6.2) satisfying $\Delta B > 10$ MeV and involving the isotope pair of ${}^3,{}^4\text{He}$. Experimental data is shown as the solid circles. The open circles are the calculations from the Botvina code. For reference, the primary temperature calculated from the present model is shown as the dashed line.	176
7.1	The symmetry potential for neutrons and protons is shown for two different density dependences of asymmetry term: asy-stiff F_1 and asy-soft F_3 (see Eqs. (7.4)).	180
7.2	Isotopic distributions from Li to O are shown for central collisions of ${}^{124}\text{Sn}+{}^{124}\text{Sn}$. The full circles are experimental data while the solid (dashed) lines denote the final (primary) calculations from the hybrid model using the density dependence asy-stiff F_1 (Eq. 7.4) for the asymmetry term of the EOS.	184

7.3	Isotopic distributions from Li to O are shown for central collisions of $^{124}\text{Sn}+^{124}\text{Sn}$. The full circles are experimental data while the solid (dashed) lines denote the final (primary) calculations from the hybrid model using the density dependence asy-soft F_3 (Eq. 7.4) for the asymmetry term of the EOS.	185
7.4	Relative isotope ratios, R_{21} , of two reactions $^{124}\text{Sn}+^{124}\text{Sn}$ and $^{112}\text{Sn}+^{112}\text{Sn}$ are shown as a function of neutron number. The upper panel presents the primary calculations using the hybrid model while the final isotope ratios after secondary decay are plotted in the lower panel. The lines denote the best fits through the symbols with the same slope.	187
7.5	Both panels: The solid circles and solid squares show values for $\hat{\rho}_p$ and $\hat{\rho}_n$, respectively; measured in central $^{112}\text{Sn}+^{112}\text{Sn}$, $^{112}\text{Sn}+^{124}\text{Sn}$ and $^{124}\text{Sn}+^{124}\text{Sn}$ collisions at $E/A=50$ MeV. Left panel: the open and cross-hatched rectangles show corresponding hybrid calculations for R_{21} calculated from the primary and final fragment yields, respectively, predicted by the hybrid calculations using the Asy-stiff EOS. Right panel: the open and cross-hatched rectangles show corresponding hybrid calculations for R_{21} calculated from the primary and final fragment yields, respectively, predicted by the hybrid calculations using the Asy-soft EOS.	189
7.6	The solid and open points in the upper and lower panels show the mirror nuclei ratios measured for $^{124}\text{Sn}+^{124}\text{Sn}$ and $^{112}\text{Sn}+^{112}\text{Sn}$ collisions, respectively. Left panels: The open and cross-hatched rectangles show corresponding hybrid calculations of the mirror nuclei ratios calculated from the primary and final fragment yields, respectively, predicted by the hybrid calculations using the Asy-stiff EOS. Right panel: The open and cross-hatched rectangles show corresponding hybrid calculations of the mirror nuclei ratios calculated from the primary and final fragment yields, respectively, predicted by the hybrid calculations using the Asy-soft EOS.	191

Chapter 1

Introduction

Nuclear matter is a strongly-interacting Fermi liquid [1, 2] at low temperature and is expected to undergo a phase transition to a nucleonic gas within a mixed phase region bounded by a critical temperature of order 15 MeV [3]-[6]. This liquid-gas phase transition is one of two bulk phase transitions in strongly interacting matter. The other is the transition between hadronic matter and the quark-gluon plasma, which is being studied at the Relativistic Heavy Ion Collider (RHIC) and elsewhere [7, 8].

The properties of mixed phase of the liquid-gas phase transition have been calculated in a number of equilibrium theories [9, 10, 11]. In general, these theories predict the equilibrium distribution will be characterized by a mixture of light particles with $Z \leq 2$ and intermediate mass fragments (IMF's) with $3 \leq Z \leq 30$. Such fragments are rarely emitted in the decay of compound nuclei at low excitation energies $E^*/A \leq 2$ MeV, but become emitted with increasing multiplicity as the excitation energy is increased significantly beyond that approximate threshold [12, 13, 14]. These excitation energies can be easily achieved at the NSCL as well as at other intermediate energy heavy ion facilities.

Experimentally there are basically three ways to generate multifragmentation. One is by central collisions of two heavy ions of comparable masses at incident en-

ergies of 40-100 MeV per nucleon. This is the type of experiment performed in this thesis. Dynamical calculations indicate that such collisions lead to dilute systems in central collisions at energies greater than $E/A=35$ MeV [15, 16]. From a purely dynamical point of view, multiple fragment production from the bulk system is very likely in such collisions when the density drops below and the system cross into the region of adiabatic instability, density fluctuations grow exponentially and spinodal decomposition may occur [17]. In addition to central collisions, one can also investigate multifragmentation in peripheral collisions (large impact parameters) of heavy ions at incident energies of a few hundred MeV per nucleon. Such studies have been pursued by groups at GSI and Berkeley [18, 19, 20]. The third approach is by light ion induced collisions with much higher bombarding energies (> 1 GeV per nucleon) [21]. All these reactions can form sources with excitation energies that exceed the threshold predicted for statistical multifragmentation and multifragmentation has been observed for the highly excited systems produced in all three reaction scenarios.

Studies of multifragmentation invoked the application of statistical techniques to nuclear systems with a finite number of particles. Such applications have a long tradition in nuclear physics that started with the description of highly excited compound nuclei. The properties of nuclei or nuclear matter have been well studied at their low-excited states, where the nuclear shell and collective models have been successfully used to predict the behaviors of these states. The beta, gamma, alpha and fission decay modes of these states have been well studied. Formalisms exist to calculate these decay rates, and to provide information about the parent and daughter nuclear states. As the system becomes more excited, the decay properties of individual states become more difficult to isolate. Then the average properties of groups of states or levels become the quantity that is measured. The natural choices for model descriptions of such average properties become the statistical formalisms by Weisskopf or

Hauser and Feshbach[22, 23] and such models describe well the emission of nucleons or light clusters.

In such models, the concept of nuclear temperature is introduced as a parameter that describes the ensemble average over the various collisions with slightly different incident energies, which contribute to the measured data. The validity of a thermal approximation for such finite systems is sometimes questioned by scientists that are more familiar with the thermal properties of much larger systems. In the nuclear case thermal approximations are justified because of the large number of initial states that one is averaging over when one collides projectile and target nuclei under well controlled conditions. To illustrate this point, consider the formation of a compound nucleus with 150 nucleons at an excitation energy of 2 MeV per nucleon ($E^* = 300$ MeV). Like all Fermionic systems at moderately low temperature, the excitation energy of such a system in contact with a thermal bath at temperature T is given by a quadratic relationship: $E^*/A = T^2/\epsilon_0$, where T is the temperature in units of MeV and ϵ_0 is a parameter which for nuclei is of order 8 MeV. It is straightforward exercise in thermodynamics to show that implies that the number of states per unit energy $\rho(E^*)$ is given by

$$\rho(E^*) \propto \exp\left(2A\sqrt{E^*/(8A)}\right) \approx \exp(200). \quad (1.1)$$

Using the K1200 cyclotron, one can study such a system using a beam with a typical energy resolution of about 0.3% ($\Delta E^* = 0.9\text{MeV}$). Taking a standard nuclear level density formula [24] one can estimate that there are about 10^{83} levels in this energy window. Even the population of a small fraction of these states in the entrance channel leads to a vast ensemble of quantum states over which one is averaging. One therefore does not need the existence of an external thermal reservoir to justify the thermal limit.

At the higher excitation energies characteristic of multifragmentation processes, the thermal limit is therefore justified provided the systems reach a state where the approximation of local thermal equilibrium may be applied. Equilibrium models simply assume that equilibrium is achieved at a given freezeout time and characterized by a freezeout density (probably $0.1-0.4\rho_0$) and temperature (typically 4-7 MeV) or excitation energy (typically $E^*/A \geq 3$ MeV). Phase transition arguments may be relevant when equilibrated system is dilute. Whether such dilute systems can be described as an equilibrated phase mixture of fragments (liquid) and light particles (gas) is one of the important questions that need to be addressed [13, 14]. Although some problems related to the finite size effects have been studied [25, 26], the question of how the system goes out of equilibrium and equilibrium observable are modified as fragments and nucleons decouple from each other and propagate to the detectors is usually not addressed.

For the interpretation of such fragment production in terms of a bulk disintegration, it was important to assess how quickly the system disintegrates and exclude the possibility of a slow sequential series of binary fission-like decays, each of which increases the fragment multiplicity by one. Two observations rule out such decays occurring over the long time scales normally associated with fission: 1) Correlations between pairs of fragments emitted in such breakups reveal an anticorrelation in the fragment emission at low fragment-fragment relative energies due to their mutual Coulomb repulsion [27]. Strong anticorrelations are observed between every pair of fragments which implies short breakup timescales that are inconsistent with a slow sequence of binary decays, but within the range expected for a bulk multifragment disintegration [28]. 2) An approximately linear mass dependence of the mean fragment energies in the center of mass has been observed indicating a collective expansion that at incident energies of $E/A=50$ MeV and above exceeds values consistent with

a purely Coulomb induced expansion. Both observations imply breakup time scales of the order of 100 fm/c or less.

Temperatures have been obtained for such events from measurements of fragment isotopic yields [29, 30, 31, 32] and excited state populations [33, 34, 35]. These measurements are consistent with there being a plateau of the nuclear caloric curve at temperatures of about $T \sim 5$ MeV and $E^*/A \approx 3$ -10 MeV [29]. In equilibrium scenarios, such a plateau is theoretically expected [36] for multifragmentation process, reflecting the latent heat for transforming the nuclear liquid to the nucleonic vapor. Scaling laws have also been observed in the fragment elemental [37, 38] and isotopic [39] distributions. The former observation has been loosely interpreted by many authors using Fisher liquid drop theory [40] to extract critical parameters and the critical temperature for nuclear multifragmentation [38]. The observation of isotopic scaling laws, discussed in this thesis, provides a powerful simplification of the dependence of the fragment isotopic distributions on the overall isospin of the system [41, 42].

Despite these interesting developments, there are many missing elements in the interpretation of fragmentation observables in terms of phase transitions. The early stages of the reaction during which energy is deposited and may or may not be equilibrated are not described by such models. Thus, practitioners have the freedom to adjust the thermal energy (or temperature) and the breakup density to improve the agreement with data. This has delayed the determination of whether equilibrium bulk fragmentation models are justified and should be used instead of time dependent rate equation [43] or dynamical fragmentation [44] approaches. There have also been very few real tests of equilibrium multifragmentation models other than comparisons to fragment charge distributions and their related multiplicities [45]. Comparisons to energy spectra within equilibrium models are not very quantitative because such require the manual inclusion of collective motion induced by the earlier dynamical

evolution. More and better tests are possible if one can compare equilibrium calculations to isotopically resolved data, excited state populations and other observables. The predictions for such observables, however, require an accurate description of the secondary decay of the excited fragments that had not been available prior to this thesis work [26, 46].

Even though most theoretical studies of multifragmentation have involved equilibrium models, it is relevant to consider the alternative approaches. More generally, theoretical models for the multifragmentation process can be divided into two categories: static and time dependent. Examples of static models include multi-particle phase space models, such as the Statistical Multifragmentation Model (SMM) [36, 9] and the Berlin multifragmentation model [47], which can incorporate specific nuclear properties more directly. Accordingly, a semi-microcanonical version of SMM [36] that incorporates detailed nuclear structure information relevant to the population and secondary decay of the excited fragments was developed [26, 46] and utilized as part of this thesis work. Additional static models include percolation [48] and lattice gas [49] approaches; these approaches have the virtue of providing relatively simple schematic algorithms suitable for the exploration of critical phenomena in finite systems.

Statistical rate equations, which allow the description of time dependent phenomena within a statistical framework, have long been the standard approach for calculating the decay of equilibrated compound nuclei and also provide an alternative description of multifragmentation [43]. An extension of these approaches to the case of fragment emission from an expanding residue has been developed by Friedman [10]. This Expanding Emitting Source (EES) model predicts a rapid emission of fragments once the density of the residue decreases below about $0.4\rho_0$, and is consistent with many basic multifragment observables [50, 51]. In its present form, however, the

description of multifragmentation is still rather schematic, leaving out many specific nuclear properties that influence fragment isotopic distributions and excited state populations.

More complete dynamical approaches, such as the Boltzmann-Uehling-Uhlenbeck transport model (BUU)[44], solve equations of motion that involve a self-consistent mean field. Solutions of the BUU equation provide the Wigner transform of the one body density matrix. Hybrid calculations that use the BUU equation to define the input excitation energies and source size for various statistical models can then be explored (e.g. [42]). The calculation of fragment yield directly via the BUU model without the hybrid approach is not feasible, however, because density fluctuations that lead to fragment formation are suppressed in the BUU equation. Therefore, alternative formalisms, such as the Stochastic Mean Field model [52] and Antisymmetrized Molecular Dynamics model (AMD)[53] have been developed to address this deficiency. These approaches, however, have not progressed to the point that accurate predictions of isotopic observables are currently possible. In the absence of a better description of dynamical fragment production, we therefore test the equilibrium assumptions via comparisons of data to equilibrium calculations or hybrid BUU-SMM calculations, using the improved SMM we developed, which can provide quantitative comparisons to fragmentation observables.

1.1 Freeze-out Conditions of Multifragmentation

Every equilibrium multifragmentation approach requires external input that specifies two independent intensive parameters of the equilibrated system at freezeout. These two parameters could be the excitation energy per nucleon and temperature. Excitation energy be somewhat constrained by measurements are sensitive to the thermal

energy of the system. Examples of such measurements are the energies and mass distributions of particles emitted from projectile- or target-like residues in peripheral heavy ion collisions [29]. Such information is not readily available in central collisions. Isotope temperatures may be extracted from measurements of double ratios of isotopic yields [29, 30, 31, 32] of IMF's using the Albergo formula[54] and excited state temperatures may be obtained from measurements of the relative populations of excited states of intermediate mass fragments [33, 34, 35]. Systematic measurements indicate that the values of $T = 5 \pm 0.5$ MeV may be expected in central nucleus-nucleus collisions temperatures at incident energies of about $E/A=50$ MeV.

The relationship between the excitation energy and the temperature is only weakly density dependent. Both excitation energy and temperature dependent observables are sensitive to preequilibrium emission prior to freezeout. Thus, it would be extremely useful to have an independent measure of the density or volume of the system, even in systems for which measurements of both quantities can be attempted. Compared to the large numbers of temperature measurements that have been performed, there are comparatively few measurements aimed at determining the density. The main attempts have involved classical analyses of fragment-fragment correlation functions [55, 56] and a recent attempt involving light particles [57].

In this thesis, we explore alternative density determinations, which utilize two particle correlation functions involving light particles and much lighter fragments. This work is more closely related to the intensity interferometry techniques, applied originally to the problem of measuring stellar radii by Hanbury-Brown and Twiss [58], adapted to strongly interacting particles by Koonin and others [59, 60] and utilized extensively in heavy ion reactions over a wide range of energies [61, 62]. Recently, Verde et al. [63] have revealed the importance of describing the detailed shape of such correlation functions; this work shows that the source size is related mainly

to the width of the correlation peak instead of the height [63]. Verde et al. also indicate how one can assess the degree to which the height of correlation functions are diminished by secondary decay effects and determine the importance of secondary decay processes [63].

Fruitful results are obtained in this dissertation by applying these ideas to multifragmentation events. In addition, such particle correlation functions are extended to much heavier particles by utilizing thermal correlation function techniques. These thermal correlation function techniques allow the extraction of additional information relevant to the freezeout assumption and suggests a new technique for spin determination of particle unstable states using correlation functions.

1.2 Fragmentation and Isospin Effects

The study of isospin effects in heavy ion reactions is expected to be a major theme for research at the CCF and later at RIA. Recently, investigations reveal the existence of isoscaling laws that govern the dependence of fragment isospin distributions on the total isospin of the system [41, 39]. This isoscaling behavior is manifested in multifragmentation, compound nuclear decay and in strongly damped heavy ion collisions [64]. The isoscaling parameters extracted for multifragmentation processes reveal the occurrence of isospin fractionation [41] whereby the gas phase manifested by the properties of the primary light particles prior to secondary decay is more enriched in neutrons than the liquid phase represented by the fragments.

The degree of fractionation appears to be sensitive to the density dependence of the asymmetry term of the nuclear equation of state (EOS). The nuclear EOS is a key property of nuclear matter that is very relevant to supernova explosions and to the structure and stability of neutron stars [65, 66, 67]. Experiments have succeeded

in constraining the EOS for symmetric matter at a variety of densities. The nuclear monopole and isoscalar dipole resonances[68], for example, have been performed to sample the curvature of the symmetric matter EOS near the saturation density ρ_0 . The collective flow measurements[69] place constraints on the symmetric matter EOS at densities as high as $4 - 5\rho_0$.

The properties of very neutron rich systems such as neutron stars, however, can be dominated by the asymmetry term. Unfortunately, the difficulties of finding observables sensitive only to the isospin effects and of creating very asymmetric matter under laboratory-controlled conditions have left the density dependence of the asymmetry term largely unconstrained. In this dissertation, we develop an improved SMM model and use it to investigate the sensitivity of the isoscaling parameters to the asymmetry term of the EOS [42]. These investigations suggest that the availability of high-intensity radioactive beams at the newly-upgraded coupled cyclotron facility (CCF) of Michigan State University and possibly at the proposed rare isotope accelerator (RIA), will make the exploration of the isospin dependence of the EOS one of the more interesting issues to be explored in coming years.

1.3 Organization of the Thesis

The following chapters are organized as follows. In Chapter 2 experimental setup for $^{129}\text{Xe}+^{197}\text{Au}$ at 50A MeV is described. Detailed specifications of the LASSA telescopes, the preparation of CsI scintillation detectors and energy calibrations of the LASSA telescopes are described in Chapter 3. In Chapter 4 the data reduction and analysis procedures are described in detail for the LASSA array. Two and three particle correlations obtained in this experiments are described in Chapter 5. There, a new technique for spin determination from particle correlations is proposed and a

probe to freeze-out density of breakup is discussed. In Chapter 6 an modified statistical multifragmentation model (SMM) which incorporates self-consistently nuclear structure information and calculates self-consistently the secondary decay of the excited fragments is described and predictions of the model and comparisons to data are discussed. In Chapter 7 possible constraints on the isospin dependence of the nuclear equation of state are presented by use of the model described in Chapter 6. Chapter 8 summarizes the findings of this dissertation.

Chapter 2

Experimental Setup

The experiment of $^{129}\text{Xe}+^{197}\text{Au}$ at 50A MeV was performed at the National Superconducting Cyclotron Laboratory (NSCL) with the K1200 accelerator. To measure the fragmentation of heavy ion collisions with particles emitted from all directions, a large detection system with nearly full solid angle coverage is required. In this experiment, the Miniball/Miniwall array[70] was utilized to cover most of the solid angle. However, the Miniball/Miniwall array alone can not fulfill the demanding measurements for this study due to its relatively coarse granularity and limited mass resolution. Therefore, a large area silicon-strip/CsI detector array (LASSA)[71, 72] was constructed to provide excellent energy, angular and isotope resolution for charged particles. This experiment was one of the four consecutive experiments conducted in the first campaign with the complete nine LASSA telescopes. More details about the LASSA will be discussed in the next chapter.

2.1 Mechanical Setup

The 92" scattering chamber at the NSCL was used to house the whole complex detector system (Miniball/Miniwall + LASSA) in vacuum. The ^{129}Xe beam with an intensity of $\sim 10^8$ particles per second was produced from the K1200 cyclotron to

bombard the 3 mg/cm^2 thick Au target.

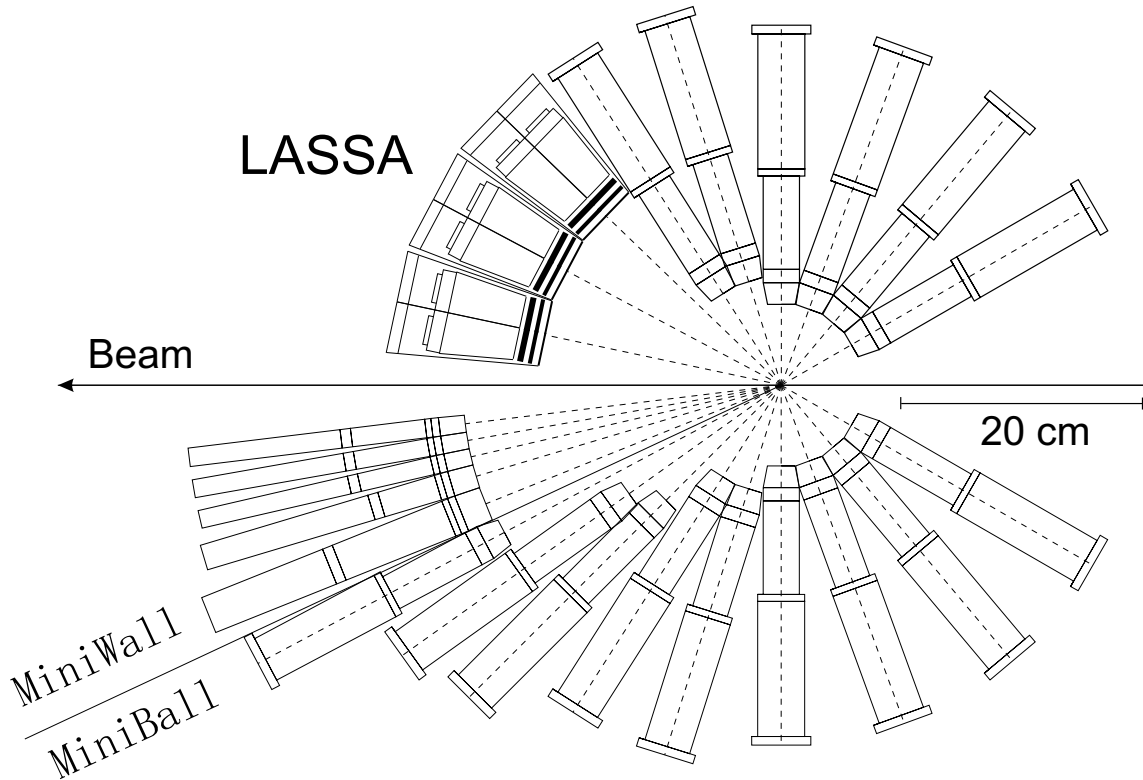


Figure 2.1: Schematic drawing of Miniball/Miniwall + LASSA setup in the vertical plane.

A schematic drawing of the detector setup in the vertical plane is shown in Figure 2.1. The 3 mg/cm^2 thick Au target was situated at the center of the Miniball array. The Miniwall array covered the forward angles $\theta \leq 25^\circ$ and provided a better granularity over this angular domain. Some of the forward elements of Miniball/Miniwall array were removed to insert the LASSA, which was centered at 35° and at a distance of 20 cm away from the target. The geometric acceptance of the combined apparatus was about 80% of 4π .

To reduce the noise level, the preamplifier system for the LASSA was mounted along with the detectors in the vacuum chamber. Photo 2.2 shows the sideview of the detector setup with these preamplifiers mounted above the array. A cooling system was run inside the chamber to remove the heat generated by the detectors and

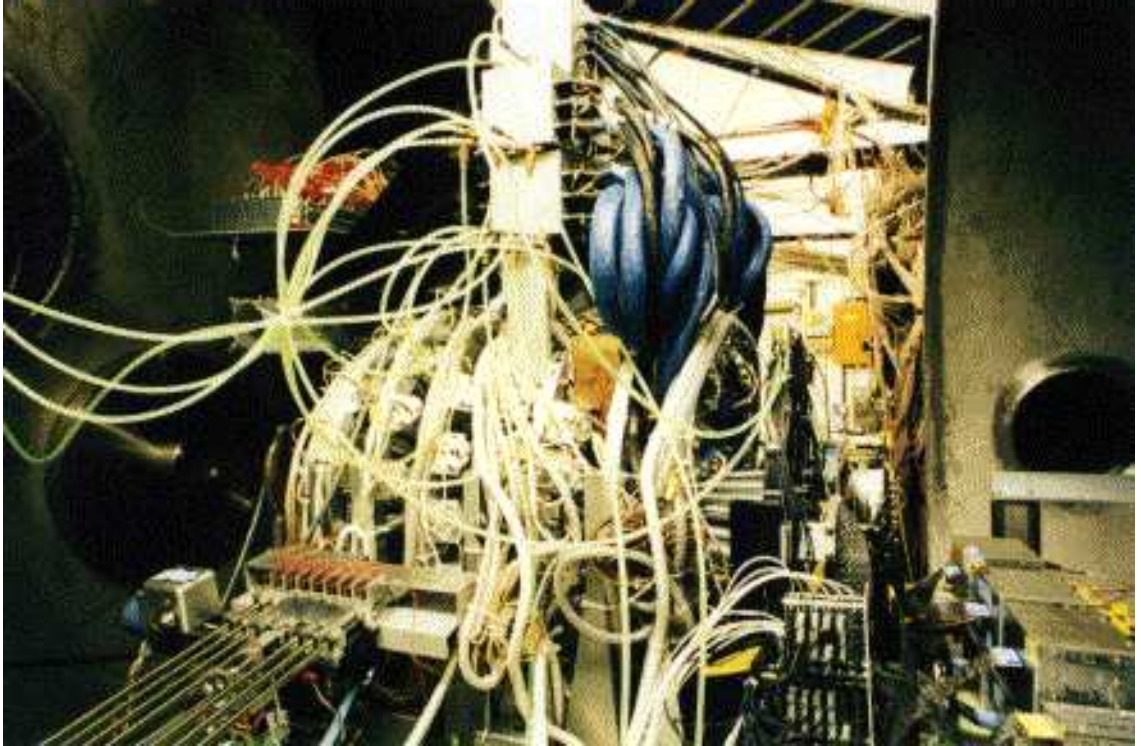


Figure 2.2: Miniball/Miniwall + LASSA setup housed in the 92" chamber.

preamplifiers. A temperature monitoring system was also installed with temperature sensors attached to critical elements and read out by a FERA module to ensure that the system remained near room temperature during the experiment.

Figure 2.3 shows a photograph viewing from the beam direction. This picture allows one an inside view of the detector setup after the experiments were finished. Some Miniball detectors in the upper and backward quadrant were removed in order to show all nine LASSA telescopes in the photo.

2.2 Electronic Scheme

The LASSA detectors required the development of a high density electronic system capable of processing the signals. Special CAMAC modules that contained 16 channels of shaping amplifiers and 16 channels of discriminators were developed by Washing-



Figure 2.3: Miniball/Miniwall + LASSA detector setup viewed inside from the beam direction.

ton university and used for the LASSA readout. A schematic of our electronic setup for processing the LASSA is shown in Figure 2.4.

2.3 Miniball/Miniwall

The original Miniball is a portable 4π phoswich detector array for the detection of charged particles. The array of 187 phoswich detectors covers the angular range $9^\circ \leq \theta_{lab} \leq 160^\circ$ with a solid angle of 89% of 4π . Each phoswich detector consists of a 0.08 mm ($8mg/cm^2$) thick plastic scintillator foil backed by a two cm thick CsI(Tl) crystal.

Particles which penetrate the plastic scintillator foil and stop in the CsI(Tl) crystal are identified by atomic number up to $Z=18$. Pulse shape discrimination in the

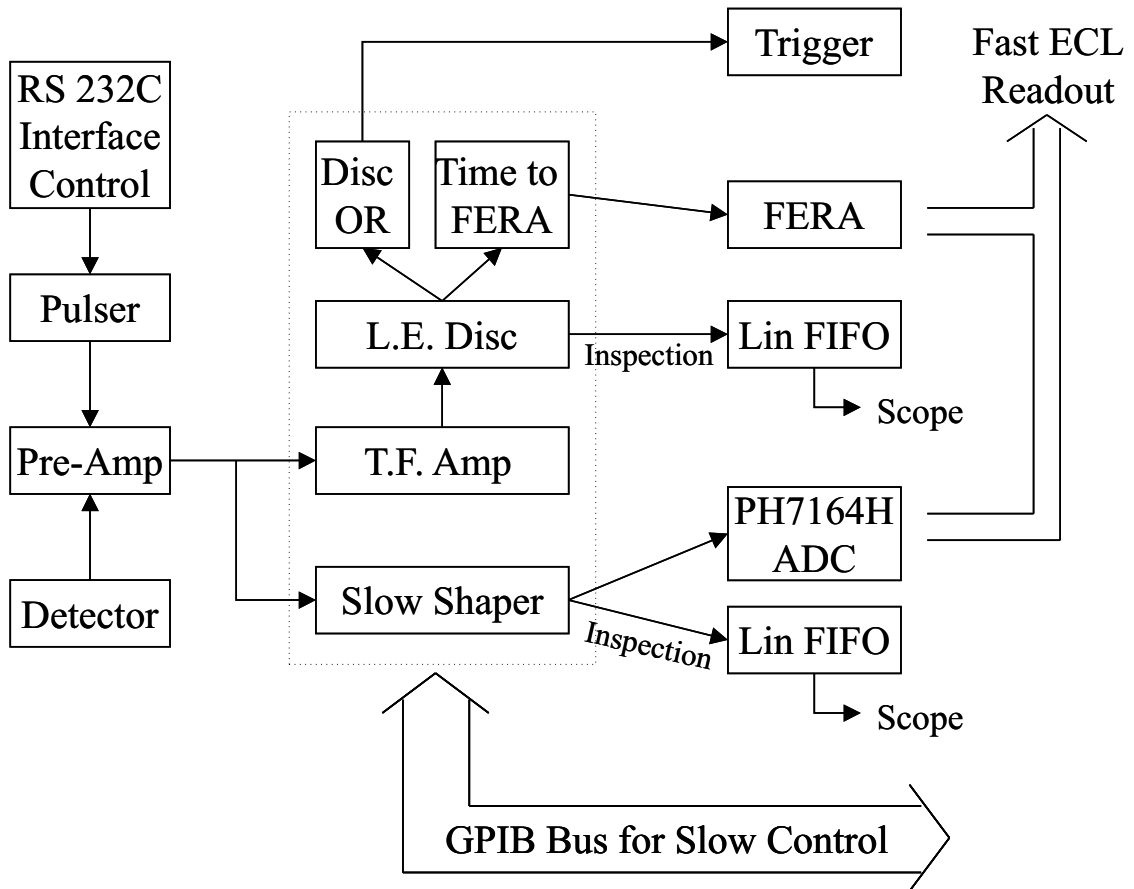


Figure 2.4: Schematic diagram of electronics setup for LASSA.

CsI(Tl) crystals provides isotopic resolution for H and He isotopes as well. Approximate energy thresholds are of the order of 1 MeV for the detection of a charged particle "hit" in the plastic scintillator. The thresholds to particle identifications are about $E_{th}/A=2$ MeV for $Z=3$, $E_{th}/A=3$ MeV for $Z=10$, and $E_{th}/A=4$ MeV for $Z=18$ fragments. However, these thresholds are not very relevant to this thesis work because the Miniball/Miniwall array were used only for providing the multiplicity of hits. The hit multiplicity was used to gate centrality of collisions as discussed in Chapter 4. More details about the detector can be found in the reference by de Souza et al., Nucl. Instr. and Meth. A295, 109 (1990).

To increase the granularity of the Miniball in the forward direction, the Washington University group (L. Sobotka and R. Charity) constructed a forward array of

128 fast plastic - CSI phoswich detectors that mates exactly to the MSU Miniball at 25° . Similar to the Miniball detectors, each Miniwall phoswich detector consists of a $\sim 8mg/cm^2$ plastic foil and a three centimeter long CsI(Tl) crystal.

In the experiment 130 Miniball phoswich detectors and 80 Miniwall detectors were mounted while the other MB/MW detectors were removed to make space for LASSA (for details see Table 2.1). The total solid angle coverage of the detectors of the combined MB/MW apparatus that were used in the experiment corresponds to about 80% of 4π . To reduce the counting rates of electrons and gamma rays, all Miniball/Miniwall detectors were covered by a layer of $4mg/cm^2$ Sn-Pb foil.

MB/MW Ring	Detectors	$\Delta\Omega(\text{msr})$	Mounted	Removed
MB3	28	11.02	15	13
MB4	24	22.9	11	13
MB5	24	30.8	20	4
MB6	20	64.8	14	6
MB7	20	74.0	19	1
MB8	17	113.3	17	0
MB9	14	135.1	14	0
MB10	12	128.3	12	0
MB11	8	125.7	8	0
MW2	16	2.57	16	0
MW3	22	2.59	17	5
MW4	26	2.85	19	7
MW5	24	5.56	15	9
MW6	24	10.64	13	11

Table 2.1: List of the original number of detectors in a ring of Miniball/Miniwall, the solid angle of a detector in that ring, and the numbers of mounted and removed detectors in that ring, respectively.

Chapter 3

LASSA Telescopes

Since the initial measurements that demonstrated the phenomenon of multifragmentation, there has been a growing need to explore this phenomenon with higher resolution devices. Measurements of isotopic distributions, excited state populations and correlation functions are much needed to extract the relevant temperatures and densities of such processes. However, existing charged particle detection arrays such as the Miniball/Miniwall[70] lack the energy, angular and isotopic resolutions for such studies.

The Large Area Silicon-Strip/CsI detector Array (LASSA)[71, 72] was designed and constructed to fulfill the highly demanding requirements of such studies. The LASSA consists of nine identical telescopes, each of which is composed of two silicon-strip detectors of 48 channels and four CsI crystals as shown in Figure 3.1 for one telescope. The whole array was centered at the forward angle of 35° in the experiment setup and positioned 20 cm from the target. The 3 mm pitch of the silicon-strip detectors corresponds to an angular resolution of $\pm 0.43^\circ$ for this setup. The total array covered a solid angle of about 540 msr with the polar angle θ ranging from 12° to 62° and the azimuthal angle ϕ ranging from 24° to 156° . Figure 2.1 indicates the distances and angular coverage of LASSA.

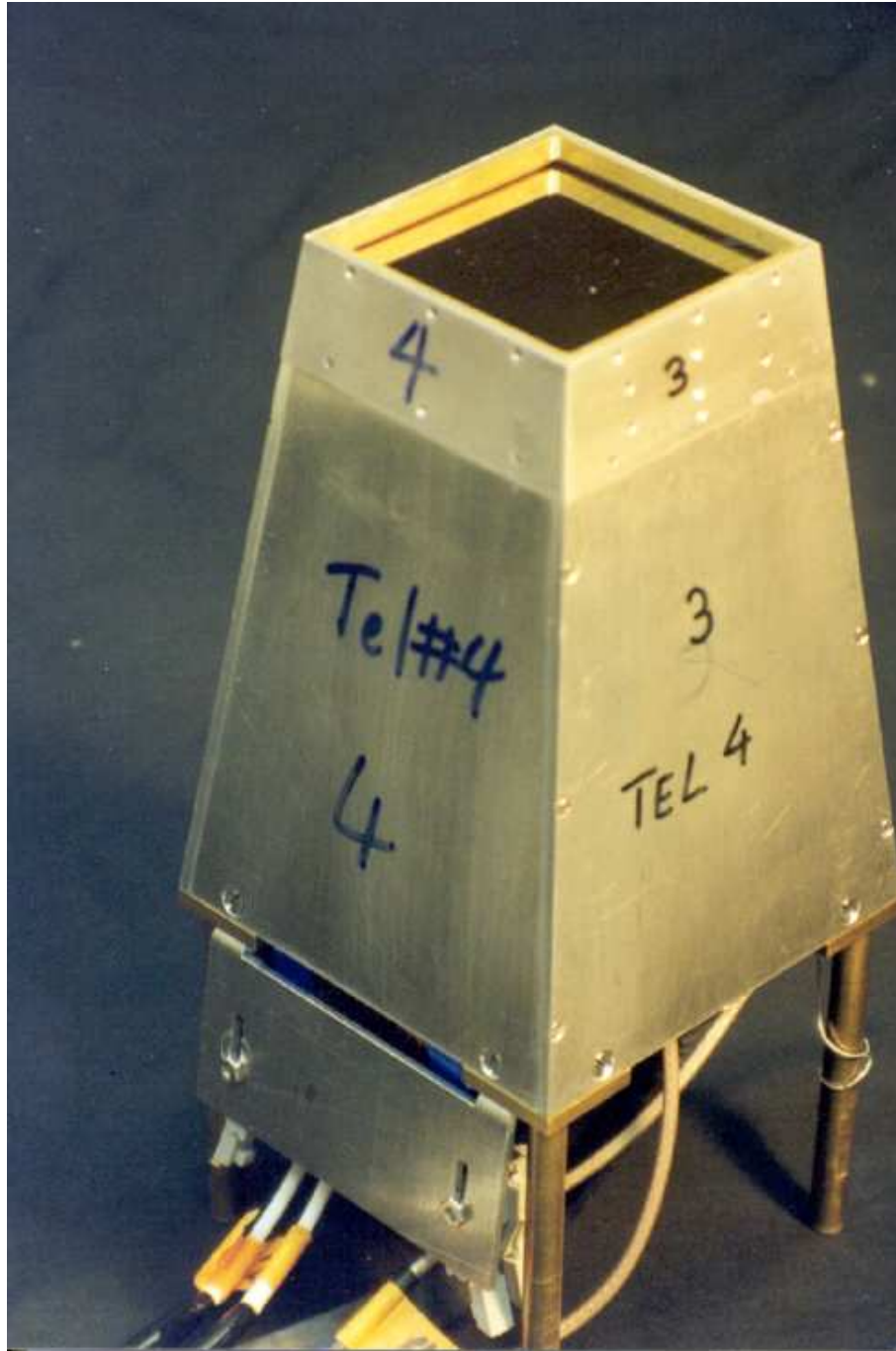


Figure 3.1: One of the nine identical LASSA telescopes.

3.1 Silicon Detectors

Silicon detectors are widely used in nuclear experiments because of their excellent energy resolution and linear response for charged particles. Extremely thin (\sim several tens of μm) to relatively thick ($\sim 1\text{mm}$) silicon strip detectors of large areas have been manufactured to provide position sensitivity for the detection of charged particles. Both layers of silicon strip detectors used in the LASSA are variants of the Micron design-W[73] and have an active area of about $5\times 5\text{ cm}^2$ (Figure 3.2).

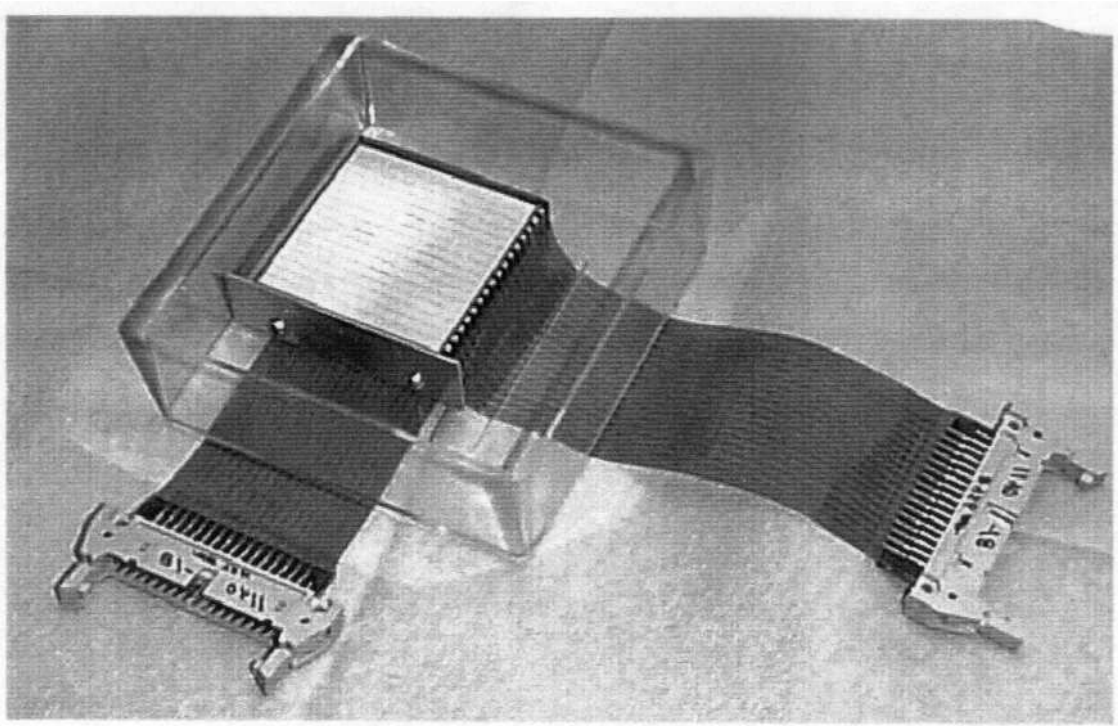


Figure 3.2: Picture of one $500\ \mu\text{m}$ thick double-sided silicon strip detector.

3.1.1 Specifications

In each LASSA telescope, the front (labelled here as "DE") silicon detector is about $65\ \mu\text{m}$ thick and $50\times 50\text{ mm}^2$ in area; it has 16 strips on the front side that are 3 mm wide each and has a single electrode (no strips) on the back. The second layer of silicon is

about $500 \mu\text{m}$ thick and is also $50 \times 50 \text{ mm}^2$ in area. It is double-sided; Each side is divided into 16 strips with 3 mm pitch. For convenience, we label 16 strips of the front side by "EF" and the strips on the back side, which are perpendicular to the front strips, by "EB". For both types of silicon detectors, there is a 0.1 mm wide interstrip region without electrodes and its effects will be discussed in the data analysis later. The thicknesses of the front layer of silicon can vary up to 10% and the back layer can vary by up to 2%. These variations will affect the particle identifications in ways that will be elucidated in the next chapter.

The closely packed design required the development of a highly flexible flat printed circuit board cable connecting the silicon strip detectors with the pre-amplifier housings. These cables were wire-bonded directly to the silicon wafer (see Figure 3.2). All 432 preamplifiers were housed in 9 boxes, each one housing 16 preamplifiers for the DE, 16 preamplifiers for the EF and 16 preamplifiers for the EB of one telescope. Each one of the preamplifiers is driven by $\pm 12\text{V}$ supply voltage and has a power consumption of approximately 300 mW. The gains of the DE preamplifiers are 15 mV/MeV and the gains of the EF and EB preamplifiers are 5 mV/MeV.

The silicon detectors need to be fully depleted to achieve the best energy resolution. Interestingly we found that the full depletion voltage listed by Micron was typically a factor of two smaller. The DE and EF strips were biased in the experiment to be fully depleted.

The stopping energy for alpha particles is 10 MeV in the first layer of silicon and 36 MeV in the second layer after passing through the first layer. Because any particle stopped in the first layer of silicon can not be identified by this device through the ΔE -E identification technique, the stopping energy of the first silicon sets the lower threshold for the corresponding particle we can analyze. Software thresholds were set

on the analysis of the experimental data, which were a little higher than the physical stopping energies. For example, the low energy cutoff for alpha particles is about 10 MeV for the LASSA.

3.1.2 Energy Calibration

One advantageous feature of silicon detectors is their linear and largely particle-independent energy response. While fission fragments have in general, rather different energy calibrations than alpha particles due to space charge effects near the stopped fragments, only one energy calibration should be needed in principle for any species of charged particles with relatively low charge number $Z \leq 8$. As few as two points should be able to define the energy calibration curve for such species. However, due to the nonlinearity of electronics system including preamplifiers, shapers and ADCs at low and high energies, the calibrations of both low and high energy particles must be treated more carefully than those of particles at the center of the energy spectrum.

An Ortec precision pulser generator was used to calibrate the silicon detectors. The pulser has a group of attenuation switches to calibrate detectors with different dynamic ranges. Three different dynamic ranges of 140 MeV, 200 MeV, and 500 MeV corresponding to three different combinations of pulser attenuation switch settings were used to calibrate LASSA silicon detectors. An absolute calibration was obtained from the measurements of ^{241}Am and ^{228}Th alpha sources for these three settings. Figure 3.3 shows the linear calibration relations of energy in MeV versus pulser dial value in Volt for the three dynamic ranges.

Right after the data-taking experiment was finished, all the electronics setup was retained the same except that the pulser calibration system was plugged in each input channel of the silicon detector preamps while the detectors were still attached. Then the one-by-one pulser calibration was carried out for all 432 silicon channels. For each

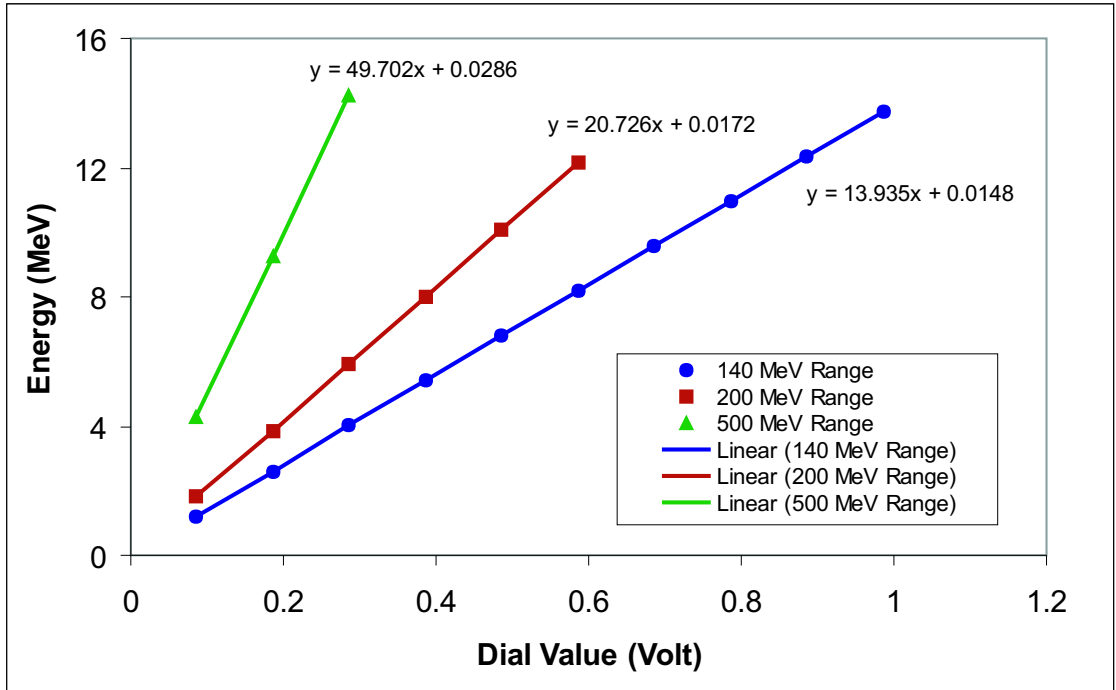


Figure 3.3: Pulsar calibration for three dynamic ranges.

channel, more calibration points were applied to the low energies and high energies to measure the possible nonlinearities on those regions as shown in Figure 3.4. In the low and middle energy regions labelled as 1 and 2, respectively, in Figure 3.4, linear fitting procedures were employed while in the high energy end (labelled as 3) a 4th order polynomial fit was adopted. Spline interpolation was used to join the three pieces together smoothly.

3.2 CsI(Tl) Detectors

CsI(Tl) scintillation crystals are cost effective for detecting charged particles with energies of $E/A=30-200$ MeV. Less expensive than silicon detectors, less hygroscopic than NaI crystals, and easily machined into different shapes, CsI(Tl) detectors have been used to stop higher energy particles in many $\Delta E-E$ type detection arrays with large solid angle coverage.

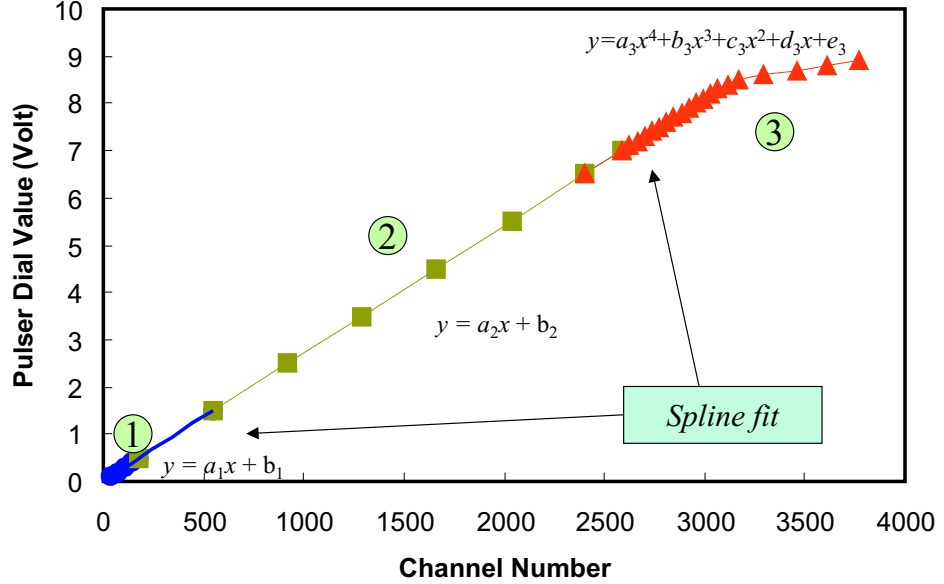


Figure 3.4: Energy calibration for a typical silicon strip.

The CsI crystals had the original dimensions of $3.5 \times 3.5 \times 6.0 \text{ cm}^3$. The final shape of CsI crystals is defined by tapering the two outer sides and making the front surface reduced to dimensions of $2.5 \times 2.5 \text{ cm}^2$ while keeping the dimensions of the back surface the same. Four crystals are grouped together and placed behind the two layers of silicon detectors. With a thickness of 6 cm, all CsI(Tl) can stop alpha particles with energies up to 580 MeV and protons with energies up to 145 MeV.

3.2.1 Pre-selecting and Scanning CsI(Tl) Crystals

To ensure that CsI crystals in LASSA have good energy resolution, only the crystals with light output uniformity better than 1% were adopted. A careful alpha-scanning procedure was applied to control the quality selection.

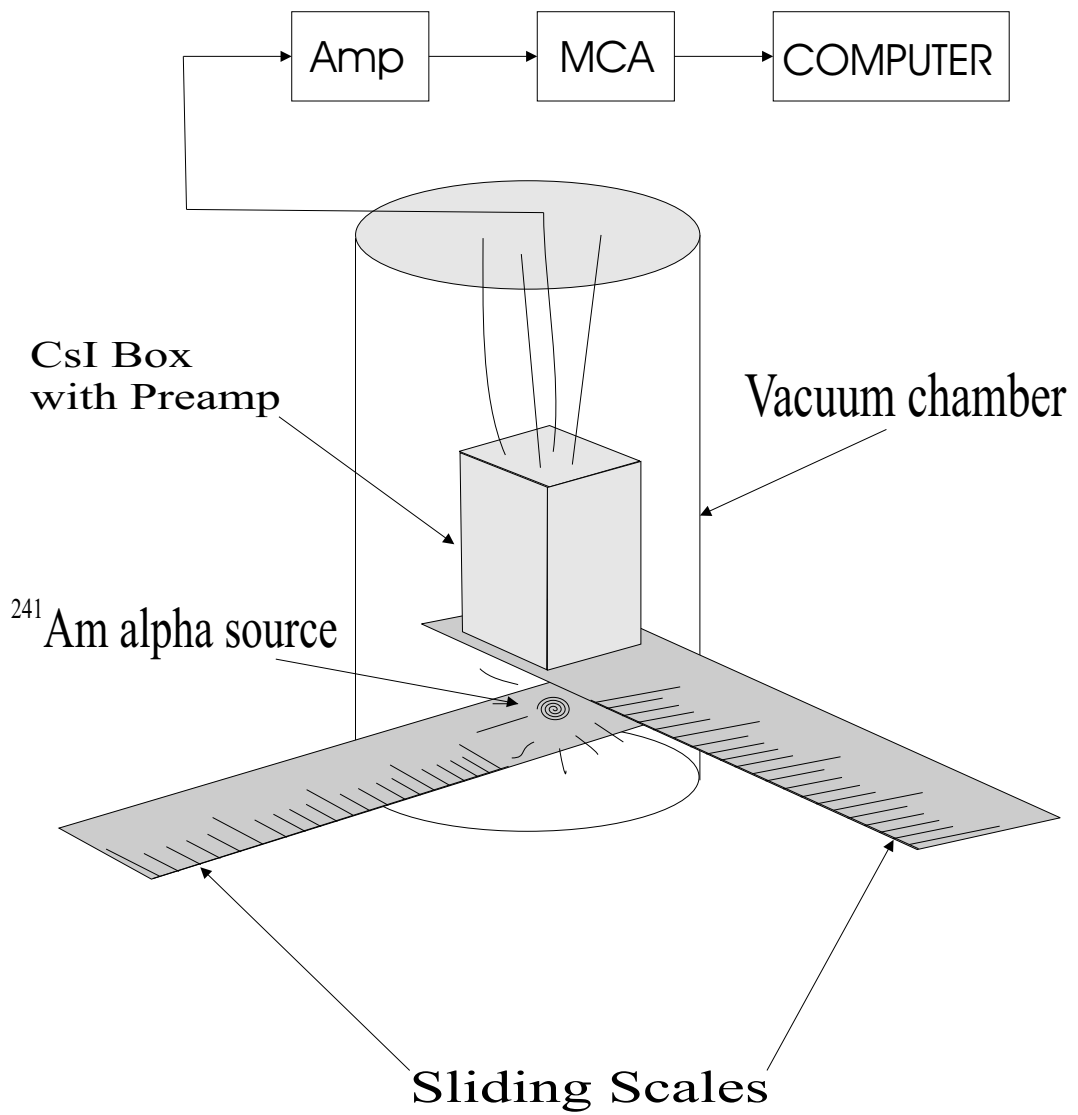


Figure 3.5: CsI crystal scanning setup with alpha source.

The CsI(Tl) crystals manufactured by Scionix[74] were originally rectangular in shape with dimensions of 3.5x3.5x6.0 cm³. The front square surface was polished and the other sides were sanded when obtained commercially. After a careful inspection for visual cracks or imperfections, the back square surface was sanded down and polished. It was then optically coupled to a clear acrylic light guide that was in turn optically connected to a 2x2 cm² photo-diode. The front surface of the crystal was covered with an aluminized mylar foil and the other sides were wrapped with two layers of teflon tape to ensure uniform light collection. Details of discussion on wrapping materials will be shown in the next section. The whole detector set was contained in a small aluminum box along with a charge sensitive preamplifier attached in the back of the box to maximize the signal to noise ratio.

The 5.486 MeV alpha particles from a collimated 1 μ Ci ²⁴¹Am alpha source were used to scan the crystals. Figure 3.5 shows the scanning setup inside a vacuum chamber. A two dimensional sliding scale supported the alpha source and the crystal box on two perpendicularly crossing arms, respectively, where the scanned surface position of the crystal was measured by the scale. For each crystal nine regions that uniformly divided the front surface were in turn irradiated by the alpha source as shown in Figure 3.5. The first point was scanned again after finishing all nine points to make sure that the scanning system was stable and not affected by temperature changes and other drifting effects. The alpha spectra corresponding to the centers of the nine sub-squares were recorded with a multi-channel analyzer equipped with a peak sensing ADC and then stored in computer for offline analysis as shown in the electronics scheme of Figure 3.5.

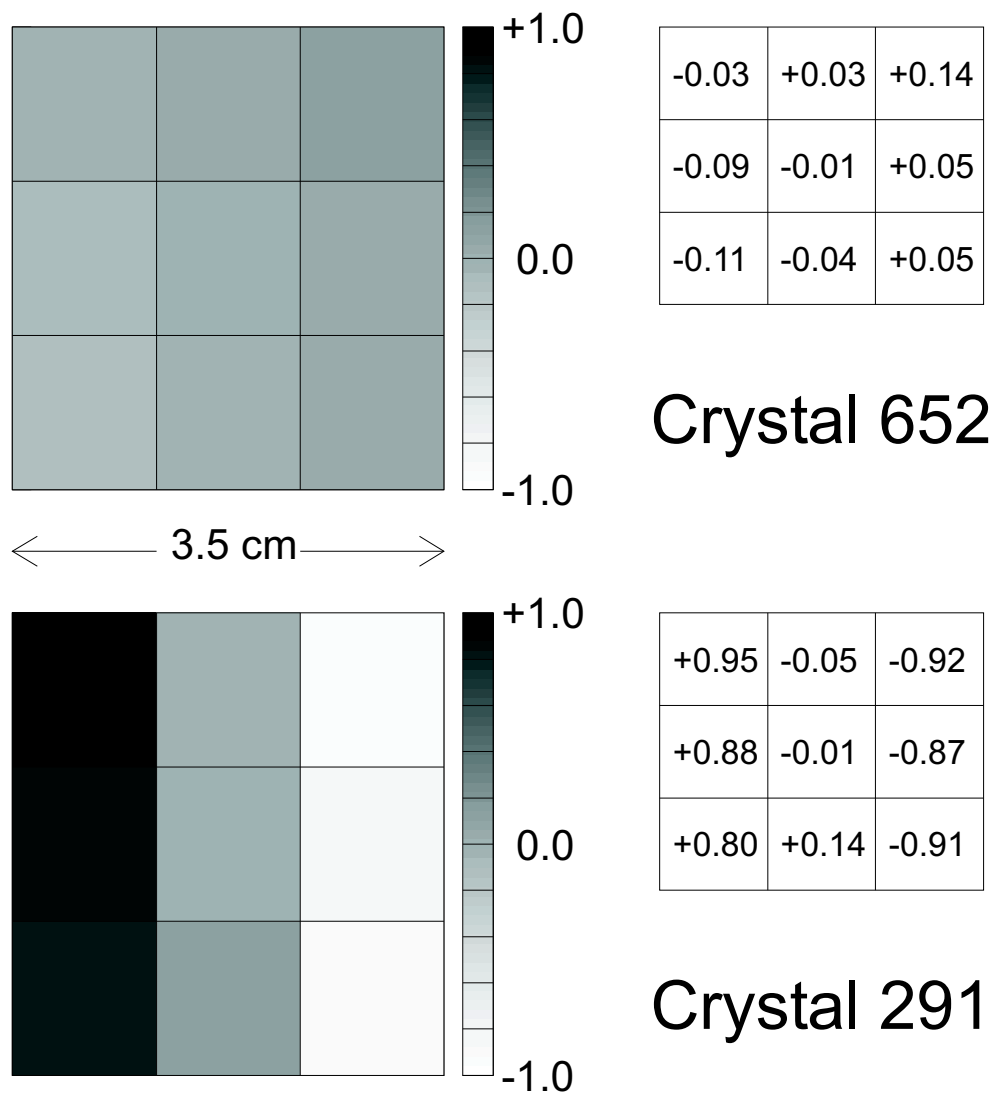


Figure 3.6: Uniformity results of accepted and rejected CsI crystals.

The different grey levels in Figure 3.6 represent the percentage deviations of the nine alpha peaks from the median value. The specific numbers of these deviations are shown in the corresponding table next to the shaded crystal surface. Only the crystals with light output varying within $\pm 0.5\%$ were accepted, such as the one shown in the top panel with deviations ranging from -0.11% to 0.05% of the mean. On the other hand, crystals with light output uniformity beyond $\pm 0.5\%$ were rejected and returned to the manufacturer. The bottom panel demonstrates one of the rejected samples, which clearly shows the existence of a light output gradient that is caused by the non-uniformity of Tl doping inside the crystal.

3.2.2 Testing Wrapping Materials

A reflective entrance foil is needed to cover the front surface of a CsI crystal for optimal light collection efficiency that improves the energy resolution. In order to minimize the dead layer loss due to the CsI front foil, a very thin layer of aluminized mylar foil ($0.15 \text{ mg/cm}^2 \text{ mylar} + 0.02 \text{ mg/cm}^2 \text{ Al}$) was applied to the CsI front surface. As for the other sides of the crystals, opaque materials are needed for diffuse light reflection. This side wrapping is very critical not only for maximizing the light collection efficiency but also for minimizing the possible light crosstalk between four bundled crystals within one telescope.

To achieve the best resolution and the thinnest wrapping, we tested different materials for wrapping up crystals. Two different materials, 0.1 mm thick white teflon tape and 0.14 mm thick white cellulose nitrate membrane with pore size of $0.2 \mu\text{m}$ are shown in fig 3.7 for different numbers of wrapping layers.

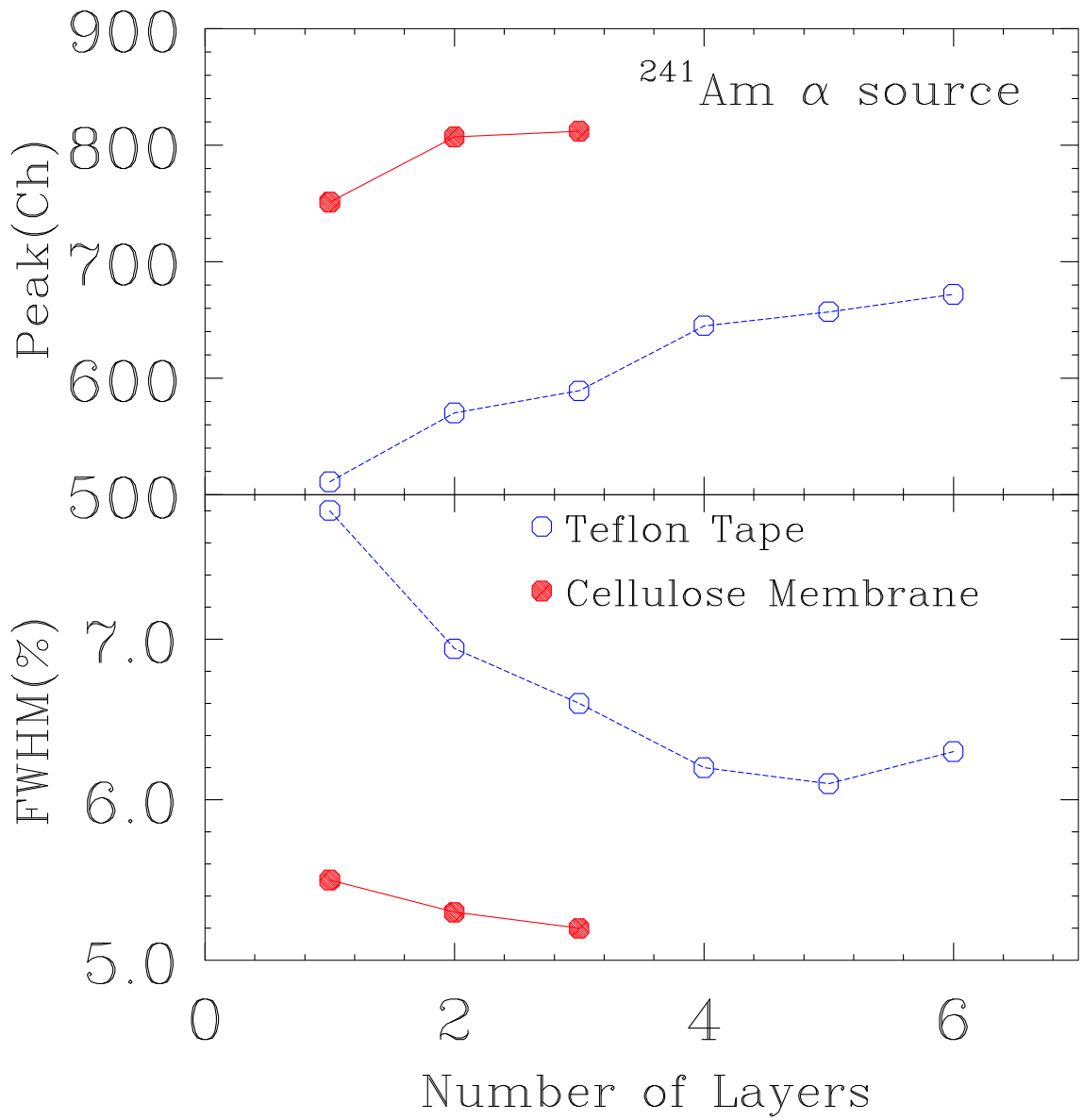


Figure 3.7: Comparisons of different wrapping materials used for CsI crystals.

Using the same ^{241}Am alpha source as used in the scanning procedure, we found that the light output, i.e., the peak channel of alpha spectrum, increases as more layers are wrapped around the crystal for both materials. This is shown in the upper panel of Figure 3.7. The improvement of the percentage of energy resolution as shown in the lower panel is directly related to the enhanced light output since the FWHM of the alpha peaks dictated by the electronic noise is constant at about 40 channels (corresponding to 250 keV for the largest light output). When the number of layers is large enough, for example, two for cellulose membrane and five for teflon tape, however, the collected light output saturates and nothing can be gained by increasing the thickness further.

The overall performance of cellulose nitrate membrane is much better than that of teflon tape. When the same number of layers are used, the cellulose nitrate membrane shows about 40 percent increase of light collection over the teflon tape, making it certainly the choice. Since four crystals are grouped together behind the two silicon detectors in each telescope, a large gap between CsI(Tl) crystals leads to a loss in solid angle. This also argues for the cellulose membrane. Based on the saturation shown in Fig. 3.7, two layers of the cellulose membrane is the optimal choice. In the final wrapping, each crystal was wrapped with two layers of cellulose nitrate membrane around the two outer sides and one layer around the two inner sides which touches two other adjacent crystals. Counting both shared layers of the adjacent crystals, each crystal had effectively two layers of cellulose nitrate membrane on all four sides. This was enough for measuring the light collection and resolution but not enough to remove all cross-talk as we discovered later.

3.2.3 Other Effects and Assembly

The light output of CsI crystals is also affected by temperature changes. During the preselection scanning, we also tested the temperature effect which typically gives a 1% decrease in light output for every three degrees centigrade increase at room temperature. In Xe+Au experiment, a cooling plate was attached right behind each telescope to stabilize the temperature within one degree centigrade at room temperature. So the variation of temperature would not be the limiting factor of energy resolution of the CsI detectors.

Optical clear front and back surfaces are essential for collecting the light and monitoring the gluing process. A step by step sanding and polishing procedure was applied by using 400 grit sanding paper and 30 μm , 15 μm , 5 μm , and 1 μm polishing paper with the aid of pure ethanol (any water-containing solvent could easily damage the CsI crystals). The final step with silk cloth and polishing compound would make the surfaces crystal clear. In addition, four other sides were slightly sanded with 400 grit sanding paper with the sanding grooves parallel to the long axis of each crystal for a better uniformity and light diffusion.

For each crystal, a 1x3.5x3.5 cm³ acrylic light guide was glued to the back surface with optical epoxy BC600[75] and a photodiode with active area of 2x2 cm² was glued with clear silicone rubber compound RTV615[76]. The gluing process was monitored to ensure that no bubbles were left in the layer of glue. To prevent the light leak and crosstalk between adjacent crystals, the outer sides of light guide and the photodiode were painted with a reflective white paint BC620[75]. Four crystals were bundled in the back of silicon detectors for stopping high energy particles.

CsI preamplifiers are attached right behind the crystals within the telescope box. Figure 3.8 shows the set of four CsI preamps and their housing which is divided

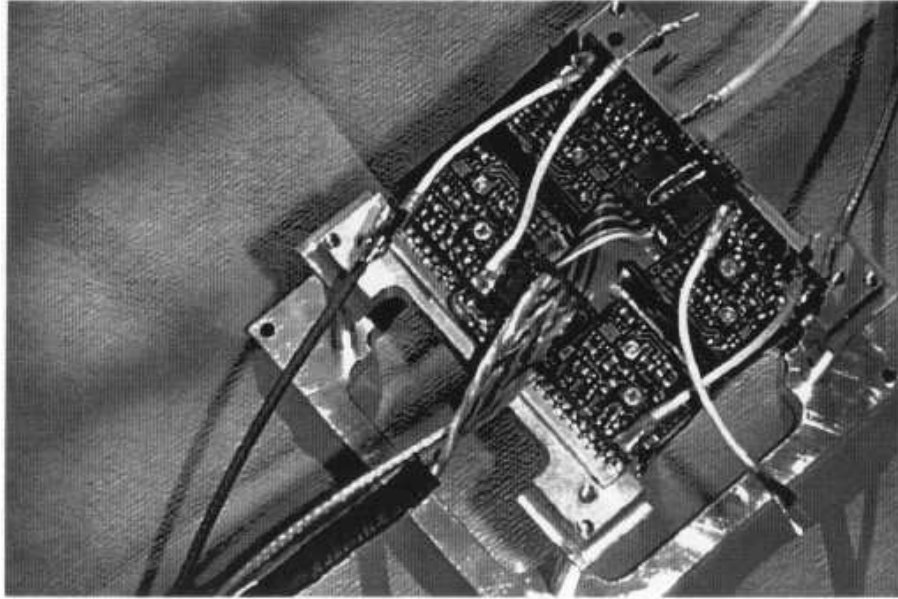


Figure 3.8: CsI preamplifiers and their housing.

and shielded with copper into four small cells to eliminate the crosstalk between the preamps. The closely packed four crystal setup in one telescope box is shown in Figure 3.9. The two layers of $5 \times 5 \text{ cm}^2$ silicon detectors and their frame sit on top of the box in the final assembly with the flexible signal cables running inside the metal box next to the wall. The silicon preamps are placed in separate boxes because there are 48 silicon channels per telescope.

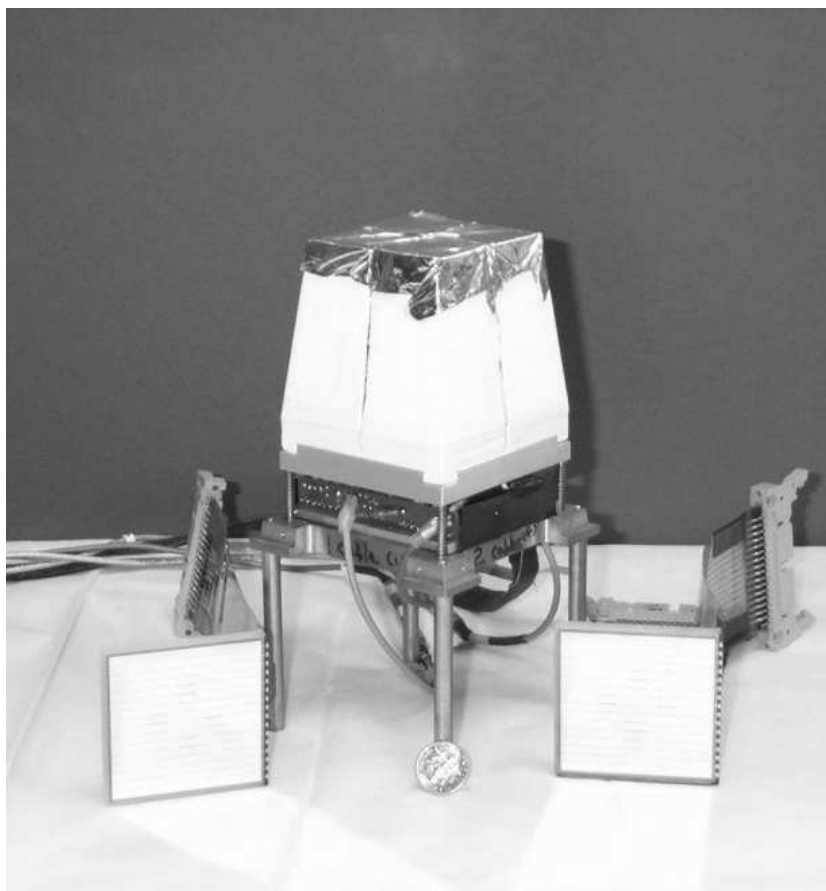


Figure 3.9: CsI packing in one telescope.

3.2.4 Energy Calibration

The fluorescent light emitted by the CsI(Tl) scintillator has two major components of a fast (500 ns) and a slow (7 μ s) decay time constants. Both components have a relationship of light output and energy that is mass and charge dependent. This property has been exploited to provide mass identification for light ions using pulse-shape discrimination. This pulse-shape discrimination capability is not needed in the Δ E-E type LASSA telescopes where silicon detectors are used as Δ E detectors and CsI crystals as the stopping detectors. However, the mass dependence of pulse shape remains important because of its influence on the energy calibration.

At low energy, the light output of a CsI crystal shows a non-linear response to the deposited energy, especially for heavy ions. It also depends on the Tl doping of CsI crystals.

To determine the energy calibration for different ions, the detectors were directly exposed to low intensity ($\sim 10^3$ particles per second) beams of different isotopes and energies. These ions were obtained by fragmenting 2160 MeV ^{36}Ar and 960 MeV ^{16}O primary beams from the NSCL K1200 cyclotron in the A1200 fragment separator. The main advantage of this method is the availability of a large number species of particles that could be detected simultaneously (up to 52 isotopes were identified in the case of the ^{36}Ar fragmentation). Since particles are selected only by their magnetic rigidity ($B\rho = 1.841$ Tm for the ^{36}Ar beam and $B\rho = 1.295$ Tm for the ^{16}O beam) one obtains a broad range of different isotopes and energies. The FWHM of the momentum widths for these particles were selected to be 0.5%. The atomic and mass numbers as well as energies of the particles used to calibrate the CsI crystals in the present work are listed in Table 3.1. Hydrogen and helium isotopes were also calibrated by elastic scattering of E/A=30 MeV p- ^4He molecular beams on a Au

target and by 240 MeV direct ^4He beam particles.

^{16}O fragmentation	E (MeV)	^{36}Ar fragmentation	E (MeV)
p	77.17		
d	39.78	d	79.57
t	26.72	t	53.75
^3He	105.00	^3He	210.00
^4He	79.99	^4He	160.00
^6He	53.64	^6He	107.90
^6Li	119.90	^6Li	240.00
^7Li	103.10	^7Li	206.80
^8Li	90.40	^8Li	181.60
^7Be	182.20	^7Be	363.40
^9Be	142.50	^9Be	285.60
^{10}Be	128.40	^{10}Be	257.90
^{10}B	199.90	^{10}B	400.00
^{11}B	182.10	^{11}B	364.90
		^{12}B	335.40
^{11}C	261.20	^{11}C	521.60
^{12}C	239.90	^{12}C	480.00
^{13}C	221.80	^{13}C	444.40
		^{14}C	413.70
^{14}N	279.90	^{14}N	560.00
		^{15}N	524.00
		^{16}N	492.40
^{15}O	340.80	^{15}O	680.70
		^{16}O	640.00
		^{17}O	603.70
		^{18}O	571.30

Table 3.1: List of fragmentation products used in the energy calibration of the LASSA CsI(Tl) crystals.

The energy calibration for each isotope was done following the mass and charge dependence of the light output described in ref. [77], which in turn was based on previous studies of the light emission of CsI-crystals and on semi-empirical model proposed by Birks [78]. In this approach, the incident particle energy E is parameterized as a function of the light output L , the charge Z , and the mass A of the particle,

as

$$E(L, A, Z) = aAZ^2L + b(1 + cAZ^2)L^{1-d\sqrt{AZ}} \quad (3.1)$$

where a , b , c and d are the fitting parameters with values greater than zero. This expression describes a linear term, dominating at high energies and a non-linear term dominating at low energies. In Fig. 3.10, the solid and dashed lines represent the best fit of Eq. 3.1 to the experimental energy calibration data corresponding to different carbon isotopes ($A=11-14$). The need for a mass dependence can be demonstrated by examining the light output of the higher energy carbon isotopes. At high energy, the light response is expected to be linear. Both the ^{11}C points should lie in the linear domain. However, a straight line joining the two ^{11}C isotopes does not pass through the high-energy ^{12}C , ^{13}C , and ^{14}C isotopes. A curve going through all points for the $^{11-14}\text{C}$ would lead to a very large and unreasonable curvature compared to other CsI(Tl) calibrations adopted elsewhere in the literature. Instead we adopt another solution which assumes a mass dependent calibration (closely related to the quenching effect)[77]. To confirm this mass dependent ansatz that could allow the construction of the full calibration curve for each isotope, several fragmentation beams of different incident energies would be required.

For light charged particles with $Z \leq 3$, the parameterization described in Eq. 3.1 did not accurately describe the detected energies. Compared to the observation of Ref. [77], a less pronounced isotopic effect was observed for light ions. This may be the result of the increased concentration of the activator element, Tl, in the LASSA CsI crystals compared to those studied in ref. [77]. We find that the AZ^2 factor in Eq. 3.1 overestimates the mass dependence. We therefore employ a modified function of Eq. 3.1 with a weaker dependence on A for the particles with $Z \leq 3$. The expression is modified for each element. For Lithium ($Z=3$) particles, we change the first term

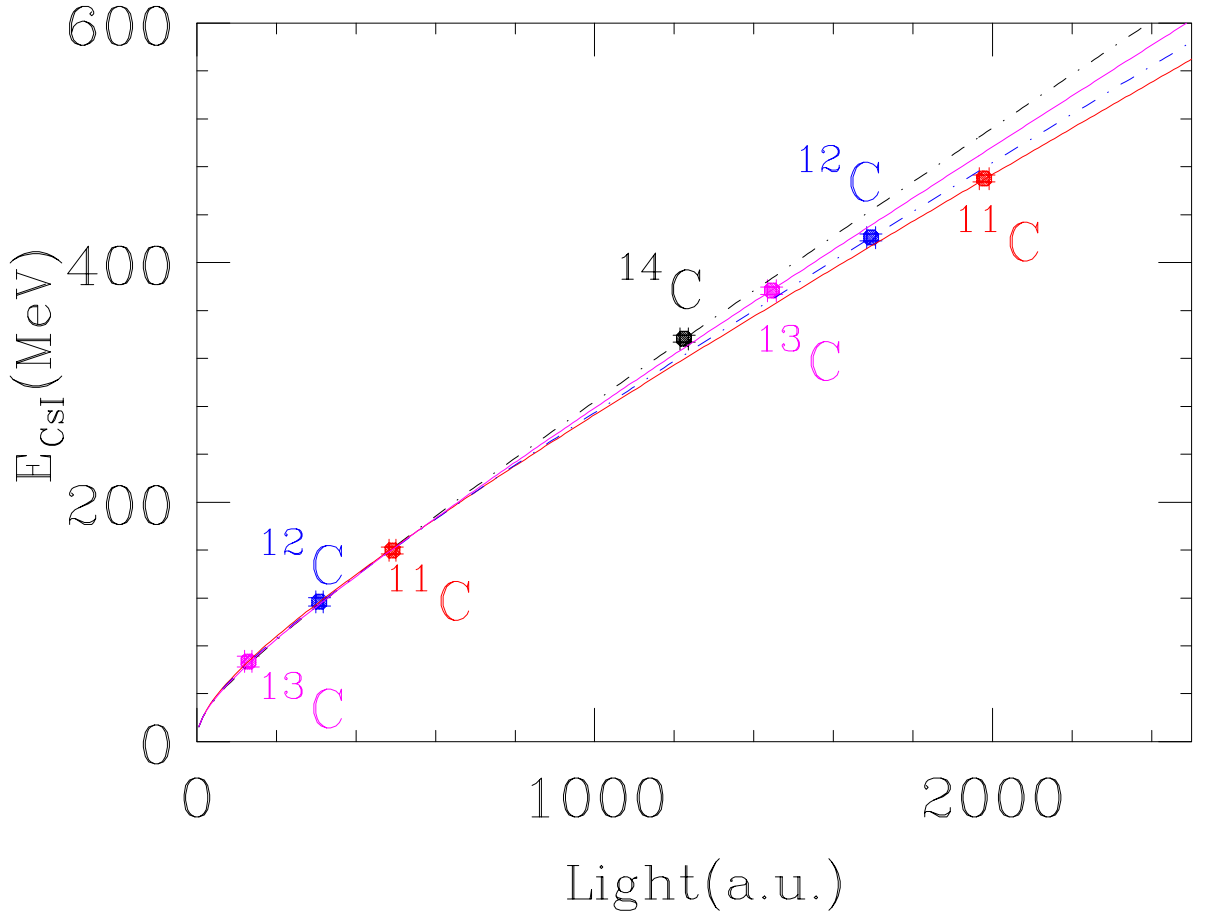


Figure 3.10: Calibration curves for ^{11}C , ^{12}C , ^{13}C and ^{14}C for the CsI (Tl) crystals obtained using direct fragmentation beams listed in Table 3.1. The curves are the best fit according to Eq. 3.1.

of Eq. 3.1 and used,

$$E(L, A, Z) = a\sqrt{AZ^2}L + b(1 + cAZ^2)L^{1-d\sqrt{AZ}} \quad (3.2)$$

For Helium ($Z=2$) isotopes, we use

$$E(L, He) = aL + bA^c(1 - e^{dL}) \quad (3.3)$$

The variables a , b , c , and d in Eq. 3.1-3.3 are fit parameters. There are sufficient data to reproduce with good accuracy the light-output response for all the isotopes of the same element using Equations 3.1-3.3. Our fitting procedure resulted in a precision of the energy calibration better than 2% for isotopes from He to O.

As we have only limited calibration points for p, d and t, two calibration points from each isotope, we adopt the simple linear function for $Z=1$ particles.

$$E(L, H) = aL + b \tag{3.4}$$

where a and b are fit parameters. A linear CsI(Tl) response is consistent with that observed for hydrogen isotopes by Handzy [79].

Chapter 4

Data Reduction and Analysis

4.1 Overview of the Analysis

The detection system is very complex with 432 silicon and 36 CsI channels from LASSA plus hundreds of detectors from Miniball/Miniwall. To reduce the complexity in the analysis, we decided to use the MB/MW array to determine the charged particle multiplicity as the impact parameter filter so that detailed energy calibration of the MB/MW system could be avoided for this experiment. Nevertheless, we did separate the light particles ($LP, Z \leq 2$) from the heavy fragments ($Z \geq 3$) in the MB/MW in order to obtain separately the IMF multiplicity in addition to the total multiplicity.

Detailed calibrations and analysis on the LASSA, on the other hand, were conducted for isotopically resolved charged particles. Figure 4.1 shows the flow chart of data analysis for the LASSA. After the raw data from the ADC was decoded and all the zero's and pulser events were suppressed, presorted data tapes were generated for further analysis. The whole analysis procedure depends on the pixelation subroutine which associates specific x and y strips (EF and EB) with specific particles to locate where they hit. This procedure also allows one to associate the particle with specific data in the proper DE strip and the CsI crystal. The silicon energy calibration, one of the two main analysis tasks, was done using the information obtained with the

LASSA Calibration Flow Chart

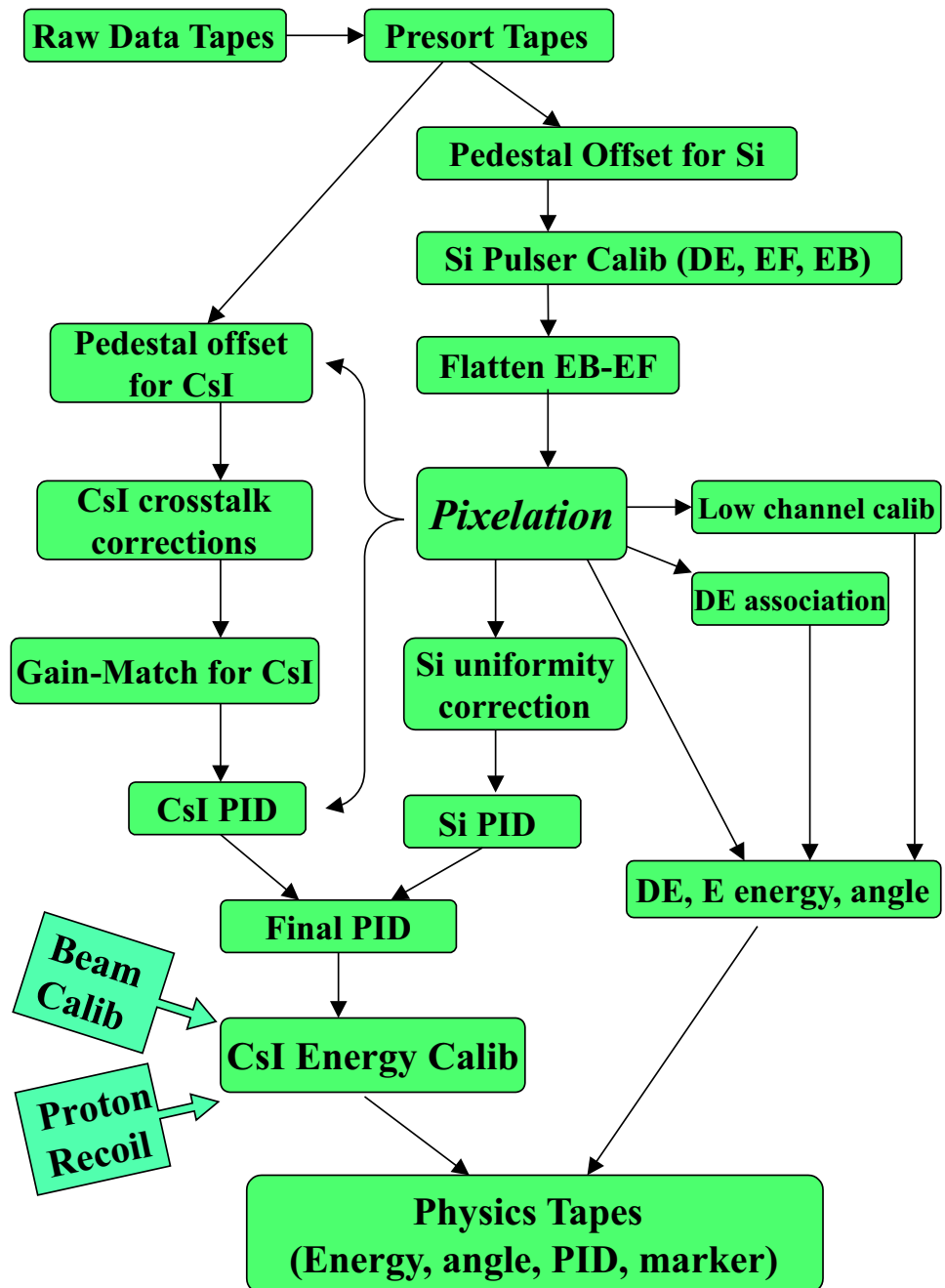


Figure 4.1: Flow chart of data analysis for the LASSA.

precision pulser (for more details see the previous chapter). The energy calibration of CsI crystals, on the other hand, was conducted using the information from a series of beam calibration runs and from measurements of proton recoils during the data-taking runs. After making the corrections for the thickness variations in the silicon detectors, particle identification (PID) gates were constructed. In the final physics tapes, the particle ID value, the total kinetic energy, and the emission angle for each particle were recorded as well as a marker to label the circumstances when the particle was identified. In the following sections, several aspects of this analysis procedure are discussed in greater detail.

4.2 Pixelation Technique

One of the most important advantages of Silicon-strip detectors is their position sensitivity. Since the second layer of Silicon in the LASSA array is double-sided, we can use this to obtain (x,y) pixelwise position resolution that tells us which pixel(3×3 mm²) a particle strikes. This is simple, in principle, if only one single particle hits the silicon in one telescope during one event. When more than one particle hits the silicon, i.e., in multiple-hit cases, however, one must use care in pairing up the signals from the vertical and horizontal silicon strips in order to obtain the correct position information for each particle. This pairing is done in the "pixelation procedure" described below.

When there are two particles or more hitting into one telescope, there can be ambiguities in assigning the position of each particle, which need to be addressed. First, one need to determine whether the particles can be identified or not. For example, if two charged particles punch through two layers of silicon detectors and stop in the same CsI crystal, then it is not feasible to obtain the correct particle ID

and energies for these particles. Second, the signals from DE, EF, EB and CsI need to be associated properly with specific particles for the analyses to be correct.

When a particle is stopped in the first layer of single-sided silicon detector its proper ID (mass and charge) and position can not be determined; such particles have to be disregarded. For the other cases (e.g., particles stopped in the second silicon or the CsI), signals from the second double-sided silicon detector can provide the best choice for the determination of particle multiplicity and position since the perpendicular EF and EB strips granulate the detector into fine pixels and have basically the same energy signal for the same particle when the calibrations for both EF and EB are accurate. We use this to pair up the signals of EF and EB and identify the particles.

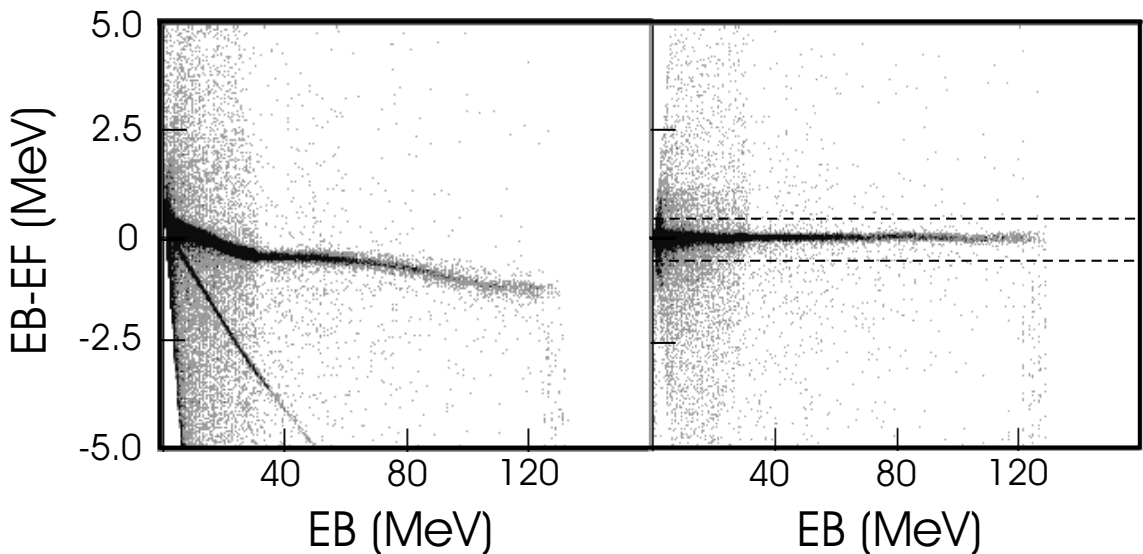


Figure 4.2: EB-EF fine-tuning calibration for pixelation. On the left panel discrepancy between EB and EF calibrated from the precision pulser is shown. After the EB-EF flattening routine is applied, the good agreement between EB and EF is shown on the right panel.

In order to make the best use of the pairing process, the energies of EF and EB should be calibrated in the same way. However, the independent silicon calibration of EF and EB strips can only offer a precision of 1% which results in larger deviations

of EF from EB signals at higher energies and consequently a difficulty in resolving two hits with similar energies. A EF-EB flattening routine was developed to enforce that the energy signals from both EF and EB for the same particle are the same.

Figure 4.2 shows how the spread of EB-EF difference changes before and after the flattening routine. On the left panel the difference between EF and EB signals before the flattening procedure is plotted. One can see one intense, nearly horizontal contour, a line that slopes downward, and a grey background. The grey background results when the EB and EF signals are from different particles. The crooked, nearly horizontal line corresponds to the correlation between EB and EF when both are calibrated properly with the alpha-sources and pulser as described in Sect. 3.1.2. The steeper line corresponds to the case that particles pass through a EB or EF strip that has problems with its calibration. After performing this procedure, one straightens out the correlation between EF and EB as shown in the right panel of Figure 4.2 and recovers these ill-calibrated silicon strips. A gate of ± 0.5 MeV (shown by the dashed lines in Figure 4.2) is applied to select the correct pairing of EF and EB signals.

For signals that can not be paired up with any EB or EF strip within the gate of ± 0.5 MeV, we need to distinguish cases where two particles hit in the same silicon strip (double-hit, which occurs about 3% of the time) and cases where the charge of one particle is split between two neighboring strips (split-hit, which occurs about 5% of the time). Specifically speaking, if the magnitude of one EB signal is close to the sum of two neighboring EF signals, then with a high probability this case can be identified as a single particle hitting into the 0.1mm wide interstrip gap with its signal split into two adjacent channels; if those two EF channels are separated, then one knows that one has the double-hit situation where two particles have gone into the same EB strip.

Due to limited dynamic range of the electronics the signals of some particles, especially heavy particles, are saturated in a small fraction ($< 1\%$) of all the signals, which need to be excluded in the data analysis since the pairing technique and energy determination become obscure for these particles. Such is the case for the particles hitting into strips that give no output signals because either their electronics has failed or the detectors or the wire bounds to the strips are bad.

4.3 CsI Crosstalk

During this experiment with the LASSA device, it was discovered that a small fraction (typically $< 2\%$) of the light emitted in one crystal could leak into an adjacent crystal. After this experiment, a thin layer of aluminized mylar (0.15 mg/cm^2 mylar + 0.02 mg/cm^2 aluminum) was inserted between adjacent crystals. This additional foil decoupled the detectors completely. Since this decoupling was achieved after this dissertation experiment was performed, the present analysis must deal with and remove the effects of the light leak as discussed below.

Four CsI crystals are closely packed together within one telescope as indicated by the sketch at the top of Figure 4.3. Figure 4.3 also shows the correlations between the light output observed in pairs of CsI crystals within one typical telescope (the reversed crosstalk is similar and not shown). Note that the Y scale is blown up for showing the light output correlation between CsI X and Y when a signal is observed in CsI X. It is clearly seen that the crosstalk is about the level of 1-2% between two directly neighboring crystals and basically vanishes between diagonal crystals. In the cases of two diagonal crystals (two middle plots in the figure), small slightly tilted lines close to Y axis are just the correlation of two crosstalk signals when one of their common neighbors has been fired.

CsI2	CsI4
CsI1	CsI3

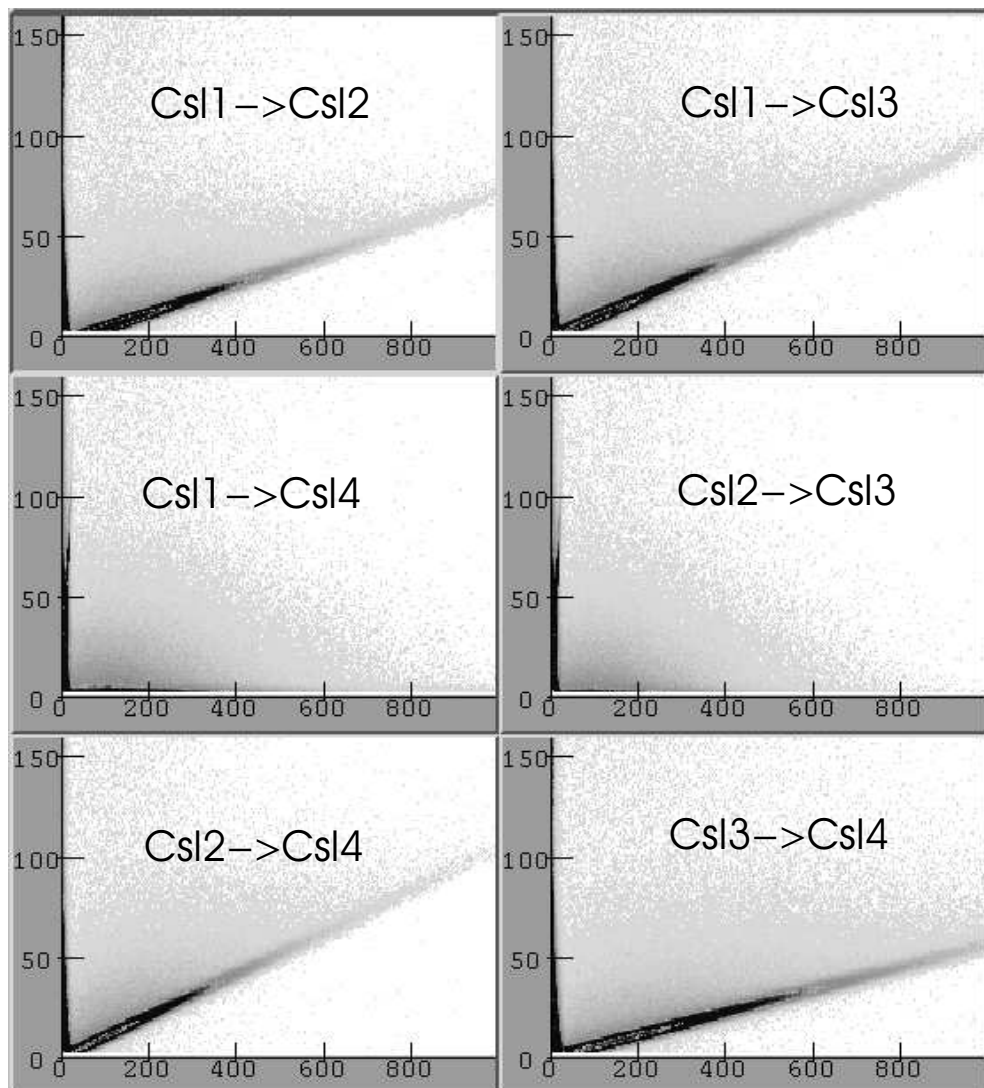


Figure 4.3: layout of CsI crystals within one telescope and typical crosstalk shown for light leakage from CsI X to CsI Y in Telescope 2. Similar results for CsI Y \rightarrow CsI X are not shown. Units are in raw channel numbers.

During the experiment, it was determined that a linear crosstalk correction could be applied. Therefore the decoupling foil was not inserted between CsI crystals in an effort to conserve data taking time. This linear assumption is demonstrated by Figure 4.3. In order to correct the light output in each crystal a conversion matrix is constructed as follows:

$$L_i = L'_i + \sum_{j \neq i} (a_{ij} g_{ij} (L'_j - L_{ij}^0)) - \sum_{j \neq i} (a_{ji} (L'_j - L_{ji}^0)) \quad (4.1)$$

where the L' is the channel number of apparent light output; L is the channel number of reconstructed light output after correcting the crosstalk between CsI crystals; a is defined as the crosstalk matrix; g is the gain factor due to the gain differences between crystals; L^0 is the channel number of the offset. The second term is the light gain from other crystals while the last term stands for the light loss to adjacent crystals. The matrix elements of a and L^0 can be easily obtained from the slope and offset parameters of the crosstalk lines in Figure 4.3.

After the reconstruction of CsI light output, calibration of individual CsI crystals were carried out according to the procedure described in Sect.3.4

4.4 Uniformity Correction

Before starting the particle identification (PID) through the DE-E technique, one has to correct the non-uniformity of Silicon thicknesses. As mentioned in Sect. 3.1.1 Large area thin silicon detectors have a disadvantage of non-uniform thickness up to 10%. Different energy losses are in general recorded for identical particles of the same energy passing through different pixels. To correct for this thickness variation, it becomes essential to apply the pixelation procedure described in Sect. 4.2 and use it to map the thickness variation.

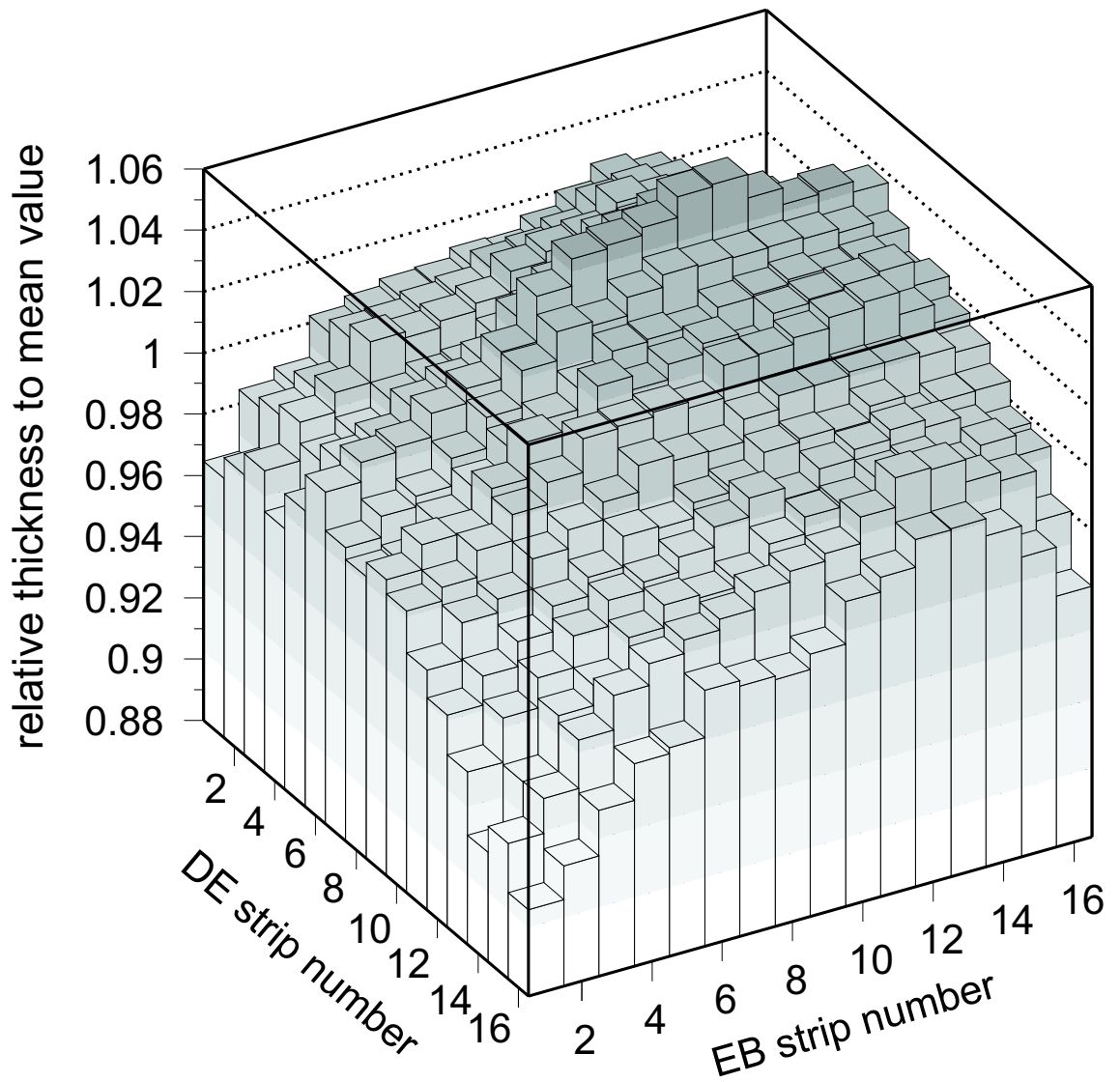


Figure 4.4: Non-uniformity of one typical 65 μm thick silicon detector.

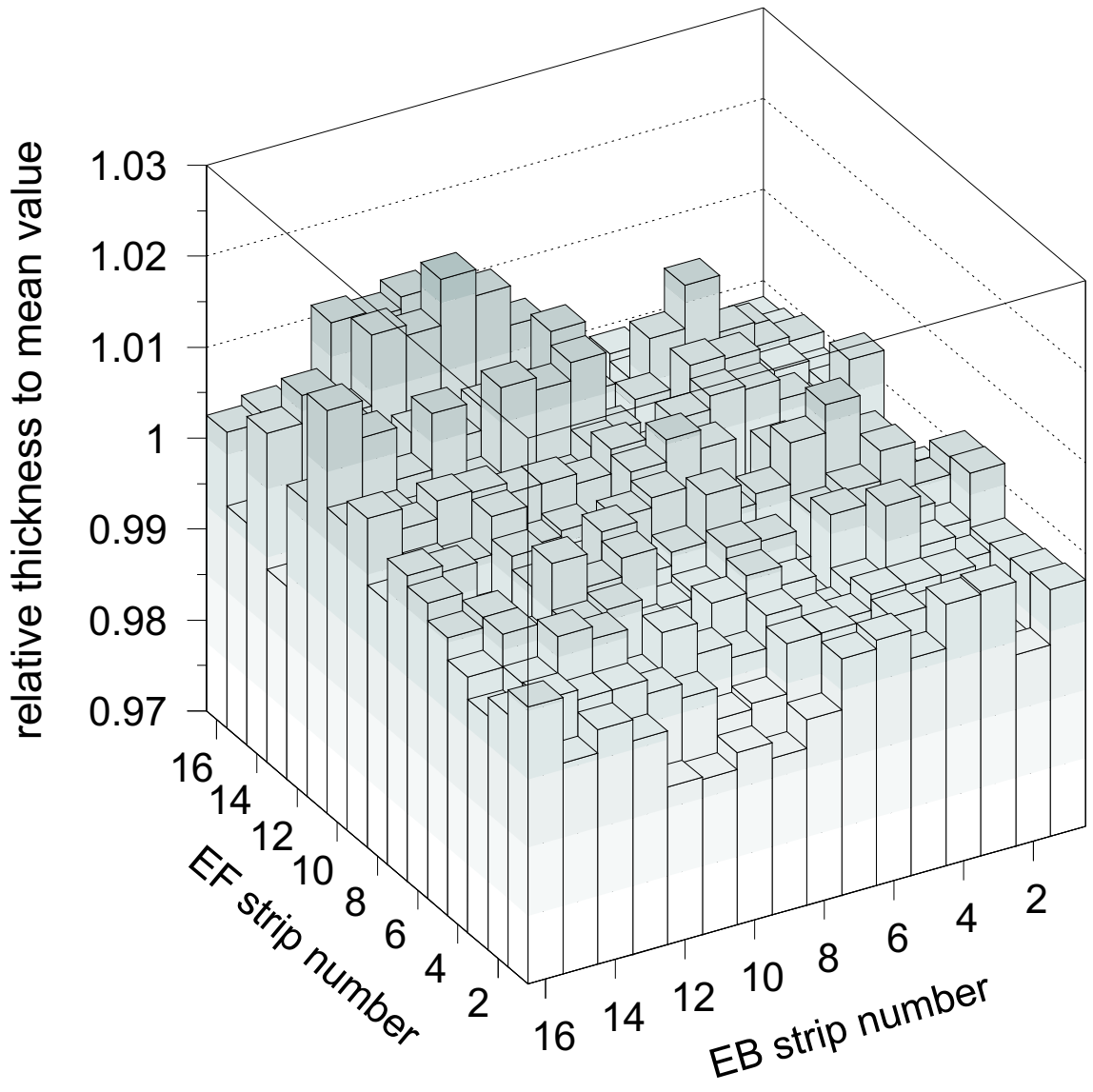


Figure 4.5: Non-uniformity of one typical 500 μm thick silicon detector.

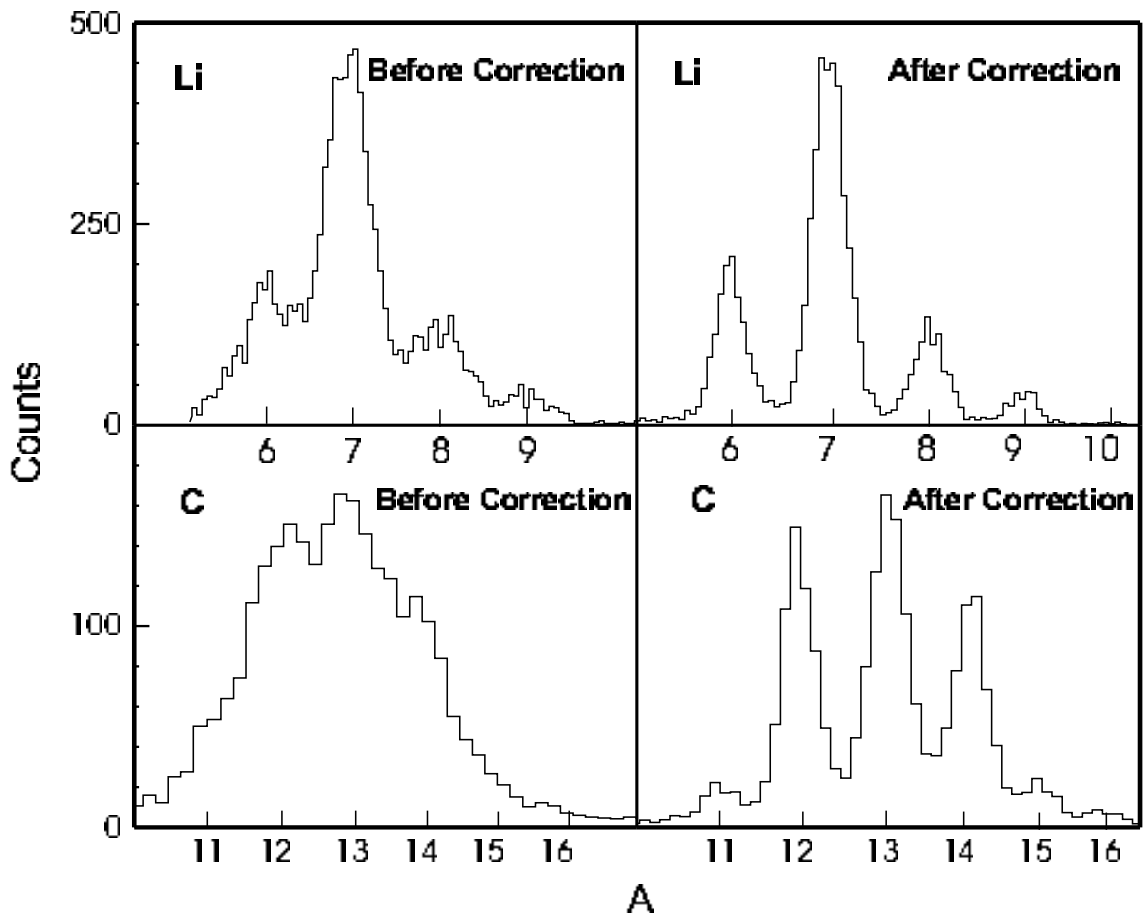


Figure 4.6: PID lines of Li and C isotopes before and after uniformity correction.

The relative thickness of silicon detectors was determined from the direct beam calibration experiment (which is also part of calibration for CsI crystals, see Sect. 3.2.4). The direct beam with fixed high energy was applied to punch through the silicon detectors. The correction matrix can then be constructed from the measured energy loss in each pixel. Assuming a linear relation between energy loss and thickness the thickness variation can be obtained according to the energy loss in each pixel. Figure 4.4 shows an example of the non-uniformity of the $65 \mu\text{m}$ silicon detectors. On the other hand, the $500 \mu\text{m}$ silicon detectors have much better uniformity as illustrated in Figure 4.5, suggesting that the absolute thickness variations of both types of detectors are comparable and the uniformity scales merely with the overall thickness.

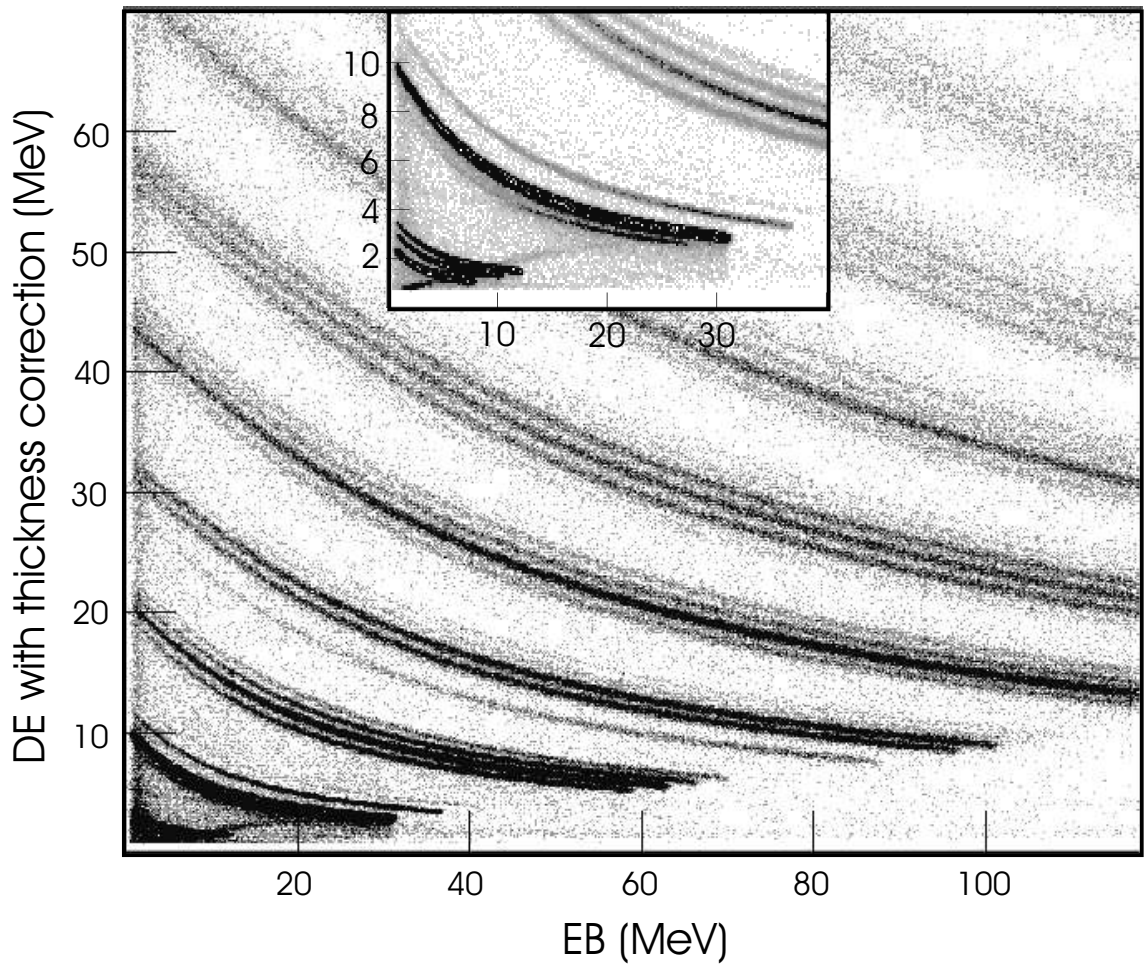


Figure 4.7: Isotopically resolved PID lines from H to O are shown for particles stopped in Silicon Detectors

After both layers of the silicon detectors have their thickness variation determined, the effects of thickness variations on particle identification (PID) can be removed so that PID gates can be imposed independent of hitting position. As showed in Figure 4.6 the PID lines of Lithium and Carbon isotopes are blurred before uniformity correction applied because the same particles don't fall in the same PID line when they go through different paths. On the right panel well defined sharp PID lines are achieved, indicating the importance of making an accurate uniformity correction.

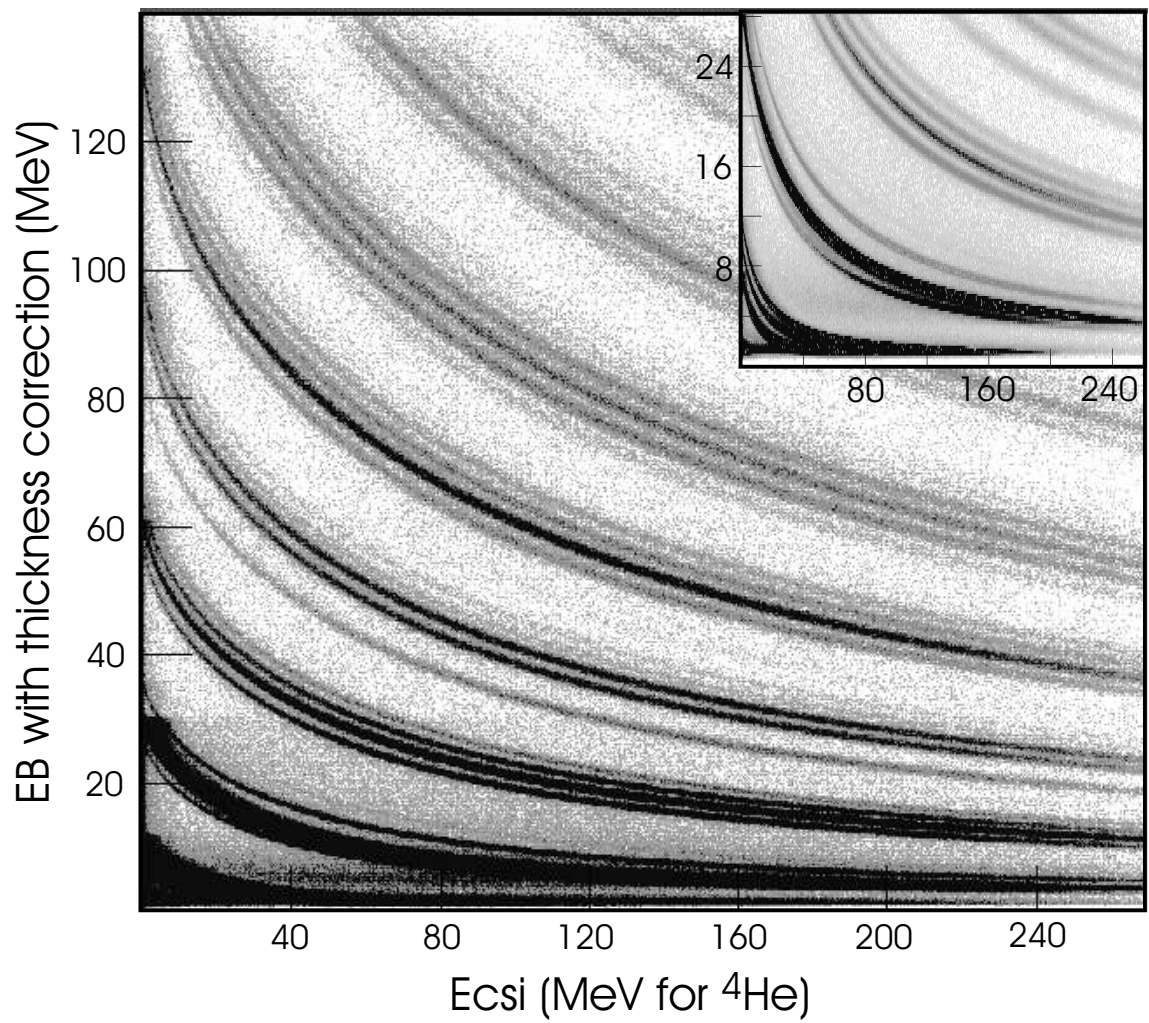


Figure 4.8: Isotopically resolved PID lines from H to O are shown for particles stopped in CsI crystals

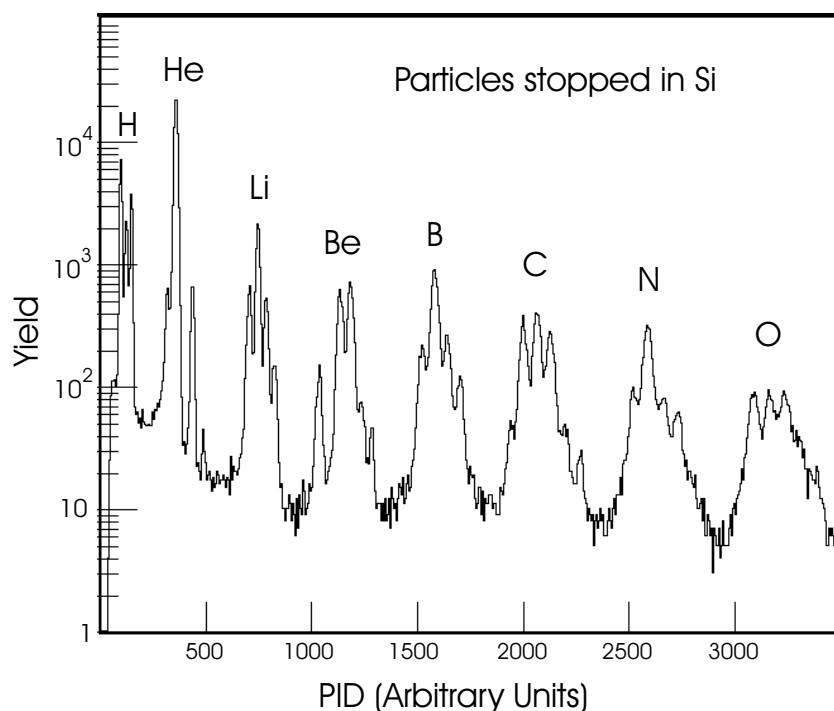


Figure 4.9: One-dimensional PID lines from H to O are shown for particles stopped in Si detectors

4.5 Isotope Resolutions and PID

Two sets of PIDs can be constructed for charged particles stopped either in the second layer of silicon or in the CsI crystal. Figure 4.7 shows the DEcorr (energy loss in DE with uniformity correction) vs. E (energy loss in Si2) for particles stopped in Si2. And similar plot in Figure 4.8 is shown for particles stopped in CsI. Different PID lines are well resolved in both plots for nuclei up to Oxygen and resolution could be achieved for heavier particles if the data were not limited by statistics and detector dynamic range.

However, these curved lines are not very convenient for identifying particles and further analysis. One solution is to straighten them out and make one-dimensional PID plot for easy-handling. To preserve the density of particle distribution on the DE-E plots, the flattened PID lines are drawn according to the intervals normalized

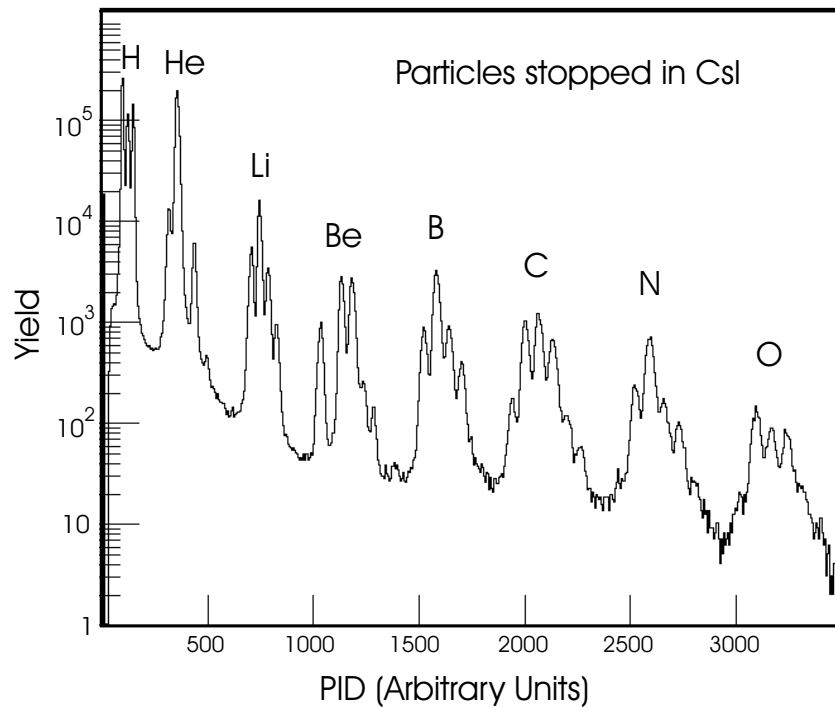


Figure 4.10: One-dimensional PID lines from H to O are shown for particles stopped in CsI crystals

along the diagonal direction of the DE-E plots. Simple one-dimensional PID spectrum can therefore be extracted as in Figures 4.9 and 4.10. Specifically for carbon isotopes the mass resolution can be seen in Figure 4.11 for carbons stopped in Silicon detectors (left panel) and in CsI crystals (right panel).

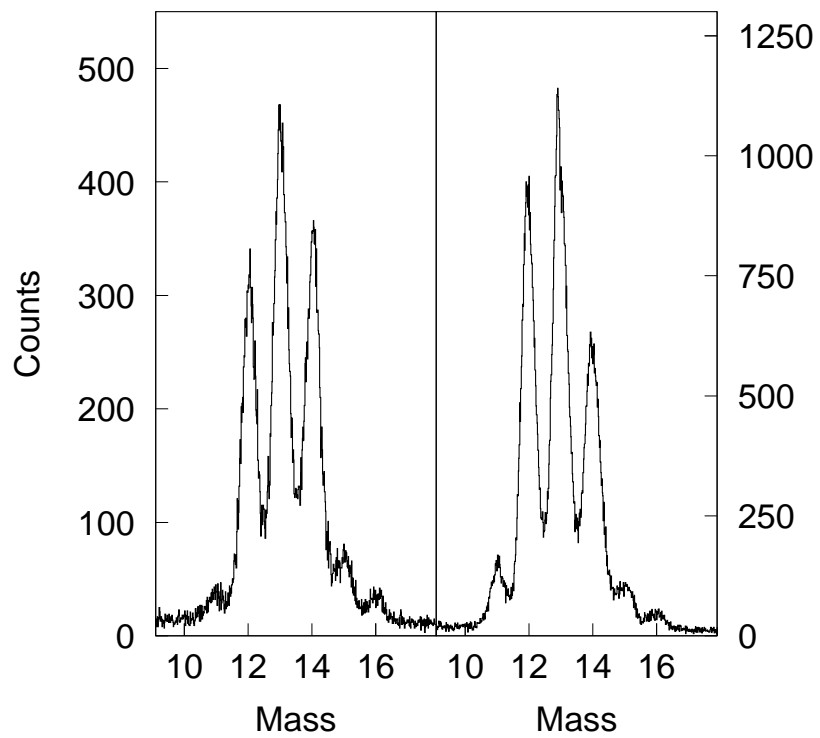


Figure 4.11: Mass resolution is illustrated from one-dimensional PID plots of Carbon isotopes. Left panel is for Carbons stopped in the second layer of Silicon detectors. Right panel is for Carbons stopped in the CsI crystals.

Chapter 5

Particle Correlations

Historically intensity interferometry via particle correlations was first studied in astrophysics. In the 1950's, Hanbury-Brown and Twiss applied this technique (now commonly called HBT) for measuring the diameters of distant astronomical objects by examining photon correlations[58]. This idea has later been generalized to correlations in nuclear physics involving various types of particles[61, 62]. The early examples such as pion-pion[80] and proton-proton[59] correlations involve identical bosons and fermions, respectively. These have been widely used for studying the properties of the sources of particles emitted in heavy ion reactions. Subsequently, non-identical particle correlations such as d-alpha correlations and correlations involving heavier fragments (up to Carbon) have also been studied; these studies have provided insight regarding the freeze-out conditions for multifragmentation processes after which interactions effectively cease [34, 81, 82]. Among such studies are the determinations of the populations of excited states of emitted fragments [83]. Considerable knowledge about the temperatures at the time of fragment emission has been gained and the hypotheses of thermal equilibrium for the emission mechanism has been tested in these studies[34].

In this chapter, we investigate the correlations of various charged particles emit-

ted during central $^{129}\text{Xe}+^{197}\text{Au}$ collisions at $E/A = 50$ MeV. The data presented here were measured with the LASSA array. We begin by discussing how to select the impact parameters included in our analyses. Then we introduce the basic correlation function observables. The correlation functions are interpreted via within the Koonin-Pratt formalism [59, 60] and within the assumption of thermal equilibrium. After discussing some of the strengths and weaknesses of the two approaches and their interrelationship, we explore the data for central $^{129}\text{Xe}+^{197}\text{Au}$ collisions more fully within the equilibrium approach. A determination of the breakup density for these multifragmentation events is attempted and the uncertainties of this determination are addressed. A technique for extracting spin information of unbound states from correlation functions is also presented, and applied to the determination of the spin of the 0.774 MeV excited state of ^8B (which is $J=1$) and to some other nuclei as well. Three particle correlations are also shown and discussed for the cases of deuteron-alpha-alpha, proton-alpha-alpha, alpha-alpha-alpha, and proton-proton-alpha correlations.

5.1 Selecting the Impact Parameters

To select the events of central collisions, we utilized charged particle multiplicity detected in both Miniball/Miniwall and LASSA as the impact parameter filter. This can be achieved from a monotonic relation between total charged particle multiplicity N_c and the reduced impact parameter \hat{b} [84],

$$\hat{b} = \frac{b}{b_{max}} = \left[\frac{\int_{N_c(b)}^{\infty} dN_c Y(N_c)}{\int_3^{\infty} dN_c Y(N_c)} \right]^{1/2} \quad (5.1)$$

where $Y(N_c)$ is the number of events associated with charge particle multiplicity N_c . b_{max} is the mean impact parameter for the collisions with $N_c = 3$. Figure 5.1 shows the above relation for this experiment, where $\hat{b} = 1$ corresponds to the glancing

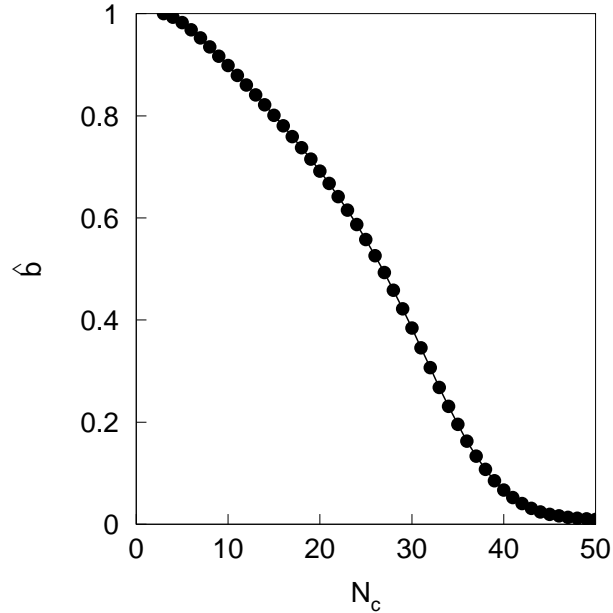


Figure 5.1: reduced impact parameter as function of total charged particle multiplicity.

collisions and $\hat{b} = 0$ represents the head-on collisions. In the following discussions, we will choose the gate of $0 < \hat{b} < 0.3$ for the selection of central collisions, which amounts to about 7% of total statistics.

Before going on to extract source information in the correlation functions, we show the single particle energy spectra. Five panels in Figure 5.2 present the differential multiplicities for p, d, t, ^3He and ^4He isotopes at angles of 17° , 27° , 37° , 47° and 57° . These nearly equally spaced angular distributions are at angles where the detection efficiencies are large. The spectra at forward angles are more energetic, reflecting that emission occurs from a frame (i.e. the center of mass) that is moving rapidly with respect to the laboratory frame. Within the energy and angular range of the correlation analysis described below, the detection coverage and efficiency is smoothly well behaved.

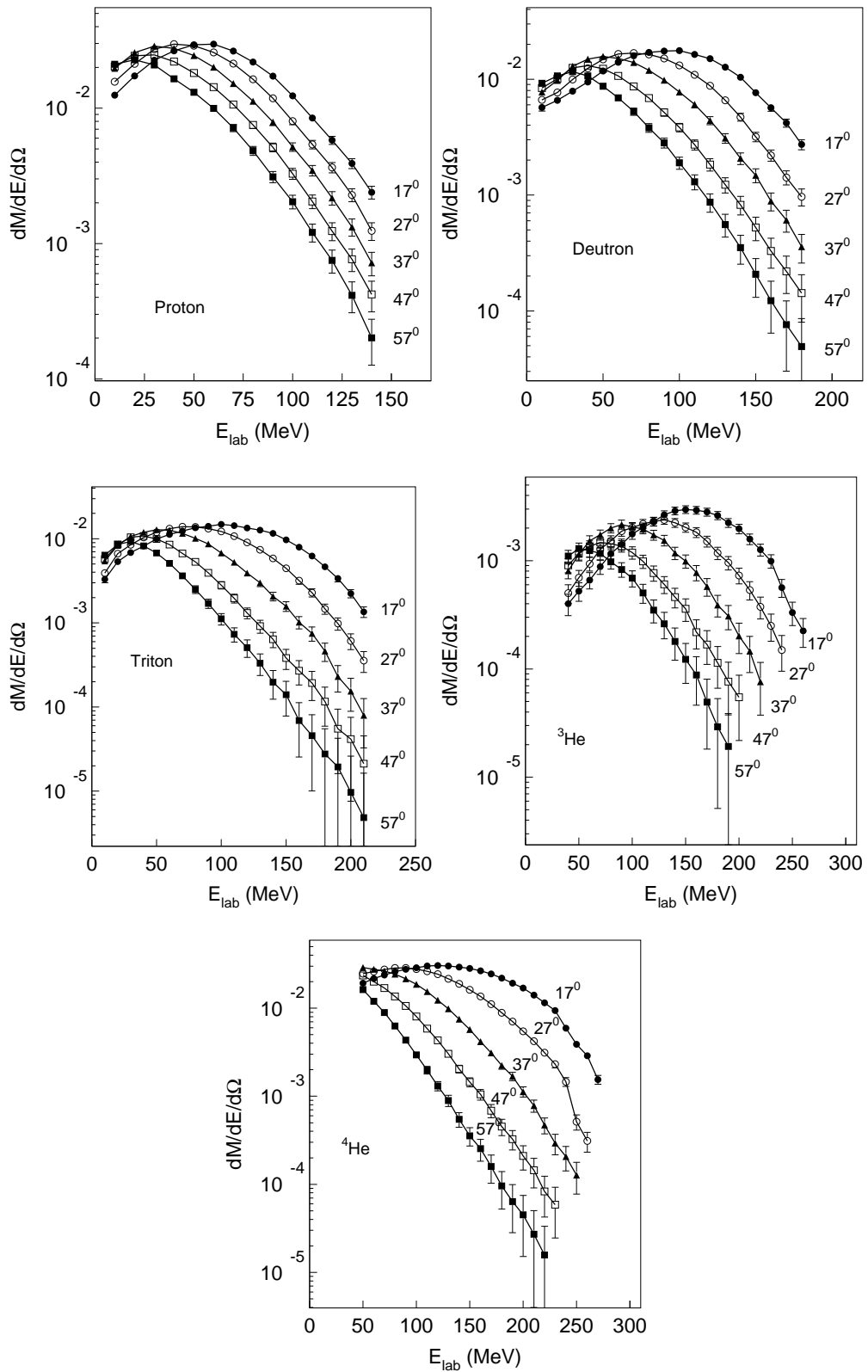


Figure 5.2: Differential multiplicities of hydrogen and helium isotopes at angles of 17°, 27°, 37°, 47° and 57°.

5.2 Two Particle Correlations and the Koonin-Pratt Formalism

Experimentally the two particle correlation function may be defined as follows,

$$\sum Y_{12}(\vec{p}_1, \vec{p}_2) = C(1 + R(q)) \sum [Y_1(\vec{p}_1)Y_2(\vec{p}_2)] \quad (5.2)$$

where Y_{12} is the two particle coincidence yield of a given pair of particles with their individual momenta \vec{p}_1 and \vec{p}_2 , respectively, and the $Y_i(\vec{p}_i)$ are the single particle yields for the two particles measured under the same impact parameter selection but not in the same event. The summations on both sides of the equation run over pairs of momenta \vec{p}_1 and \vec{p}_2 corresponding the same bin in relative momentum q . The correlation function describes how the correlation between coincidence particles measured in the same event differs from the underlying correlation dictated largely by phase space and modelled by mixing the single particle distributions of particles from two different events (the so-called event-mixed yield). The correlation constant C is typically chosen to ensure that $R(q) = 0$ at large relative energies where the correlations due to final state interactions and quantum statistics can be neglected. If the yields are normalized to be the appropriate differential multiplicities, C will be of order unity.

In the case of proton-proton and pion-pion correlations, most correlation function analyses have compared data to the Koonin-Pratt equation [59, 60]. If the summation in Eq. (5.2) does not involve strong constraints on the emission angles of particles 1 and 2, the appropriate comparison is to the angle-averaged Koonin-Pratt equation [59, 60],

$$C(q) \equiv 1 + R(q) = 1 + 4\pi \int dr r^2 K(q, r) S(r), \quad (5.3)$$

where the source function $S(r)$ is defined as the probability distribution for emitting a pair of particles with relative distance r at the time when the second particle is emitted; it should be normalized to unity if all the emission components are included. The angle-averaged kernel, $K(q, r)$, is obtained from the radial part of the antisymmetrized two-proton relative wave function as follows [59, 60],

$$K(q, r) = |\Phi_q(r)|^2 - 1 \quad (5.4)$$

where the wave function $\Phi_q(r)$ describes the propagation of the pair from a separation r out to the detector at infinity, where relative momentum q is reached.

Correlation functions have been analyzed using Eq. (5.3) for a variety of correlations involving hydrogen and helium isotopes [85, 61, 62]. Figure 5.3 shows the proton-proton correlation function measured in central $^{129}\text{Xe}+^{197}\text{Au}$ collisions at $E/A = 50$ MeV. The p-p correlation function, as a function of the relative momentum, is measured over angles of $12^\circ \leq \theta \leq 62^\circ$ covered by LASSA without c.m. energy cut. The maximum at relative momentum $q \simeq 20$ MeV/c is caused by the strongly attractive singlet S-wave proton-proton interaction; the minimum at $q \simeq 0$ MeV/c arises from the interplay between antisymmetrization and the long range repulsive Coulomb interaction[59].

The p-p correlation function with different c.m. energy cuts is also analyzed as shown in Fig. 5.4. The bottom panel shows the p-p correlation function for the same angular gate and with a gate which selects low energy protons with $0 < E_{cm} < 15$ MeV. The middle panel demonstrates the corresponding correlation function with a gate of $15 < E_{cm} < 30$ MeV and the top panel presents the p-p correlation function with a gate of $E_{cm} > 30$ MeV. Consistent with previous observations, the correlation function is clearly more enhanced for protons with higher energies, corresponding to the emission of more energetic protons from sources that are smaller or shorter-lived

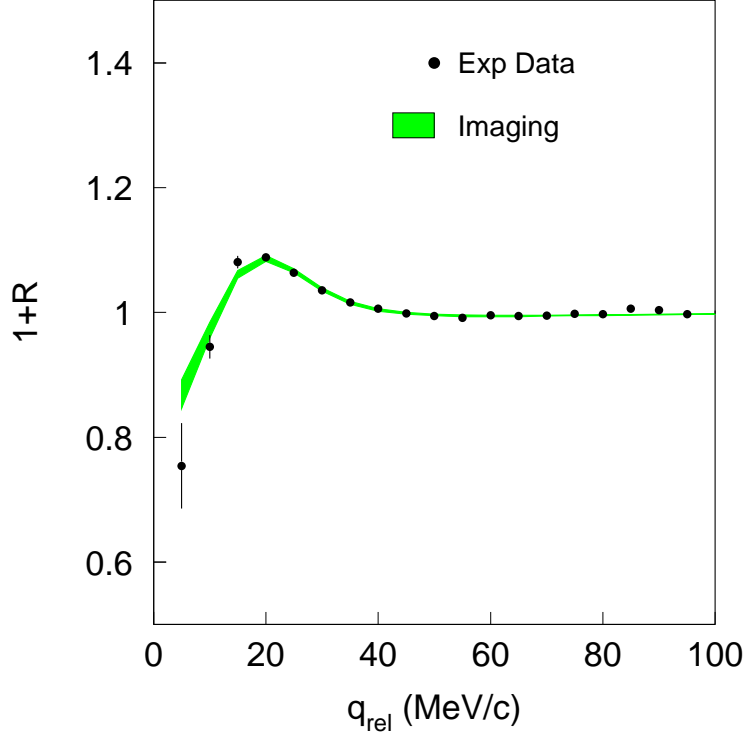


Figure 5.3: Inclusive p-p correlation function in central $^{129}\text{Xe}+^{197}\text{Au}$ collisions at $E/A = 50$ MeV is shown. The black points are experimental data and the grey line is the best fit by the imaging technique. See table 5.1 for specific parameters.

(or both) than the sources that emit lower energy protons.

In studying the properties of the two proton emission sources, the simple assumption of a single Gaussian source [85], with unit normalization, has been used but could not reproduce all the features of the correlation functions. Here, we use the less model-dependent imaging technique of refs. [86, 87, 88, 63] where p-p correlation functions have been analyzed by numerically inverting the correlation function in Eq. (5.3) to obtain the source. Such an inversion is not completely straightforward because one has to take into account experimental factors (limited statistics, finite widths of momentum bins, etc.) and the intrinsic resolution of the kernel $K(q, r)$.

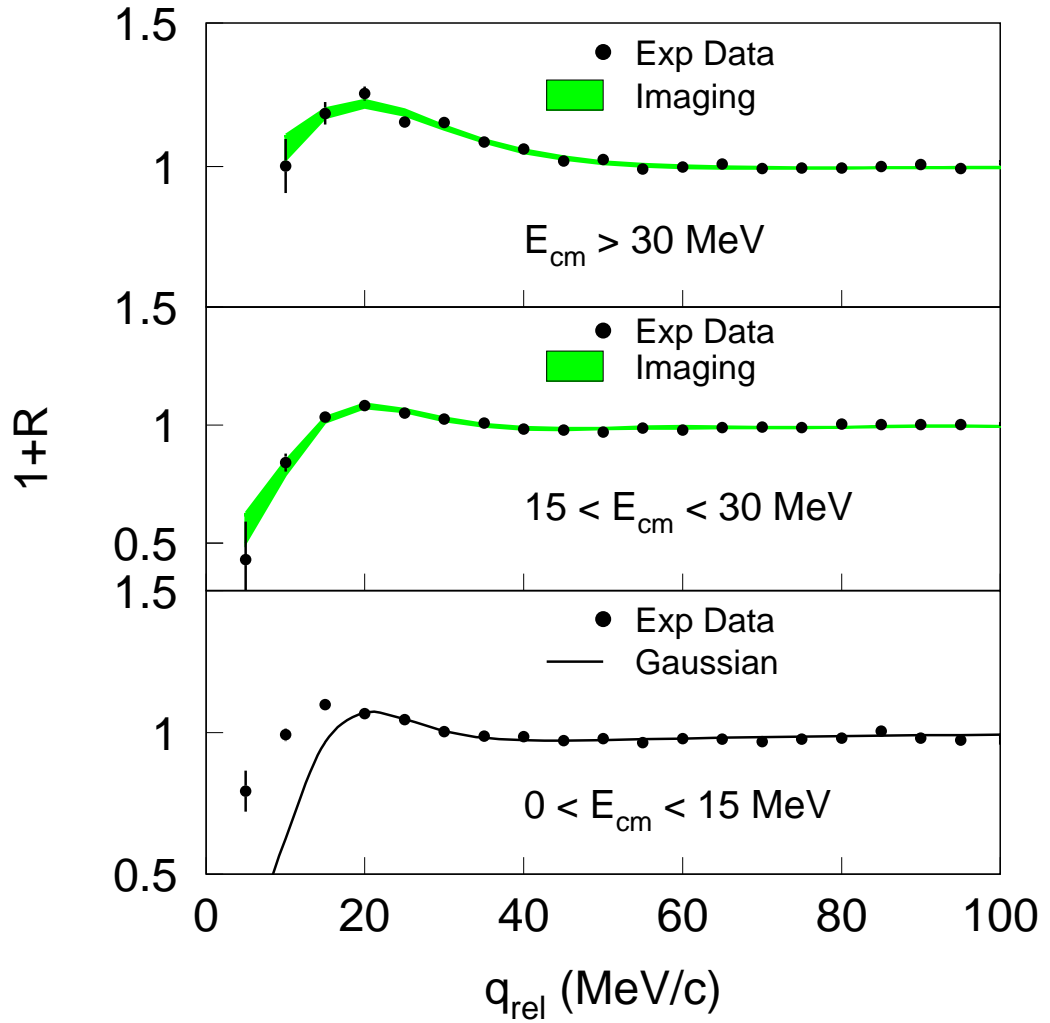


Figure 5.4: The p-p correlation functions are shown for three c.m. energy gates of $0 < E_{\text{cm}} < 15 \text{ MeV}$, $15 < E_{\text{cm}} < 30 \text{ MeV}$, and $E_{\text{cm}} > 30 \text{ MeV}$. For the middle and high energy gates, the image technique is used. The simple Gaussian source parametrization in Eq. 5.6 is applied for the low energy gate. See table 5.1 for specific parameters.

Small fluctuations in the data, even if well within statistical or systematic errors, can lead to large changes in the imaged source function. On the other hand, successful inversion of the correlation function has the virtue of being model independent.

The numerical inversion of the correlation in Eq. (5.3) was achieved via the optimization algorithm of refs. [87, 88, 63]. Using the imaging technique, we analyzed the data shown in Fig. 5.3 by decomposing the source in a superposition of six b-spline polynomials of the 3rd order over the interval $0 \leq r \leq 20$ fm [87, 88, 63].

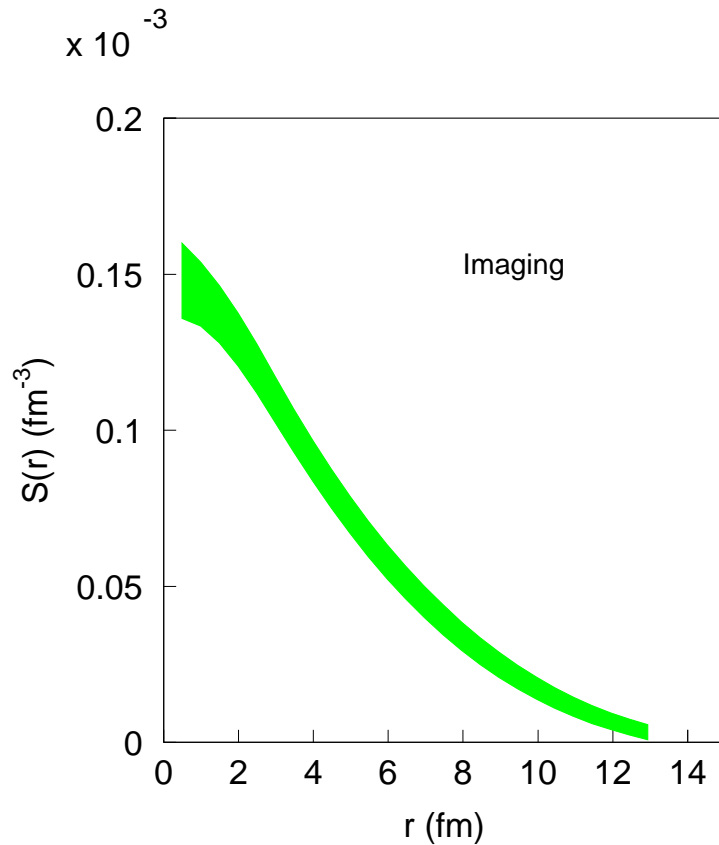


Figure 5.5: The imaged source function is shown by inverting the p-p correlation in Fig. 5.3. See table 5.1 for the extracted source radius.

The thick gray line in Fig. 5.3 is the best fit of the imaging approach to the experimental data (black points) of the two proton correlation. The imaged source function is shown by the thick grey line in Fig. 5.5 where the width of the line

indicates the uncertainty in the inversion. Since the correlation function is difficult to measure at low relative momentum (say, $q < 10$ MeV/c), the imaging technique could not reliably produce the tail of the source at large radii (say, $r > 13$ fm) where the dominant sources are delayed emissions of protons, such as from secondary decay. Thus the source is only specified for $r < 13$ fm. Better data of the correlation function at small relative momentum could provide better estimation on the source at larger radii where the source shape is mainly affected by the slow emissions of protons. The extracted rms radius of the source is $r_{rms} = 7.97$ fm for fast protons that contribute to $r < 13$ fm (see Table 5.1). However, the fraction of protons from these slow sources can be obtained via the integration of the imaged source [63]. Due to the omission of those long-lived components in the imaging of the source, the integration of the source is no longer unity [63],

$$f^2 \equiv \lambda = \int S(r) d^3\mathbf{r}, \quad (5.5)$$

where f is the fraction of protons emitted from fast sources while $1-f$ stands for the fraction of protons emitted from slow sources like secondary decay which can not be imaged in the long tail of the source profile. By integrating out the source shown in Fig. 5.5, we obtain $f=0.48$, which indicates that the emitted protons with a slow time scale (or in other words, $r > 13$ fm in the source profile) amount to about half of all the protons.

The two proton emission sources are also analyzed for the p-p correlation function with different c.m. energy gates in Fig. 5.4. For the middle and high energy gates, the extracted source functions are shown in the middle and top panels of Fig. 5.6 using the imaging technique. Unfortunately, the higher energy gate has no data at low relative momentum and the data at lowest point in relative momentum is measured with poor statistics. Thus the inversion provides no reliable information at $r > 7$ fm. We have

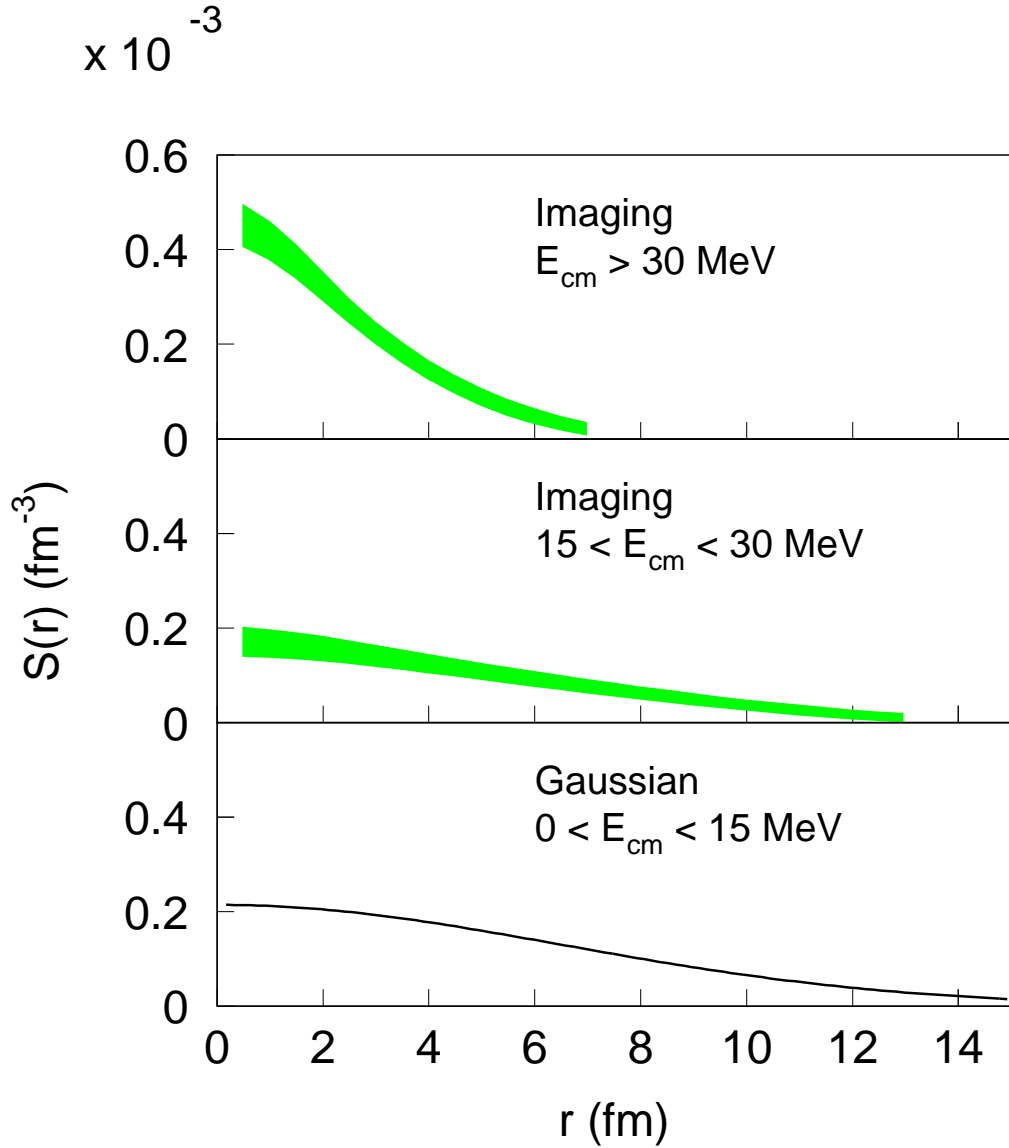


Figure 5.6: The source functions are shown for the p-p correlation functions in Fig. 5.4 for three c.m. energy gates of $0 < E_{\text{cm}} < 15 \text{ MeV}$, $15 < E_{\text{cm}} < 30 \text{ MeV}$, and $E_{\text{cm}} > 30 \text{ MeV}$. For the middle and high energy gates, the image technique is used. The simple Gaussian source parametrization in Eq. 5.6 is applied for the low energy gate. See table 5.1 for extracted source radii.

p-p Correlation	Inclusive	$0 < E_{p,cm} < 15$ MeV	$15 < E_{p,cm} < 30$ MeV	$E_{p,cm} > 30$ MeV
λ	0.22	0.93	0.50	0.14
λ'	0.11	0.22	0.16	0.14
r_{rms}	7.97	11.26	10.95	4.69
ρ/ρ_0	0.52	0.18	0.20	2.52

Table 5.1: List of quantities are shown for the p-p correlations (Figs. 5.3-5.6) for inclusive and three different c.m. energy gates. The λ that relevant to the fraction of protons contributed to the fitted source and the rms radius r_{rms} of the two proton source are extracted from the fitted source distribution. The λ' values are calculated from the integral of the source functions for $r < 7$ fm in Eq. 5.5. The density ρ/ρ_0 is estimated by taking into account collective effects in Eq. 5.9.

calculated r_{rms} by integrating the source for the highest energy gate over $r < 7$ fm and the source for the medium energy gate over $r < 13$ fm and obtained sources sizes of $r_{rms} = 10.95, 4.69$ fm and corresponding fast proton fractions $\lambda = 0.50, 0.14$ for the middle and high energy bins, respectively (see Table 5.1). The corresponding reconstructed correlation functions are shown by the grey lines in the middle and top panels of Fig. 5.4. Because the correlation data for the high energy gate (top panel in Fig. 5.4) has no points below $q < 10$ MeV/c one cannot say what are the source contributions at $r > 7$ fm. If the source function obtained from a better measurement that includes data below $q < 10$ MeV/c reveals a tail on the source function at larger radii $r > 7$ fm similar to that for the middle energy gate, the extracted λ value for the high energy gate will be much higher. On the other hand, if the tail of the source function for the middle energy gate are cut off, its λ value will be much lower, which is shown by column λ' in Table 5.1 for the integration of the source functions in Eq. 5.5 for $r < 7$ fm.

As for the lowest energy gate, however, we have not succeeded in stably imaging the data because the data do not conform to the shape expected for a correlation function of the Koonin-Pratt type. Instead we have fitted the correlation function

data with a non-unity Gaussian source of the form,

$$S(r) = \frac{\lambda}{(2\pi)^{3/2}r_0^3} \exp\left(-\frac{r^2}{2r_0^2}\right), \quad (5.6)$$

where r_0 is the source radius parameter and λ corrects for the fact that some of the protons are emitted over long time scales. The Gaussian source function fit is shown in the lowest panel of Fig. 5.6 and the corresponding correlation function is shown by the solid line in the bottom panel of Fig. 5.4. The quality of the fit is poor, especially at low relative momentum where there is an enhancement in the yield whose origin we do not understand. Whether this is some effect caused by secondary decay of some heavier isotope, we cannot say, but we have analyzed the correlation function under that assumption by fitting only the data at $q > 20$ MeV/c.

In general, the extracted sources for lower energy protons display larger source radii, which is consistent with emission from a source that has expanded and may be disassembling over a time frame that is somewhat longer than is the characteristic of the higher energy protons. With the uncertainties in the present correlation functions, we can not image the sources for these long-lived decays. We do, however, have indirect sensitivity to those decays from the fraction of fast protons $f = \sqrt{\lambda}$ extracted from the integral of the source in Eq. 5.5, which indicates there is a significant contribution from secondary decay to the proton emission.

Before relating the proton source functions to the density of the multifragmenting source, we investigate d-alpha correlations, which can also be addressed by the more conventional correlation function techniques involving the Koonin-Pratt equation. At present, d-alpha correlations have not been successfully inverted with the imaging technique. Instead, we illustrate the fit here with the simple Gaussian source parametrization described previously.

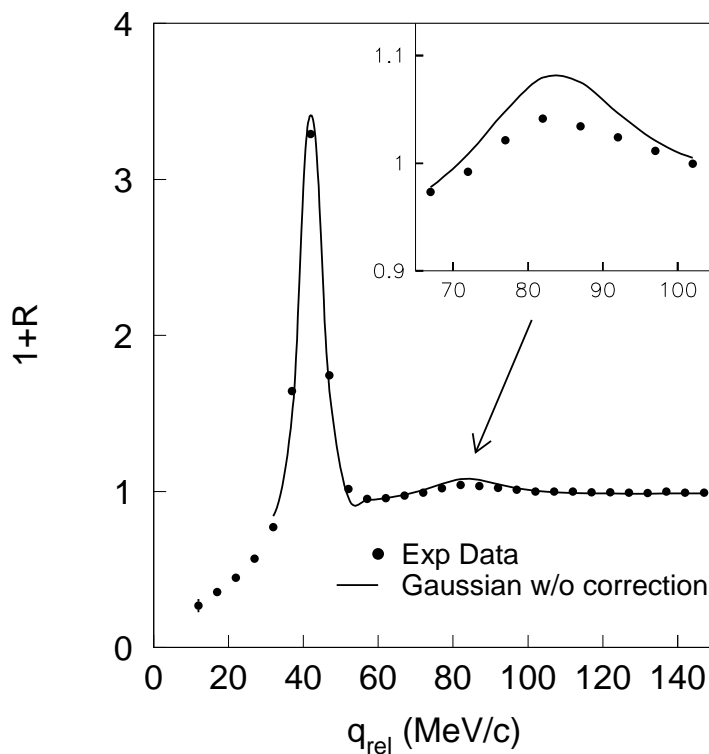


Figure 5.7: The inclusive d- α correlation function for the central collision gate is shown as a function of relative momentum by the black points. The solid line is the fit by the simple Gaussian source parametrization in Eq. 5.6 without corrections for collective motion. The blown-up in the top right shows the poor quality of the fit to the second peak of the d- α correlation.

Figure 5.7 shows the inclusive d-alpha correlation function as a function of relative momentum. The solid line in Fig. 5.7 shows the best fit to the experimental data with Gaussian source without making any correction for collective motion. The Coulomb suppression of the correlation function at small relative momentum $q_{rel} < 30$ MeV/c can not be fit with one single Gaussian source assumption like the case of the p-p correlation due to the existence of slow sources like secondary decay. Therefore the fit is performed at $q_{rel} > 30$ MeV/c and describe the magnitude and shape of the first excited state of ${}^6\text{Li}$ at 2.186 MeV well. However, the magnitude of the second peak at

4.31 MeV (see the blown-up in Fig. 5.7) is overpredicted and its shape is incorrect, a problem that has been noted by previous authors. Before interpreting this correlation data further, some discussion of the possible effects due to collective motion is needed because collective motion may be responsible for this difficulty. After this discussion, we will return to the interpretation of both d- α and p-p correlation functions.

5.3 Influence of Collective Motion

Collective motion is characterized by an average velocity field that assumes values that are defined by time and by the location within the colliding system. Examples of collective motion include the collective radial expansion of an excited system under the influence of pressure due to compression and to the repulsive Coulomb interaction, or collective "rotation" induced by a collision that is at non-zero impact parameter. Another form of collective flow, directed transverse flow [89], is small at $E/A=50$ MeV due to the balancing of repulsive and attractive momentum transfers at the "balance energy" and will not be discussed further here.

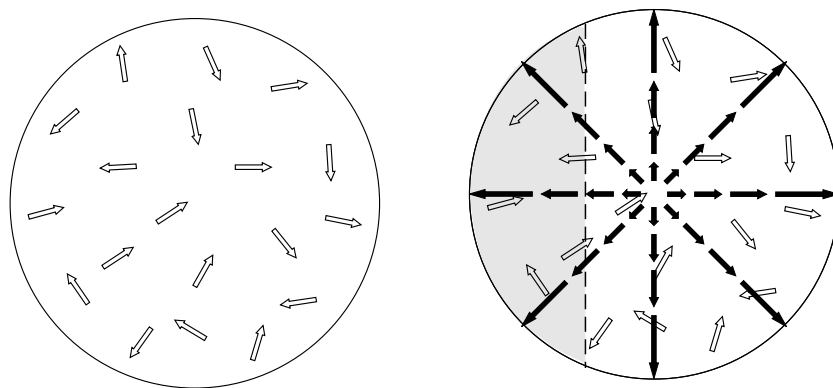


Figure 5.8: A source with only thermal motion (open arrows) is shown on the left. The collective velocity field (solid arrows) is drawn on the right and results in a grey area of the source where emission into the right half plane is improbable.

Collective motion has several impacts on the behavior of correlation functions. First, it effectively decreases the "source size", i.e., size of the region that can con-

tribute to the emission at the measured angles and energies. The origin of this effect is simply illustrated in Fig. 5.8. On the left side, we consider the scenario where there is no collective velocity and on the right side, we include a collective velocity field. In this drawing, the collective velocity field is drawn by the solid arrows and the random, i.e., thermal velocities are drawn in open arrows. The grey area indicates the region of the source where emission into the right half plane is improbable. In the long mean free path scenario, the source without collective motion corresponds to the total volume of the system. With collective motion, however, emission to the right is precluded in the grey region where the collective velocity has a component to the left that exceeds the typical random velocity, which if thermal in origin would decrease with mass as $v \propto (m)^{-1/2}$.

To estimate the influence of collective motion on the source sizes, we simulate the interplay between the collective and random source velocities as follows. We assume a spherical source of $A_{source} = 0.8(A_{projectile} + A_{target}) = 260$ nucleons, of which 106 are protons and that the source moves with the velocity of the center of mass. Within this spherical source, the collective velocity field at \vec{r} is given by

$$\vec{v}_{coll}(\vec{r}) = v_{r,max} \frac{\vec{r}}{R} + v_{t,max} \hat{\omega} \otimes \frac{\vec{r}}{R}, \quad (5.7)$$

where $v_{r,max}$ is the radial velocity of the surface expansion of the system at freeze-out, $v_{t,max}$ is the tangential collective velocity at the surface, R is the radius of the expanded source, and $\hat{\omega}$ defines the direction of the rotational velocity field. The orientation of $\hat{\omega}$ is approximately perpendicular to the beam axis, but the azimuthal orientation with respect to LASSA is unknown. Therefore, the azimuthal orientation is varied randomly assuming the relative azimuthal orientation between LASSA and $\hat{\omega}$ is isotropic.

We consider first the fraction of the source that can contribute to particle emission

into LASSA. Emission was simulated via Monte Carlo for the interplay of this collective velocity field with random or thermal motion [90]. In this simulation, the thermal velocity was calculated by assuming $v_{th} = \sqrt{3T/m}$ for simplicity where m is the mass of the particle and the temperature $T = 4$ MeV is roughly consistent with isotope and excited state temperatures in this bombarding energy domain. We choose a radial expansion velocity consistent with a radial kinetic energy of expansion of 2 MeV (and it is also affected by the additional Coulomb energy gained by continuing to accelerate the particles by the Coulomb field of the source). It is rather approximate but consistent with the radial expansion velocities reported in the literature. In addition, we choose an tangential velocity of $v_{t,max} = 0.16$ c, which corresponds to a surface tangential velocity consistent with the initial velocities of the projectile and target. We use the above collective flow parameters for the "maximum" flow discussed below and reduce them to see the dependence on the collective motion.

To demonstrate the mass dependence of the source size decreased by the collective motion, two particle sources from p-p, d-d, up to ^{20}Ne - ^{20}Ne are studied assuming 80% in velocity (or 64% in energy) of the "maximum" collective motion discussed above. In essence, the rms radius for a two particle source is calculated as $r_{rms}^2 = \langle (\vec{r}_2 - \vec{r}_1)^2 \rangle$, where \vec{r}_i is the location of the i^{th} particle at the time of emission and the average is over particles that make it into the LASSA array. If the two particles are emitted from the same source, the rms radius for the two particle source is $\sqrt{2}$ times the rms radius for a single particle source. The velocity field in Eq. 5.7 is constructed so as to make the ratio of the rms radii to the overall system radius invariant with respect to the system size. The ratio f_{coll} , of the rms radius with collective motion divided by the rms radius without collective motion for the two particle sources, is plotted as the solid line in Fig. 5.9 as a function of the mass number while the ratio without collective motion is denoted by the dashed line. The solid line was obtained

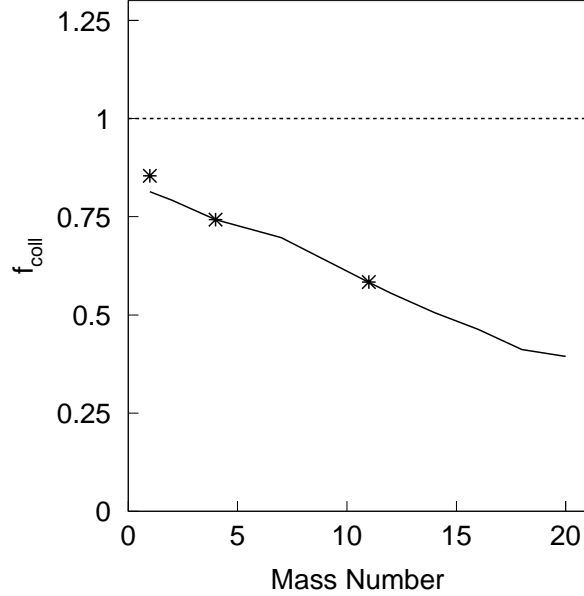


Figure 5.9: The source reduction factor, f_{coll} , obtained from the ratio of the rms radius to the system radius for the two particle sources with collective motion, are shown by the solid line as a function of the mass number. The ratio without collective motion is denoted by the dashed line. The solid line is calculated for a uniform spherical system with a radius of 11 fm while the three symbols denote the corresponding calculations for a system with a radius of 7 fm.

from calculations for a uniform spherical system with a radius of 11 fm. The three symbols denote the corresponding calculations for a system with a radius of 7 fm; this demonstrates the independence of this ratio with respect to the system size.

The corresponding reduction in the fraction of the participating source, f_{coll}^3 , essentially dictates the fraction of the participating source, i.e. the mass fraction, independent of the actual source volume. It depends on $v_{r,max}$, $v_{t,max}$, and the random velocity $v_{th} = \sqrt{3T/m}$, but not on the source radius R . Clearly, the collective velocity field decreases the mass of the source significantly, for example, by about a factor of 2 for the p-p correlation. In Fig. 5.9 no cuts on relative momentum are applied since we want to show the mass dependence of the source reduction factor.

In reality, we need to obtain the f_{coll}^3 factor for a gate of relative momentum where we study the correlation function. The corresponding reduction of the d- α source is also calculated for the purposes of density extraction from the d- α correlation to be discussed later in this section. This calculation yields a mass reduction factor of about 5 for a relative momentum gate of 0-150 MeV/c.

In addition, the collective motion causes the particles to be more frequently emitted in the plane perpendicular to $\hat{\omega}$. This leads to a preference for the relative azimuthal angle of the two particles to be 0° or 180° [91] and also modifies the shapes and magnitudes of broad correlation function peaks. In such cases, the two particles are emitted from nearly the same point and experience nearly the same collective velocity field. On the other hand, the mixed event background includes particles that are from two different events in which the collective velocity fields are completely different. Thus the relative velocity distribution for the resonant contribution is dictated essentially by thermal motion and consequently narrower than the relative velocity distribution for the non-resonant and mixed event backgrounds, for which the relative velocity reflects differences in the collective velocities as well.

Fig. 5.10 shows a simulation of that effect for the d-alpha correlation. The solid line shows the relative energy distribution between two particles that lie within a distance of 2 fm from each other as they would be if they were both emitted from a particle unbound fragment formed at freezeout. This relative energy distribution is essentially consistent with an exponential decline of the form $\propto \sqrt{E_{rel}} \exp(-E_{rel}/T)$ given by the thermal motion. The dashed line shows the corresponding relative energy distribution for pairs of particles that are chosen randomly throughout the system as they would be for the non-resonant background. Here the relative energy distribution is much wider consistent with significant contributions from the difference between the collective velocity field at the two emission points. The dotted curve in the same figure

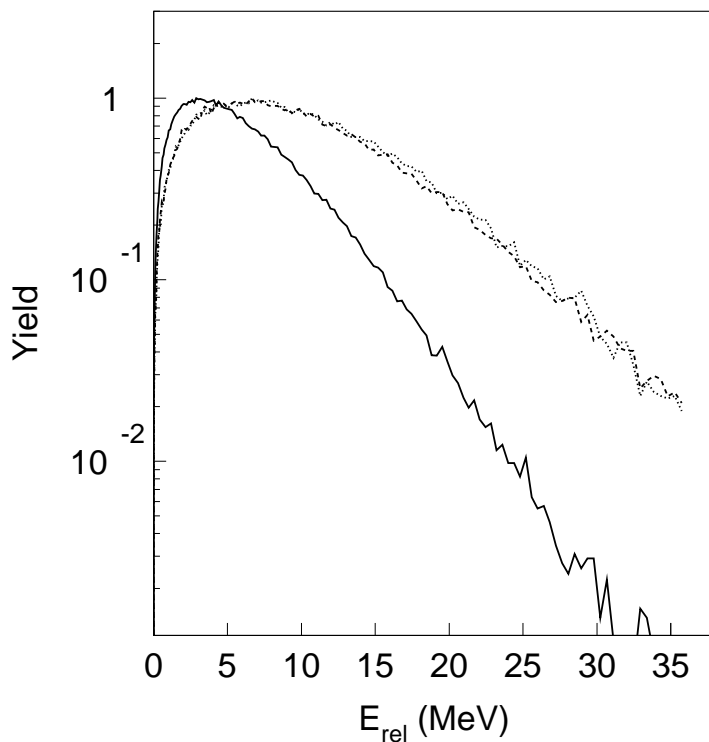


Figure 5.10: The solid line shows a simulation of the resonant distribution as a function of relative energy for the d-alpha correlation. The dashed line denotes the simulation for non-resonant background while the dotted line demonstrates the relative energy distribution for mixed event background. All the distributions are normalized to one for comparisons.

shows the additional broadening that occurs in the event mixing in the denominator of the correlation function where the two particles originate from different events with different orientations of the reaction plane, i.e., different azimuthal orientations for $\hat{\omega}$. For simplicity, we could describe the distribution of relative energies here by $\propto \sqrt{E_{rel}} \exp(-E_{rel}/T_{mix})$.

The different broadening in these distributions has important consequences for the correlation function, where the two distributions are essentially divided by each other. The division of the resonant yield by the mixed event distribution is illustrated in the

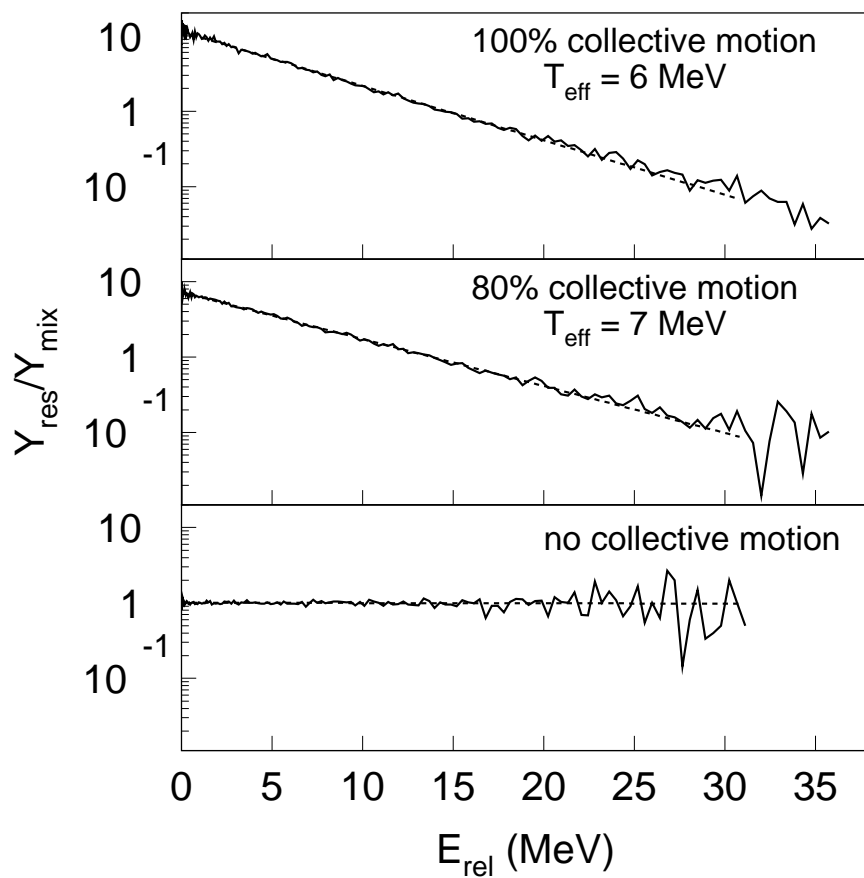


Figure 5.11: The ratios of the resonant yield over the mixed event distribution for the d- α correlation are shown in three panels for maximum, 80% and zero of the collective motion, respectively. The corresponding values of T_{eff} are extracted from the fits (dashed lines).

three panels of Fig. 5.11 for maximum, 80% and zero of the collective motion discussed above, respectively. The dashed lines in the figure are the best fits of an exponential function $\propto \exp(-E_{rel}/T_{eff})$, which have values of $T_{eff} = 6, 7$ MeV for maximum and 80% of collective flow, respectively; the line is flat in the bottom panel without collective motion. This simulation indicates that one should expect the resonant peaks in the correlation function to decline exponentially with the relative energy or relative momentum according to $\propto \exp(-E_{rel}/T + E_{rel}/T_{mix}) = \exp(-E_{rel}/T_{eff})$. The non-resonant background is also expected to decline somewhat, but to a much reduced extent.

Taking the simulations in Fig. 5.11 into account, we return to the d- α correlation in Fig. 5.7. Consistent with the simulations, we find that the non-resonant background is relatively well represented in the original calculations. However, the resonant yield can be much better described by multiplying the resonant contribution by a factor $\exp(-E_{rel}/T_{eff})$ with $T_{eff} = 6.5$ MeV. This revised correlation function is given by the solid line in Fig. 5.12, which fits the second peak of the d- α correlation function at $q_{rel} = 84$ MeV/c (the blown-up) much better than that in Fig. 5.7. The extracted source radius is $r_0 = 3.3$ fm and the rms value and λ can be seen in Table 5.2. Using this empirical correction, we have explored the sensitivity of the d- α correlation function in general for the extraction of information about the size of the emitting source using a Gaussian source of the form discussed in Eq. 5.6. Consistent with conclusions recently obtained for d- α correlations on other systems [92], we find that the width of the second peak in the correlation function at $q_{rel} = 84$ MeV/c is very sensitive to the source size. This is illustrated in Fig. 5.12 where two other fits are shown by the dashed and dotted lines with the assumption of source radii of $r_0 = 2.0$ fm and 5.0 fm, respectively. This situation is similar to that for the p-p imaging analysis where the source radius information is primarily obtained from the

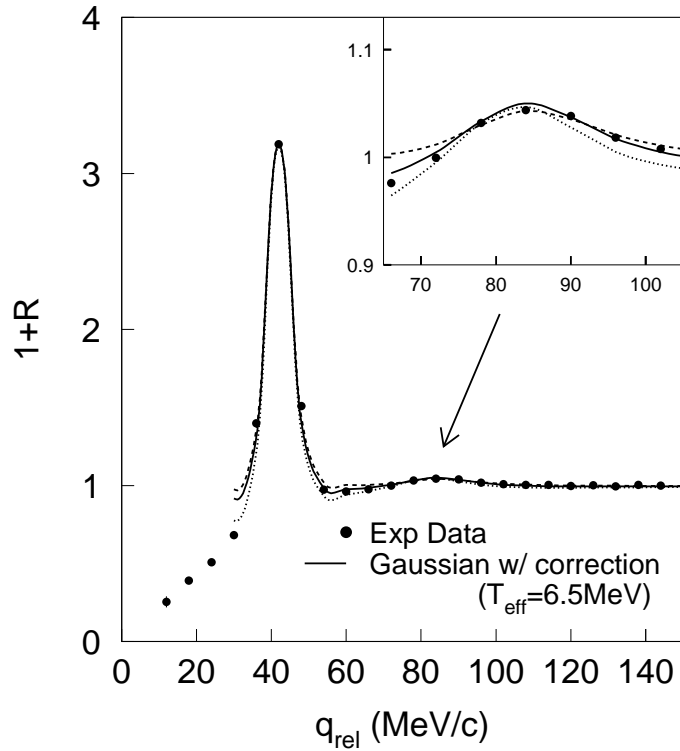


Figure 5.12: The inclusive d- α correlation function for the central collision gate is shown as a function of relative momentum by the black points. The solid line is the best fit by the simple Gaussian source parametrization in Eq. 5.6 with T_{eff} corrections for collective motion. The blown-up in the top right shows the good reproduction of the second peak of the d- α correlation after T_{eff} corrections. The extracted source radius is $r_0 = 3.3$ fm (see Table 5.2 for the rms value). The dashed and dotted lines are the fits assuming that the source radius is $r_0 = 2.0$ fm and $r_0 = 5.0$ fm, respectively.

width of the p-p correlation function, not its height[63].

d- α Correlation	Inclusive	$0 < E_{d,cm} < 20$ $0 < E_{\alpha,cm} < 25$ MeV	$20 < E_{d,cm} < 40$ $25 < E_{\alpha,cm} < 45$ MeV	$E_{d,cm} > 40$ $E_{\alpha,cm} > 45$ MeV
λ	0.11	0.14	0.13	0.13
r_{rms}	5.72	7.35	5.58	3.01
ρ/ρ_0	0.54	0.37	0.59	3.74

Table 5.2: List of quantities are shown for the d- α correlations (Figs. 5.12-5.13) for inclusive data and three different c.m. energy gates. The λ that relevant to the fraction of the involved particles contributed to the fitted source and the rms radius r_{rms} of the two proton source are extracted from the fitted source distribution. The density ρ/ρ_0 is estimated by taking into account collective effects in Eq. 5.9.

Different energy gates for the d-alpha correlation are also studied as shown in Fig. 5.13. By varying the parameter T_{eff} from collective effects, we can fit the correlation functions for the high, middle, and low energy gates, especially for the second peak at $q = 84$ MeV/c which is blown up in the top right corner of the corresponding panel. While the first peak can be fitted somewhat better by adjusting T_{eff} in this simple one Gaussian source parametrization and the Coulomb suppression at low relative momentum can be fitted better by adding a tail to the gaussian source, we will defer further discussion of the first peak until the next section and devote our attentions here to achieving the best fit to the second peak.

The collective motion effects are more evident for the lower energy gate where the T_{eff} value is lower than for the highest energy gate where the effects virtually vanish and no T_{eff} correction is needed. The extracted rms radii and λ values for the three energy gates are in Table 5.2. Same as the case in the p-p correlation, the sources extracted from the d- α correlation functions have smaller radii for the higher energy gates.

In principle, sources extracted by inverting p-p correlation functions may also be influenced by collective motion. Fig. 5.14 shows the corresponding results from simu-

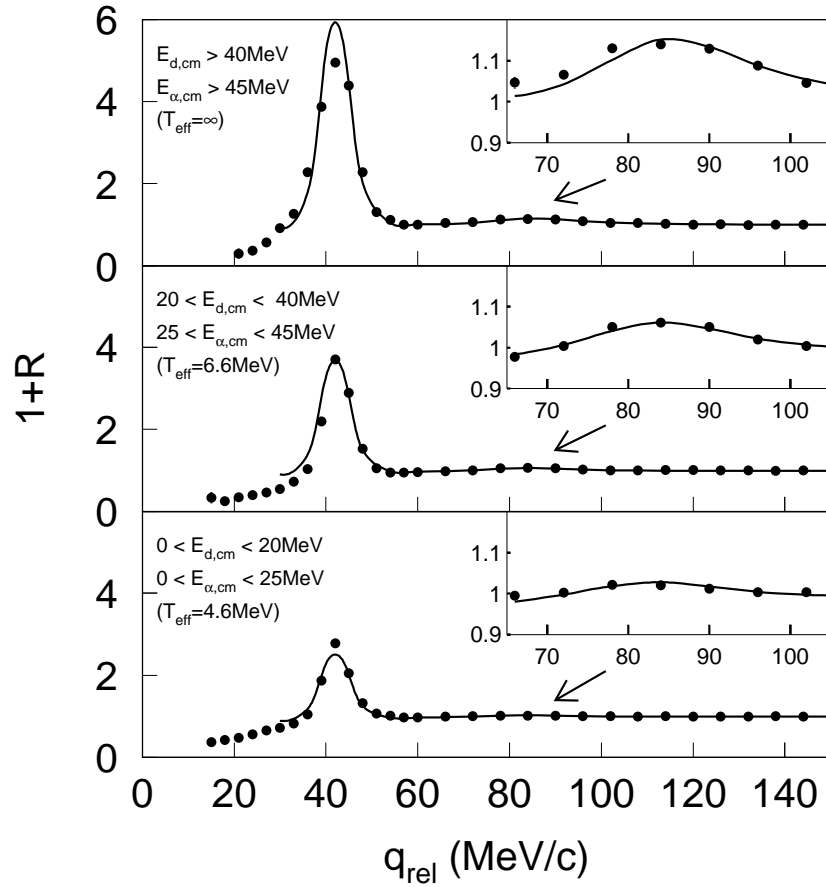


Figure 5.13: The d- α correlation functions are shown for three c.m. energy gates of $0 < E_{d,cm} < 20$ MeV and $0 < E_{\alpha,cm} < 25$ MeV, $20 < E_{d,cm} < 40$ MeV and $25 < E_{\alpha,cm} < 45$ MeV, and $E_{d,cm} > 40$ MeV and $E_{\alpha,cm} > 45$ MeV. Fits by the simple Gaussian source parametrization in Eq. 5.6 are shown by the solid lines after T_{eff} corrections for collective motion. See table 5.1 for extracted source radii and λ values.

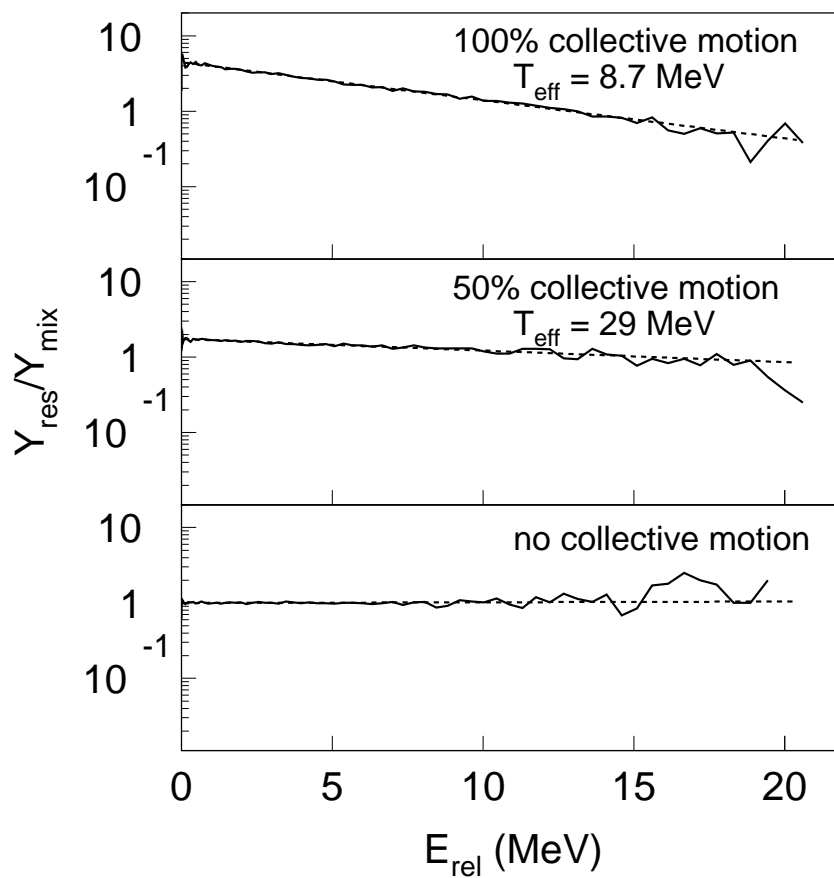


Figure 5.14: The ratios of the resonant yield over the mixed event distribution for the p-p correlation are shown in three panels for maximum, 50% and zero of the collective motion, respectively. The corresponding values of T_{eff} are extracted from the fits (dashed lines).

lations of the influence of collective motion on the p-p correlation functions assuming three different sets of collective flow parameters. The corresponding values of the effective temperature T_{eff} are much larger than the values extracted from the d- α correlation, which indicates this effect is much smaller for the p-p correlation. In addition, the peak of the p-p correlation function falls within the very low energy region of $E_{rel} < 0.5$ MeV, unlike the case of the second peak in the d- α correlation function which is at $E_{rel} = 2.836$ MeV. Therefore, the distortion effects from T_{eff} should be much smaller for the p-p correlation than those for the d- α correlation. In the interest of brevity, we neglect them in the following analyses.

Using these analyses of the p-p and d- α correlations, we attempt to place some constraints on the densities of the system at the time of particle emission. Because we are using source radii determined from the widths of the p-p correlation function and the width of the second peak in the d- α correlation, we are *insensitive* to how collective motion reduces the fraction of deuterons, alphas or protons that come to the LASSA and contribute to the mixed event background to the correlation function. On the other hand, we are *sensitive* to how the imaged region may be effectively shrunk by the collective motion and we must make some correction for that effect. For these estimates, we use the factor f_{coll}^3 determined earlier using $T_{eff} = 7$ MeV, which is close to the value obtained for most inclusive correlation functions, to determine the fraction of the system that is contributing to these emissions. Take the p-p correlation function shown in Fig. 5.3, for example, the rms source radius $r_{rms} = 7.97$. The simulation in Fig. 5.9 suggests that the p-p correlation function, actually originates from a fraction of the source. This fraction is given by f_{coll}^3 where $f_{coll} = 0.8$. We assume that the mass contained in the region sampled by the p-p correlation function to be $f_{coll}^3 \cdot A_{prefragment} = (0.8)^3 \cdot A_{prefragment}$ where $A_{prefragment}$ is the mass of the system after the end of pre-equilibrium emission. For this estimate, we take

$A_{prefragment} \approx 260$ corresponding to 80% of the total system.

To obtain an averaged density, we need to find the volume V_{source} of the breakup source measured by the two particle source function. It is important to note that the rms radius of the two particle source function is obtained by adding the rms radii of single particle source functions in quadrature, i.e., $r_{rms} = \sqrt{2}r_1$. For an equivalent sharp uniform spherical source with a radius of R , the rms radius of the two proton source has a relation of $r_{rms} = \sqrt{(6/5)}R$ and consequently we can obtain the source volume,

$$V_{source} = \frac{4\pi}{3}R^3 = \frac{4\pi}{3} \left[\sqrt{\frac{5}{6}}r_{rms} \right]^3. \quad (5.8)$$

Therefore, the density can be written as,

$$\rho/\rho_0 = \frac{f_{coll}^3 \cdot A_{prefragment}}{\frac{4\pi}{3} \left[\sqrt{\frac{5}{6}}r_{rms} \right]^3 \rho_0} \quad (5.9)$$

where the saturation density $\rho_0 = 0.16$ nucleons/fm³ is assumed. Densities obtained for the all energy gates for the p-p correlations are given in Table 5.1 by using Eq. 5.9. The extracted value of the density for the low energy gate is not as reliable as those obtained by the imaging technique since the Gaussian source approach does not reproduce the correlation for the low energy gate in Fig 5.4. However, one does see a trend that the system is at a higher density when higher energy protons are being used to construct the correlation. The density value from the high energy gate is so high ($\rho/\rho_0 = 2.52$) that it seems the correlation either 'sees' the very early source (compressed and before being expanded) since fast protons tend to emit earlier, or it just 'sees' a smaller fraction of the source. The latter case would apply if the source in the early stage is limited to the surface due to the short mean free path in the dense interior.

For the d- α correlation, we have a different collective correction factor $f_{coll} = 0.58$, which is obtained by simulating d- α correlation sources as discussed previously at low relative momentum where we fit the data. Values for the density obtained from the d- α correlation functions are given in Table 5.2 by using Eq. 5.9. Since the simple Gaussian source parametrization is used in this case, it can not reproduce all the features of the d- α correlation functions and the presumed Gaussian shape for the sources may be rather schematic. Consequently, the extracted source radii and densities may not be as reliable as those obtained from the p-p correlation functions by the imaging technique. After taking into account the effects of collective motion properly, however, we obtain similar values of density (0.52 and 0.54, respectively) from both the inclusive p-p and d- α correlation functions. Moreover, a similar trend of the energy dependence of the density is observed, which indicates that higher energy particles are emitted at denser regions or earlier times. We note that it can be argued that more accurate values for the density could be obtained if f_{coll} were calculated for each of these energy gates via simulations tuned to reproduce the values for T_{eff} observed for each gate. Since lower values of T_{eff} will result in smaller f_{coll} , the values for density in this case would be somewhat lower.

Clearly, there are large uncertainties in this approach. These uncertainties stem from several different sources. First concerns whether the corrections for reduction of the source sizes from the Monte Carlo simulations are of the correct magnitude. We believe that while they are qualitatively correct, they could be off in their magnitudes somewhat and we are considering ways to try to estimate this uncertainty more quantitatively. Secondly, we have some concerns about the assumption of an infinite mean free path that this density estimate employs. Clearly, this assumption is more correct if the estimated density is small. When it is large, however, transport theoretical calculations indicate a sensitivity of two particle correlation functions to the in-medium

cross section. Thus the estimated values for density for the p-p correlation functions in Table 5.1 and the d- α correlation function in Table 5.2 are somewhat uncertain on this account and if there are corrections needed, it would be in the direction of reducing the density.

5.4 Equilibrium Correlation Functions

One of the factors limiting the extension of the Koonin-Pratt equation to heavier particles is the care needed to construct the Kernel $K(q,r)$. Essentially, one must search for a set of attractive nuclear potentials that can reproduce the experimental phase shifts. Right now, we have only the necessary potentials for the p-p and d- α correlation functions. To rapidly extend the correlation function to heavier particles and to facilitate the comparison to statistical models, we develop here a formalism for calculating the correlation function within equilibrium theory.

The starting point for this development is the consideration of elements needed for the equilibrium description. First, one needs to have a compact method for incorporating both the long range Coulomb and short range nuclear interactions. Second, one must address the volume that is occupied by other particles. We choose to address the second issue by invoking the excluded volume approximation. This essentially amounts to counting as particles only those that are isolated, a procedure that is consistent with most equilibrium multifragmentation approaches [9, 10].

Equilibrium correlation function expressions are derived by considering how the two particle phase space is modified by interactions. For simplicity, we consider the simplified geometry wherein the pair of spinless particles with charges Z_1 and Z_2 is with its center of mass at the center of a volume V . To calculate how the phase space of relative motion is modified by the Coulomb interaction, we follow semi-classical

theory which states that the phase space density is given as a function of the relative spatial separation \vec{r} and relative momentum \vec{q} by

$$\frac{dn}{d^3\vec{r}d^3\vec{q}_L} = \frac{1}{h^3}, \quad (5.10)$$

where \vec{q}_L is the local momentum given in terms of q , the reduced mass $\mu = M_1M_2/(M_1+M_2)$ and the Coulomb potential by

$$q_L = \sqrt{q^2 - \frac{2\mu Z_1 Z_2 e^2}{r}}. \quad (5.11)$$

Reexpressing Eq. 5.10 in terms of the momentum \vec{q} at large distances where the Coulomb interaction can be neglected, we have

$$\frac{dn}{d^3\vec{r}d^3\vec{q}} \Big|_{Coulomb} = \frac{dn}{d^3r d^3q_L} \frac{d^3q_L}{d^3q} = \frac{1}{h^3} \cdot \sqrt{1 - \frac{2\mu Z_1 Z_2 e^2}{rq^2}}. \quad (5.12)$$

If the above equation is integrated over a volume V and divided by the corresponding integral of the relative phase space density of two free particles, $dn/d^3\vec{q} = V/h^3$, an expression for the Coulomb correlation function $1 + R_{Coul}$ may be obtained as follows,

$$1 + R_{Coul}(q) = \frac{1}{V} \int_V d^3r \sqrt{1 - \frac{2\mu Z_1 Z_2 e^2}{rq^2}}. \quad (5.13)$$

The extension of this Coulomb correlation scenario to include the influence of short ranged nuclear interactions can be accommodated using a formalism for calculating the second virial coefficient[93]. One begins by imagining that two interacting particles are placed in a spherical container centered about their common center of mass. Assume that the appropriate boundary condition is for the wavefunction of relative motion to vanish at the container walls. In the asymptotic region, the radial wavefunction is of the form

$$\Psi \propto \frac{\sin [qr/\hbar - \eta \ln (2qr/\hbar) - \ell\pi/2 + \delta_\ell(q)]}{qr} Y_{\lambda\mu}. \quad (5.14)$$

The boundary condition therefore requires

$$qR/\hbar - \eta \ln(2qR/\hbar) - \ell\pi/2 + \delta_\ell(q) = m\pi, \quad (5.15)$$

where $\eta = Z_1 Z_2 e^2 / \hbar v$ is the Coulomb parameter. Separating the phase shift into Coulomb σ_ℓ and strong interaction δ'_ℓ components, the density of states is

$$\begin{aligned} \frac{dn}{dq} &= (2\ell + 1) \frac{dm}{dq} \\ &= \frac{1}{\pi} \sum (2\ell + 1) \left\{ \frac{R}{\hbar} + \frac{d}{dq} [\eta \ln(2qR/\hbar) + \sigma_\ell(q)] \right\} + \frac{1}{\pi} \sum (2\ell + 1) \left\{ \frac{d\delta'_\ell}{dq} \right\} \end{aligned} \quad (5.16)$$

In Eq. 5.16, the first term represents the density of states for the pure Coulomb problem and the second term is the density of states due to the strong interaction. Since the first term is difficult and unwieldy to use, one can use the semiclassical expression in Eq. 5.13 or some similar shape for the Coulomb density of states. We will use the second term for the strong interaction effects. Taking the spin of the particles and resonances into account, the two particle phase space of relative motion becomes

$$\begin{aligned} \frac{dn_{12}}{d^3 \vec{q}} &= \frac{(2S_1 + 1)(2S_2 + 1)V_f}{h^3} \frac{V_f}{V} \int_V d^3 \vec{r} \sqrt{1 - \frac{2\mu Z_1 Z_2 e^2}{rq^2}} \\ &\quad + \frac{1}{4\pi^2 q^2} \sum_{J,\ell} (2\ell + 1) \frac{d\delta'_{J\ell}}{dq}, \end{aligned} \quad (5.17)$$

where V_f and V are the free (unoccupied) and total (including occupied) volumes of the system, respectively. Given this relationship, the correlation function as a function of relative momentum becomes

$$\begin{aligned} 1 + R(q) &= 1 + R_{Coul}(q) + R_{nuc}(q) \\ &= \frac{1}{V} \int_V d^3 \vec{r} \sqrt{1 - \frac{2\mu Z_1 Z_2 e^2}{rq^2}} \end{aligned} \quad (5.18)$$

$$+ \frac{h^3}{4\pi^2 q^2 V_f \cdot (2S_1 + 1)(2S_2 + 1)} \sum_{J,\ell} (2\ell + 1) \frac{d\delta'_{J\ell}}{dq},$$

and as a function of relative energy E_{rel} becomes

$$\begin{aligned} 1 + R(E_{rel}) &= 1 + R_{Coul}(E_{rel}) + R_{nuc}(E_{rel}) \\ &= \frac{1}{V} \int_V d^3r \sqrt{1 - \frac{Z_1 Z_2 e^2}{r E_{rel}}} \\ &\quad + \frac{h^3}{4\pi^2 V_f \cdot (2S_1 + 1)(2S_2 + 1) \mu \sqrt{2\mu E_{rel}}} \sum_{J,\ell} (2\ell + 1) \frac{d\delta'_{J\ell}}{dE_{rel}}. \end{aligned} \quad (5.19)$$

It is useful to reflect on how the equilibrium correlation function both resembles and differs from the correlation functions calculated via the Koonin-Pratt equation. While the general case of a finite emission time lies outside the equilibrium correlation formalism, there is a close connection in the limit of instantaneous emission between equilibrium and Koonin-Pratt predictions for the second term in Eq. 5.18, stemming from the influence of strong interactions. This term in the equilibrium correlation picture represents static modifications in the phase space distributions due to resonances and other strong interaction effects. In this respect, the resonances can be regarded as "pre-existing". On the other hand, the correlations within the Koonin-Pratt formalism have been examined in the "prompt" or instantaneous emission limit for a source that is much larger than intrinsic "size" of the resonance itself by Boal et al., and can be expressed by [94, 95]

$$R_{nuc}(q) = S(0) \cdot \frac{h^3}{4\pi^2 q^2 \cdot (2S_1 + 1)(2S_2 + 1)} \sum_{J,\ell} (2\ell + 1) \frac{d\delta'_{J\ell}}{dq}, \quad (5.20)$$

for the strong interaction correlation function. If the source is taken to be uniformly spherical, the $S(0) = 1/V_f$, and the equilibrium and Koonin-Pratt formalisms yield identical expressions. Thus, the assumption of instantaneous emission implies that the resonance structures predicted by the Koonin-Pratt formalism are those of unstable particles that are "pre-existing" at breakup.

Unlike the general situation for correlation functions calculated within the Koonin-Pratt formalism (see section 5.2), the width of the resonance structure within this large source approximation is given by the line shape of the resonance state. The source size information is therefore only contained in the magnitude of the correlation structure through its dependence on $S(0) = 1/V_f$. For states that are much narrower than the intrinsic resolution of the detection apparatus, such as the case for the 2.186 MeV resonance in the d- α correlation, this does not lead to a significant loss of information. Comparisons between analyses performed in equilibrium and Koonin-Pratt limits by Jennings et al. indicate that the correlation function predictions for the magnitude of this resonance peak by both approaches are about the same for gaussian sources with typical source radii [95].

5.5 Interpretations of Correlation Functions Using the Equilibrium Correlation Approximation

To extend correlation function analyses to heavier particles that are more identified with multifragmentation and the liquid-gas phase transition, we can at the present time only apply the equilibrium correlation approximation. As mentioned in the previous section, this approximation is equivalent in many respects to the Koonin-Pratt formalism. However, it does limit one to examine only the magnitude of the two particle correlation function peaks and there remains a sensitivity to the secondary decay corrections that cannot be determined from the technique itself, unlike the case for the imaging procedure. This sensitivity means that one must employ statistical models to estimate the secondary decay and make the necessary corrections as discussed below.

We begin our discussion of equilibrium correlation functions by returning to the d- α correlation function, as shown again in figure 5.15 as a function of relative energy.

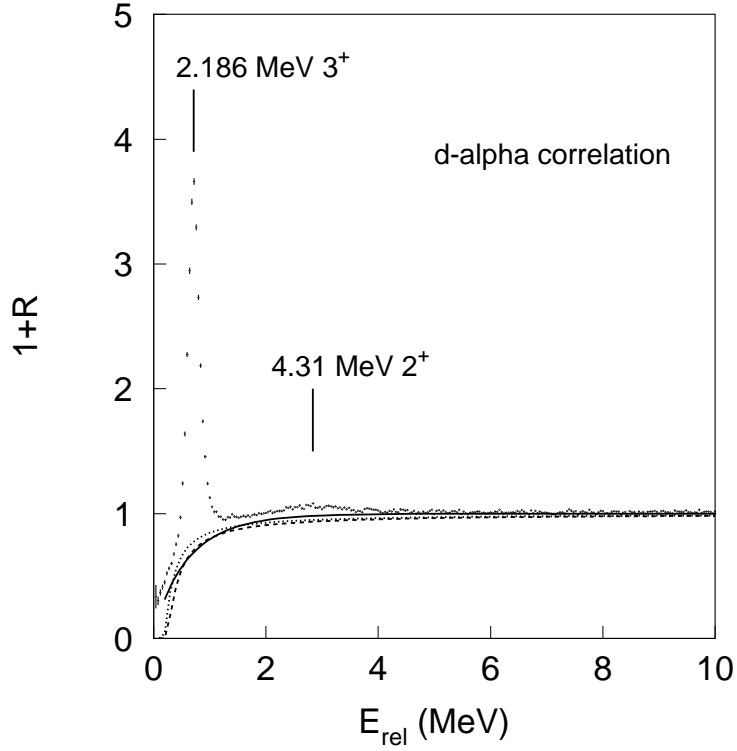


Figure 5.15: The experimental d- α correlation function is shown. The smooth solid line is the empirical background used for the analysis. The dashed and dotted lines are the Coulomb correlation calculated from Eq. 5.21 for sharp sphere radii of $R=12.4$ and 15.6 fm, respectively.

Here one can see clearly the peaks from the resonance states of ${}^6\text{Li}$: the 3^+ state at 2.186 MeV and the 2^+ state at 4.31 MeV. Also shown by the dashed and dotted lines in the figure are Coulomb correlation functions calculated for a spherical volume of radius R as follows,

$$\begin{aligned}
 1 + R_{Coul}(E_{rel}) &= \frac{1}{V} \int_V d^3r \sqrt{1 - \frac{Z_1 Z_2 e^2}{r E_{rel}}} & (5.21) \\
 &= \left[1 - \frac{r_{\min}}{R}\right]^{1/2} \cdot \left[1 - \frac{1}{4} \frac{r_{\min}}{R} - \frac{3}{8} \left(\frac{r_{\min}}{R}\right)^2\right]
 \end{aligned}$$

$$-\frac{3}{8} \left(\frac{r_{\min}}{R} \right)^3 \ln \left[\sqrt{\frac{R}{r_{\min}}} + \sqrt{\frac{R}{r_{\min}} - 1} \right].$$

where $r_{\min} = Z_1 Z_2 e^2 / E_{rel}$ and we have used the spherical source radii of $R_1=8.77$ and 11.05 fm (corresponding approximately to the two-particle source radii of $R = \sqrt{2}R_1=12.4$ and 15.6 fm) consistent with breakup at densities of $1/6\rho_0$ and $1/3\rho_0$, respectively, if half of the 260 nucleon source can be "seen" by the correlation due to collective effects (see sect. 5.3).

While the general trend of the predicted Coulomb correlation functions are similar to that (solid line) experimentally observed, the calculated correlation functions underpredict the measured one at very low relative energies and there are some differences in the overall shape. The extra measured yield in the data at very low relative energies may reflect long lived secondary decays that are not modelled by the equilibrium Coulomb correlation function. Other differences, however, may reflect the fact that the long ranged behavior of the Coulomb interaction makes it difficult to distinguish two body from multi-body Coulomb effects. For example, a third fragment in between the two measured fragments would repel them in opposite directions, widening the correlation function minimum. Thus we have decided not to insist upon fitting the measured correlation function with Eq. 5.21, but simply fit an empirical background function (solid line) to the data, instead.

We therefore extract information about the source volume by considering what is required to fit the resonance peaks with the nuclear correlation function in Eq. 5.19. This fit, however, requires the application of the empirical correction for collective motion described in Section 5.3. When this correction is applied and the derivative of the nuclear phase shift is given in a Breit-Wigner form [96]

$$\frac{d\delta'_{J\ell}}{dq} \approx \frac{\Gamma_i/2}{(E_{rel} - E_i^*)^2 + \Gamma_i^2/4} (B.R.), \quad (5.22)$$

the nuclear correlation function in Eq. 5.19 becomes,

$$\begin{aligned}
R_{nuc}(E_{rel}) &= \frac{1}{(2S_1 + 1)(2S_2 + 1)} \frac{h^3}{4\pi V_f \mu \sqrt{2\mu E_{rel}}} e^{-E_{rel}/T_{eff}} \\
&\times \frac{1}{\pi} \sum_i (2J_i + 1) \frac{\Gamma_i/2}{(E_{rel} - E_i^*)^2 + \Gamma_i^2/4} (B.R.)
\end{aligned} \tag{5.23}$$

For resonance states, the population will not be affected by collective motion and if equilibrium is achieved, it should populate according to the breakup thermal temperature $T_{thermal}$. If there is no collective motion, the relative energy spectrum for the mixed event background in the denominator of correlation function will also be described by the same temperature $T_{thermal}$. On the other hand, due to collective motion of the hot source, the relative energy of the two particles in the event-mixing case tends to be higher because the particles originate from different places with different collective velocities and because the reaction plane may also be different from one event to another. Therefore, the effective temperature of the two particles from different events is characterized by a much higher value T_{coll} . This results in an extra factor in the resonance correlation R_{nuc} where

$$\frac{1}{T_{eff}} = \frac{1}{T_{thermal}} - \frac{1}{T_{coll}}. \tag{5.24}$$

We find that d- α correlations are well described by assuming, $T_{eff} = 7$ MeV (see sect. 5.3), which could arise if the breakup temperature $T_{thermal} = 4$ MeV and collective "temperature" is $T_{coll} = 9.3$ MeV. Such values are typical of the temperatures observed for isotopic and excited state temperatures ($T_{thermal} = 4$ MeV) and for the slopes of energy spectra ($T_{coll} = 9.3$ MeV) [30, 97]. If one is interested mainly in resonance states near the threshold, i.e., $E_{rel} \leq 2$ MeV, then the uncertainty of the correlation R_{nuc} caused by the uncertainty of T_{eff} (i.e., varying between 5-10 MeV) is less than 10%.

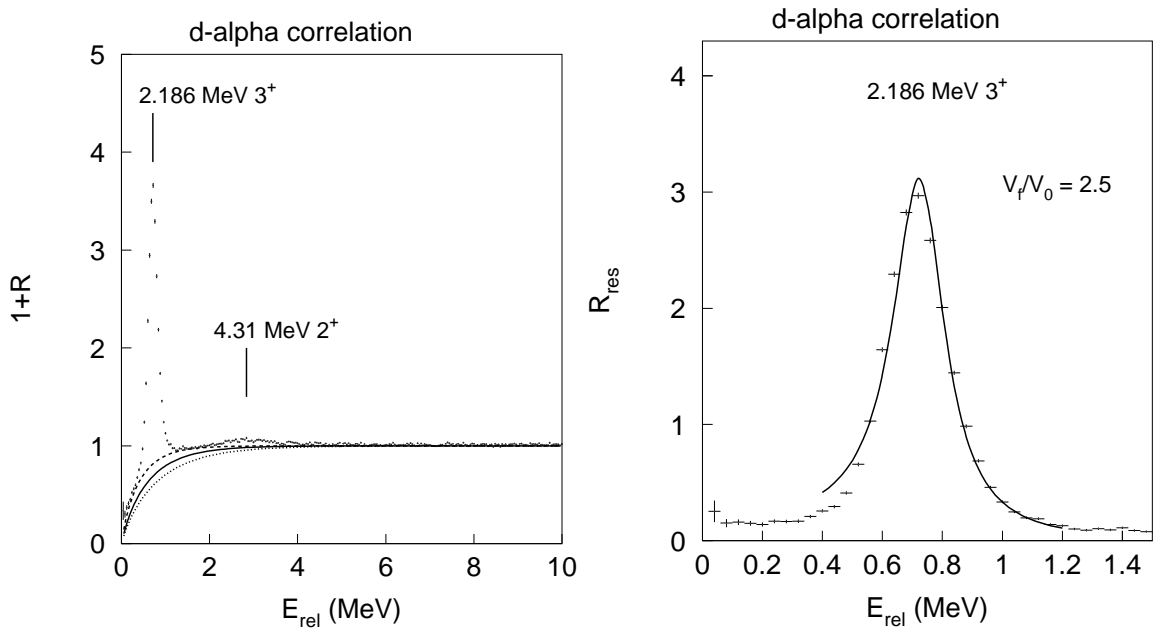


Figure 5.16: The left panel shows the experimental d- α correlation function. The solid, dashed and dotted lines are the different backgrounds used for the estimation of uncertainty. The right panel exhibits the fit of the first resonance peak after subtracting the background (solid line in the left panel).

Another uncertainty factor is the Coulomb correlation shape. We have used particle-correlations in other channels that display fewer resonances to assess the shape of the Coulomb correlation for interesting cases. For example, the p-d, and t-t correlations have no resonances. Either may be used to estimate the background of the p-t correlation. When we pay concentration on strong peaks, we also significantly reduce the sensitivity to the Coulomb correlation uncertainties. Nevertheless, this remains a significant potential source of uncertainty, which we must assess by considering other shapes for the Coulomb correlation.

In the left panel of Figure 5.16 for the d- α correlation, we show three different backgrounds (solid, dashed, dotted lines) that we have considered in order to assess the uncertainty in the peak. In the right panel, we show the nuclear correlation of the first excited state of ${}^6\text{Li}$ after subtracting the background correlation denoted by the solid line in the left panel. The remaining correlation function can be di-

	J^π	E^* (MeV)	$\Gamma_{\text{c.m.}}$ (MeV)	Channel	B.R. (%)
${}^6\text{Li}$	3^+	2.186	0.024	d- α	100
	2^+	4.31	1.7	d- α	97
${}^7\text{Li}$	$7/2^-$	4.63	0.093	t- α	100
	$5/2^-$	6.68	0.88	t- α	100
	$5/2^-$	7.46	0.089	t- α	18
	$7/2^-$	9.67	0.4	t- α	40(fit)
	$3/2^-$	9.85	1.2	t- α	40(fit)
${}^7\text{Be}$	$7/2^-$	4.57	0.175	${}^3\text{He}$ - α	100
	$5/2^-$	6.73	1.2	${}^3\text{He}$ - α	100
${}^8\text{Be}$	0^+	g.s.	6.8eV	α - α	100
	2^+	3.04	1.5	α - α	100

Table 5.3: Relevant spectroscopic information of ${}^6\text{Li}$, ${}^7\text{Li}$, ${}^7\text{Be}$ and ${}^8\text{Be}$ which is adopted from ref. [98] is listed for the correlation functions discussed in this section.

rectly compared to the nuclear correlation $R_{nuc}(E_{rel})$. We have done so by fitting this spectrum with Eq. 5.23 and using the known structural information, given in Table 5.3. Applying Eq. 5.23 without any further considerations, we have only one parameter, the free volume V_f , that can be varied to reproduce the correlation function. We find that the correlation is well described with free volume of the breakup $V_f/V_0 = 2.50 \pm 0.27$, where V_0 is the volume of the total system (326 nucleons) at nuclear saturation density. Uncertainties in the background constitute the main uncertainty in the extracted volume. Before discussing the constraints in density that this places on the breakup, we examine other correlations between fragments with $Z < 3$ to see whether any consistent trends emerge.

The triton-alpha correlation function is shown in Figure 5.17 with the resonance states of ${}^7\text{Li}$ (see Table 5.3): $7/2^-$ at 4.63 MeV, $5/2^-$ at 6.68 MeV, $5/2^-$ at 7.46 MeV, $7/2^-$ at 9.67 MeV and $3/2^-$ at 9.85 MeV. In the left panel, different backgrounds (solid, dashed and dotted lines) are plotted for estimating the uncertainties. As shown in the right panel, the very pronounced first resonance above the threshold is used to extract the breakup volume and this gives a value $V_f/V_0 = 2.55 \pm 0.28$ that is very

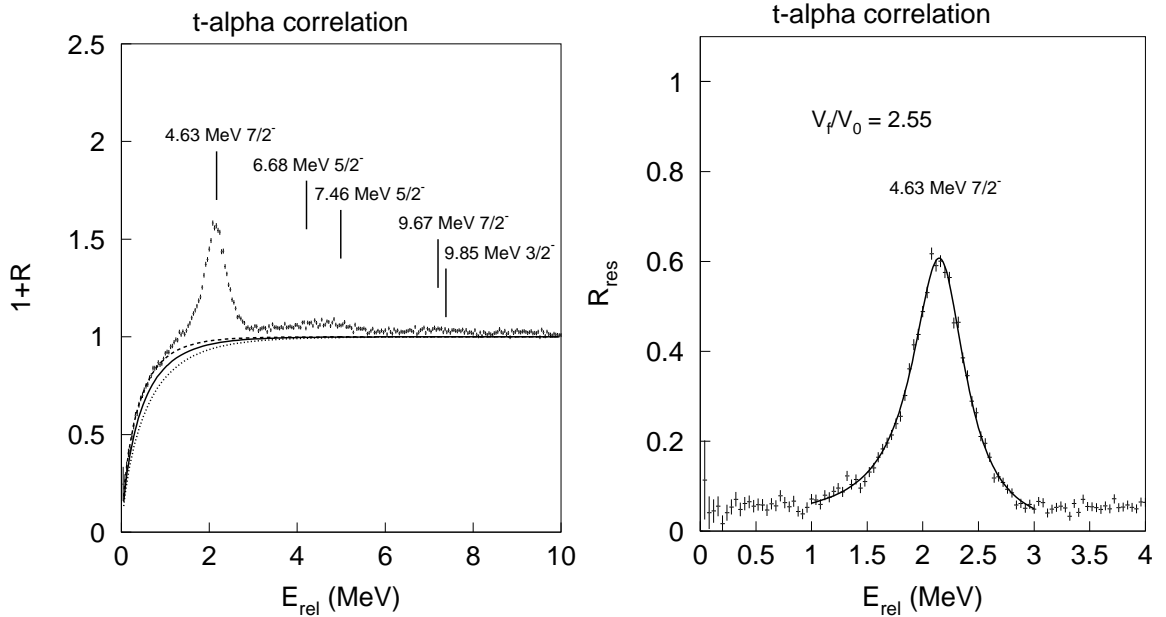


Figure 5.17: The experimental t - α correlation function is shown in the left panel. The solid, dashed and dotted lines are the different backgrounds used for the estimation of uncertainty. The right panel exhibits the fit of the first resonance peak after subtracting the background (solid line in the left panel).

similar to the one obtained from the d - α correlation function.

Similarly the resonance states of 4.57 MeV $7/2^-$ and 6.73 MeV $5/2^-$ (see Table 5.3) of the mirror nucleus ${}^7\text{Be}$ are depicted in the ${}^3\text{He}$ - α correlation in Figure 5.18. The $5/2^-$ state at 7.21 MeV is not shown due to a large decay branching ratio of about 97% through the p - ${}^6\text{Li}$ channel. The rise close to the threshold most likely comes from the contaminant in the ${}^3\text{He}$ PID from alpha particles and what one sees is the ground state of ${}^8\text{Be}$ from the alpha-alpha correlation (see below). Nevertheless, it does not detract from our efforts to extract the free volume, which yielded $V_f/V_0 = 2.22 \pm 0.36$ from the fit to the resonant state at 4.57 MeV.

In the case of the alpha-alpha correlation as shown in Figure 5.19, the ground state 0^+ of ${}^8\text{Be}$ and its first excited state 2^+ at 3.04 MeV are illustrated (see Table 5.3). In addition, the peak at about $E_{rel} = 0.6$ MeV is mainly from the decay of the 2.43 MeV state of ${}^9\text{Be}$ [81]. In this example the identical particle effect is observed.

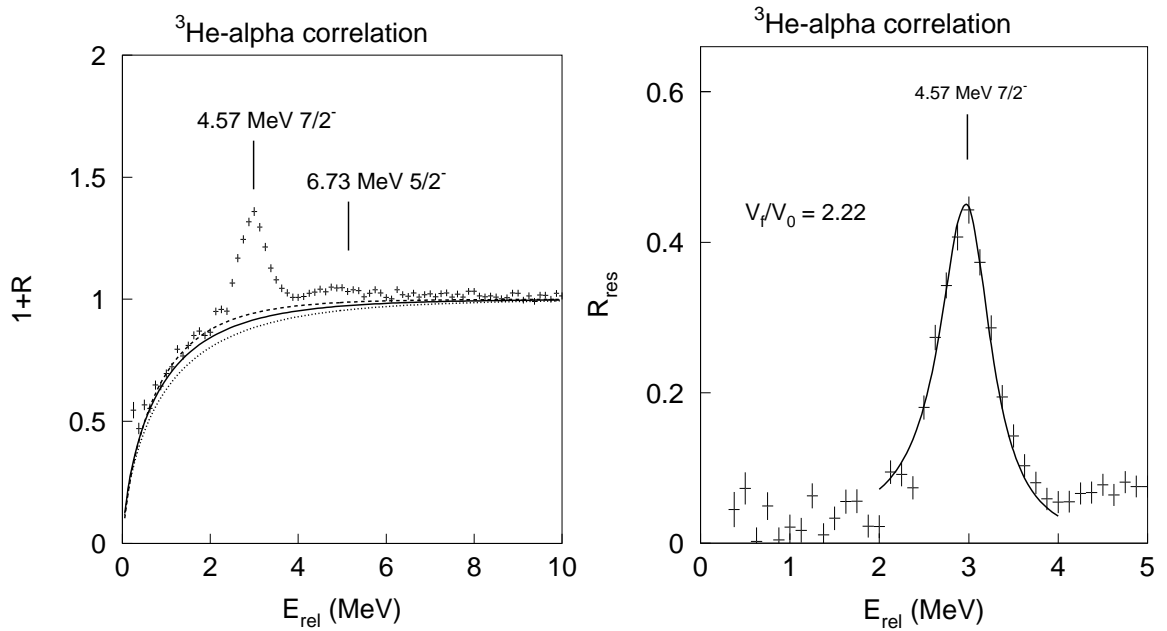


Figure 5.18: The left panel shows the experimental ${}^3\text{He}-\alpha$ correlation function. The solid, dashed and dotted lines are the different backgrounds used for the estimation of uncertainty. The right panel exhibits the fit of the first resonance peak after subtracting the background (solid line in the left panel)

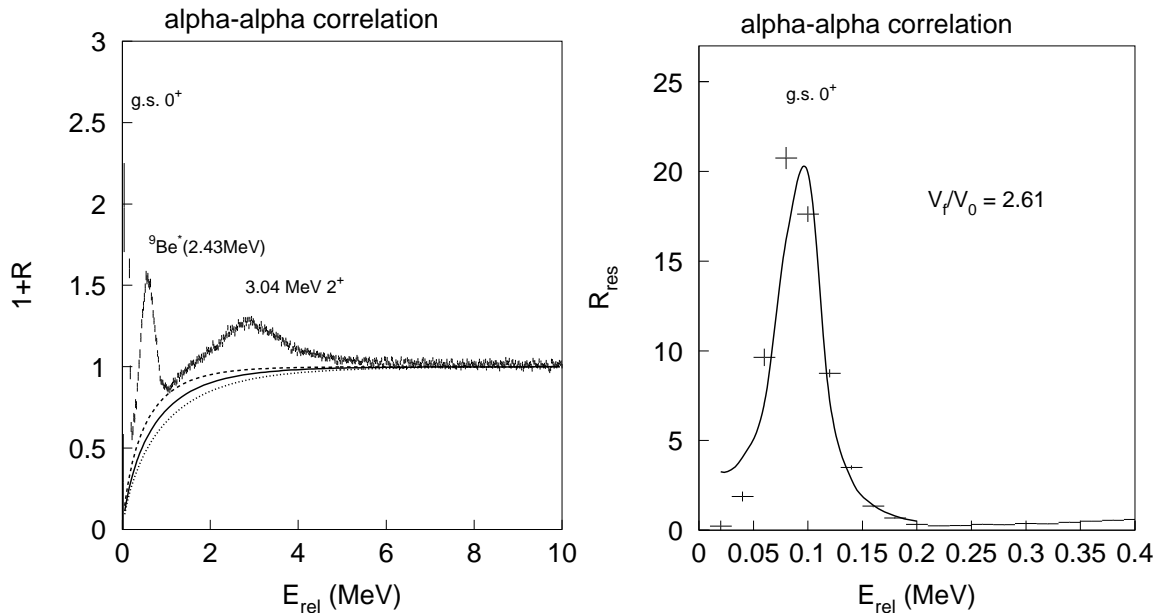


Figure 5.19: The experimental $\alpha-\alpha$ correlation function is shown in the left panel. The solid, dashed and dotted lines are the different backgrounds used for the estimation of uncertainty. The right panel exhibits the fit of the first resonance peak after subtracting the background (solid line in the left panel).

That is, the phase space of the two identical particles is reduced by a factor of 2 and consequently the resonance correlation R_{nuc} becomes twice as large as in Eq. 5.23. By taking into account this effect, one obtains a free volume of $V_f/V_0 = 2.61 \pm 0.03$ from the ground state of unstable ${}^8\text{Be}$ as shown in the right panel of Figure 5.19.

In all the above correlations, only the first most pronounced peak is fitted for this study, which is sensible in reducing the sensitivity to the uncertainty of the temperature factor and the background. Nevertheless, it is an interesting consistency test to see if we can fit all the peaks we observed. In figure 5.20, we explore this issue. To make these higher peaks more visible, we divide the nuclear correlation function by the prefactors in Eq. 5.23. This leaves only the free volume and the density of resonance states coming from the derivative of the strong interaction phase shifts given below

$$\begin{aligned}
& R_{nuc}(E_{rel}) \cdot \left[\frac{1}{(2J_1 + 1)(2J_2 + 1)} \cdot \frac{h^3}{4\pi V_0 \mu \sqrt{2\mu E_{rel}}} e^{-E_{rel}/T_{eff}} \right]^{-1} \quad (5.25) \\
& = \frac{1}{V_f/V_0} \frac{1}{\pi} \sum_i (2J_i + 1) \frac{\Gamma_i/2}{(E_{rel} - E_i^*)^2 + \Gamma_i^2/4} (B.R.) \equiv V_0/V_f \rho_{res}(E_{rel}).
\end{aligned}$$

Performing this operation on the correlation function data provides those data points in Fig. 5.20. The solid lines are the sum of the resonance line shapes calculated using the parameters in Table 5.3. To make a good representation of these peaks at higher excitation energies, a careful normalization of the Coulomb correlation background is essential as is the correction due to collective motion corresponding to the exponential with $T_{eff} = 7$ MeV. In other words, fitting over the domain of these higher resonance states is useful to constrain the background and the parameter T_{eff} . After fitting over this extended excitation energy range, the numbers obtained for free volume of the breakup are changed very slightly: $V_f/V_0 = 2.63$ for the d-alpha correlation; $V_f/V_0 = 2.79$ for the t-alpha correlation; $V_f/V_0 = 2.44$ for the ${}^3\text{He}$ -alpha correlation;

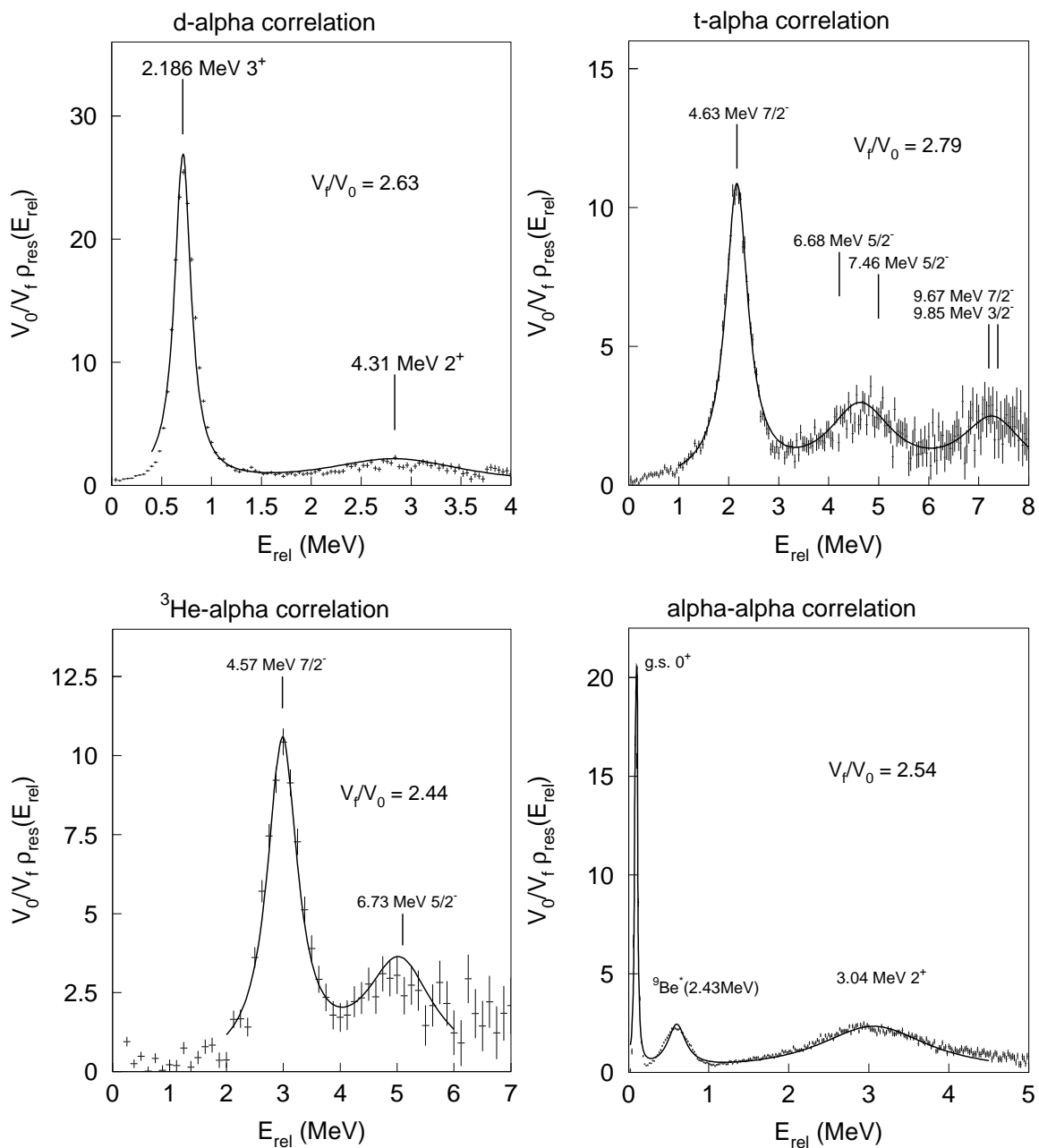


Figure 5.20: The densities of the resonance states from d- α , t- α , ^3He - α and α - α correlations are fitted after subtracting the backgrounds carefully selected by the solid lines in Figures 5.16-5.19.

$V_f/V_0 = 2.54$ for the alpha-alpha correlation. The free volume measurements are given in Table 5.4.

The consistency between the preliminary numbers given for the free volume in the " V_f/V_0 " column in Table 5.4 is surprising. However, further estimates on the breakup density need the consideration of corrections from collective motion and from the secondary decay of heavier particle unstable isotopes that can produce the particles in the correlation as well as nuclei in the resonance states we observe. Here we attempt a correction for such effects. To consider the effects of collective motion, we need to revisit the discussion in Section 5.3 on collective motion where the reduction of the source size due to the interplay of collective and thermal motion is discussed. The problem we need to solve is more complex than the problem we needed to solve in order to determine the density from the p-p correlation function and from the second peak in the d- α correlation function. In those latter cases, the shape of the resonance was sufficient to determine the volume of the source while one needed the simulation to determine the mass in the source. Here we need to consider how the collective motion influences the magnitudes of both the resonant, non-resonant and mixed event yields. (The previous analysis showed that the latter two are influenced similarly.)

Generally speaking, rearranging Eq. (5.2) yields the correlation function $1 + R(q)$ expressed as a ratio of 5 dimensional integral over the coincidence yield divided by a corresponding 5 dimensional integral over the mixed event yield product. If we try a Monte Carlo simulation as in Section 5.3 of these yields, we break down the spatial origins of the contributions to the momentum distributions. This means that starting from these phase space distributions at breakup, we need to do an 11 dimension integral: 3 spatial and 3 momentum integrations for each particle minus one integration corresponding to the non-integrated dependence on E_{rel} . Collective motion builds

correlations between the emission points and momenta of the emitted particles that effectively reduce the fraction of the source contributing to the correlation function. This reduction factor, however, is dependent on E_{rel} as the exponential dependence in Fig. 5.11 demonstrates.

Fig. 5.11, however, suggest a simple way to deal with collective motion. Let us assume that the data are consistent with $T_{eff} = 7$ MeV. Thus, for the source volume of this simulation and this specific collective velocity field, the resonant correlation function should be proportional to the middle panel. Without collective motion, the same source volume leads to the lower panel. The ratio of the middle panel divided by the lower panel is what one would expect for the ratio of correlation function from a source of the same dimension with collective motion divided by the correlation function without it. This ratio is independent of the actual volume of the source. Like the volume reduction factors in Fig. 5.9, it depends on $v_{r,max}$, $v_{t,max}$, and the random velocity $v_{th} = \sqrt{3T/m}$, but not on the source radius R . Thus the inverse of this ratio f_{ratio} provides a way to correct for the collective motion effects and obtains what the correlation function should be without collective motion. Fig. 5.11 shows what the correction factor f_{ratio} should be for the d- α correlation function in figure 5.15.

In applying this correction factor, we simply need to extract the value for the correction factor $f_{ratio}(E_{rel})$ at the energy of the resonance in question. This dictates the factor by which the correlation functions would have been smaller without collective motion. This smaller correlation function would have resulted in the extraction of a new free volume that would be larger by a factor of $f_{ratio}(E_{rel})^{-1}$. The production of heavier particle unstable nuclei and their decay into the particles included in the correlation function or into the observed resonance peak also alter the correlation function by increasing the yields of the involved nuclei. It is the correlation function

of primary fragments before decay which has the simple dependence on the emission volume predicted by Eq. 5.19. Preliminary calculations of secondary decay suggest that the shape of the spectrum after decay is not very different from the shape before decay. Under this assumption, the primary correlation functions before decay differ from the corresponding ones after decay by a multiplicative factor F_{dec} , where in the case of the d- α correlation

$$F_{dec} = \frac{DR_d \cdot DR_\alpha}{DR_{6Li^*}}, \quad (5.26)$$

where the factor DR_d reflects the multiplicative factor by which the yield for deuterons is enhanced by secondary decay, and the other factors in F_{dec} reflect the application of the same considerations to the yields of α 's and to the resonance in 6Li as well. Secondary decay correction factors were obtained by calculating the equilibrated multifragment decay of a system consisting of 260 nucleons and 106 protons at an excitation energy of $E^*/A = 4$ MeV using the SMM model described in the next chapter of this dissertation. The secondary decay factors for the correlation functions shown in Figs. 5.16-5.19 are given in the third column of Table 5.4.

We note that these secondary decay corrections are rather large. In particular, a value for F_{dec} of 6.09 is obtained for the d- α correlation, which should be compared to the reciprocal of the value for $\lambda = 0.11$ that was obtained by fitting the shape for the second peak of the inclusive d- α correlation in Section 5.3. This suggests that the SMM predicts about the same (differ by 49%) secondary decay contributions as the Koonin-Pratt approach. To get a feeling for what a 49% correction implies, we increase all the F_{dec} factors in the third column of Table 5.4 by 49%. These modified values of $F_{dec}(KP)$ are also shown in Table 5.4. These modified values should be viewed with caution beyond some indication of how sensitive the densities are to the secondary decay corrections.

Based on the above discussions, a correlation function $R_{nuc,pri}$ without collective motion before secondary decay can be obtained by $R_{nuc,pri} \sim R_{nuc} \cdot F_{dec} \cdot f_{ratio}(E_{rel})$. Since the factor $\exp(-E_{rel}/T_{eff})$ consistent with Fig. 5.11 has already been taken into account in Eq. 5.23 in extracting the free volumes for the correlation functions shown in Figs 5.16-5.19, the normalization of the exponential factor $f_{ratio,0} \equiv f_{ratio}(E_{rel} = 0)$ should be directed out to correct the free volumes for the remaining effects of collective motion. Therefore an estimate of the expanded free volume after corrections for secondary decay and collective motion might be given by

$$V_{f,source} = \frac{V_f}{F_{dec} \cdot f_{ratio,0}}, \quad (5.27)$$

and the freezeout density ρ/ρ_0 by

$$\rho/\rho_0 = \frac{\rho_f}{\rho_f + \rho_0} \quad (5.28)$$

where

$$\rho_f/\rho_0 = \frac{A_{prefragment}}{V_{f,source}\rho_0} = \frac{0.8f_{ratio,0} \cdot F_{dec}}{V_f/V_0}. \quad (5.29)$$

where the correction factor $f_{ratio,0} = 0.15$ is obtained from Fig. 5.11 for the d- α correlation and for simplicity it is used for calculating the densities for the correlations shown in Figs. 5.16-5.19 assuming they all have the similar collective correction factors. We note that they all have similar effective temperature of $T_{eff} = 7$ MeV.

Values for the density, in units of saturation density ρ_0 are calculated from Eqs. 5.28-5.29 and given in Table 5.4, indicating that the freezeout density of the system is about $1/5$ - $1/3\rho_0$. For comparisons, the density values of $\rho/\rho_0(KP)$ are also shown by applying the source reduction factor $f_{coll}^3 = 0.2$ obtained for the Koonin-Pratt analyses instead of the factor $f_{ratio,0}$ discussed here, and using the modified secondary decay factor $F_{dec}(KP)$. If we omit the contributions of the excluded volume as in the case of

the Koonin-Pratt approach and apply the same secondary decay and collective motion corrections as the results from the Koonin-Pratt approach, the $\rho_f/\rho_0(KP)$ should be comparable to the density obtained from the Koonin-Pratt approach in Sect. 5.3. For the d- α correlation, indeed, the value of the density ($\rho_f/\rho_0(KP) = 0.57$ in Table 5.4) extracted in the equilibrium limit are similar to the value ($\rho/\rho_0 = 0.54$ in Table 5.2) extracted from the Koonin-Pratt analysis. Such a conclusion is in agreement with the work by Jennings et al. [95], which equate the thermal and Koonin-Pratt approaches for Gaussian sources under the assumptions of instantaneous emission and no corrections from secondary decay and excluded volume.

The density extracted from the equilibrium approach has similar large uncertainties as in the Koonin-Pratt analysis, which have been discussed in the end of Sect. 5.3. Especially the estimates of the correlation enhancement factor $f_{ratio}(E_{rel})$ due to collective motion are in need of better accuracy. On the other hand, the secondary decay process significantly modifies the extracted free volume in the opposite direction. The resulting correction factor F_{dec} also need to be studied more carefully by accurately checking the modelling of secondary decay by the statistical model.

Correlation	V_f/V_0	F_{dec}	$F_{dec}(KP)$	ρ_f/ρ_0	ρ/ρ_0	$\rho_f/\rho_0(KP)$	$\rho/\rho_0(KP)$
d- α	2.50 ± 0.27	6.09	9.09	0.29	0.23	0.57	0.37
t- α	2.55 ± 0.28	7.09	10.6	0.33	0.25	0.66	0.40
$^3\text{He}-\alpha$	2.22 ± 0.36	8.45	12.6	0.46	0.31	0.90	0.47
$\alpha-\alpha$	2.61 ± 0.03	4.76	7.11	0.22	0.18	0.43	0.30

Table 5.4: List of quantities are shown for the d- α , t- α , $^3\text{He}-\alpha$ and $\alpha-\alpha$ correlations (Figs. 5.16-5.19). The values of V_f/V_0 are obtained from the corresponding experimental correlation functions. F_{dec} is the correction factor in Eq. 5.26 calculated from secondary decay contributions in the SMM. The density ρ/ρ_0 is estimated in Eq. 5.28 using the secondary decay correction factor F_{dec} from the SMM while $\rho/\rho_0(KP)$ is obtained using $F_{dec}(KP)$ (see text). The corresponding ρ_f/ρ_0 and $\rho_f/\rho_0(KP)$ are calculated in Eq. 5.29 without considering excluded volumes.

Besides the density extraction, it is interesting to see via the above multi-peak

fittings that unknown spin of one resonance can possibly be obtained if the structural information is well known for the other states. In the following section we will discuss how to use this technique to determine spins of particle unstable nuclei.

5.6 Spin Determination of Particle Unstable States

One of the striking observations of this work is the degree to which the equilibrium assumption can describe the relative magnitudes of the various peaks in the correlation function. This is illustrated by the good agreement between the calculated and measured values of the nuclear correlation function in Fig. 5.20. Noting the dependence of the correlation function on the spin of the state (see Eq. 5.23), we now explore whether this can be used to determine the spin of a nuclear state, if that spin is unknown. By analyzing density spectra of resonance states like those shown in Fig. 5.20, we try to determine the unknown values of spins and even unveil new structures of nuclei.

To ensure the validity of applying this technique on studying the structures of unbound nuclei, one simple case is examined in the following. In Figure 5.21, the proton- ${}^7\text{Li}$ correlation function is shown with the resonance states of excited ${}^8\text{Be}$ that are close to the threshold: 17.64 MeV 1^+ , 18.15 MeV 1^+ , 18.91 MeV 2^- , 19.07 MeV 3^+ and 19.24 MeV 3^+ [98]. The branching ratios of these states through the proton decay channel are as follows [98], the 17.64 MeV state is 100%, the 18.15 MeV state is 100% where 96% goes to the ground state of ${}^7\text{Li}$ and 4% to the first $1/2^-$ excited state of ${}^7\text{Li}$ at 0.478 MeV, the 18.91 MeV state is 86%, the 19.07 MeV state is 100% and the 19.24 MeV state is 50%.

The reason why we choose the p- ${}^7\text{Li}$ correlation as an example is the structural information of ${}^8\text{Be}$ is quite complete and these pronounced resonance states are very

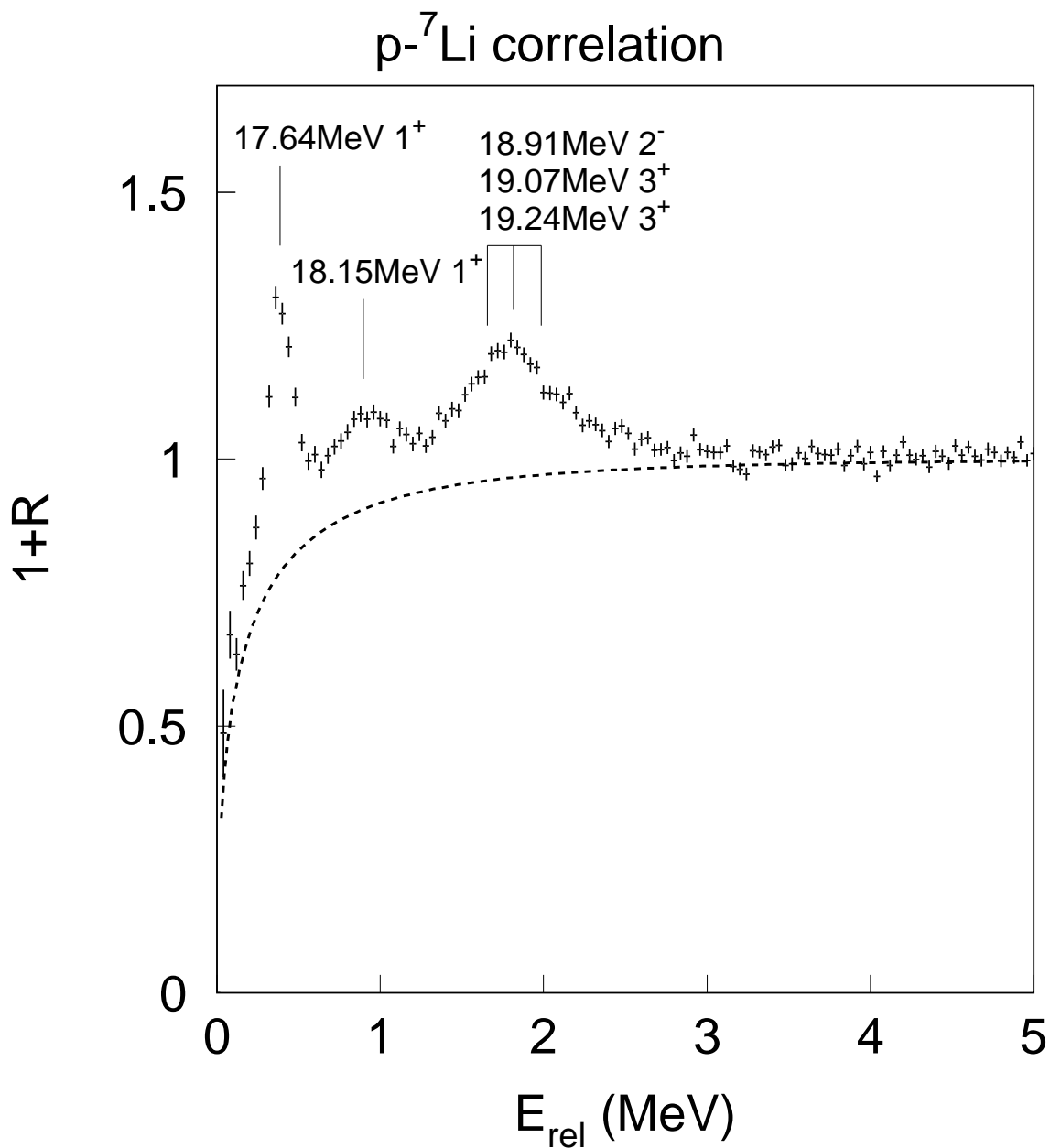


Figure 5.21: The proton-⁷Li correlation function is plotted. The dashed line is the selected background. See text for details.

close to the threshold, which can help reduce the sensitivity to the background selection. For simplicity, we will parameterize the background correlation function as follows,

$$1 + R_{bg} = 1 - \exp[-(E_{rel}/E_c)^\alpha] \quad (5.30)$$

which vanishes at zero relative energy and reaches unity at large relative energy. By comparing with the proton-⁶Li and proton-⁸Li correlations, the background of the proton-⁷Li correlation function (the solid line in Figure 5.21) is selected with parameters $E_c = 0.16$ MeV and $\alpha = 0.5$ since these correlations should have similar Coulomb interaction. After subtracting this background, the density of resonances is plotted in Figure 5.22. The dotted lines represent the individual resonance states and the solid line is the convoluted fit by applying the known structural information of these resonances. The fit is good everywhere except at the high energy end where the contributions from higher lying states are not included due to incomplete spectroscopic information.

To further test the reliability of the background selection and the sensitivity to the spin factor, a fit to the overall correlation function is carried out by varying the parameters in the background expression (Eq. 5.30) and the spin value of the 17.64 MeV state. In Figure 5.23, the best fit (solid line) yields a background shown as the dashed line with parameters of $E_c = 0.152$ MeV and $\alpha = 0.547$ which are very similar to what we have assumed above and a spin value of 1.06 ± 0.1 which is consistent with the experimental value. To illustrate the sensitivity of this technique to the spin determination, calculated correlations (dotted lines) are also shown in Figure 5.23 assuming that the spin of the 17.64 MeV state is 0 and 2, respectively and meanwhile keeping the other parameters the same. The significant separation of $J = 0, 2$ calculations from the $J = 1$ fit shows a good sensitivity to spin determination.

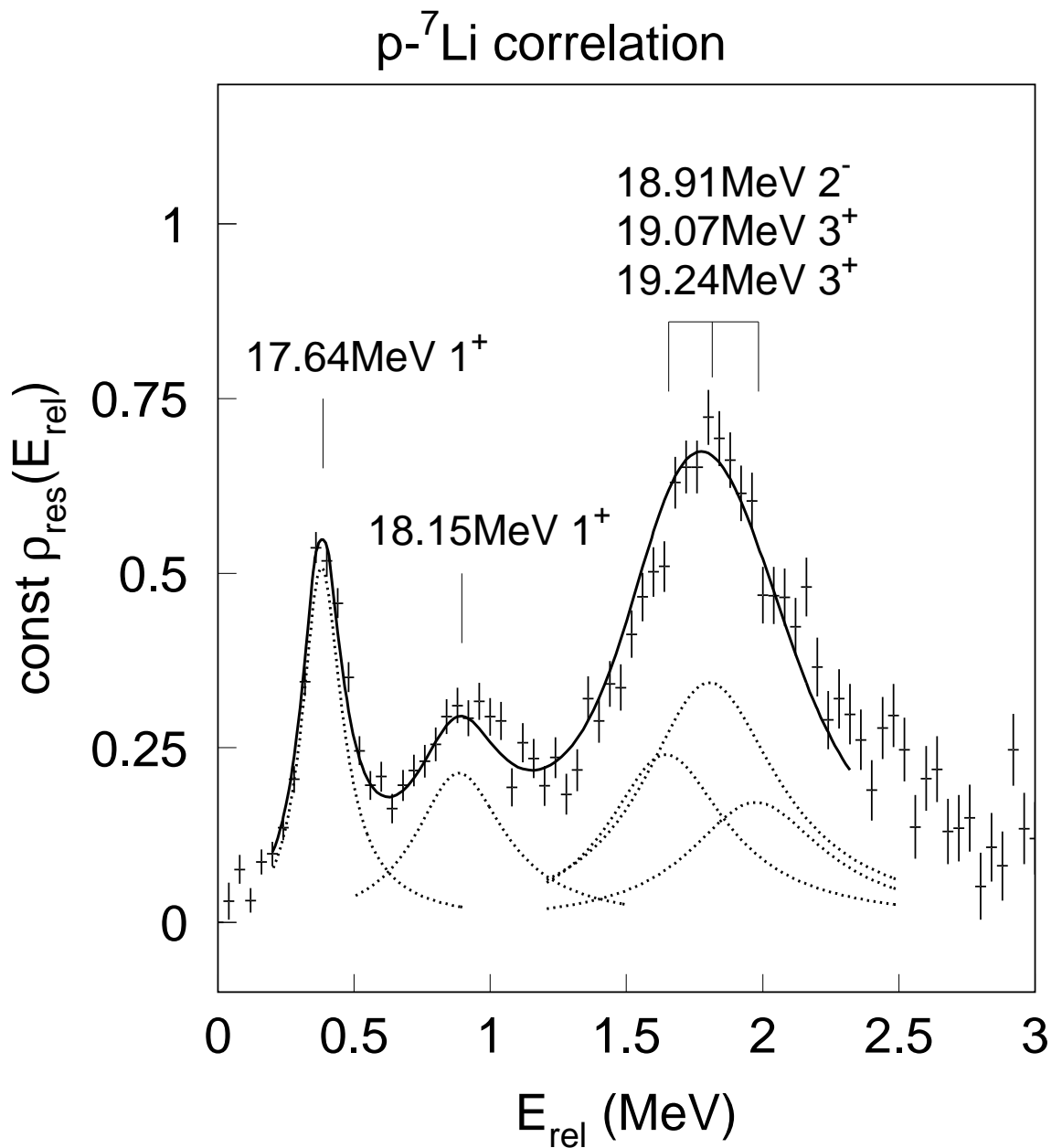


Figure 5.22: The density profile of the resonances of ${}^8\text{Be}$ is shown in the p - ${}^7\text{Li}$ correlation after subtracting the background selected in Figure 5.21.

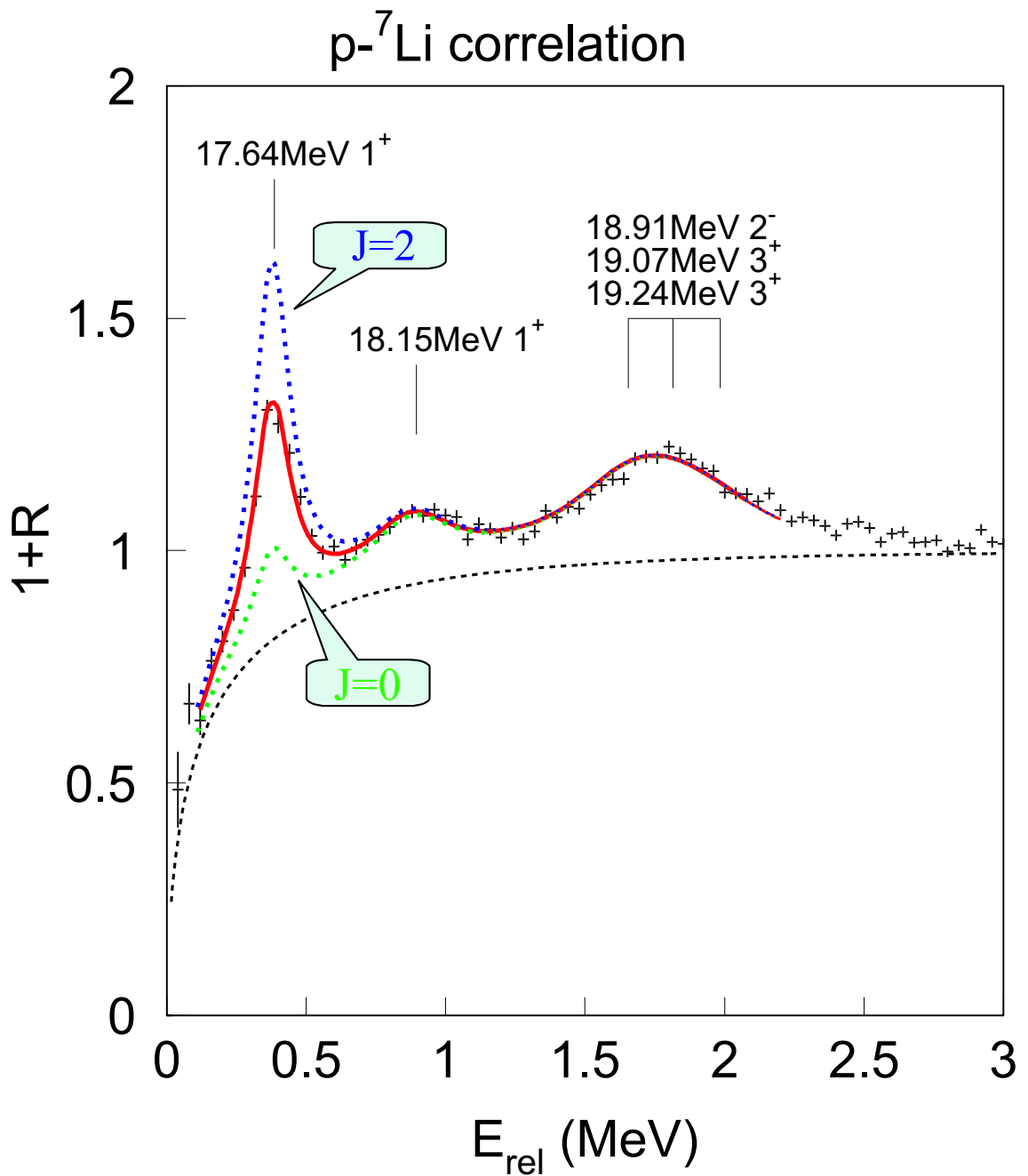


Figure 5.23: The best fit (solid line) is performed for the p-⁷Li correlation by varying the background and the spin value of the 17.64 MeV state. The dashed line is the fitted background. Two calculations are shown as the dotted lines assuming that the spin of the 17.64 MeV state is 0 and 2, respectively and keeping the other parameters the same.

As one can see from the above example, this technique can provide access to the spin information of resonances. In Figure 5.24, the proton- ${}^7\text{Be}$ correlation function is shown for an example with an unknown spin to be determined. In this case the two obvious peaks correspond to the first excited state of ${}^8\text{B}$ at 0.774 MeV and the 3^+ state at 2.32 MeV, respectively [98]. Interestingly the spin value for the 0.774 MeV state has not been measured although it is believed to be the 1^+ analog of the 17.64 MeV state in ${}^8\text{Be}$ [98, 99]. Also from the corresponding state in the mirror nucleus ${}^8\text{Li}$, a 1^+ assignment would be expected for this state. However, experimental efforts have yet to justify that statement. If we assume that only these two states exist in the interesting region, the solid line in Figure 5.24 is the best fit to the correlation function, which fits a background (dashed line) along with the resonances and yields a spin value of $J_1 = 0.98 \pm 0.29$. The result confirms the hint from the mirror nucleus.

However, the fit does not present all the features of the experimental correlation function. Especially a small bump at about 1.4 MeV seems to exist in between the two known states. The calculations in ref. [100] predict a 1^+ state of ${}^8\text{B}$ at 1.4 MeV. In Figure 5.25, the three resonances including the one at 1.4 MeV are fitted. A similar spin value $J_1 = 0.95 \pm 0.33$ of the first state is extracted. But the background (dashed line) is shallower than that of the previous fit to accommodate the additional 1.4 MeV resonance. If we can reduce the background by measuring a reaction with a small system or constrain more strongly the background contribution to the correlation function in some way and have better statistics and resolution in the correlation, we may determine further if there indeed is a state at 1.4 MeV. Nevertheless the spin of the first state at 0.774 MeV is confirmed to be one in either case. In both cases, the underestimated tail of the 2.32 MeV state seems to indicate the existence of other nearby states at slightly higher energy which have not been identified yet in experiments. However, we don't have the resolution to distinguish these states.

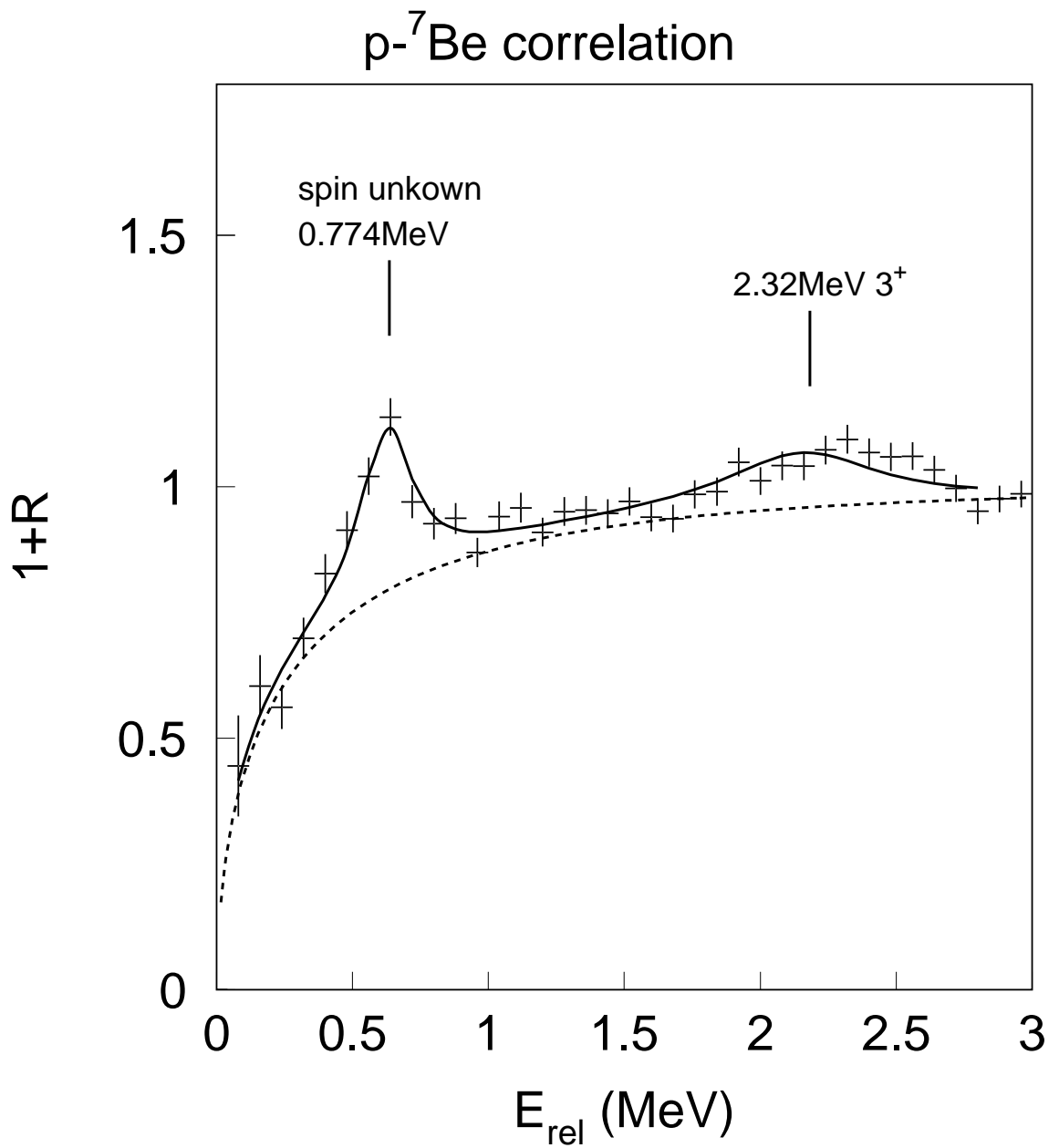


Figure 5.24: The p-⁷Be correlation function is fitted by the solid line assuming only two states at 0.774 MeV and 2.32 MeV. The dashed line is the fitted background.

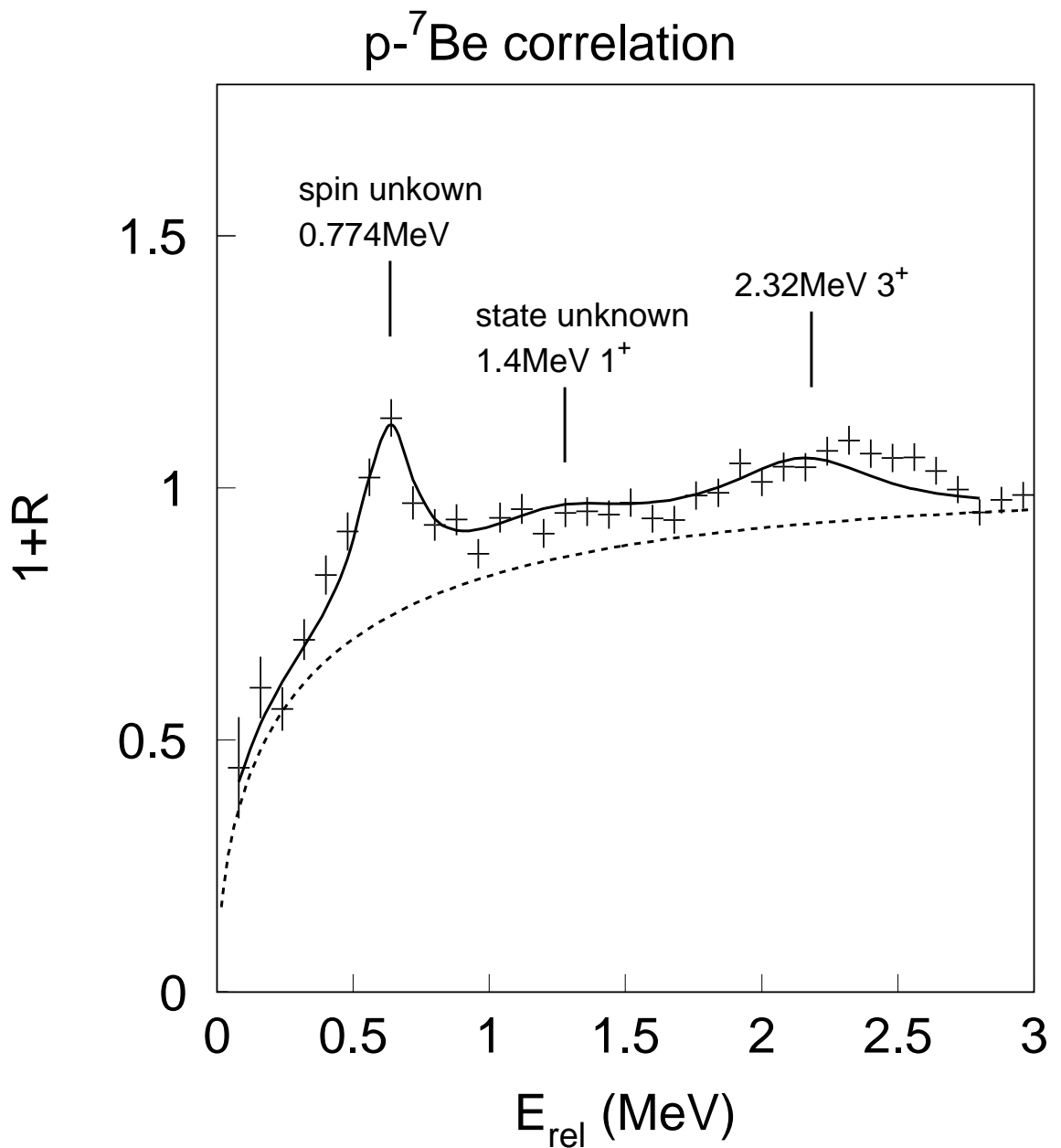


Figure 5.25: The p-⁷Be correlation function is fitted by the solid line assuming the existence of an additional state at 1.4 MeV. The dashed line is the fitted background.

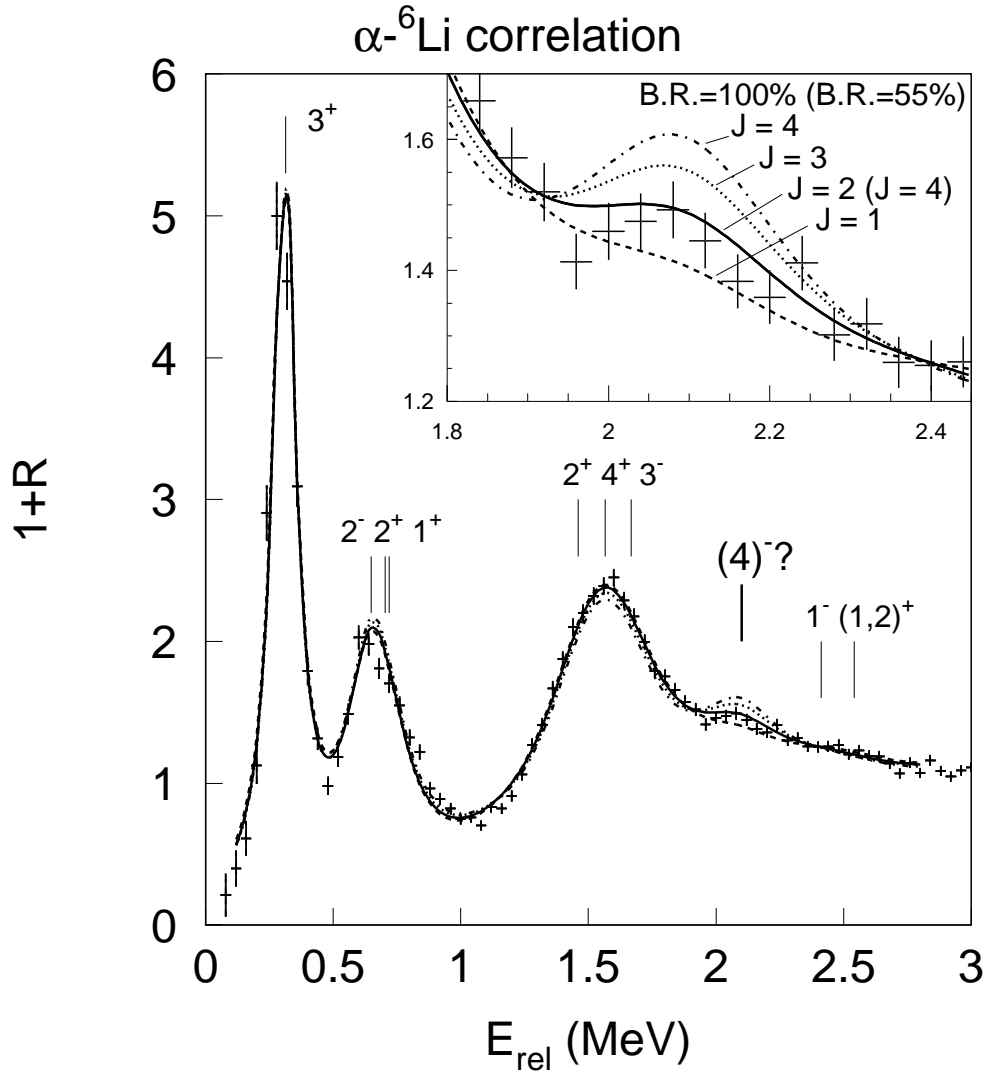


Figure 5.26: The α - ${}^6\text{Li}$ correlation function is fitted by taking into account all the spectroscopic information shown in Table 5.5 except for the 6.56 MeV state. By varying the spin of the 6.56 MeV state from 1 to 4 and assuming the decay branching ratio is 100%, one obtains the dashed, solid, dotted and dot-dashed fitting lines, respectively. If a branching ratio of 55% is assumed, the solid line represents a fit of $J=4$.

In the following case, the α - ${}^6\text{Li}$ correlation is shown with ample resonance states forming peaks near the decay threshold. The structural information of ${}^{10}\text{B}$ resonances is listed in Table 5.5 where we notice that the spin of 6.56 MeV state is not well measured ($J=4$ is tentatively suggested [98]). Figure 5.26 shows the fit with the known structural information except for the state at 6.56 MeV. The spin $J=1$ of the 7.002 MeV state and its B.R. of 30% (see the d - α - α correlation in sect. 5.7) are used in the fitting, which have little effects on determining the spin and B.R. of the 6.56 MeV state. In this fit we vary the spin value of this state from 1 up to 4 while assuming that 100% of this state decays to the ground state of ${}^6\text{Li}$. As we can see, it seems $J=2$ gives the best fit while the cases of $J=1,3$ are still possible due to poor resolution. On the other hand, if $J = 4$ is assumed for the 6.56 MeV state, then a branching ratio of this state decaying to α - ${}^6\text{Li}$ channel can be obtained as about 50%.

J^π	E^* (MeV)	$\Gamma_{\text{c.m.}}$ (keV)	B.R. (%)
3^+	4.774	8.4×10^{-3}	100
2^-	5.1103	0.98	100
2^+	5.1639	1.76×10^{-3}	13
1^+	5.180	110	100
2^+	5.9195	6	100
4^+	6.025	0.05	100
3^-	6.1272	2.36	97
$(4)^{-?}$	6.560	25.1	100?
1^-	6.873	120	38
$(1,2)^+$	7.002	100	small
2^-	7.43	100	<30
2^+	7.478	74	<35

Table 5.5: Spectroscopic information of ${}^{10}\text{B}^* \rightarrow \alpha + {}^6\text{Li}$ adopted from ref. [98]. The state at the 6.56 MeV is assigned tentatively with $J=4$ and only alpha decay is confirmed. The last three states contribute very little to the fitting. For details see text.

An extra 3^+ state is predicted at about 6 MeV in ref. [101]. If this additional 3^+ state exists and all states are populated with their full statistical weights, we

must have overestimated that background in the fit above. If instead, one lowers the background to accommodate the 3^+ state, the fitted spin value for the 6.56 MeV state could be a little higher. But it still can not account for a spin of $J=4$ if we assume that the branching ratio to the α - ${}^6\text{Li}$ channel is 100%. In the next section, we see some weak evidence of a resonance at $E_{rel} = 0.6$ MeV in the deuteron- α - α correlation indicates that some of the 6.56 MeV state decays via either the d- α - α three-particle channel or the d- ${}^8\text{Be}$ two-particle channel. If it accounts for half of the decay of the 6.56 MeV state, then the best fit (solid line) in Figure 5.26 favors a spin of $J = 4$. We don't have enough statistics, however, to determine the branching ratio for the decay of the 6.56 MeV state to this channel, leaving the determination of spin for the 6.56 MeV state open at the present time. Further studies on the branching ratios are needed to clarify this issue.

To further apply this technique on probing nuclear structures, better statistics and resolution are important to distinguish overlapping resonances. Better statistical accuracy and lower backgrounds can help reduce the uncertainty in the fit. Lower backgrounds can be attained by using a smaller system. However, the agreement with equilibrium correlation functions could be worse because there may be stronger non-equilibrium contributions. Resonance peaks far from the threshold are suppressed significantly due to the energy dependent suppressing factor in R_{nuc} which comes from two particle phase space and collective effects. Therefore the states close to the decay threshold are easier to study by this technique. As far as the secondary decay effects concerned, proton-rich nuclei are preferred in this technique. In addition, all the decay branching ratios, if not known, for the low-lying resonances of proton-rich nuclei can in principle be determined by studying all relevant particle correlations. In this case we don't need to deal with neutron decay which can be omitted for proton-rich nuclei. It will be an advantage when only charged particles are detected

in experiments.

5.7 Multiple Particle Correlations

Similar to two particle correlation functions, correlation of three or more particles can be constructed in heavy ion reactions. While we have not analyzed them in detail, it is nevertheless interesting for future studies to examine them. Choosing some of the stronger correlation functions, we discuss some of their properties in this section.

In Figure 5.27 the three-alpha correlation function is shown. The resonance peaks of ^{12}C [102] are labelled in the plot. In two particle correlations one sees a weak energy dependent factor $1/\sqrt{E_{rel}}$ in Eq. 5.23 which stems from the two-body phase space. In contrast to two particle correlations, three body phase space yields a more strong and singular energy dependent factor in three-particle correlation functions. For a three body decay, this factor can be as strong as $1/E_{rel}^2$ and consequently increases the height of resonance states well below 1 MeV enormously and suppresses the peaks at higher energies. Due to this singular factor the first peak is extremely pronounced corresponding to the 0^+ state of ^{12}C at 7.654 MeV. The second peak showing the 3^- state at 9.64 MeV is much reduced compared to the first peak even though it has a larger spin degeneracy factor. The states of 0^+ at 10.3 MeV and 1^- at 10.844 MeV are less evident because they are much broader and have low spins. A broad pronounced group is observed consisting of five states of 2^+ at 11.16 MeV, 2^- at 11.828 MeV, 1^+ at 12.71 MeV, 2^- at 13.352 MeV and 4^+ at 14.083 MeV, which can not be distinguished from each other due to poor resolution. Beyond the broad 2^+ state at 15.44 MeV the proton decay channel becomes dominant.

In Figure 5.28 the proton-proton-alpha correlation is plotted depicting the resonances of the 0^+ ground state and the 2^+ state at 1.67 MeV from ^6Be [98]. Figure

5.29 shows the proton-alpha-alpha correlation function from the decay of ${}^9\text{B}$. The first resonance of the $3/2^-$ ground state of ${}^9\text{B}$ is so pronounced because of the singular three-body phase space factor discussed above. And the $5/2^-$ state at 2.361 MeV is also pronounced while there is a weak evidence showing the existence of a broad state at about 1.6 MeV [98].

In Figure 5.30 the deuteron-alpha-alpha correlation function shows the resonance peaks from the decay of ${}^{10}\text{B}$ in the range of 6-8 MeV [98]. Although poor statistics, one can see a suggestion of a resonance from the 6.56 MeV state to this decay channel, which is just above the detection threshold. This might indicate that the branching ratio for the α - ${}^6\text{Li}$ channel from the 6.56 MeV state is less than 100%. Thus there is a possibility that the spin of this state could be larger than the magnitude of the peak in the α - ${}^6\text{Li}$ channel might indicate. The second peak in Fig. 5.30 could be the decay of the 1^- state at 6.873 MeV and the $(1, 2)^+$ state at 7.002 MeV. A shoulder on the spectrum corresponds to the decay from the 2^- state at 7.43 MeV and the 1^+ state at 7.67 MeV and there is a pronounced peak showing the decay of the 2^+ state at 8.07 MeV.

As well as identifying resonance states of particle unstable nuclei, we can gain access to other valuable information in correlation functions, which is difficult to be obtained elsewhere. The three-body Coulomb correlation can be examined in these three particle correlation functions. Although the resonance states far from the threshold are difficult to access due to the large phase space suppressing factor $1/E_{rel}^2$, this factor also makes the peaks very close to the threshold astoundingly pronounced, which may be useful for further studies on the properties of sources and so on. However, more needs to be done on the formalism for three body correlations before this can be a quantitative tool.

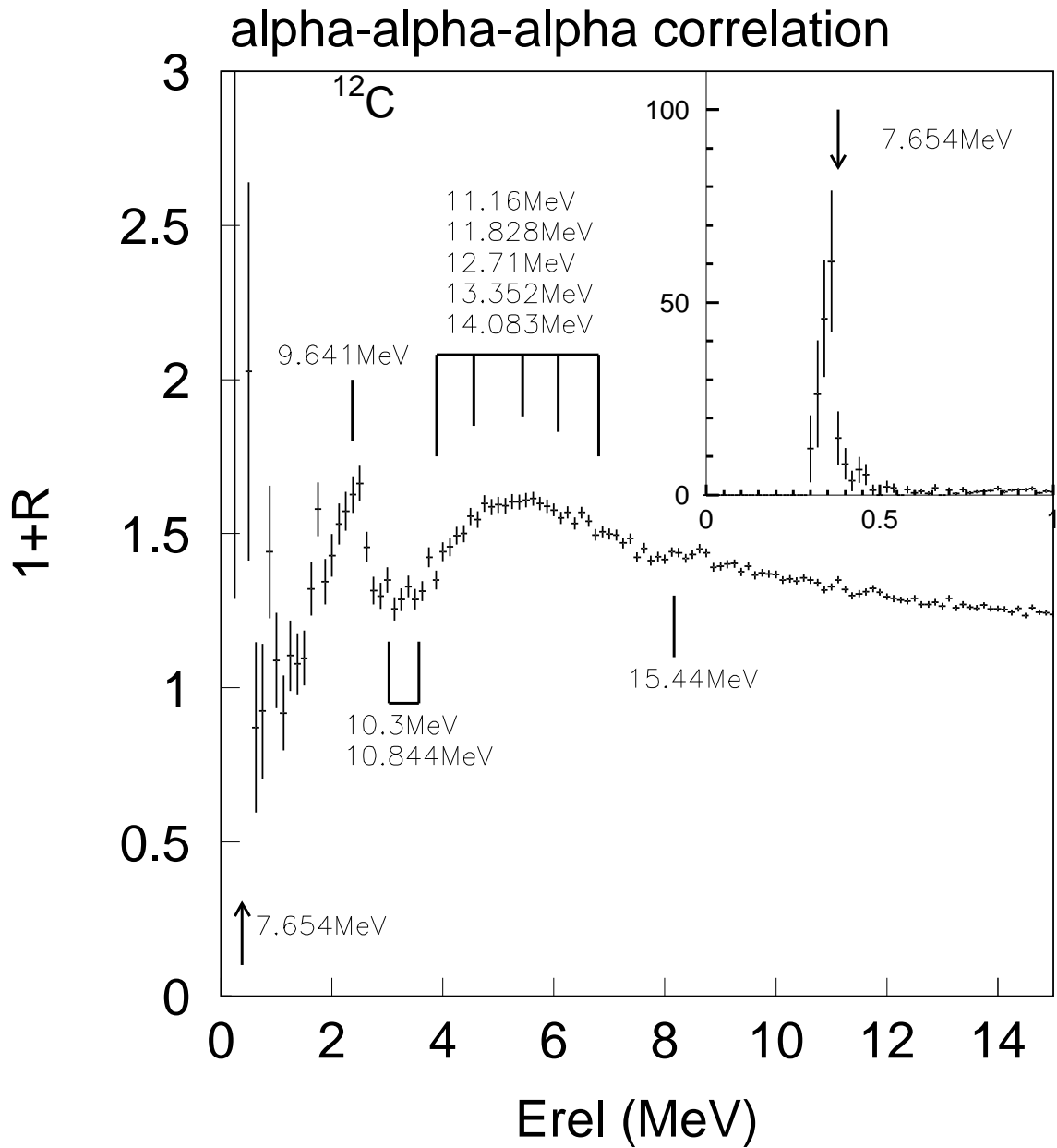


Figure 5.27: The α - α - α correlation function is shown. Resonances from the excited states of ^{12}C are labelled with the first peak seen more clearly in the inner upright panel.

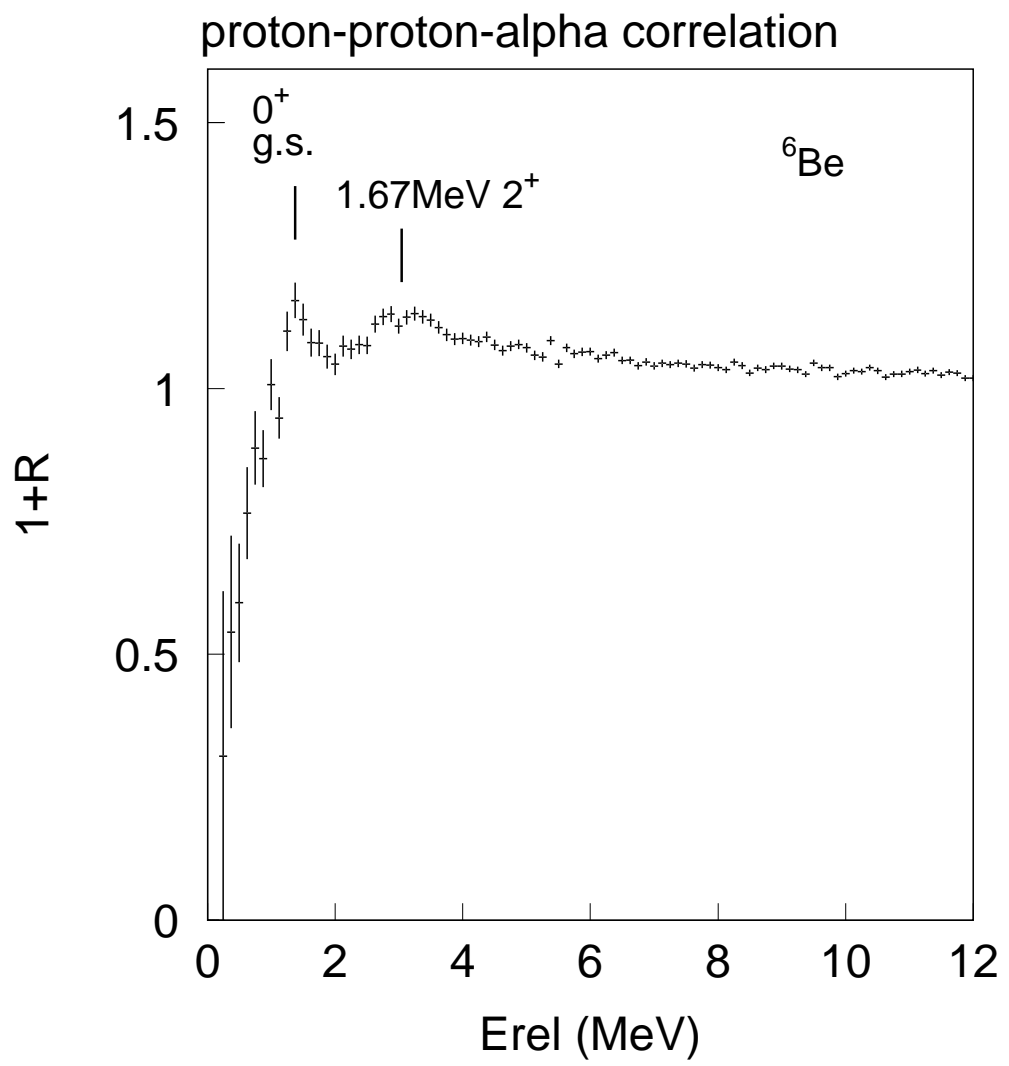


Figure 5.28: The p-p- α correlation function is shown.

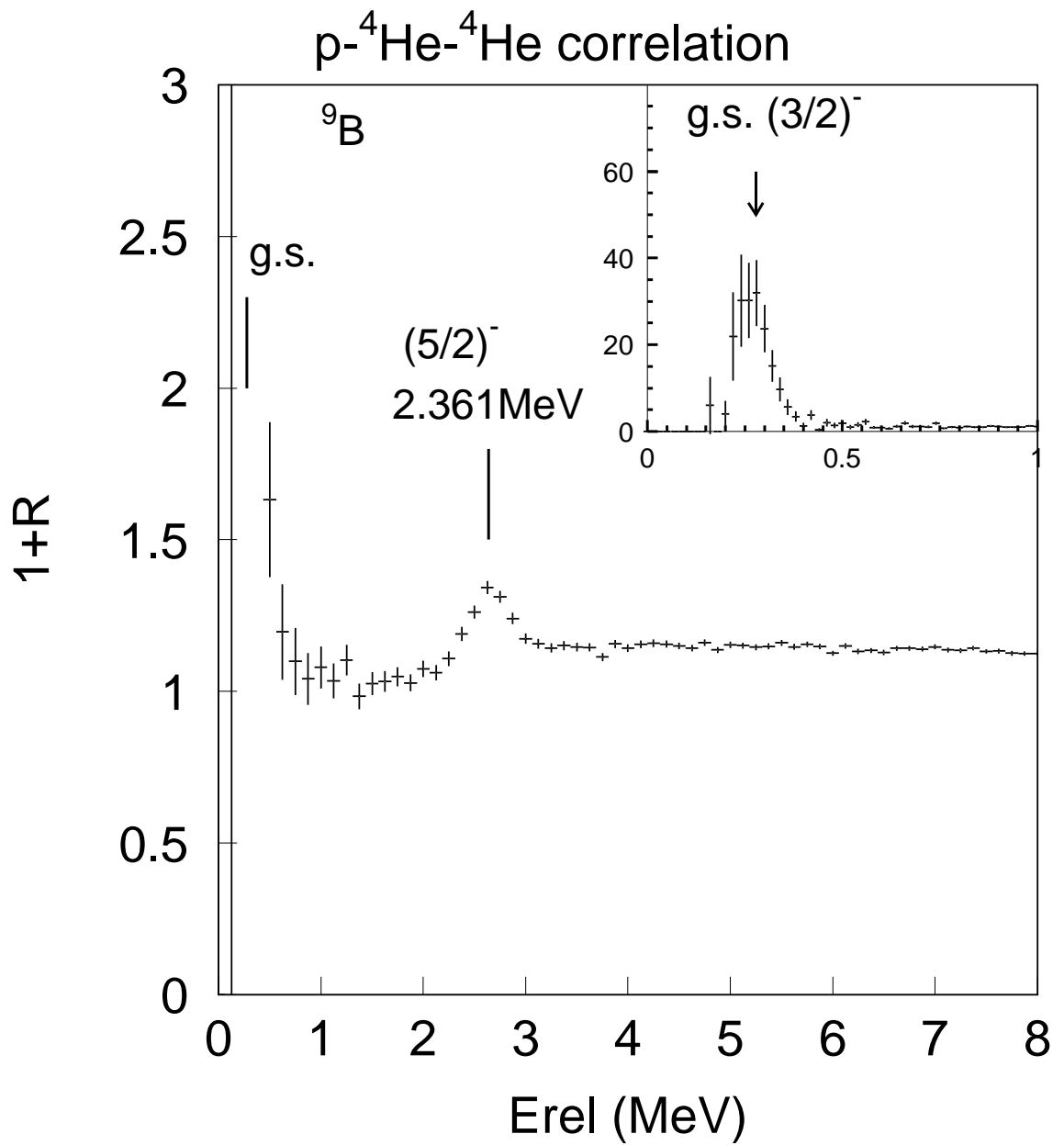


Figure 5.29: The $p\text{-}\alpha\text{-}\alpha$ correlation function is plotted. The resonances from the decay of ${}^9\text{B}$ are shown.

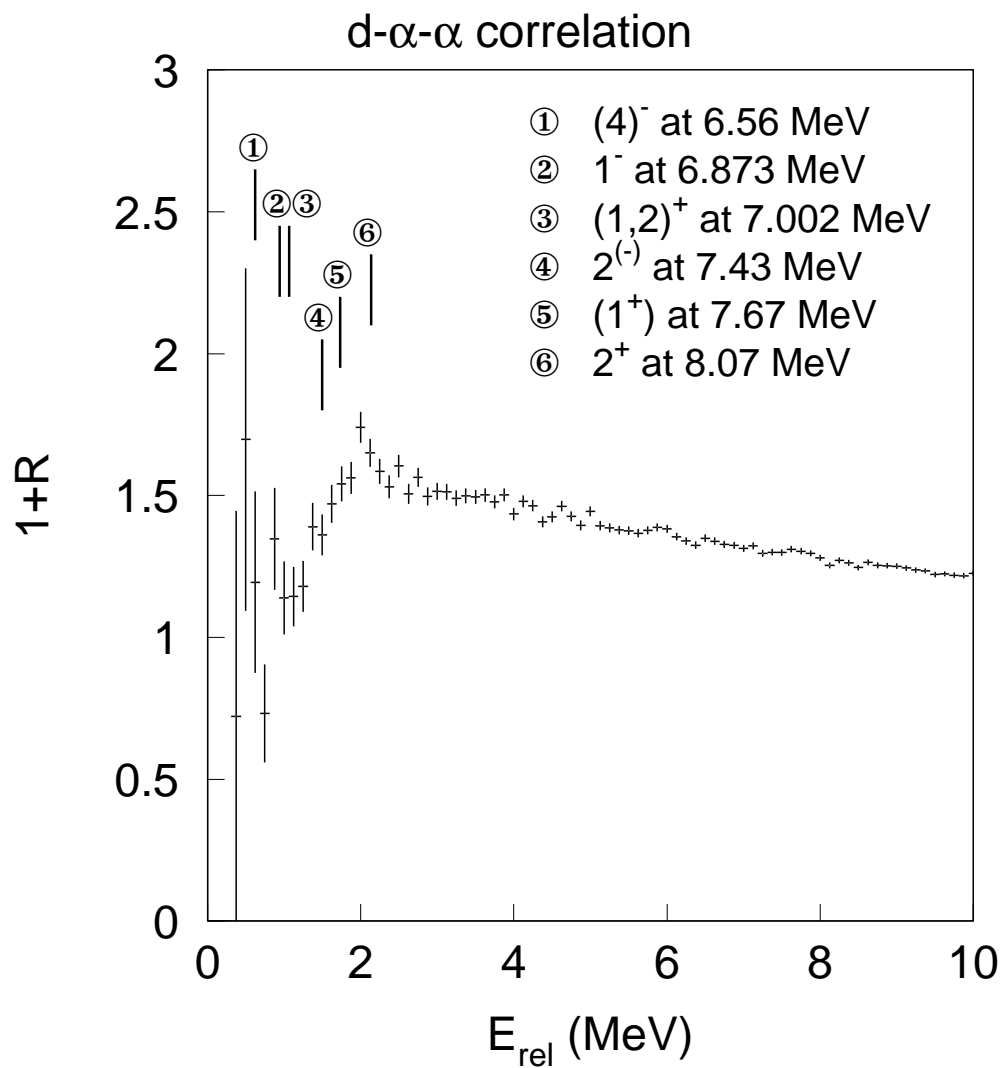


Figure 5.30: The d- α - α correlation function is shown. The resonance states of ^{10}B that contribute this decay are listed. See detailed discussions in text.

Chapter 6

Statistical Multifragmentation Model with Empirical Modifications

The statistical multifragmentation model (SMM)[36] has been successful in describing the thermodynamical properties of multifragmentation processes, especially for comparisons to measured fragment multiplicities, mass and charge distributions and so forth[19, 21]. Further studies on the degree of thermalization of such reactions involve accurately constructing thermometric observables such as isotopic thermometers[54, 31]. Isospin effects in multifragmentation are also being explored for the study of isospin fractionation[41], isotope scaling[39] and even the isospin dependence of the nuclear equation of state[42]. Such studies, however, have been rendered less conclusive because of the inaccurate modelling of the later stages of the breakup in current models where detailed nuclear structural information are critical to accurately model the secondary decay process. In this chapter, an empirical statistical multifragmentation model incorporated with an empirical secondary decay procedure is described by taking into account experimental information such as binding energies and level densities as much as possible. By means of this improved model, nuclear thermometry and isospin effects are studied and compared with experimental data.

6.1 Microcanonical Statistical Multifragmentation Model (SMM)

6.1.1 Underlying Formalism

In the SMM, it is assumed that an excited, expanded and equilibrated source is formed after the most violent stages of a heavy ion reaction and it then decays simultaneously and statistically. The microcanonical version of the SMM uses the Monte Carlo method and averages observables with the statistical weight over fragmentation modes[36]. A multifragment decay mode is *defined* in the SMM approach as a specific set of emitted fragments and light particles. For simplicity, each fragmentation mode in the SMM approach is weighted according to the entropy of the mode. This entropy is approximated by analytical expressions rather than by an event by event sampling of the phase space as in ref. [11]. These approximations rely upon that fact that the dominant contribution to this entropy comes from internal phase space of fragments which plays the role of a heat bath within the SMM approach just as an excited residue plays the role of a heat bath within compound nuclear decay theory [43].

The characteristics of this source, such as its thermal excitation energy E_0^* , density, mass and atomic numbers, A_0 and Z_0 , respectively, are taken for granted in the model. For a given fragmentation mode, mass and charge conservation is strictly imposed:

$$A_0 = \sum_{\{A,Z\}} N_{AZ} A \quad \text{and} \quad Z_0 = \sum_{\{A,Z\}} N_{AZ} Z \quad (6.1)$$

where N_{AZ} is the multiplicity of a fragment with mass number A and Charge number Z. By making a Wigner Seitz approximation to the Coulomb energy, energy conservation within the SMM approach leads to the expression [36],

$$E_0^{gs} + E_0^* = a_c \frac{Z_0^2}{A_0^{1/3}} \left(\frac{V_0}{V} \right)^{1/3} + \sum_{\{A,Z\}} N_{AZ} E_{AZ} \quad (6.2)$$

where E_0^{gs} is ground state energy of the fragmenting source. The first term on the right hand side stands for the Coulomb energy of a homogeneous sphere of matter containing the total charge Z_0 and mass A_0 at a density $\rho = \rho_0 (V_0/V)$ where V_0 is the normal volume at saturation density ρ_0 and V is the breakup volume occupied by the system. The second term is the sum of the energy of each individual fragment in this decay mode. E_{AZ} is the kinetic plus internal energy for each of these fragments. It is related to the temperature by assuming all fragments are at a common temperature as follows,

$$E_{AZ} = \frac{3}{2}T + E_{AZ}^*(T) + E_{AZ}^C - B_{AZ} \quad (6.3)$$

where the internal excitation energy of the fragments, $E_{AZ}^*(T)$, may be approximated by an extension of the semi-empirical mass formula to finite temperatures [36], and the extra Coulomb energy of the fragment in the fragmentation volume, E_{AZ}^C , may be calculated within the Wigner-Seitz approximation (see below). B_{AZ} stands for the ground state binding energy for the fragment. Eqs. 6.2 and 6.3 result from an average of the microcanonical expression for energy conservation over the phase space corresponding to the specific fragmentation mode.

By applying the energy conservation relationship in Eqs. (6.2-6.3) one obtains a temperature T that describes the internal excitation and translational energies of fragments within a given fragmentation mode. Even though the overall system is assumed to be in equilibrium at a fixed excitation energy E_0^* , different decay modes have different Coulomb, binding, and translational energies and, consequently, different excitation energies of the emitted fragments. Consistency with Eqs. (6.2-6.3) therefore requires that the temperature T of the fragments varies from one decay mode to another, reflecting the differences between the Coulomb, binding and translational energies of the various fragmentation modes.

Labelling the fragmentation mode $\{N_{AZ}\}$ with the index, m , a physical observable O , such as the yield of a fragment or the temperature, can be expressed by a weighted average over decay modes as,

$$\langle O \rangle = \frac{\sum_m W_m O_m}{\sum_m W_m} \quad (6.4)$$

where the statistical weight associated with the mode m ,

$$W_m = \exp \left[\sum_{\{A,Z\}} N_{AZ} S_{AZ}(T) \right] \quad (6.5)$$

may be found by expressing the entropy of the fragments, S_{AZ} , through the thermodynamical relation with free energy,

$$S = -\frac{\partial F}{\partial T} , \quad (6.6)$$

The corresponding free energy associated with each fragment can be written as,

$$\begin{aligned} F_{AZ}(T) &= -B_{AZ} - a_c \frac{Z^2}{A^{1/3}} \left(\frac{V_0}{V} \right)^{1/3} \\ &+ F_{AZ}^K(T) + F_{AZ}^*(T) , \end{aligned} \quad (6.7)$$

where the kinetic term corresponds to:

$$\begin{aligned} F_{AZ}^K(T) &= -T \ln \left[g_{AZ} V_f \left[\frac{m_n A T}{2\pi \hbar^2} \right]^{3/2} \right] \\ &+ T \ln (N_{AZ}!) / N_{AZ} . \end{aligned} \quad (6.8)$$

where $V_f = V - V_0$ is the free volume, m_n represents the nucleon mass, and g_{AZ} is the spin degeneracy factor. Empirical values at ground state are used for $A < 5$ since one assumes that these nuclei have no excited states, except ${}^4\text{He}$. In all the other cases, $g_{AZ} = 1$ because we assume that this effect is, to some extent, already taken into account by the level density used in the model. The Coulomb term in Eq. (6.7)

is associated with the remaining corrections in the Wigner-Seitz approximation. The excitation of the intrinsic degrees of freedom is taken into account by $F_{AZ}^*(T)$, and therefore it is zero for the light particles as just mentioned.

To calculate the properties of the multifragment emission from the excited source, one should sum the contributions of all the fragmentation modes consistent with mass, charge and energy conservation imposed by Eqs. (6.1)-(6.2). However, this would be extremely time consuming owing to the huge number of possible fragmentation modes [103]. Therefore, the present approach samples the more probable modes via a Monte Carlo calculation. This is carefully discussed in ref. [103]; we note in passing that the Monte Carlo procedure introduces a bias since not all the mass and charge partitions enter with the same weight. Therefore ω_m must be modified to correct for this bias [103].

In the standard SMM formalism, simple parametrizations [36] of the ground state energy and internal free energy are adopted for convenience. In order to have accurate calculations, however, more careful treatments related to the nuclear structures are needed, especially for the secondary decay process. Before we introduce an empirically modified SMM with an consistent empirical secondary decay procedure in section 6.2, issues related to primary temperatures need to be addressed in the following.

Temperatures have been extracted from the isotopic yields of heavy ion collisions using the isotope thermometry method proposed by Albergo *et al.* [54]. The idea of the method is to obtain temperature from the double ratios of the yields of four suitably chosen isotopes, (A_1, Z_1) , $(A_1 + 1, Z_1)$, (A_2, Z_2) , $(A_2 + 1, Z_2)$ via the relation[54],

$$T_{ISO} = \frac{\Delta B}{\ln(a\Delta Y)} \quad (6.9)$$

where

$$\Delta Y = \frac{Y(A_1, Z_1)/Y(A_1 + 1, Z_1)}{Y(A_2, Z_2)/Y(A_2 + 1, Z_2)}, \quad (6.10)$$

$$\begin{aligned} \Delta B &= B(A_1, Z_1) - B(A_1 + 1, Z_1) \\ &\quad - B(A_2, Z_2) + B(A_2 + 1, Z_2), \end{aligned} \quad (6.11)$$

and

$$a = \frac{(2J_{Z_2, A_2} + 1)(2J_{Z_1, A_1+1} + 1)}{(2J_{Z_1, A_1} + 1)(2J_{Z_2, A_2+1} + 1)} \left[\frac{A_2(A_1 + 1)}{A_1(A_2 + 1)} \right]^{3/2}. \quad (6.12)$$

Here $Y(A, Z)$ is the yield of a given fragment with mass A and charge Z ; $B(A, Z)$ is the binding energy of this fragment; and $J_{Z,A}$ is the ground state spin of a nucleus with charge Z and mass A . However, this isotope thermometry method is derived within the context of the grand canonical ensemble which could be doubtful as compared with experiments which are probably closer to microcanonical limit. In the following sections, the validity of the Albergo formula (Eq. 6.9) will be tested within this approximate microcanonical SMM.

6.1.2 Temperature Distributions

The SMM procedure expressed in Eqs.(6.2-6.4) leads to a distribution of the temperatures of the fragmenting system for a given excitation energy in the same sense that the temperature of the daughter nucleus in compound nuclear decay theory varies as a function of the Coulomb barrier and separation energy of each decay channel. The points in Fig. (6.1) denote the temperature distributions for the fragmentation of an excited ^{112}Sn nucleus at three different excitation energies obtained with the SMM. These distributions are well fitted by gaussian functions, shown by the curves in the figure, with variances σ_T^2 that are fairly independent of the energy, $\sigma_T \approx 0.4$ MeV, in the range $3 \text{ MeV} \leq E_0^*/A \leq 10 \text{ MeV}$. At each excitation energy, we average over

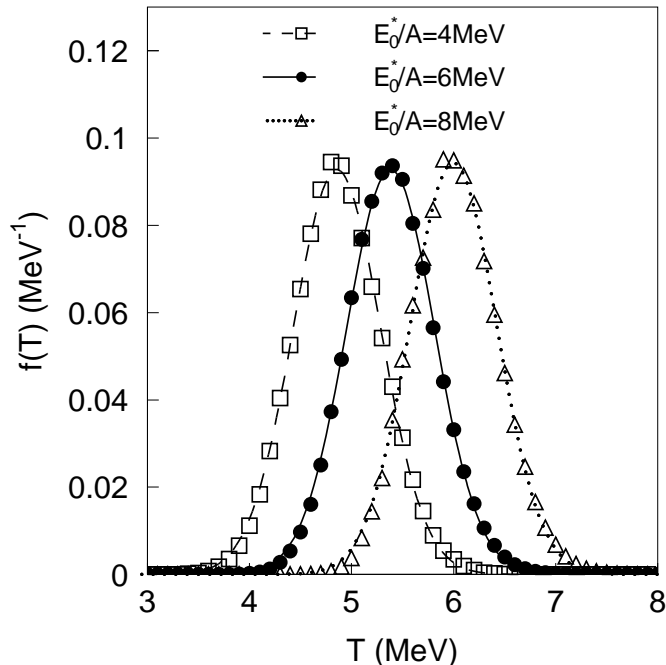


Figure 6.1: The points denote distributions of temperatures calculated with the SMM approach for the decay of a ^{112}Sn nucleus at three different excitation energies. The lines denote gaussian fits to the calculated distributions.

all of the fragmentation modes and define this average value as the "approximate microcanonical" temperature T_{MIC} .

Since each of the isotopes employed in the thermometer has a specific mass, charge and binding energy, the application of conservation laws sets a constraint on the values available to the remainder of the system. Because of this finite size effect, the temperature distribution obtained when a specific isotope is present is slightly different from the one obtained when all fragmentation modes are considered. In particular, a small difference (≤ 0.1 MeV) is observed between the average temperatures for the various isotopes; this is illustrated in Fig. (6.2) for carbon isotopes from the fragmentation of a ^{112}Sn nucleus at $E_0^*/A = 6$ MeV. Even though the average temperatures

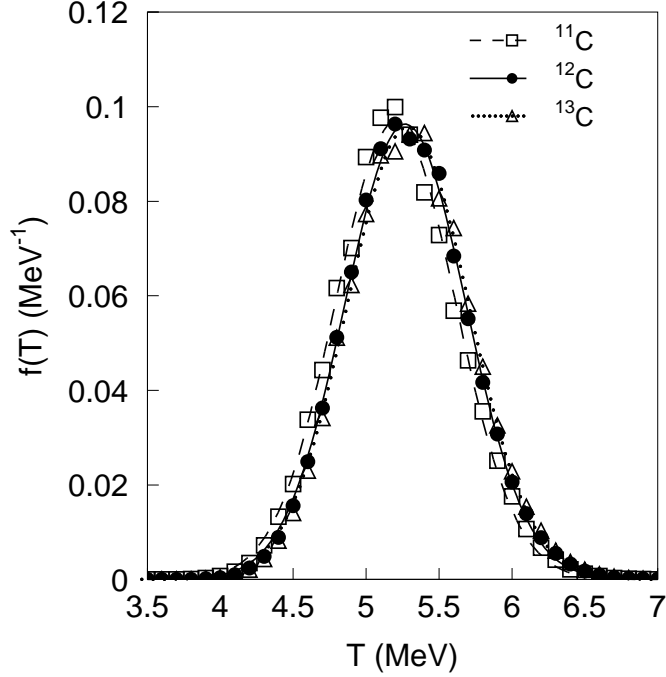


Figure 6.2: The points denote temperature distributions calculated with the SMM approach for the different isotopes considered in the carbon thermometer for an excitation energy of $E_0^*/A = 6\text{MeV}$. The lines denote gaussian fits to the calculated distributions.

are different reflecting the different binding energies of the three isotopes, all these distributions are gaussians with nearly the same variances. We can extract another temperature T_{IMF} by averaging over fragmentation modes which contain an Intermediate Mass Fragment (IMF) with $3 \leq Z \leq 10$. It's interesting to note that T_{MIC} can exceed T_{IMF} at low energies by as much as 0.2 MeV, in part because it takes more energy to emit an IMF than to emit an equivalent mass in the form of alpha particles, leaving less energy for thermal excitation.

The basic idea contained in Eq. (6.9) was derived under the assumption that the primary yields are well represented by the grand canonical approximation at a single breakup temperature; the double ratio was invoked to cancel out the contribution to

the yields coming from the neutron and proton chemical potentials. In the SMM, however, the temperature varies from one fragmentation mode to another and the chemical potentials, which appear within the grand canonical formalism as Lagrange multipliers that conserve charge and mass, are not explicitly invoked. Thus, we can not presume the validity of the Albergo's formula (Eq. 6.9) in the SMM and must test its validity instead.

We begin with a test of the validity of Eq. (6.9) when one employs the primary yields. The primary yield for the ground state can be related to the total yield by

$$N_{AZ}^{gs} = N_{AZ} \cdot g_{AZ}^{gs} \exp [F_{AZ}^*(T)/T] \quad (6.13)$$

for a given fragmentation mode. Following the procedure described in the previous section, we will use this expression and Eq. (6.4) to obtain the average g.s. yield distribution $\langle N_{AZ}^{gs} \rangle$. This, in turn, can be used in Eq. (6.9) to extract isotopic temperatures as follows,

$$\frac{\langle N_{A_1, Z_1}^{gs} \rangle / \langle N_{A_1+1, Z_1}^{gs} \rangle}{\langle N_{A_2, Z_2}^{gs} \rangle / \langle N_{A_2+1, Z_2}^{gs} \rangle} = C \exp \left(\frac{\Delta B}{T_{iso}^{smm}} \right). \quad (6.14)$$

In previous SMM calculations, experimental binding energies and spin degeneracy factors g_{AZ}^{gs} were used for light nuclei with $A < 5$. Liquid drop binding energies and spin degeneracy factors of unity were used for $A \geq 5$. In this work, we will retain these conventions on spin degeneracy factors so as to be consistent with prior calculations, but we will use empirical binding energies for all nuclei.

In Fig. (6.3), the isotopic temperatures T_{iso}^{smm} for the carbon thermometer ($Z_1 = Z_2 = 6, A_1 = 11, A_2 = 12$) are plotted as the stars for the multifragmentation of a ^{112}Sn source at excitation energies $E_0^*/A = 3 - 10$ MeV. For comparisons, the corresponding T_{MIC} and T_{IMF} for the same system are also shown in Fig. (6.3) as

the dashed and solid lines, respectively. While supporting the concept of isotopic thermometry, the good agreement between T_{IMF} and T_{iso}^{smm} is somewhat surprising, given the strong dependence of the Boltzmann factor on temperature for large ΔB and the width of the temperature distribution shown in Fig. (6.1). As shown in the following section, it occurs in part due to a large cancellation involving the Boltzmann factor and the temperature dependences of the effective chemical potentials. Fig. (6.3) also reveals that fairly precise information about T_{IMF} and somewhat less precise information about T_{MIC} is provided by the primary yields. This suggests that given a precise relationship between primary to the final yields, it would be possible to determine the breakup temperature from the measured yields.

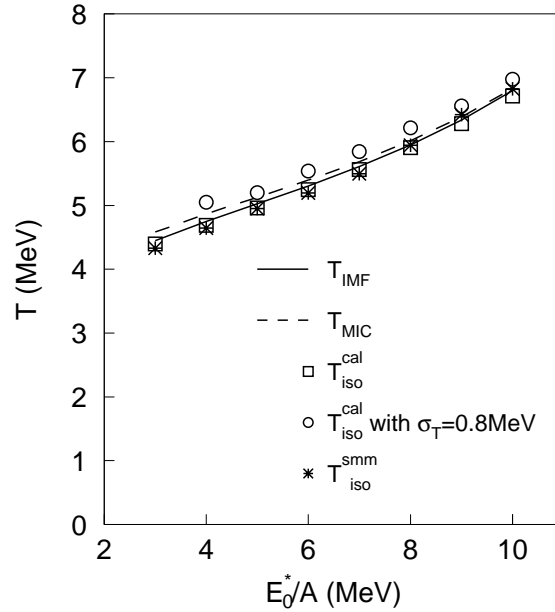


Figure 6.3: Comparisons of various primary temperatures T_{MIC} , T_{IMF} and T_{iso}^{smm} from the SMM and T_{iso}^{cal} from the analytical calculation in the grand canonical limit. For details see the text. One point is missing for T_{iso}^{cal} with $\sigma_T = 0.8$ MeV because the calculated value for p for the correction term in Eq.(6.17) becomes negative at $E_0^*/A = 3$ MeV, i.e. the expansion breaks down in this case.

6.1.3 Effects of Temperature Variations

The surprising consistency between T_{IMF} and T_{iso}^{smm} in Fig. (6.3) suggests that the corrections to the grand canonical prediction for the isotope temperatures are small, and one may utilize this approach to understand why the temperature variations have so little influence on the results. Taking this tact, we assume that the isotopic distributions are well approximated for each fragmentation mode by the grand canonical limit, use this limit to gain insight into the finite size effects and at the same time, investigate the accuracy of this approximation. We take this approach to consider first the influence of the temperature variations and later the consequences of the finite size on the effective chemical potentials.

Considering the influence of the temperature variations in this approximation, we average the grand canonical approximation over the temperature distribution in Fig. (6.1). If the approximation works, the expressions that result from this average should be appropriate for the consideration of the effects of temperature distributions arising from other effects and within other equilibrium models of multifragmentation as well. Taking this approach, the yield of a particular isotope i in the framework of Albergo's method [54], when averaged over all possible fragmentation modes, becomes:

$$\langle Y_i \rangle = V \int_0^\infty dT f(T) \frac{A_i^{3/2} \zeta_i(T)}{\lambda_T^3} \exp [(Z_i \mu_{PF}(T) + N_i \mu_{NF}(T) + B_i)/T] \quad (6.15)$$

where $f(T)$ is the temperature distribution, V represents the free volume of the system, $\lambda_T = \sqrt{2\pi\hbar^2/mT}$, m is the nucleon mass and μ_{PF} (μ_{NF}) stands for the

chemical potential associated with free protons (neutrons) at temperature T . The internal partition function of the fragment i is given by:

$$\zeta_i(T) = \sum_j g_i^j \exp \left[-\frac{\Delta E_j}{T} \right] \quad (6.16)$$

where ΔE_j is the excitation energy of the state j with respect to the ground state and g_i^j stands for the spin degeneracy factor of this excited state.

Assuming that $f(T)$ is a gaussian centered at $\langle T \rangle$ and with width $\sigma_T \ll \langle T \rangle$ (see Fig. 6.1), one may expand $1/T$, $T^{3/2}$, and the chemical potentials. By considering only fragments observed in the ground state, *i.e.* $\zeta_i(T) = g_i^0$, we obtain that

$$\begin{aligned} \langle Y_i^{gs} \rangle &= \frac{g_i^0 V A_i^{3/2} \langle T \rangle^{3/2}}{\lambda_*^3} \\ &\cdot \exp \left[\frac{B_i}{\langle T \rangle} + \frac{\mu_{PF}(\langle T \rangle) Z_i + \mu_{NF}(\langle T \rangle) N_i}{\langle T \rangle} \right] \\ &\cdot \frac{1}{\sqrt{2p}} \cdot \exp \left[\frac{q^2}{4p} \right]. \end{aligned} \quad (6.17)$$

where $\lambda_* \equiv \sqrt{2\pi\hbar^2/m}$. In the above expression, the corrections to the grand canonical relationship are provided by the correction factor $\frac{1}{\sqrt{2p}} \cdot \exp \left[\frac{q^2}{4p} \right]$ which depends on assumed width of the temperature distribution, the binding energy of the i -th fragment, the neutron and proton chemical potentials and their derivatives through the parameters p and q . These two parameters are defined by

$$\begin{aligned} p &= \frac{1}{2} + \left[\frac{\sigma_T}{\langle T \rangle} \right]^2 \cdot \left[Z_i \alpha_{PF} + N_i \alpha_{NF} + \frac{3}{4} - \frac{B_i}{\langle T \rangle} \right] \\ q &= \frac{\sigma_T}{\langle T \rangle} \left(Z_i \beta_{PF} + N_i \beta_{NF} + \frac{3}{2} - \frac{B_i}{\langle T \rangle} \right), \end{aligned} \quad (6.18)$$

where

$$\begin{aligned}
\alpha_{PF} &= \mu'_{PF}(\langle T \rangle) - \frac{\mu_{PF}(\langle T \rangle)}{\langle T \rangle} - \frac{1}{2} \mu''_{PF}(\langle T \rangle) \langle T \rangle \\
\beta_{PF} &= \mu'_{PF}(\langle T \rangle) - \frac{\mu_{PF}(\langle T \rangle)}{\langle T \rangle} \\
\alpha_{NF} &= \mu'_{NF}(\langle T \rangle) - \frac{\mu_{NF}(\langle T \rangle)}{\langle T \rangle} - \frac{1}{2} \mu''_{NF}(\langle T \rangle) \langle T \rangle \\
\beta_{NF} &= \mu'_{NF}(\langle T \rangle) - \frac{\mu_{NF}(\langle T \rangle)}{\langle T \rangle}.
\end{aligned} \tag{6.19}$$

The isotopic temperature can be extracted from the above corrected yields. Replacing $Y(A, Z)$ in Eq. (6.9) by the right hand side of Eq. (6.17), one cancels out the spin and mass dependent term C and then obtains:

$$\exp \left[\Delta B / T_{iso}^{cal} \right] = \frac{G(A_1, Z_1) / G(A_1 + 1, Z_1)}{G(A_2, Z_2) / G(A_2 + 1, Z_2)}, \tag{6.20}$$

where

$$\begin{aligned}
G(A, Z) &= \exp \left[\frac{B_i}{\langle T \rangle} + \frac{\mu_{PF}(\langle T \rangle) Z + \mu_{NF}(\langle T \rangle) N}{\langle T \rangle} \right] \\
&\quad \cdot \frac{1}{\sqrt{2p}} \cdot \exp \left[\frac{q^2}{4p} \right].
\end{aligned} \tag{6.21}$$

In the above double ratio the terms involving the chemical potentials evaluated at the average temperature cancel; however, terms in the correction factor involving the derivatives of the chemical potentials remain.

Quantitative estimates of the correction factor require one to obtain estimates for the effective chemical potentials and their derivatives with respect to temperature.

The proton and neutron chemical potentials at temperature T may be calculated from the free proton and neutron multiplicities via the expression:

$$\mu_{PF}(T) = T \log \left[\frac{\lambda_T^3 Y_{PF}(T)}{g_{PF} V} \right], \quad (6.22)$$

$$\mu_{NF}(T) = T \log \left[\frac{\lambda_T^3 Y_{NF}(T)}{g_{NF} V} \right]$$

where $g_{PF}(g_{NF})$ represents the spin degeneracy factor of the proton(neutron). For the calculations presented in this work, it has proven advantageous and reasonably accurate to approximate the yields $Y_{PF}(T)$ and $Y_{NF}(T)$ over a modest range in temperature by power law expressions in the temperature. In this approximation,

$$Y_{PF}(T) = c_{PF} T^{\gamma_{PF}}, \quad (6.23)$$

$$Y_{NF}(T) = c_{NF} T^{\gamma_{NF}}$$

For the decay of ^{112}Sn nuclei at temperatures ranging over $4 \leq T \leq 7 \text{ MeV}$, Y_{PF} and Y_{NF} are well described by $\gamma_{PF} = 4.5$ and $\gamma_{NF} = 1.0$ ($c_{PF} = 1.33 \times 10^{-4}$ and $c_{NF} = 0.267$) according to the SMM; comparisons of this parameterization to yields calculated with the SMM model are shown Fig. (6.4). These values depend on the density, which has been chosen to be one third that of the saturation density of nuclear matter. Larger values of the free nucleon yields are obtained at lower density.

Using this approximation, the explicit forms of the correction factors in Eqs. (6.17)-(6.19) become $2\alpha_{PF} = \beta_{PF} = \left(\gamma_{PF} - \frac{3}{2}\right) = 3$ and $2\alpha_{NF} = \beta_{NF} = \left(\gamma_{NF} - \frac{3}{2}\right) = -\frac{1}{2}$. We note that the correction factor to the temperature T_{iso}^{cal} in Eq. (6.20) depends

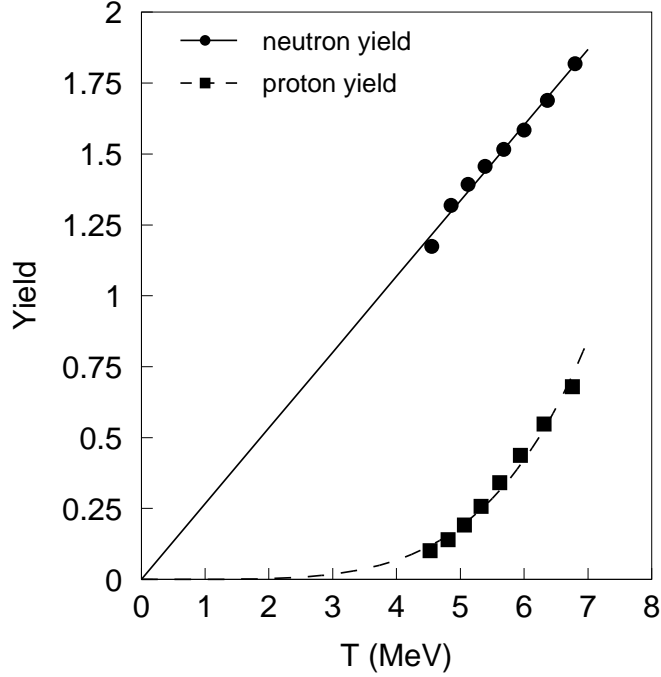


Figure 6.4: The solid squares and circles denote the free proton and neutron yields, respectively, calculated via the SMM approach. The solid and dashed lines denote fits to the calculated yields following Eq. (6.23).

on the power law exponents $\gamma_{PF}(\gamma_{NF})$ and not on the absolute values of the proton(neutron) yields.

Even though Eq. (6.15) has an exponent that appears to be strongly temperature dependent, there is a strong cancelation between the contributions from the chemical potentials and binding energy factors in the expressions for p and q . As a result, the correction factor is of order unity. Values in the range of $\frac{1}{\sqrt{2p}} \cdot \exp\left[\frac{q^2}{4p}\right] \approx 1 - 2$ are obtained, for example, in the decay of ^{112}Sn nuclei at temperatures in the range of $4 \leq T \leq 7\text{MeV}$.

The isotopic temperatures T_{iso}^{cal} calculated from Eq. (6.20) for carbon thermometer are shown in Fig. (6.3) in comparisons with temperatures T_{MIC} , T_{IMF} and T_{iso}^{smm}

derived from the SMM in the previous session. The very good agreement between T_{iso}^{cal} , T_{iso}^{smm} and T_{IMF} indicates that the corrections to the isotopic temperatures associated with these temperature variations are small, although the yields can change by as much as a factor of two. This comparative insensitivity arises because the isotopic thermometers depend logarithmically on the yields.

This insensitivity depends on the nature and magnitude of the temperature variation. The corrections to the isotopic temperatures will be somewhat larger in other contexts or other models where the temperature variations are larger. The limited precision with which systems may be selected experimentally may also have a similar influence because the excitation energy and temperature varies experimentally from collision to collision due to variations in the impact parameter or in the energy removed by preequilibrium particle emission. The influence of this temperature variation, which may exceed the variation in temperature caused by the averaging over decay modes, can also be estimated via techniques outlined in the present section. To illustrate how one can estimate the possible corrections due to an imprecision in the excitation energy definition, the circles in Fig. (6.3) show calculations using Eq. (6.20) for carbon thermometer assuming a width of $\sigma_T \approx 0.8$ MeV for the temperature distribution, which is twice as large as that predicted in Figs. (6.1) and (6.2). This width is not based upon a dynamical calculation; it is only to illustrate that larger isotopic temperatures can result if the excitation energy is poorly defined.

6.1.4 Chemical Potentials

The grand canonical limit has a great advantage of providing a simple analytic expression for the isotopic yields from which other useful expressions can be derived. However, the concept of uniform chemical potentials is not a prediction of micro-canonical or canonical models and must be investigated to determine its applicability

to finite systems. We do this by trying to comparing the grand canonical expression for the isotopic yields to the predictions of approximately microcanonical SMM calculations. We start by assuming that these isotopic distributions can be calculated within the grand canonical approximation and then test this assumption as follows. Using a pair of adjacent isotopes, we invert the grand canonical expression for the isotopic yields of two adjacent isotopes to obtain an equation for the *effective* neutron chemical potential:

$$\begin{aligned} \mu_n^{eff}(A, Z) = & T \log \left[\frac{g_{AZ}^{gs}}{g_{A+1Z}^{gs}} \left(\frac{A}{A+1} \right)^{3/2} \right. \\ & \left. \exp \left((B_{AZ} - B_{A+1Z}) / T \right) \frac{Y_{A+1Z}^{gs}}{Y_{AZ}^{gs}} \right] \end{aligned} \quad (6.24)$$

where g_{AZ}^{gs} , B_{AZ} and Y_{AZ}^{gs} are the ground state spin degeneracy, the binding energy and the ground state primary yield for a fragment with (A,Z), respectively. If the Y_{AZ}^{gs} taken to be the ground state yields predicted by the SMM, $\mu_n^{eff}(A, Z)$ becomes an "effective SMM" chemical potential. By performing SMM calculations, we find the temperature- and isotopic- dependences of the effective neutron chemical potentials given in Fig. (6.5) for Carbon and Lithium isotopes from the decay of a ^{112}Sn nucleus at excitation energies of $E_0^*/A = 3, 6, 9 \text{ MeV}$.

These effective chemical potentials are essentially the same for the Carbon and Lithium isotope chains. This insensitivity to element number is consistent with the concept of a chemical potential and offers support for the use of the grand canonical expression to describe isotopic distributions. There is a dependence on the neutron number of the isotope, however, that lies outside of the grand canonical approximation. This variation in the neutron chemical potential basically comes as a result of mass, charge and energy conservation for a finite-size system. We can understand

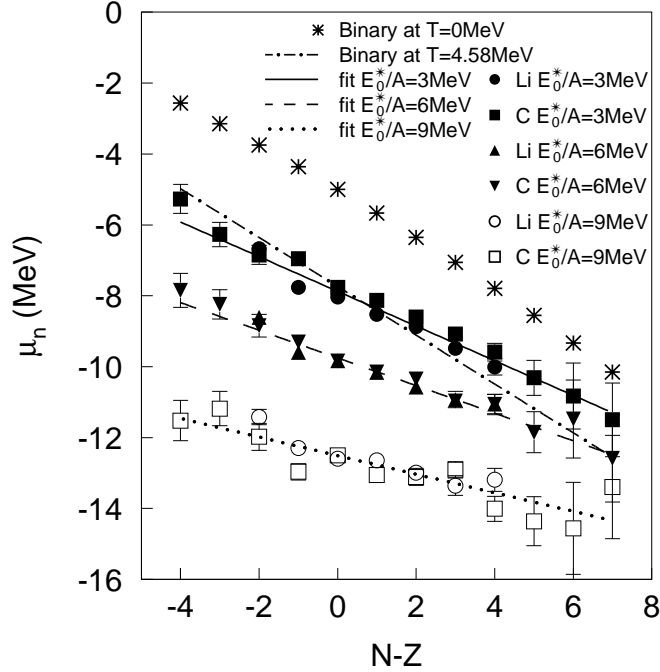


Figure 6.5: The squares, circles and triangles denote neutron chemical potentials derived from Eq. (6.24) using SMM predictions for Carbon and Lithium isotopic yields at various initial excitation energies for the decay of the nucleus ^{112}Sn . The stars and the dot-dashed line denote approximate values calculated from Eq.(6.28) for $T=0$ and 4.58 MeV, respectively. The error bars denote the statistical errors in the calculation, which in many cases are too small to be observed in the figure.

the influence of these conservation laws most easily at low excitation energies, where the two largest fragments in the final state are the IMF (Carbon or Lithium in this case) and a heavy residue which contains most of the remaining charge and mass. We estimate the influence of conservation laws at low excitation energy qualitatively by considering binary decay configurations. Assuming that a parent nucleus (A_0, Z_0) decays into a light fragment (A, Z) and a heavy residue $(A_0 - A, Z_0 - Z)$, we can approximate the yield of fragment (A, Z) in its ground state by

$$\begin{aligned}
Y_{AZ}^{gs} &\propto \rho^{gs}(A, Z) \rho^*(A_0 - A, Z_0 - Z) \bar{\rho}_{REL} \\
&\approx g_{AZ}^{gs} \cdot \exp[S^*(A_0 - A, Z_0 - Z)] \\
&\quad \cdot \left[\frac{A \cdot (A_0 - A)}{A_0} \right]^{3/2} \frac{1}{\lambda_T^3}
\end{aligned} \tag{6.25}$$

where $\rho^{gs} = g_{AZ}^{gs}$, ρ^* and S^* are the density of states for the light nucleus in its ground state level, the density of states and entropy of the heavy residue in its excited state, respectively, The other factor, $\bar{\rho}_{REL} \approx \left[\frac{A \cdot (A_0 - A)}{A_0} \right]^{3/2} \lambda_T^{-3}$, is the thermal average of the state density of relative motion.

Replacing the yields in Eq.(6.24) with Eq.(6.25) and assuming $A \ll A_0$, one finds that the effective chemical potential depends on the difference in residue entropies, $S^*(A_0 - A - 1, \bar{Z}) - S^*(A_0 - A, Z_0 - Z)$. Using an expansion for small changes in the nuclear entropy from ref. [43], this difference can be expressed in terms of the difference of binding energies,

$$\begin{aligned}
&S^*(A_0 - A - 1, \bar{Z}) - S^*(A_0 - A, Z_0 - Z) \\
&= -(B_{A_0 - A, Z_0 - Z} - B_{A_0 - A - 1, Z_0 - Z})/T \\
&\quad -(B_{AZ} - B_{A+1Z})/T + f^*/T
\end{aligned} \tag{6.26}$$

plus a term depending on the free excitation energy per nucleon, $f^* = E^*/A_0 - TS/A_0$. This difference in binding energies is further related to the neutron separation energy:

$$s_n(A_0 - A, Z_0 - Z) = B_{A_0 - A, Z_0 - Z} - B_{A_0 - A - 1, Z_0 - Z}. \tag{6.27}$$

One consequently obtains the following expression for the effective chemical potential:

$$\mu_n = -s_n(A_0 - A, Z_0 - Z) + f^*. \tag{6.28}$$

where the reduced free excitation energy has been approximated by its low energy limit,

$$f^* = -\frac{T^2}{\varepsilon_0}, \quad \varepsilon_0 = 8MeV. \quad (6.29)$$

For the decay $^{112}\text{Sn} \rightarrow ^{12}\text{C} + \text{X}$, the chemical potential at $T = 0$, i.e., $-s_n(A_0 - A, Z_0 - Z)$, is plotted as the stars in Fig.(6.5); the binding energies for these calculations were calculated using the liquid-drop parametrization in ref.[103]. The reduced free energy f^* gives a reasonable estimate for the trend with excitation energy. The dot-dashed line in Fig.(6.5) gives the chemical potential predicted from Eq. (6.28) for $E_0^*/A = 3 \text{ MeV}$ ($T = 4.58 \text{ MeV}$). The predicted trend is close to that predicted by the SMM model (solid circles and squares) but has a somewhat stronger dependence on $N - Z$.

In general, the slope of the effective neutron chemical potential is getting slightly flatter as the excitation energy or temperature increases. If we consider that the system undergoes a multiple fragment decay at higher temperatures, it is clear that approximating the entropy of the remaining system by that of a residue of comparable mass becomes rather inaccurate. The constraints imposed on the total system by the isospin asymmetry of one observed fragment should, in that case, be less significant. While there is a mass dependence to the effective chemical potential that is inconsistent with the grand canonical approach, it is useful to note that the mass dependence of the chemical potential (for these systems of more than 100 nucleons) is small if one is mainly concerned with nuclei near the valley of stability. If one cancels the chemical potential effects by constructing double ratios like that of the Albergo formula, the consequence of such finite size effects becomes negligible indeed.

6.2 Empirically Improved Model

6.2.1 Ground State Energies

Since the predicted primary yields of excited fragments is exponentially related to their binding energies, it is natural to assume that accurate values for the ground state masses for the observed fragments are needed. Recently, however, it has been observed that the masses of nuclei far from the valley of stability can also influence the predicted observables through their influence on the primary distribution[26]. The conclusion of such studies was that that Liquid Drop Mass (LDM) parametrizations used in most current SMM codes [103] are insufficiently accurate for the prediction of isotopic distributions.

To address this problem, we use a more accurate description of the masses. In particular, we use the recommended binding energies values from ref. [104] when available. Although the sampling of the most probable decay modes discards too exotic fragments, which would contribute with a vanishing statistical weight, it is still necessary to know some binding energies whose empirical values are not reported in the literature. Therefore, Souza, Tsang and Danielewicz [105] modify the parametrization of the LDM formula given in ref. [106]:

$$\begin{aligned} B_{AZ}^{LDM} &= (a_v A - a_s A^{2/3}) \left[1 - k \left(\frac{A - 2Z}{A} \right)^2 \right] \\ &- a_c \frac{Z^2}{A^{1/3}} + \delta_{AZ} A^{-1/2} + a_d \frac{Z^2}{A}, \end{aligned} \tag{6.30}$$

where a_v and a_s are the coefficients of volume and surface contributions to the binding energy and k is the factor of asymmetry modification. The coefficient δ_{AZ} corresponds

to the usual pairing term:

$$\delta_{AZ} = \begin{cases} +\delta_{pairing}, & N \text{ and } Z \text{ even} \\ 0, & A \text{ odd} \\ -\delta_{pairing}, & N \text{ and } Z \text{ odd} \end{cases} \quad (6.31)$$

where N and Z are the numbers of neutrons and protons, respectively. This formula is as simple as the others adopted in similar statistical multifragmentation models. However, it is superior to those since it includes corrections to the surface term due to asymmetry, which are usually neglected. Furthermore, the extra Coulomb term $a_d Z^2/A$, also disregarded in the models, takes into account corrections of the Coulomb energy associated with the diffuseness of the nuclear surface.

Although the parameter set given in ref. [106] predicts binding energies which are in very good agreement with the recommended values of ref. [104], we used those data to improve the fit, considering all nuclei in the table with $A \geq 5$. The parameters corresponding to the best fit of the experimental data are listed in table 6.1. To illustrate the improvement in the model, the top panel of Figure 6.6 shows the difference between the calculated binding energies from the parametrization of the LDM of ref. [103] used in most current SMM codes and the empirical values (labelled as A). The middle panel shows the corresponding comparison between the calculated binding energies using Eq. (6.30) with the improved parameters and the empirical values (labelled as B). One should note that the *total* binding energies are used, rather than the binding energy per nucleon. This improved agreement suggests that the predictions for unmeasured masses will also be improved.

Despite the improvement in the overall mass predictions, there can be discontinuity between the extrapolated (dashed lines) and empirical values (symbols) as illustrated in Fig. 6.7. To improve the matching between the binding energies of the known masses and the ones predicted by our mass formula, we compute average

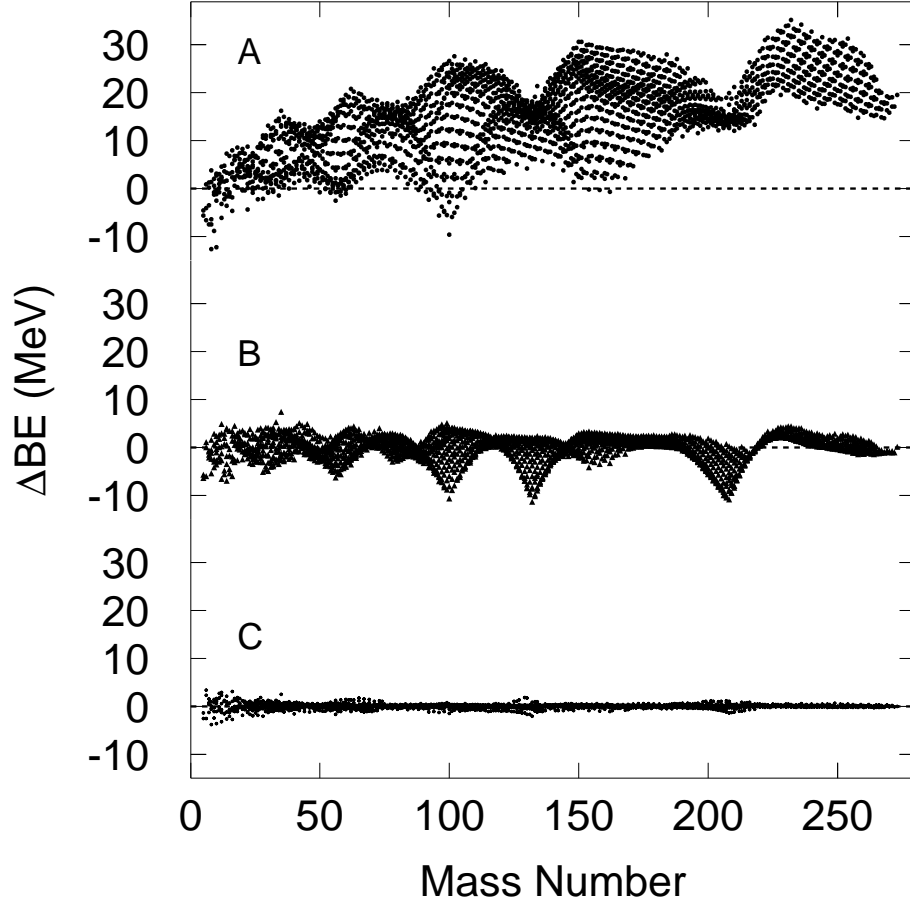


Figure 6.6: Difference between the *total* binding energies predicted by the LDM and those recommended in ref. [104]. Plot A corresponds to the parameter set adopted in standard SMM [103], whereas Plot B is obtained using the parameters presented in this work.

Table 6.1: Best fit parameters to the LDM formula of ref. [105]-[106]. All the values are given in MeV, except for k which is unitless.

a_v	a_s	k	a_c	$\delta_{pairing}$	a_d
15.6658	18.9952	1.77441	0.720531	10.8567	1.74859

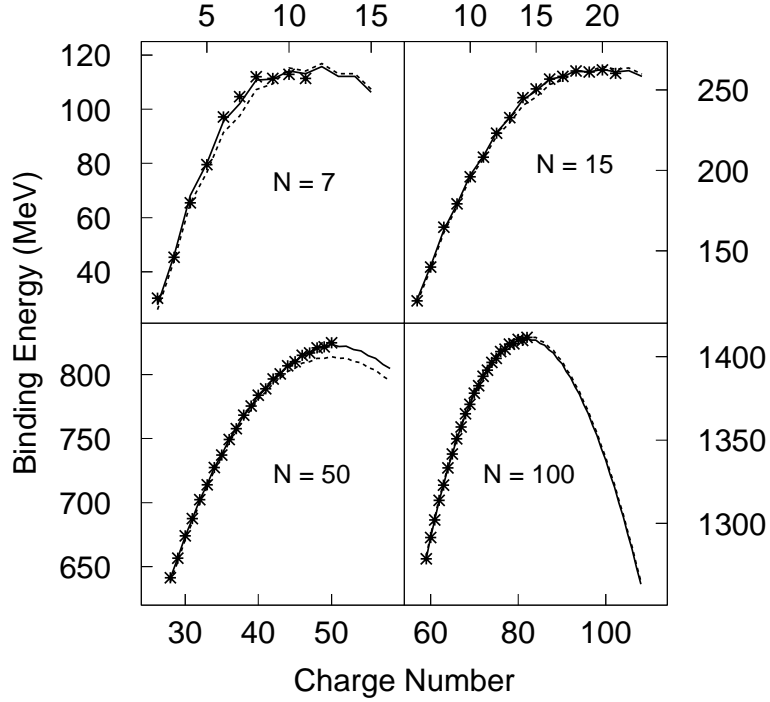


Figure 6.7: Total binding energies for different nuclei. The full lines correspond to the corrected LDM formula, whereas the symbols represent the experimental data of ref. [104]. The dashed lines correspond to the predictions given by Eq. (6.30). For details see text.

shifts of the LDM formula from the empirical values and use these shifts to correct the values in Eq. (6.30). For an isotone that has a lower charge than its isotonic partners in the compilation of ref. [104] we use the three lightest isotones with the same value of N in the compilation to compute the shift. Similarly for an isotone that has a higher charge than its isotonic partners in the compilation of ref. [104] we use the three heaviest isotones with the same value of N in the compilation to compute the shift. This shift is then subtracted from the prediction of the LDM formula:

$$B_{AZ}^{extrap} = B_{AZ}^{LDM} - \Delta_N, \quad (6.32)$$

where

$$\Delta_N = \frac{1}{3} \sum_{i=1}^3 (B_{A_i, Z_i}^{LDM} - B_{A_i, Z_i}^{Audi}), \quad (6.33)$$

B_{A_i, Z_i}^{Audi} is the corresponding value from the compilation of ref. [104]. Two shifts are therefore computed for each value of N . This procedure minimizes the systematic deviations from the recommended values, as is illustrated for four cases in fig. 6.7 with the solid lines denoting the corrected values. Although we use B_{AZ}^{Audi} whenever it is available, the solid lines in this figure also include the corrections to the LDM in the mass region where empirical values are known. In this case, the corrected values are calculated through an expression similar to Eqs. (6.32)-(6.33), but one takes 2 neighbors to the left and to the right to calculate the average shift. For comparison, we also show in this picture the uncorrected values of the LDM formula, which are represented by the dashed lines. The overall behavior of the corrections shows that the discontinuity between the empirical and extrapolated values is removed. The difference of these values and the empirical values is also shown in the bottom panel (labelled as C) of Fig. 6.6. However, we stress the fact that we only use these corrected values if the empirical information is not available.

6.2.2 Internal free energy

In this work, we have modified the SMM so as to allow accurate predictions of isotopic properties, but have limited the extent of these modifications in an effort to retain as many of the predictions of the original theory. In particular, we have retained the high temperature properties of the fragment free energies, $F_{A,Z}^*$, which are parameterized here and in the original SMM as:

$$F_{A,Z}^*(T) = A^{2/3} \beta_0 \left[\left(\frac{T_C^2 - T^2}{T_C^2 + T^2} \right)^{5/4} - 1 \right] - A \frac{T^2}{\epsilon_0}, \quad (6.34)$$

where $\beta_0 = 18.0$ MeV, $\epsilon_0 = 16.0$ MeV, and $T_C = 18.0$ MeV. This expression holds only for temperatures smaller than T_C . For $T < T_C$, this expression has the some of the expected qualitative behavior of a Fermi liquid: it depends quadratically on T at

low temperatures, and falls to zero at the critical temperature T_C where the surface tension vanishes. We do not calculate decays at higher temperatures than that and therefore do not concern ourselves here with the properties of the system at $T \geq T_C$. For $3 \text{ MeV} < T < 10 \text{ MeV}$, where multifragmentation is important, however, other expressions for $F_{A,Z}^*(T)$ with very different thermal properties are conceivable and should be explored.

Instead we turn our attention to the fact that most fragments at $T > 2 \text{ MeV}$ are particle unstable and will sequentially decay after freezeout. This decay is sensitive to nuclear structure properties of the excited fragments such as their nuclear levels, binding energies, spins, parities and decay branching ratios. The first three of these quantities also influence the free energies; this can be calculated via the fragment internal partition functions. There is a self-consistency requirement in the freeze-out approximation which dictates that the states from which these fragments decay after freezeout should be consistent with the Helmholtz free energies used in calculating the primary yields of the hot fragments at freeze-out.

In order to discuss this self-consistency requirement, we must consider the density of states $\rho_{states}(E)$ and its mathematical relationship with the Helmholtz free excitation energy $F^*(T)$:

$$e^{-F^*/T} = \int_0^\infty dE e^{-E/T} \rho_{states}(E), \quad (6.35)$$

where the integral is over the excitation energy E of the nucleus. Here we have, for simplicity, neglected the complications of a degenerate ground state. In the original papers on the SMM, the level densities corresponding to the SMM were not stipulated. We now consider what is required of the density of states to achieve the high temperature behavior for $F^*(T)$ given by Eq. (6.34). Then we will address the general issue of making the level densities consistent with empirical information and how that

impacts the free energies. Finally, we will discuss specific details of the incorporation of the empirical information into the level density expressions.

High temperature behavior

First we investigate what forms of level densities may be consistent with the free energies in Eq. (6.34). We note that the functional dependence of $F^*(T)$ used in Eq. (6.35) makes its analytical inversion difficult at high temperatures. It may be more reasonable to find a smooth real functional form for $\rho_{states}(E)$ that reproduces the numerical values for $F^*(T)$ at high temperatures than it would be to perform an inverse Laplace transformation of $F^*(T)$ in the complex plane. We note that a Taylor expansion of $F^*(T)$ up to 2-nd order in $1/T$ yields the Fermi gas expression:

$$\rho_{FG,states}(E) = \frac{1}{2} \frac{a_{SMM}^{1/4}}{\sqrt{2\pi} E^{3/4}} \exp\left(2\sqrt{a_{SMM}E}\right), \quad (6.36)$$

where a_{SMM} is the coefficient of the 2-nd order term of the expansion:

$$a_{SMM} = \frac{A}{\epsilon_0} + \frac{5}{2}\beta_0 \frac{A^{2/3}}{T_c^2}. \quad (6.37)$$

However, this expression is unsatisfactory at high temperatures, as is illustrated in Fig. 6.8 when the free energies obtained from Eq. (6.36) (dashed lines) are compared with the standard SMM free energies in Eq. (6.34) (solid lines). Instead, we take Eq. (6.36) as a starting point and obtain a useful analytic expression by multiplying $\rho_{state,FG}(E)$ by an *ad hoc* energy dependent term to obtain free energy values in numerical agreement with Eq. (6.34):

$$\rho_{SMM,states}(E) = \rho_{FG,state}(E) e^{-b_{SMM}(a_{SMM}E)^{3/2}}, \quad (6.38)$$

where b_{SMM} is given by:

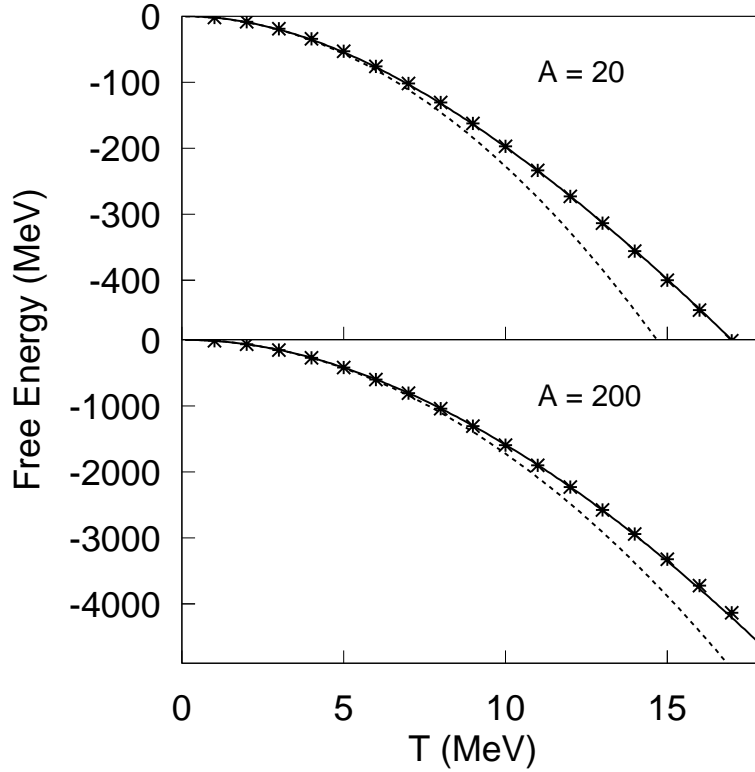


Figure 6.8: Internal free energies for $A = 20$ (upper panel) and $A = 200$ (lower panel). The standard SMM expression [Eq. (6.34)] is represented by the full line whereas the dashed lines stand for the results obtained with the Taylor expansion [Eq. (6.36)]. The Free energy calculated through the level density given by Eq. (6.38) is depicted by the symbols.

$$b_{SMM} = 0.07A^{-\tau}, \quad (6.39)$$

$$\tau = 1.82 \left(1 + \frac{A}{4500} \right). \quad (6.40)$$

The free energies obtained through Eqs. (6.35) and (6.38) are also displayed in Fig. 6.8 as symbols for two different mass regions. This simple parameterization is fairly accurate at temperatures in the range of interest, i.e. $T \leq 10$ MeV.

Empirical Level densities at low excitation energies for $Z \leq 15$

Several factors motivate the efforts to develop an accurate treatment for the level densities at low excitation energy for $Z \leq 15$. The first factor is that multifragmentation experimental data are available for lighter fragments in this mass range. The second is that empirical nuclear structure information[107] is also available for such light nuclei. A comparable treatment of the level density for the heavier fragments would be interesting, but necessary structure information is frequently incomplete or entirely missing. Fortunately, the absence of an accurate treatment for the secondary decay of the heavier nuclei does not negatively impact the calculation of the final yields of the lighter nuclei so one can proceed towards accurate predictions at the present time.

At lower excitation energies, it is customary to discuss the density of levels ρ_{levels} rather than the density of states because this definition is more useful experimentally when the spins of specific levels are not accurately known. Mathematically, the density of states is related to the densities of levels for individual spin values $\rho_{levels}(E, J)$ by:

$$\rho_{states}(E) = \sum_J (2J + 1) \rho_{levels}(E, J) \quad (6.41)$$

While the spacings between energy levels in a given nucleus generally decrease smoothly with excitation energy, one often as a practical matter decomposes the empirical level density $\rho_{emp,levels}(E, J)$ into two expressions that apply in two different approximate excitation energy domains: (1) one (labelled as $\rho_{D,levels}(E, J)$) containing discrete well separated states at low excitation energies and (2) another (labelled as $\rho_{C,levels}(E, J)$) containing a continuum of overlapping states at higher excitation energies. For $Z \leq 15$, empirical level information[107] is applied as much as possible to the low-lying discrete

level density, wherever the experimental level scheme seems complete,

$$\rho_{D,levels}(E, J) = \sum_i \delta(E_i - E), \quad (6.42)$$

where the summation runs over the excitation energies E_i corresponding to states of spin J . Examples for ^{20}Ne and ^{31}P are shown as bars in Fig. 6.9. For higher excitation energies, a good approximation to the continuum level density has been obtained by ref. [108] by combining Fermi liquid theory, a simple spin dependence and experimental knowledge. The relevant expressions (shown as dashed lines in Fig. 6.9) for $E > E_c$ are [109],

$$\rho_{C,levels}(E, J) = \rho_C(E) f(J, \sigma) \quad (6.43)$$

where

$$\rho_C(E) = \frac{\exp[2\sqrt{a(E - E_0)}]}{12\sqrt{2}a^{1/4}(E - E_0)^{5/4}\sigma}, \quad (6.44)$$

$$f(J, \sigma) = \frac{(2J + 1) \exp[-(J + 1/2)^2/2\sigma^2]}{2\sigma^2}, \quad (6.45)$$

$$\sigma^2 = 0.0888\sqrt{a(E - E_0)}A^{2/3}, \quad (6.46)$$

and the level density parameter $a = A/8$. E^* , J , A and Z are the excitation energy, spin, mass and charge numbers of the fragment. E_0 is determined by matching the total high-lying level density to the total low-lying level density as follows,

$$\int_{E_0}^{E_c} dE \int dJ \rho_{C,levels}(E, J) = \int_0^{E_c} dE \int dJ \rho_{D,levels}(E, J). \quad (6.47)$$

The comparison in Eq. (6.47) is between the total level densities summed over spin. This is done primarily to reduce the sensitivity in the matching to uncertainties in the spin assignments for some of the discrete states. By adjusting the parameter

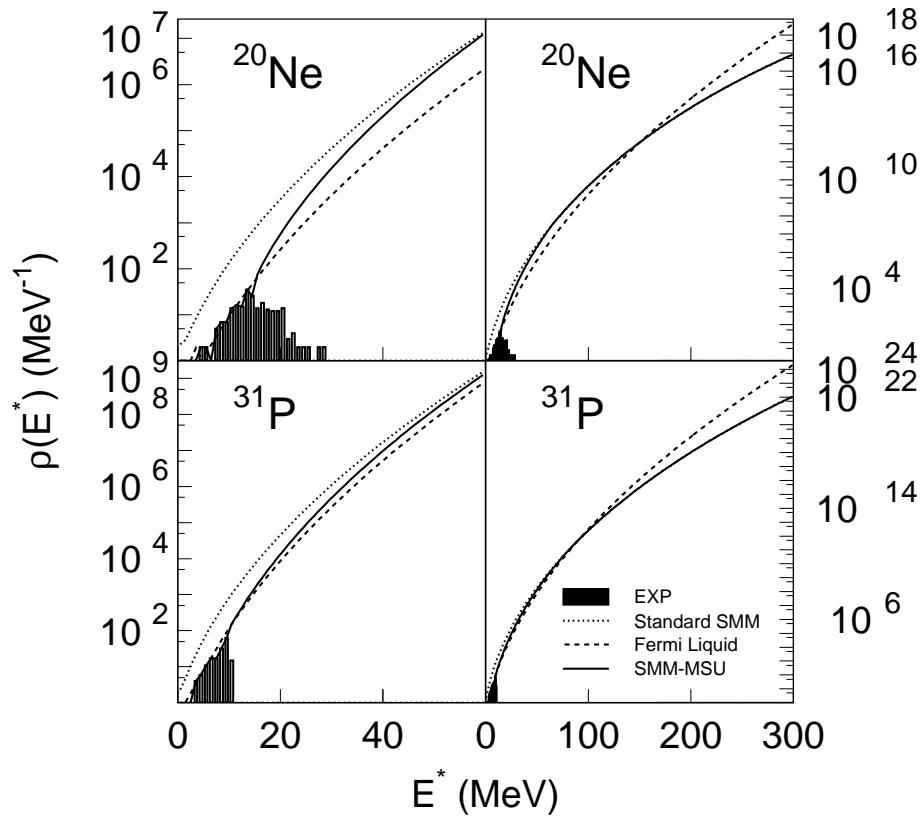


Figure 6.9: Level densities as a function of excitation energy for ^{20}Ne and ^{31}P . Two energy ranges are plotted to show the behaviors of level densities at both low and high energy ends. The density of experimentally known levels is shown as bars in the low energy region. The dashed lines are the extrapolations of the empirical values according to Eq. 6.43. The dotted lines are the level density (Eq. 6.38) parametrized from the standard SMM. The solid lines are the level density adopted in this work (Eqs. 6.49-6.52).

E_0 , the total level density for continuum states can be made to connect smoothly to the total level density for low-lying states at $E < E_c$ and $Z < 12$.

For the case of $Z \geq 12$, low-lying states are not well identified experimentally and a continuum approximation to the discrete level density [109] was used by modifying the empirical interpolation formula of Ref. [108] to include a spin dependence:

$$\begin{aligned} \rho_{D,levels}(E, J) &= \frac{1}{T_1} \exp[(E - E_1)/T_1] \\ &\times \frac{(2J + 1) \exp[-(J + 1/2)^2/2\sigma_0^2]}{\sum_i (2J_i + 1) \exp[-(J_i + 1/2)^2/2\sigma_{0i}^2]}, \end{aligned} \quad (6.48)$$

for $E \leq E_c$, where the spin cutoff parameter $\sigma_0^2 = 0.0888\sqrt{a(E_c - E_0)}A^{2/3}$. For $Z \geq 12$, the values of $E_c = E_c(A, Z)$ were taken from Ref. [108] as well as parameters $T_1 = T_1(A, Z)$ and $E_1 = E_1(A, Z)$, and in this case, the approximate level density (Eq.6.48) was used to complement the empirical level density for low-lying states. The connection point E_c to high-lying states, for $Z < 12$, was chosen to be the maximum excitation energy up to which the information concerning the number and locations of discrete states appears to be complete so that the empirical level density (Eq. 6.42) was solely applied for low-lying states.

Matching low and high excitation energy behavior

Now, we turn to the requirement of self-consistency between the expression for $F^*(T)$ and the level density relevant to secondary decay. In general, secondary decay is more sensitive to nuclear structure quantities such as the excitation energies, spins, etc. as the system decays towards the ground state. At low excitation energies, it is more accurate using empirical level densities in place of the expression in Eq. (6.34), which does not even depend on Z . As the excitation energy is increased, however, the continuum level density becomes very large, little sensitivity to nuclear structure

details remains and a simpler expression like Eq. (6.34) may suffice.

In the following, we take $\rho_{SMM,states}(E)$ to be the behavior of the state density at high energies and match it to the continuum part of the empirical state densities at lower excitation energies. The net result is a set of level density and state density expressions that span the range of excitation energies relevant to multifragmentation phenomena. For $E^* < E_c$, one uses the expression for the discrete, low-lying state density,

$$\rho(E, J) = \rho_D(E^*, J). \quad (6.49)$$

For $E_c < E < E_c + \Delta E$, the new level density is an interpolation involving the continuum expression relevant at low excitation energies between $\rho_C,states$ and $\rho_{SMM,states}$,

$$\begin{aligned} \rho(E^*, J) &= \rho_C(E^*, J) \left(1 - \frac{E^* - E_c}{\Delta E}\right) \\ &\quad + \rho_{SMM}(E^*, J) \frac{E^* - E_c}{\Delta E}, \end{aligned} \quad (6.50)$$

where $\Delta E = 2.5A$ MeV provides a smooth transition from ρ_C to ρ_{SMM} . The SMM level density (shown as dotted lines in Fig. 6.9) can be incorporated with a similar spin dependence as in Eq. (6.43),

$$\rho_{SMM}(E^*, J) = \rho_{SMM}(E^*) f(J, \sigma). \quad (6.51)$$

For $E^* > E_c + \Delta E$, the new density simply becomes the same as the SMM level density ρ_{SMM} ,

$$\rho(E^*, J) = \rho_{SMM}(E^*, J). \quad (6.52)$$

In Fig. 6.9, the empirically modified level density described in Eqs. (6.49-6.52) is plotted as solid lines for ^{20}Ne and ^{31}P .

This procedure uses the empirical information for excitation energies $E < E_c$, a linear interpolation for $E_c < E < E_c + \Delta E$, and $\rho_{SMM,states}(E)$ at higher values of the excitation energy. The level density ρ_C in Eq. (6.43) can be used as an proper extension to the low-lying level density ρ_D in Eqs. (6.42) and (6.48) and a bridge for matching to the SMM level density at continuum. Such a matching procedure provides a state density that is empirically based at low excitation energies but become progressively more uncertain as the excitation energy is increased above $E^* \approx E_c$. This uncertainty in the thermal properties of nuclei at such high excitation energies is not a question of finding an appropriate interpolation, but is, in fact, a fundamental issue that must be resolved by comparisons to experimental data. For example, other expressions can be proposed for the level density at $E^* > E_c$ and comparisons of experimental data to SMM predictions of sensitive multifragment observables can be used to constrain the level densities at high excitation energies.

Free energies $F^*(T)$, which reflect contributions from the discrete excited states are obtained by inserting this parametrization for $\rho_{states}(E)$ into Eq. (6.35), and performing a numerical integration. To facilitate the insertion of these free energies into the SMM algorithm, we parameterize $F^*(T)$ by:

$$F^*(T) = F_{std}^*(T) \left(1 - \frac{1}{1 + \exp[(T - T_0)/\Delta T]} \right), \quad (6.53)$$

where $F_{std}^*(T)$ stands for the standard SMM internal free energy, Eq. (6.34). The parameters T_0 and ΔT are adjusted to reproduce the numerical calculation of $F^*(T)$ provided by Eqs. (6.35) and (6.49)-(6.52) for $T \leq 10$ MeV. In these fits, a value for $\Delta T = 1.0$ MeV is used for most nuclei (The exceptions are mainly very light nuclei.), while T_0 is varied freely. The accuracy of the fit is illustrated in Fig. 6.10, which compares the exact values of $F^*(T)$ (symbols) to the approximation given by Eq. (6.53) (solid line), for a ^{20}Ne nucleus. The dashed line in this figure represents the free

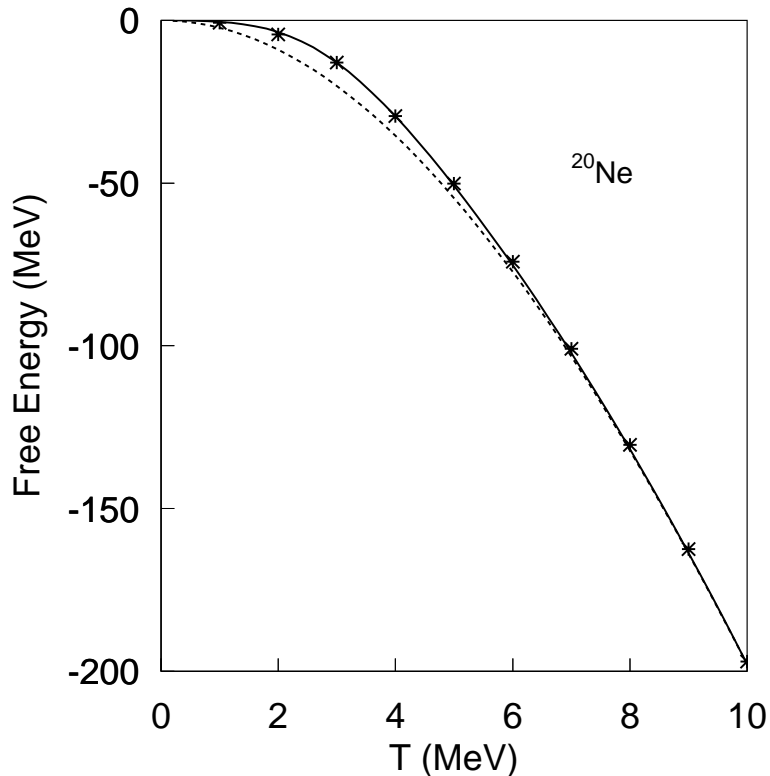


Figure 6.10: Comparison between $F^*(E)$ calculated through Eqs. (6.35) and (6.49)-(6.52), symbols, and the approximation given by Eq. (6.53), full line. To illustrate the influence of quantum effects at low temperatures, the dashed line represents the free energy used in standard SMM calculations Eq. (6.34). For details see text.

energy used in standard SMM calculations in which the experimental discrete levels are neglected. The matching procedure allows the discrete excited states to dominate the low temperature behavior, while the high temperature behavior remains similar to that of the original SMM consistent with the goals stated above.

Because the empirical level densities vary from nucleus to nucleus, the parameters T_0 and ΔT used to obtain $F^*(T)$ must be fitted for each nucleus. Fits of the same quality as that for ^{20}Ne are achieved for all the light nuclei ($Z \leq 15$). These fitted values of T_0 are shown as symbols in Fig. 6.11. We do not perform such fits for $Z > 15$, because the level density information there is less complete. We nevertheless extrapolate the main trend of the parameters to heavy nuclei, for which detailed experimental information on discrete excited states is not available in order to prevent

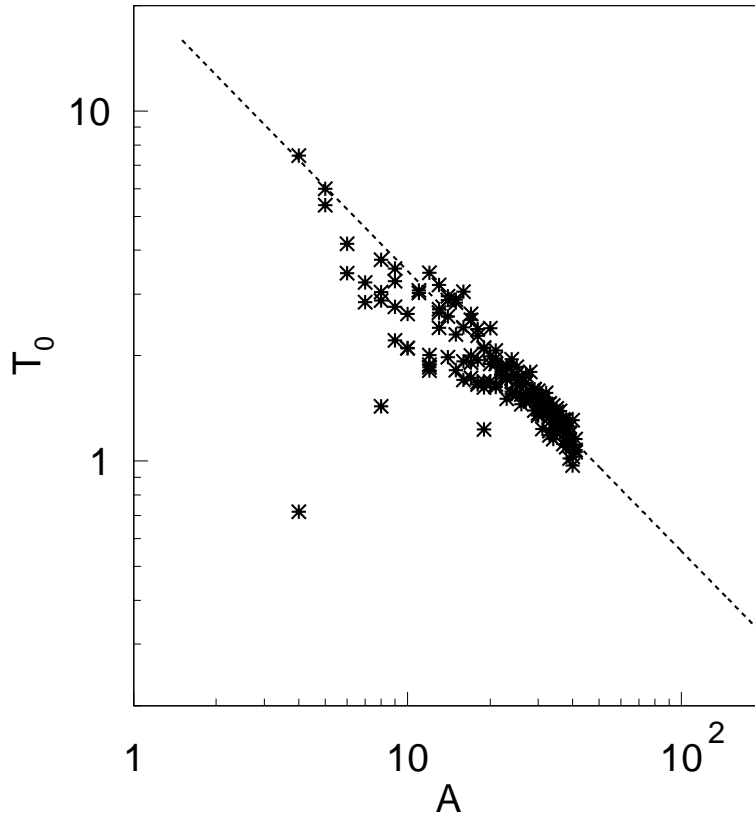


Figure 6.11: Best fit values of T_0 for different nuclei (symbols). The dashed line corresponding to Eq. 6.54 is used for $Z > 15$.

spurious discontinuities in the equilibrium primary yields. As mentioned above, there seems to be a very weak dependence on ΔT and, therefore, we assume $\Delta T = 1.0$ MeV for $Z > 15$. In spite of the uncertainty in extrapolating T_0 , the dashed line in Fig. 6.11 shows that

$$T_0 = 22.0A^{-0.8} \text{ MeV} \quad (Z > 15) \quad (6.54)$$

describes the trend for the lower masses and we adopted it at for the higher masses as well.

6.2.3 Empirical Sequential Decay

The typical time scale for a multifragmentation process is less than about 100 fm/c. The final production of isotopes is modified greatly by secondary decay from the hot

primary fragments at a much longer time scale. However, only the contaminated final yields can be directly measured in this type of heavy ion reactions. Therefore, an accurate secondary decay procedure is indispensable to assess the contributions from secondary decay and deduce the information of the primary hot system from experimental data.

An empirical sequential decay procedure was developed to decay the hot fragments produced in the primary SMM code. The strategy is to include as much experimental information as possible for a precise calculation of secondary decay and to make secondary decay and primary breakup procedures intrinsically consistent, such as using the same level density and empirical information. Basically the sequential decay procedure consists of two parts. One is to decay particles with $Z \leq 15$ through a large empirical table including all the states of nuclei with known information such as binding energy, spin, isospin, parity and decay branching ratios. The other part is to use the Gemini code[110] for particles outside the empirical table (usually $Z > 15$).

Decay table for $Z \leq 15$

From the implementation of the level density (Eqs. (6.49-6.52)), we can construct a 'table' containing properly sampled levels associated with properties like spins, isospins, parities and so on. For excitation energies $E < E_c$ and $Z \leq 15$, each of the entries in the table corresponds to one of the tabulated empirical levels. When the information on the level is complete, it is used. For known levels with incomplete spectroscopic information, values for the spin, isospin, and parity were chosen randomly as follows: spins of 0-4 (1/2-9/2) were assumed with equal probability for even-A (odd-A) nuclei, parities were assumed to be odd or even with equal probability, and isospins were assumed to be the same as the isospin of the ground state. This simple assumption turns out to be sufficient since in effect most of spectroscopic

information is known for these low-lying states.

For unknown low-lying states and high-lying states, the levels were sampled according to the sophisticated level density algorithm discussed in the previous section at discrete excitation energy intervals of 1 MeV for $E^* < 15$ MeV, 2 MeV for $15 < E^* < 30$ MeV, and 3 MeV for $E^* > 30$ MeV in order to reduce the computer memory requirements. The results of these calculations do not appear to be sensitive to these binning widths. A cutoff energy of $E_{cutoff}^*/A = 5$ MeV was introduced corresponding to a mean lifetime of the continuum states at the cutoff energy about 125 fm/c. For simplicity, parities of these states were chosen to be positive and negative with equal probability and isospins were taken to be equal to the isospin of the ground state of the same nucleus.

Sequential decay algorithm

Before sequential decay starts, hot fragments from primary breakup need to be populated over the sampled levels in the prepared table according to the temperature. For the i th level of a given nucleus (A,Z) with its energy E_i^* and spin J_i , the initial population is,

$$Y_i = Y_0(A, Z) \frac{(2J_i + 1) \exp(-E_i^*/T) \rho(E_i^*, J_i)}{\sum_i (2J_i + 1) \exp(-E_i^*/T) \rho(E_i^*, J_i)} \quad (6.55)$$

where Y_0 is the primary yield of nucleus (A,Z) and T is the temperature associated with the intrinsic excitation of the fragmenting system at breakup.

Finally all the fragments will decay to their final states from top to bottom throughout the table. Eight decay branches of n, 2n, p, 2p, d, t, 3He and alpha were included for particle unstable decays of nuclei with $Z \leq 15$. The decays via gamma rays were taken into account for calculations of the final particle stable yields. If known, tabulated branching ratios were used to describe the decay of particle unstable states.

Where such information was not available, the branching ratios were calculated from the Hauser-Feshbach formula[23],

$$\frac{\Gamma_c}{\Gamma} = \frac{G_c}{\sum_d G_d} \quad (6.56)$$

where

$$G_d = \langle I_d I_e I_{d3} I_{e3} | I_p I_{p3} \rangle^2 \times \sum_{J=|J_d-J_e|}^{|J_d+J_e|} \sum_{l=|J_p-J|}^{|J_p+J|} \frac{1 + \pi_p \pi_d \pi_e (-1)^l}{2} T_l(E) \quad (6.57)$$

for a given decay channel d (or a given state of the daughter fragment). J_p , J_d , and J_e are the spins of the parent, daughter and emitted nuclei; J and l are the spin and orbital angular momentum of the decay channel; $T_l(E)$ is the transmission coefficient for the l th partial wave. The factor $[1 + \pi_p \pi_d \pi_e (-1)^l]/2$ enforces parity conservation and depends on the parities $\pi = \pm 1$ of the parent, daughter and emitted nuclei. The Clebsch-Gordon coefficient involving I_p , I_d , and I_e , the isospins of the parent, daughter and emitted nuclei, likewise allows one to take isospin conservation into account.

For decays from empirical discrete states and $l \leq 20$, the transmission coefficients were interpolated from a set of calculated optical model transmission coefficients; otherwise a parameterization described in Ref. [109] was applied.

6.3 Model Predictions and Comparisons

6.3.1 Caloric Curve

Before presenting predictions for isotope distributions and other observables for which the present theoretical developments were undertaken, we examine predictions of the

present model for the caloric curve and the primary fragment multiplicities, both of which displayed features in prior SMM calculations that are characteristic of low density phase transition. For example, SMM calculations predict an enhanced heat capacity for multifragmentating systems reflecting the latent heat for transforming nuclear fragments (Fermi liquid) into nucleonic gas. Fig. 6.12 shows the caloric curve, i.e. the dependence of the mean fragmentation temperature $\langle T_m \rangle$ on excitation energy, for a system with $A_0=168$ and $Z_0=75$. In both panels, the dotted lines indicate the relationships predicted by the original SMM, the solid lines denote the corresponding predictions of the SMM with all the modifications discussed in this paper and the dashed lines present the results provided by an SMM calculation that uses the new binding energies of Eqs. (6.30-6.33) and the old parameterization of ref. [36] for the Helmholtz free energies. These latter calculations allow one to assess the impact of the changes in the binding energies and free energies independently.

The two panels provide the caloric curves corresponding to two different constraints on the density. In the lower panel, a multiplicity-dependent breakup density [36] is assumed, corresponding to a fixed interfragment spacing at breakup; this leads to a pronounced plateau in the caloric curve for all three calculations. By taking into account kinetic motion and Coulomb interaction, we have calculated the pressure using the relationship

$$P = \frac{M \cdot T}{V_f} + \frac{Z_0^2 e^2}{5RV}, \quad (6.58)$$

where P is the pressure, M is the total multiplicity, V_f is the free breakup volume and V is the total volume. The pressure corresponding to these multiplicity-dependent breakup densities is plotted in the lower panel of Fig. 6.13. The corresponding primary fragment multiplicities are shown in the lower panel of Fig. 6.14. Consistent with the conclusions of ref. [111], we find the requirement of approximately constant

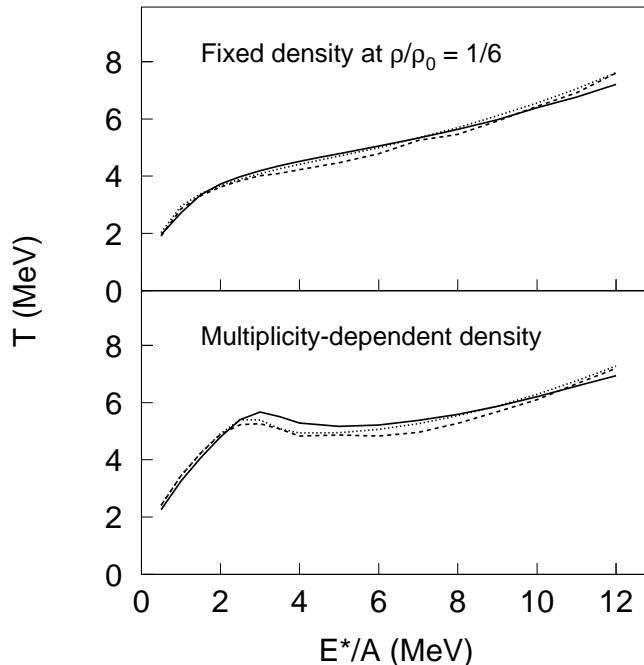


Figure 6.12: Caloric curves are shown for calculations of the system of $A=168$ and $Z=75$ at fixed breakup density and multiplicity-dependent density. The dotted lines are calculated from the standard SMM. The dashed lines are calculated as empirical binding energies are taken into account. The solid lines are obtained from the improved model with empirical modifications of both binding energies and free energies.

interfragment spacing corresponds to nearly constant breakup pressures. In the upper panel of Fig. 6.12, we show the corresponding caloric curves calculated at fixed breakup density $\rho/\rho_0 = 1/6$; these show a steeper dependence on excitation energy and the small maximum displayed in the lower panel at excitation energies of about 3 MeV disappears. The corresponding pressures at constant density, shown in the upper panel of Fig. 6.13, increase strongly with excitation energy.

These figures reveal the trends of three models to be similar. In general, the temperatures in the plateau region at $E^*/A = 3 - 8$ MeV in the lower panel are larger for the calculations using the improved free excitation energies. Calculations

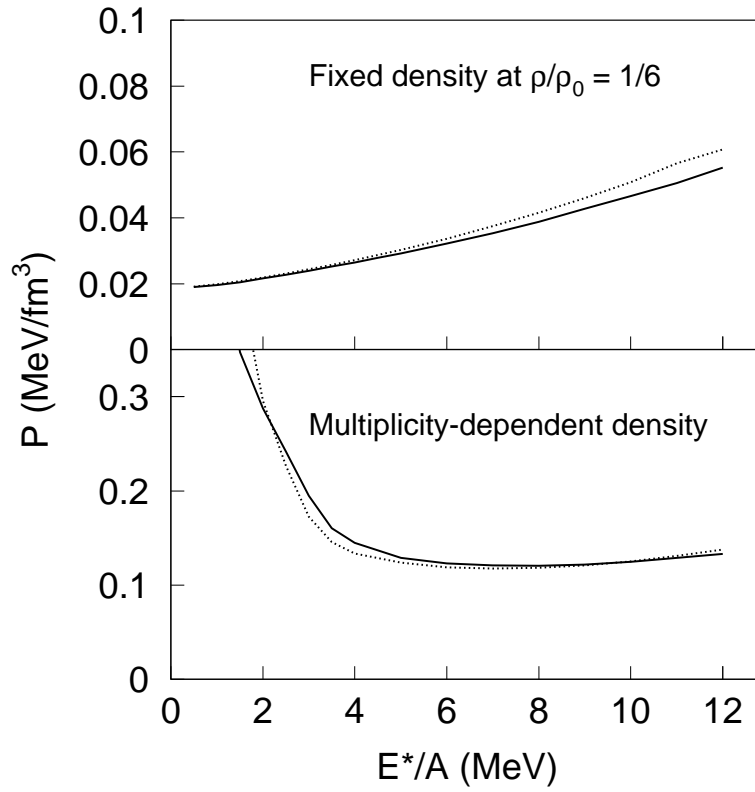


Figure 6.13: Pressure curves due to kinetic motion and Coulomb interaction (see Eq. 6.58) are plotted for the system of $A=168$ and $Z=75$ at fixed breakup density and multiplicity-dependent density. The dotted lines are calculated from the standard SMM while the improved SMM presents the solid lines.

with the improved free excitation energies require lower mean total excitation energies to achieve the same temperature than do calculations with the original free excitation energies. This lowers the latent heat for the transformation from excited fragments to nucleon gas and lowers the temperature at which the transition occurs. The influence of the improved binding energies on the caloric curve is less obvious, but this change seems to be largely responsible for the differences between the original SMM and the final improved model at $E^*/A = 6$ MeV.

Discussions of the nuclear caloric curve usually focus on the excitation energy dependence of the temperature and ignore the density dependence. To illustrate that the phase diagram is two dimensional and a density dependence does exist, we

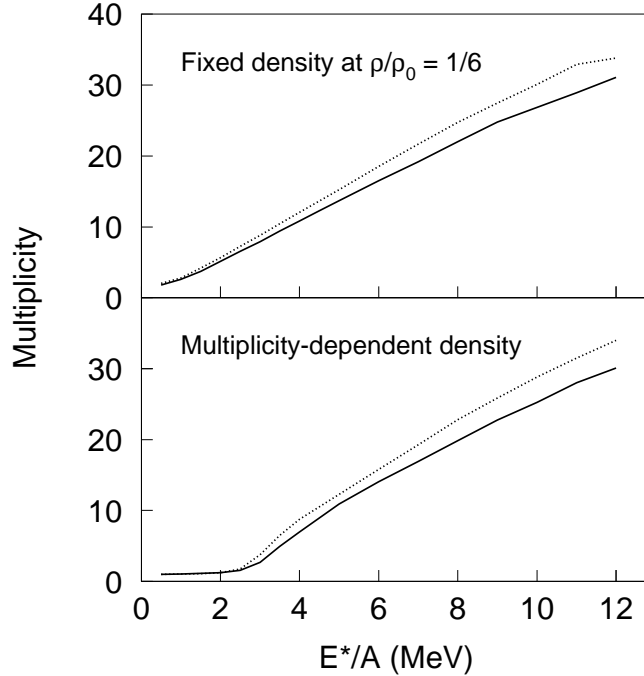


Figure 6.14: Average breakup multiplicities are shown for the system of $A=168$ and $Z=75$ at fixed breakup density and multiplicity-dependent density. The dotted lines are calculated from the standard SMM while the improved SMM presents the solid lines.

contrast in Fig. 6.15 the density dependence (upper scale) of the temperature at a fixed excitation energy of $E^*/A=6$ MeV (open squares) to the excitation energy dependence (lower scale) of the temperature at a fixed density of $\rho/\rho_0 = 1/6$ (solid circles). Both the excitation energy and the density dependences of the caloric curve are clearly important. It is therefore relevant to find and measure observables that constrain significantly the freezeout density.

6.3.2 Elemental and Mass Distributions

Calculations of the mass distribution (left panel) and charge distribution (right panel) for excited primary fragments are shown in Fig. 6.16 for a system with $A_0 = 186$

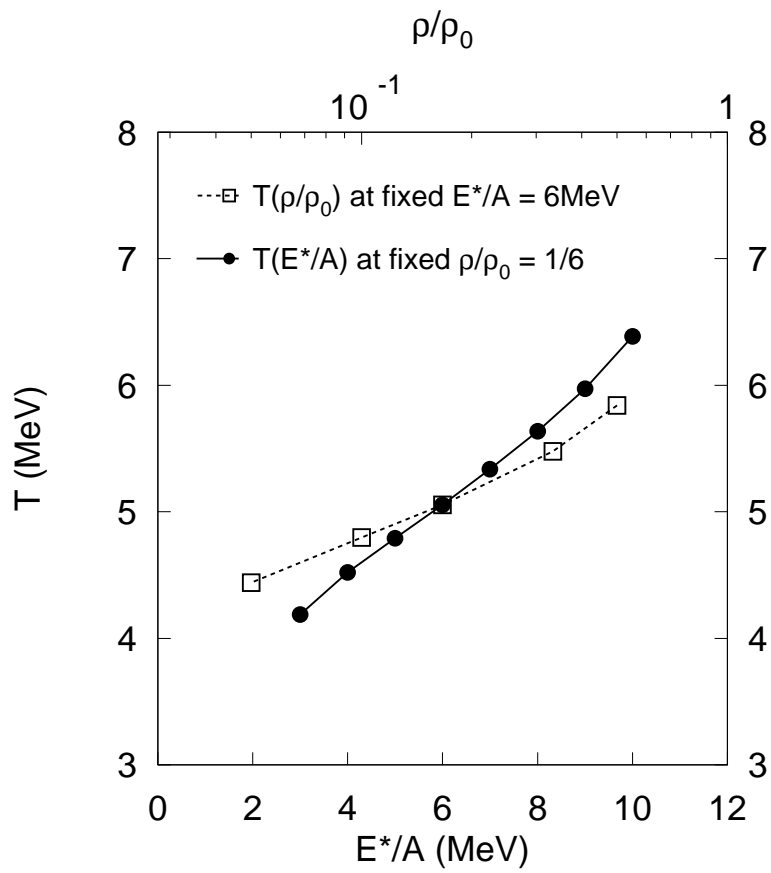


Figure 6.15: Dependences of temperature on excitation energy and breakup density are shown for the system of $A=168$ and $Z=75$. Calculations as function of excitation energy at fixed density of $1/6$ normal density are shown as solid circles. Calculations as function of density at fixed excitation energy are shown as open squares.

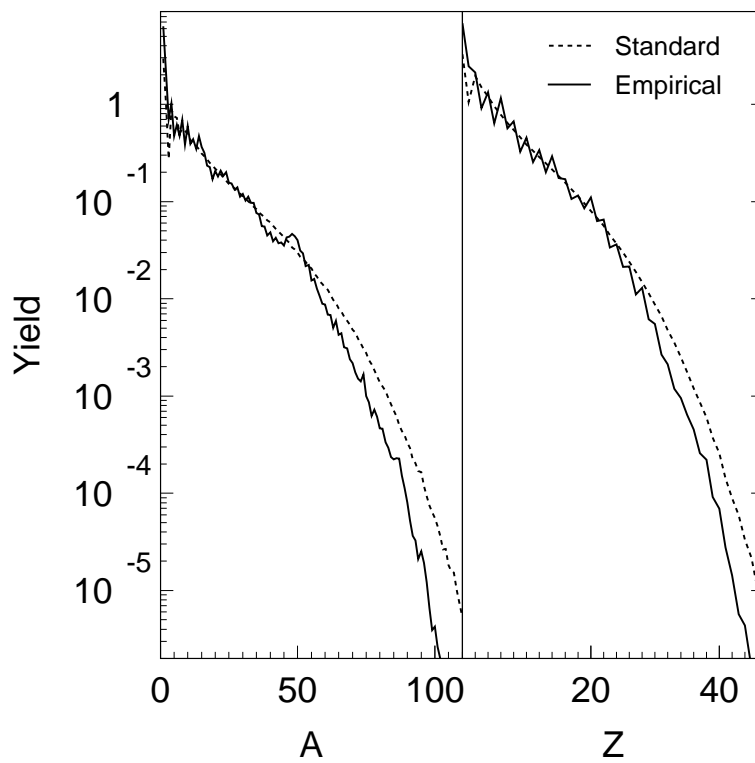


Figure 6.16: Mass and charge distributions are shown for the system of $A=186$ and $Z=75$. The dashed lines are the calculations from the standard SMM. The solid lines are calculated using the improved model.

and $Z_0 = 75$ at $E^*/A = 6$ MeV. The dashed lines denote the predictions using the original SMM and the solid lines denote the predictions using the improved SMM. The improved SMM calculations for the primary distributions fluctuate about the smooth distributions of the original SMM for $Z < 20$ and $A < 60$ and then fall below the original SMM at higher mass and charge. This trend of reduced yields at higher masses and charges is related to the tendency shown in Fig. 6.6 for the binding energies in the original SMM to consistently exceed the empirical values at $Z > 20$ and $A > 60$. Because conservation of mass and charge dictates that an increase in the yields of heavier fragments must be compensated by a decrease in the yields of the lighter ones, one does not see a comparable over-prediction of the primary yields of the lighter fragments by the original SMM. Besides the decrease in the yields of heavier fragments, there is a tendency of the improved SMM predictions for the lighter fragments to fluctuate about the smoother predictions for the original SMM. These fluctuations are related to the influence of shell and pairing effects on the ground state masses. These fluctuations have no significant impact on the final yields after secondary decay as discussed below.

The corresponding final mass (left panel) and charge (right panel) distributions after secondary decay are shown in Fig. 6.17. The solid lines denote the predictions using the improved SMM. To explore how significant are the fluctuations in the primary distributions due to the influence of shell and pairing effects on the ground state masses, we have decayed the primary fragments from the standard SMM via the same empirical secondary decay procedure discussed in Sect. 6.2.3. The final mass and charge distributions of the standard SMM are shown as the dashed lines in Fig. 6.17. Minimal discrepancies are seen in low mass and charge regime indicating that the secondary decay mechanism washes out the fluctuations in the primary distributions due to the influence of shell and pairing effects on the ground state masses.

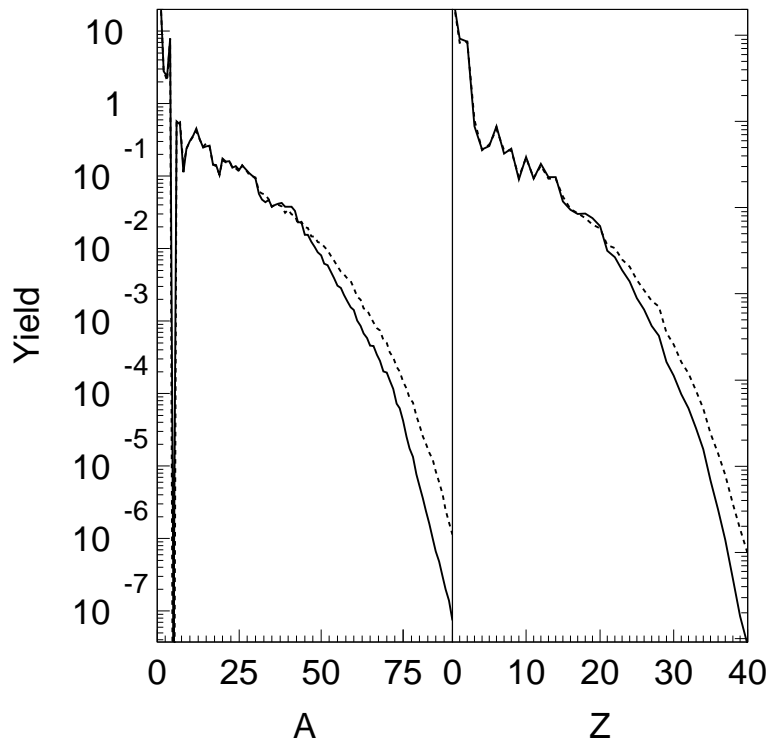


Figure 6.17: Final mass and charge distributions after applying the empirical secondary decay procedure discussed in Sect. 6.2.3. The dashed lines are calculated from the primary results of the standard SMM while the solid lines are from the improved model.

Meanwhile, significant differences on heavy fragments remain.

Secondary decay corrections to the standard SMM have been implemented by Botvina et al. in ref. [112], and the latter code has provided the bulk of the comparisons to experimental data prior to the development of the present model. In the Botvina code [112, 9], the secondary decay is calculated by the Weisskopf or Fermi breakup formalisms and the final ground state masses of nuclei with $A > 4$ are taken from a liquid drop mass formula. In the following, we compare the predictions of the present model for the final yields to the corresponding predictions of the Botvina code [112, 9] and to the experimental data for central $^{124}\text{Sn}+^{124}\text{Sn}$ collisions at $E/A=50$ MeV of refs. [41, 113]. The predictions of the Botvina code for the same system are shown by the dashed lines and the results from the present model by the solid lines

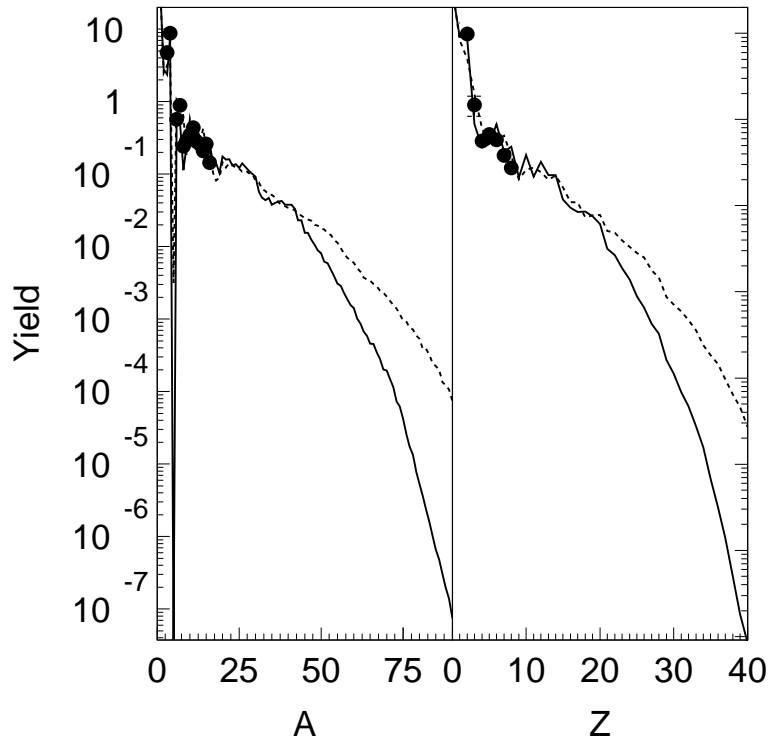


Figure 6.18: Final mass and charge distributions from the present model (solid lines) and the Botvina version (dashed lines) are shown. For reference, some measured data is plotted as solid circles.

in Fig. 6.18. For reference, the solid points show the corresponding experimental data. No special attempt has been made to optimize the parameters of the calculations to achieve the best representation of the data. Clearly the present model and the Botvina code differ significantly in their predictions for the elemental and mass distributions, especially for the heavy fragments, and more important comparisons of isotopic composition are shown in the next section.

6.3.3 Isotope Thermometry

In Fig. 6.19, the primary isotopic distributions for four elements emitted are shown for a system with $A_0=186$ and $Z_0=75$ at $E^*/A = 6$ MeV. The solid lines show predictions for the present model and the dashed lines show predictions of the Botvina code [112, 9]. The two calculations produce primary isotopic distributions that are

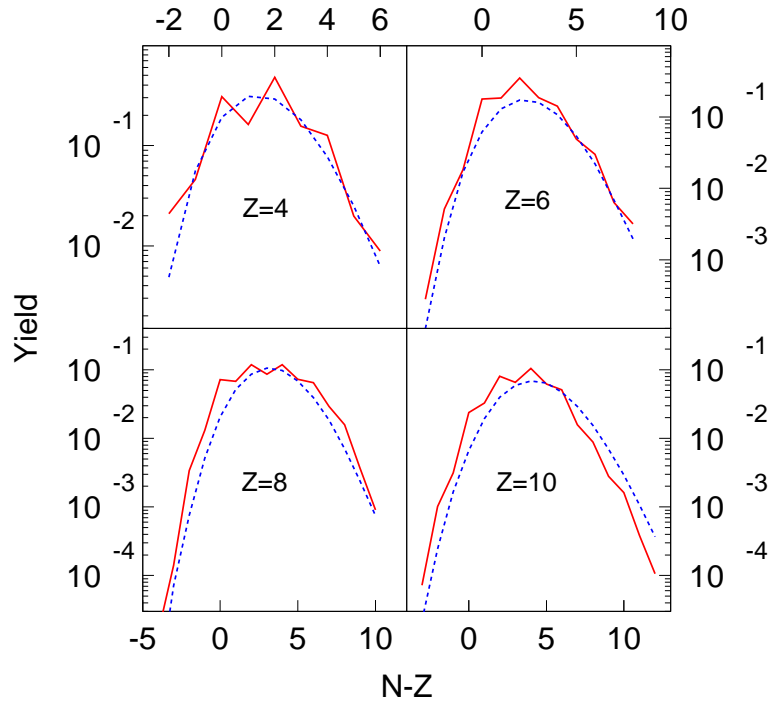


Figure 6.19: Primary isotopic distributions are shown for Be, C, O and Ne nuclei. The dashed lines correspond to the calculations of the Botvina code while the solid lines represent the results of the improved model.

considerably broader and more neutron rich than corresponding distributions after secondary decay shown in Fig. 6.20. The final distributions for the present model (solid histograms) are also broader and more neutron-rich than the corresponding distributions predicted by the Botvina code (dashed histograms); the major differences between the two calculations are found primarily in the predictions of the neutron rich isotopes, where the fall-off for the Botvina code is more precipitous than it is for the present code. The differences in the yields for isotopes on the proton rich side are not as large. The measured isotopic distributions denoted by the solid points are broader than those predicted by the Botvina code and more neutron rich than either calculation; however, the parameters of the two codes were not optimized to reproduce the data.

Isotope thermometers have been utilized as the primary probes for extracting the

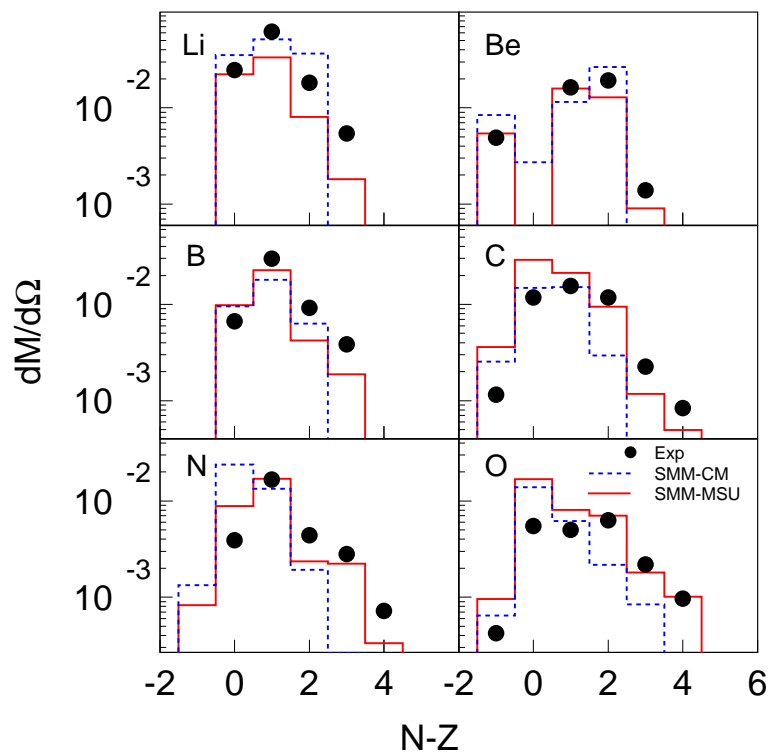


Figure 6.20: Isotopic distributions are shown for isotopes from Li to O. Experimental data is shown as the solid circles. The dashed lines denote the Botvina calculations and the solid lines are the final distributions after decaying the hot primary fragment via the empirical secondary decay procedure discussed in Sect. 6.2.3.

Table 6.2: List of isotopic thermometers with $\Delta B > 10$ MeV. The left column shows the IMF thermometers involving isotopes of $3 \leq Z \leq 8$. The right column lists the He thermometers involving the isotope pair of ${}^3,4\text{He}$.

IMF-thermometers	$\Delta B(\text{MeV})$	a	He-thermometers	$\Delta B(\text{MeV})$	a
${}^6,7\text{Li}/{}^{11,12}\text{C}$	11.472	5.898	${}^2,3\text{H}/{}^3,4\text{He}$	14.321	1.591
${}^7,8\text{Li}/{}^{11,12}\text{C}$	16.690	5.361	${}^6,7\text{Li}/{}^3,4\text{He}$	13.328	2.183
${}^8,9\text{Li}/{}^{11,12}\text{C}$	14.658	3.351	${}^7,8\text{Li}/{}^3,4\text{He}$	18.546	1.984
${}^9,10\text{Be}/{}^{11,12}\text{C}$	11.910	1.028	${}^8,9\text{Li}/{}^3,4\text{He}$	16.514	1.240
${}^{11,12}\text{B}/{}^{11,12}\text{C}$	15.352	3.000	${}^9,10\text{Be}/{}^3,4\text{He}$	13.766	0.380
${}^7,8\text{Li}/{}^{15,16}\text{O}$	13.631	2.773	${}^{11,12}\text{B}/{}^3,4\text{He}$	17.208	1.110
${}^{12,13}\text{B}/{}^{11,12}\text{C}$	13.844	5.278	${}^{12,13}\text{B}/{}^3,4\text{He}$	15.700	1.953
${}^{12,13}\text{C}/{}^{11,12}\text{C}$	13.776	7.917	${}^{12,13}\text{C}/{}^3,4\text{He}$	15.632	2.930
${}^8,9\text{Li}/{}^{15,16}\text{O}$	11.599	1.733	${}^{13,14}\text{C}/{}^3,4\text{He}$	12.401	0.726
${}^{13,14}\text{C}/{}^{11,12}\text{C}$	10.545	1.962	${}^{15,16}\text{N}/{}^3,4\text{He}$	18.089	3.578
${}^{15,16}\text{N}/{}^{11,12}\text{C}$	16.233	9.669	${}^{16,17}\text{O}/{}^3,4\text{He}$	16.434	8.536
${}^{11,12}\text{B}/{}^{15,16}\text{O}$	12.293	1.551	${}^{17,18}\text{O}/{}^3,4\text{He}$	12.534	0.236
${}^{16,17}\text{O}/{}^{11,12}\text{C}$	14.578	23.069			
${}^{12,13}\text{B}/{}^{15,16}\text{O}$	10.785	2.729			
${}^{12,13}\text{C}/{}^{15,16}\text{O}$	10.717	4.094			
${}^{17,18}\text{O}/{}^{11,12}\text{C}$	10.678	0.637			
${}^{15,16}\text{N}/{}^{15,16}\text{O}$	13.174	5.000			
${}^{16,17}\text{O}/{}^{15,16}\text{O}$	11.519	11.930			

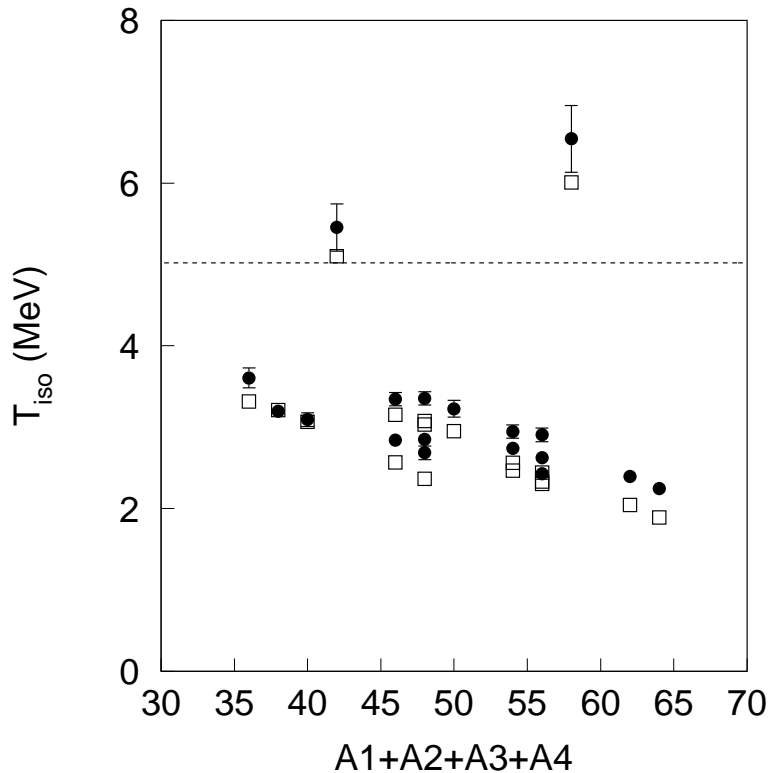


Figure 6.21: Isotopic temperatures are extracted from 18 IMF thermometers (see table 6.2) with $3 \leq Z \leq 8$ and $\Delta B > 10$ MeV. Experimental data is shown as the solid circles. The open squares are the calculations from the improved model. For reference, the primary temperature calculated from the present model is shown as the dashed line.

caloric curve of the nuclear liquid-gas phase transition. Since these observables are constructed from the isotopic distributions, they share the sensitivity to structure effects in the secondary decay discussed above. In the isotopic thermometer technique, the temperature is extracted from a set of four isotopes produced in multifragment breakups [54] as shown in Eqs. (6.9-6.12) of section 6.1.1. Although this isotopic thermometry method is derived within the context of the grand canonical ensemble, it is still valid in the microcanonical ensemble as discussed in section 6.1.2. It has been applied to a wide variety of reactions where it has been regarded as an effective or "apparent" temperature that may differ somewhat from the true temperature T because of the extra yield in the ground state due to feeding from secondary decay.

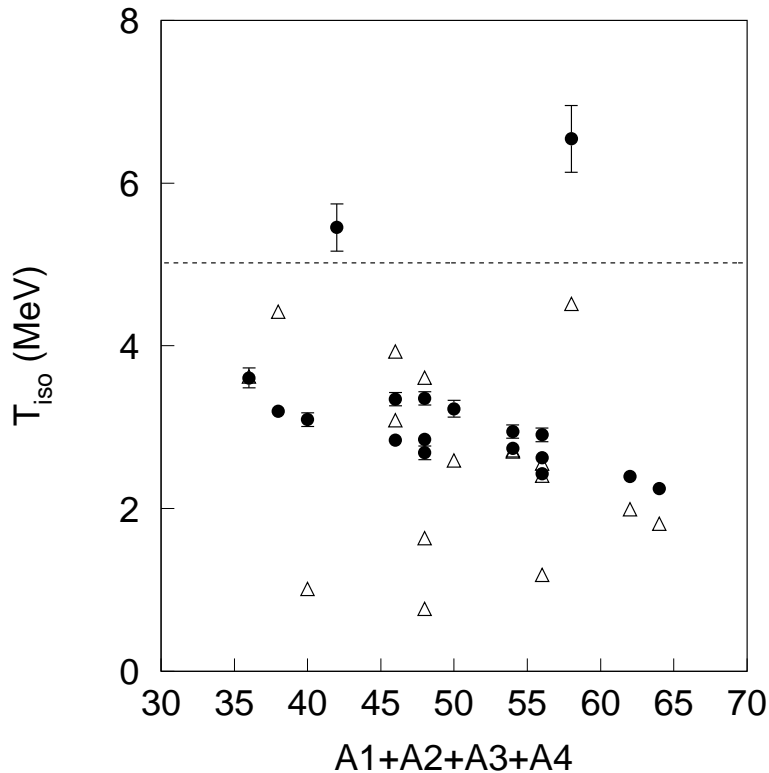


Figure 6.22: Isotopic temperatures are extracted from 18 IMF thermometers (see table 6.2) with $3 \leq Z \leq 8$ and $\Delta B > 10$ MeV. Experimental data is shown as the solid circles. The open triangles are the calculations from the Botvina model. For reference, the primary temperature calculated from the present model is shown as the dashed line.

The relationship between T_{ISO} and T can be calculated within an appropriate statistical model for the fragmentation process if one exists. In general, one should choose a set of four isotopes with large ΔB if one want to extract reliable values of apparent temperature T_{iso} .

To studying the corrections due to secondary decay, measured and calculated temperatures are extracted from the double ratios of suitably chosen isotopes. In Fig. 6.21, 18 IMF thermometers are plotted with the requirement of $3 \leq Z \leq 8$ and $\Delta B > 10$ MeV (see details in Table 6.2) in order to limit the effects of nonequilibrium emissions and reduce the temperature fluctuations. As one can see in Fig. 6.21, the calculated isotopic temperatures (open squares) from the improved model agree

well with the corresponding experimental values (solid points). The two thermometers involving ^{10}Be and ^{18}O are significantly higher than the others due to structural effects[31], which are well reproduced by the improved SMM since we have already incorporated the experimental structural information in secondary decay. All the other 16 IMF thermometers give a much lower temperature than the primary temperature (dashed line) calculated in the model, which shows the effect of the additional feeding to the ground states due to secondary decay. The calculations give somewhat smaller values for T_{ISO} than the data, which may indicate that the secondary decay corrections are overestimated or that the internal temperature or density are not optimal. In addition, these 16 thermometers follow a decreasing trend as a function of the total mass number of the four involved isotopes, indicating that the heavier fragments are more strongly influenced by secondary decay. The open triangles in Fig. 6.22 represent the corresponding predictions of the Botvina Code of ref. [112, 9] where the secondary decay of hot primary fragments is calculated without regard to the detailed structure of the discrete levels in the excited nuclei. The neglect of this structural information is probably responsible for the poor level of agreement with the experimental isotopic temperatures for the heavier isotopes.

On the other hand, light isotopic thermometers are also studied to show the possible effects from the radiative emission of light particles prior to the multifragment breakup. In Fig. 6.23, He thermometers involving the pair of $^{3,4}\text{He}$ with $\Delta B > 10$ MeV (see details in Table 6.2) are shown. Although the calculated temperatures with the present model (open squares) are systematically lower than the experimental values, they seem to track the measured trends. And indeed a better reproduction of the experimental values can be obtained by assuming that 2/3 of the measured ^3He yield is of a pre-equilibrium origin such as surface emission from the expanding system prior to breakup. Adding such a contribution to the predicted yields results in

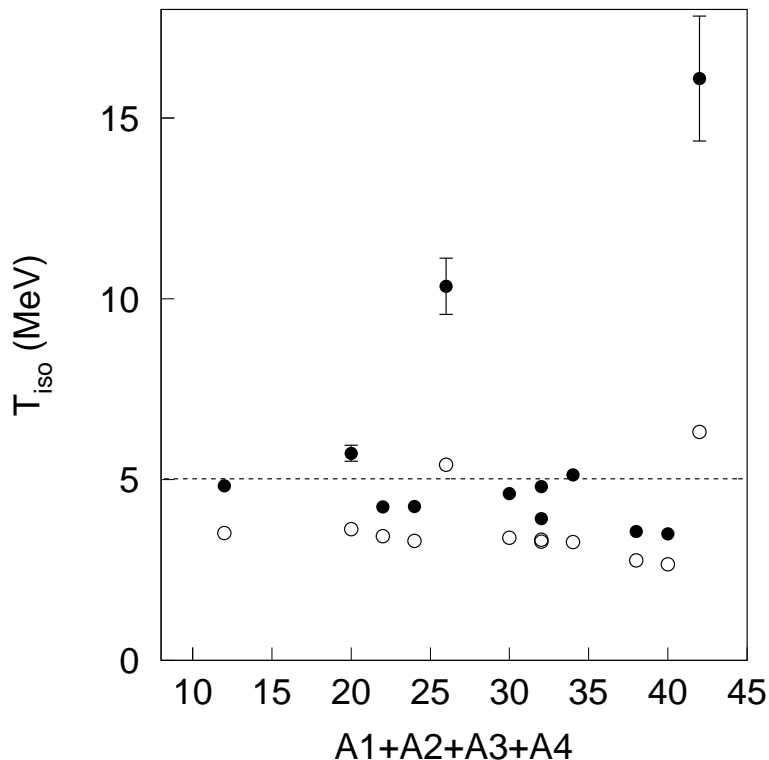


Figure 6.23: Isotopic temperatures are extracted from 12 light thermometers (see table 6.2) satisfying $\Delta B > 10$ MeV and involving the isotope pair of ${}^3,4\text{He}$. Experimental data is shown as the solid circles. The open circles are the calculations from the present model without corrections of nonequilibrium emissions. For reference, the primary temperature calculated from the present model is shown as the dashed line.

predictions given by the open squares in Fig 6.24 which are in good agreement with the experimental data (solid circles). In contrast to the improved SMM, the isotopic temperatures calculated in the Botvina code are compared to the same measured values for these He thermometers in Fig 6.25. The calculations from the Botvina code don't follow the experimental trends well although they do better replicate the temperatures of the H/He and Li/He thermometers without corrections. The isotopic yields relevant to these thermometers reflect the secondary decay of heavier fragments that is calculated for $A > 16$ using the Weisskopf model and for $A \leq 16$ via a "Fermi breakup" model; both models neglect the detailed structure of the lighter nuclei that is included in the present model. If this structure information were

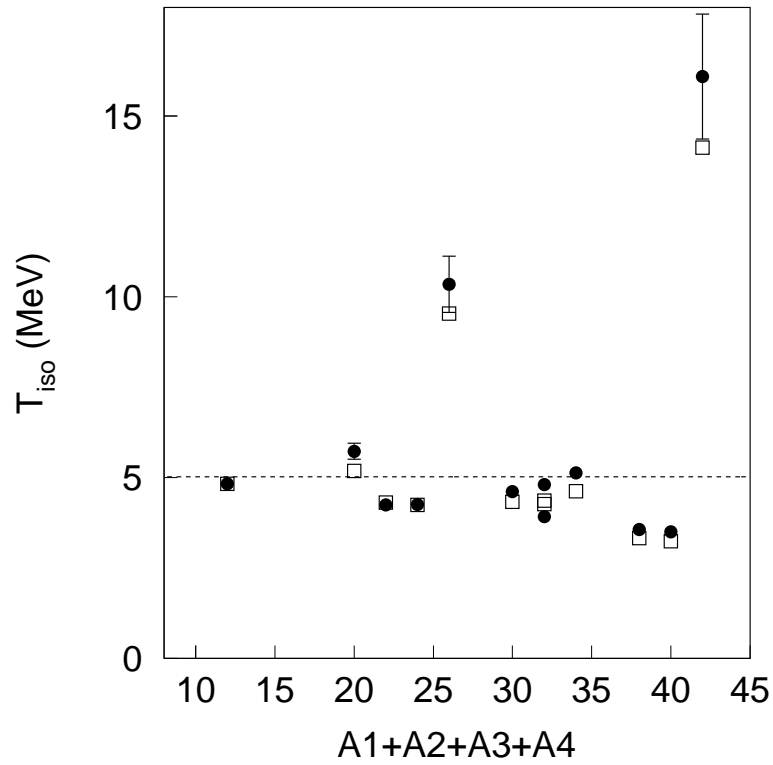


Figure 6.24: Isotopic temperatures are extracted from 12 light thermometers (see table 6.2) satisfying $\Delta B > 10$ MeV and involving the isotope pair of ${}^3,4\text{He}$. Experimental data is shown as the solid circles. The open squares are the calculations from the present model with corrections of nonequilibrium emissions of ${}^3\text{He}$. For reference, the primary temperature calculated from the present model is shown as the dashed line.

included in the Botvina Code, it is likely that the predictions shown in Fig. 6.25 would be changed; the agreement shown for the H/He and Li/He thermometers may be somewhat fortuitous.

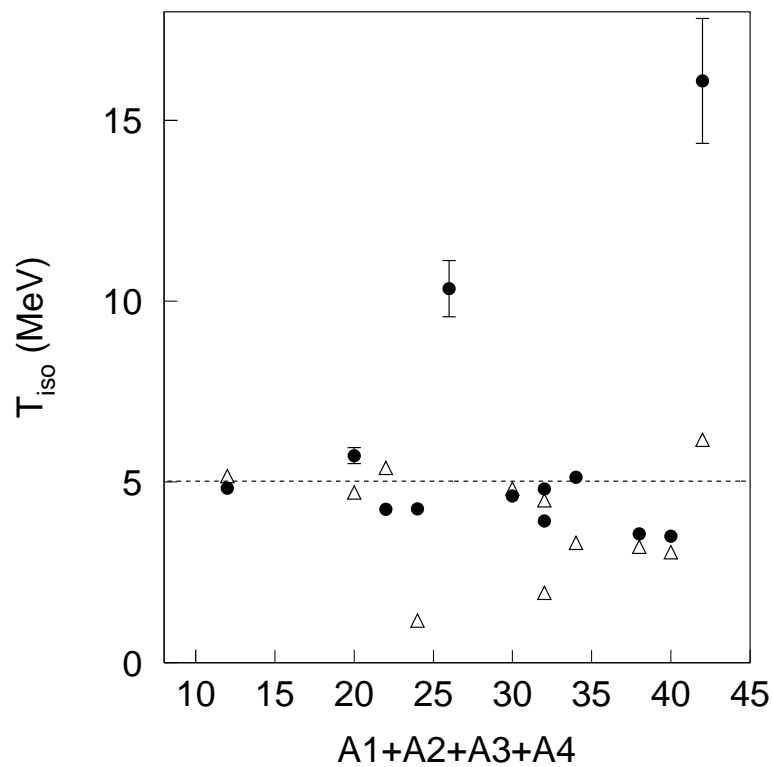


Figure 6.25: Isotopic temperatures are extracted from 12 light thermometers (see table 6.2) satisfying $\Delta B > 10$ MeV and involving the isotope pair of ${}^3,{}^4\text{He}$. Experimental data is shown as the solid circles. The open circles are the calculations from the Botvina code. For reference, the primary temperature calculated from the present model is shown as the dashed line.

Chapter 7

Isospin Dependence of the EOS

The nuclear equation of state (EOS) has been one of the main topics on studies of nuclear matter recently. To better understand astrophysics phenomena such as supernovae [65] and neutron stars [66, 67] as well as nuclear physics, a better understanding of the nuclear EOS is in need. For example, maximum mass of neutron stars [114] and explosion mechanisms in core-collapsed supernovae [67] require accurate knowledge of the EOS. Under laboratory-controlled conditions, the EOS has been investigated by colliding nuclei and measuring compression sensitive observables. The nuclear monopole and isoscalar dipole resonances, for example, sample the curvature of the EOS near the saturation density ρ_0 [68]. Measurements of the collective flow of particles emitted from the dense and compressed matter formed at relativistic incident energies can sample the EOS at densities as high as $4\rho_0$ [69]. In both types of experiment, investigations have primarily focused upon terms in the EOS that describe symmetric matter (equal numbers of protons and neutrons), leaving the asymmetry term that reflects the difference between neutron and proton densities largely unexplored [115]. For very asymmetric matter, however, details of this asymmetry term are critically important. For example, the asymmetry term dominates the pressure within neutron stars at densities of $\rho \leq 2\rho_0$, determines certain aspects of neutron star structure, and modifies proto-neutron star cooling rates [66, 67].

In the following sections hybrid model calculations are performed with the isospin dependent BUU model [116, 117] and the microcanonical SMM model incorporated with an empirical secondary decay procedure [26]. The isotopic distributions of final fragments are shown to compare the model calculations with the experimental data. Two observables of relative free n/p densities and mirror nuclei ratios are discussed to elucidate the sensitivity to the density dependence of the asymmetric terms in the EOS.

7.1 Density Dependence of Asymmetric EOS

Various studies have shown that the mean energy per nucleon $e(\rho, \delta)$ in nuclear matter at density ρ and isospin asymmetry parameter $\delta = (\rho_n - \rho_p) / (\rho_n + \rho_p)$ can be approximated by a parabolic function

$$e(\rho, \delta) = e(\rho, 0) + S(\rho)\delta^2 \quad (7.1)$$

where $e(\rho, 0)$ provides the EOS of symmetric matter, and $S(\rho)$ is the symmetry energy [66, 67, 115]. Different functional forms for $S(\rho)$ have been proposed [114], all consistent with constraints on $S(\rho_0)$ from nuclear mass measurements. Some theoretical studies have explored the influence of the density dependence of $S(\rho)$ on nuclear reaction dynamics [114]-[119].

Calculations of energetic nucleus-nucleus collisions [116]- [119] reveal that the relative emission of neutrons and protons during the early non-equilibrium stages has a robust sensitivity to the density dependence of $S(\rho)$. In general, pre-equilibrium neutron emission increases relative to pre-equilibrium proton emission when the density dependence of $S(\rho)$ is made weaker, e.g. “softer”. Enhanced pre-equilibrium neutron emission reduces the neutron-to-proton ratio in the dense region that remains behind [116, 118].

Central collisions of complex nuclei of comparable mass provide the principal means to produce and study nuclear matter at densities either significantly above or below the saturation value. In near central Sn+Sn collisions at an incident energy of $E/A=50$ MeV, for example, matter is compressed to densities of about $1.5\rho_0$ before expanding and disassembling into 6-7 fragments with charges of $3\leq Z\leq 30$ plus assorted light particles. Detailed analyses imply that such multifragment disassemblies occur at an overall density of $\rho \approx \rho_0/6-\rho_0/3$ and over a time interval of about $\tau \approx 30-100$ fm/c [120]-[125]. Essentially all initial isotopic compositions are determined by the properties of the system during this narrow time frame when the density is significantly less than ρ_0 . This implies that fragment isotopic distributions may have a significant sensitivity to the density dependence of $S(\rho)$. One can also enhance the sensitivity to the asymmetry term $S(\rho) \cdot \delta^2$ by varying the N/Z of the initial system.

Following the reference By M. Prakash et al [114] we write down the symmetry energy,

$$S(\rho) = (2^{2/3} - 1)\frac{3}{5}E_F^0[u^{2/3} - F(u)] + S_0F(u) \quad (7.2)$$

where E_F^0 is the Fermi energy at saturation, $u \equiv \rho/\rho_0$ is the reduced nucleon density, $S_0 \equiv S(\rho_0)$ is the symmetry energy at normal nuclear density and $F(u)$ represents the potential contributions to the symmetry energy with $F(1) \equiv 1$. The mean-field potentials for neutrons and protons due to the symmetry energy can be defined via $F(u)$ as follows,

$$V_{asy}^{n(p)}(\rho, \delta) = e_a \frac{\partial(\rho F(u)\delta^2)}{\partial \rho_{n(p)}} \quad (7.3)$$

where $e_a \equiv [S_0 - (2^{2/3} - 1)\frac{3}{5}E_F^0]$. In this chapter two specific forms of $F(u)$ are investigated [114, 117],

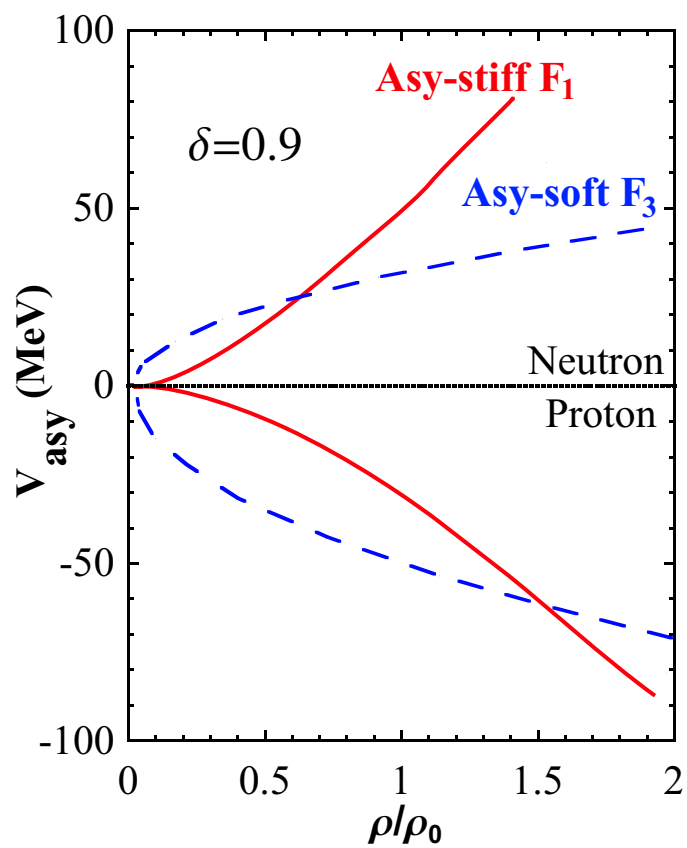


Figure 7.1: The symmetry potential for neutrons and protons is shown for two different density dependences of asymmetry term: asy-stiff F_1 and asy-soft F_3 (see Eqs. (7.4)).

$$\begin{aligned}
F_1(u) &= \frac{2u^2}{1+u}, \\
F_3(u) &= u^{1/2}.
\end{aligned}
\tag{7.4}$$

In Figure 7.1, the symmetry potentials for the two parametrizations are shown for given $\delta = 0.9$. In the following, the stronger dependence F_1 will be labelled as asy-stiff and the weaker dependence F_3 as asy-soft. As one can see from Figure 7.1, the asy-stiff term gives lower neutron potential and higher proton potential at low density, which means more protons and less neutrons are emitted at the preequilibrium stage leaving the hot "prefragment" more neutron rich, and vice versa for the asy-soft term. In the next section, calculations were performed in an effort to distinguish the two different asymmetry terms.

7.2 Hybrid Model Calculations

As discussed previously, the isospin asymmetries of the excited systems prior to multifragment breakup are sensitive to the density dependence of the asymmetry term of the EOS [116]- [118]. The "prefragment" is reduced in size relative to the total system by preequilibrium emission when it disintegrates into the final fragments. Both the Stochastic Mean Field (SMF) [52] and the Boltzmann-Uehling-Uhlenbeck (BUU) [44] formalisms, which describe the time evolution of the collision using a self-consistent mean field (with and without fluctuations, respectively), predict preequilibrium emission that is increasingly neutron-deficient and corresponding prefragments that are more neutron-rich for symmetry terms $S(\rho)$ that have a stiffer density dependence [116, 126]. These two formalisms are essentially identical during the early stages of the collision when the densities exceed $\rho_0/2$ and fluctuations in the mean field are negligible.

The mechanism for the disintegration of the prefragment into the observed fragments with $3 \leq Z \leq 30$ is an issue that is not settled but, instead, is evolving considerably as new measurements and models become available. Dynamical multifragmentation models [121, 127] have been used with some success, as have statistical models either with fragment emission probabilities determined from the rates for evaporative surface emission [10] or from the yields assuming thermal equilibrium [9, 11]. Here, we examine the isotopic effects in the latter limit, which assumes that thermal equilibrium is achieved at breakup. Such calculations have provided surprisingly accurate predictions for the fragmentation of projectile- and target-like residues in peripheral and mid-impact parameter heavy ion collisions at incident energies $E_{\text{beam}}/A > 200$ MeV [128, 129], central heavy ion collisions at $E_{\text{beam}}/A \leq 50$ MeV [55, 45] and in light ion induced collisions at $E_{\text{beam}} > 4$ GeV [130], after some accounting is made for preequilibrium light particle emission. Comparisons of experimental data to such approaches provide an assessment of the importance of non-equilibrium phenomena; accordingly, more difficulties in such approaches are encountered in central heavy ion collisions at $E_{\text{beam}}/A > 50$ MeV, reflecting the decreased time available for equilibration [45, 131].

To examine the isospin dependence of the EOS, hybrid model calculations were carried out for central collisions ($b=1\text{fm}$) of $^{112}\text{Sn}+^{112}\text{Sn}$, $^{112}\text{Sn}+^{124}\text{Sn}$ and $^{124}\text{Sn}+^{124}\text{Sn}$ at $E/A=50$ MeV. Specifically, we solved the isospin dependent BUU equation to obtain predictions for the dynamical emission of light particles during the compression and expansion stages of the collision. Then, we calculate the multifragment disintegration of the denser portions of the system via the Statistical Multifragmentation Model (SMM) as discussed in the previous chapter [26, 36]. In the first step of the hybrid calculations described here, the mean field for symmetric nuclear matter in the BUU calculations was chosen to have a stiff EOS ($K = 386$ MeV) [132]. Calcu-

lations were performed with the two different expressions for the asymmetry term, “asy-stiff” and “asy-soft”, corresponding to $F_1(\rho/\rho_0)$ and $F_3(\rho/\rho_0)$, respectively, as shown in Figure 7.1. Using these mean fields, BUU calculations were followed through the initial compression and subsequent expansion for an elapsed time of 100 fm/c at which point the central density decreased to a value of about $\rho_0/6$. The regions with densities $\rho > \rho_0/8$ were then isolated and their decay was calculated with the SMM.

Table 7.1: The first two columns provide the N/Z ratio and number of nucleons in the prefragments produced in the calculations for an elapsed time of 100 fm/c and density cutoff of $\rho_0/8$. The next two columns provide corresponding information for the same cutoff density but a shorter elapsed time of 80 fm/c. All calculations were performed at an impact parameter of 1 fm.

reaction	t=100 fm/c, $\rho_c=\rho_0/8$				t=80 fm/c, $\rho_c=\rho_0/8$			
	asy-soft		asy-stiff		asy-soft		asy-stiff	
	N/Z	A	N/Z	A	N/Z	A	N/Z	A
$^{112}\text{Sn}+^{112}\text{Sn}$	1.16	153	1.27	152	1.17	165	1.27	165
$^{112}\text{Sn}+^{124}\text{Sn}$	1.19	161	1.36	162	1.22	174	1.36	175
$^{124}\text{Sn}+^{124}\text{Sn}$	1.23	172	1.44	173	1.27	183	1.45	185

The N/Z ratio and the nucleon number A of these fragmenting systems (“prefragments”) are given in two leftmost columns in Table 7.1. To illustrate the sensitivity of prefragment size and asymmetry to the elapsed time and density cutoff, values for N/Z and A are also given in Table 7.1 for an elapsed time of 80 fm/c. Calculations have shown that the N/Z ratio is not sensitive to the density cutoff [116]. While A is sensitive to these parameters, the N/Z ratio is relatively insensitive; to within 3% , values of N/Z of 1.27 (1.16), 1.36 (1.19) and 1.44 (1.23) are obtained for the source asymmetry of asy-stiff (asy-soft) calculations for $^{112}\text{Sn}+^{112}\text{Sn}$, $^{112}\text{Sn}+^{124}\text{Sn}$ and $^{124}\text{Sn}+^{124}\text{Sn}$ collisions independent of matching condition. The excitation energy per nucleon of the prefragment depends strongly on the matching condition; however, this quantity is presently difficult to calculate accurately. A range of values for the

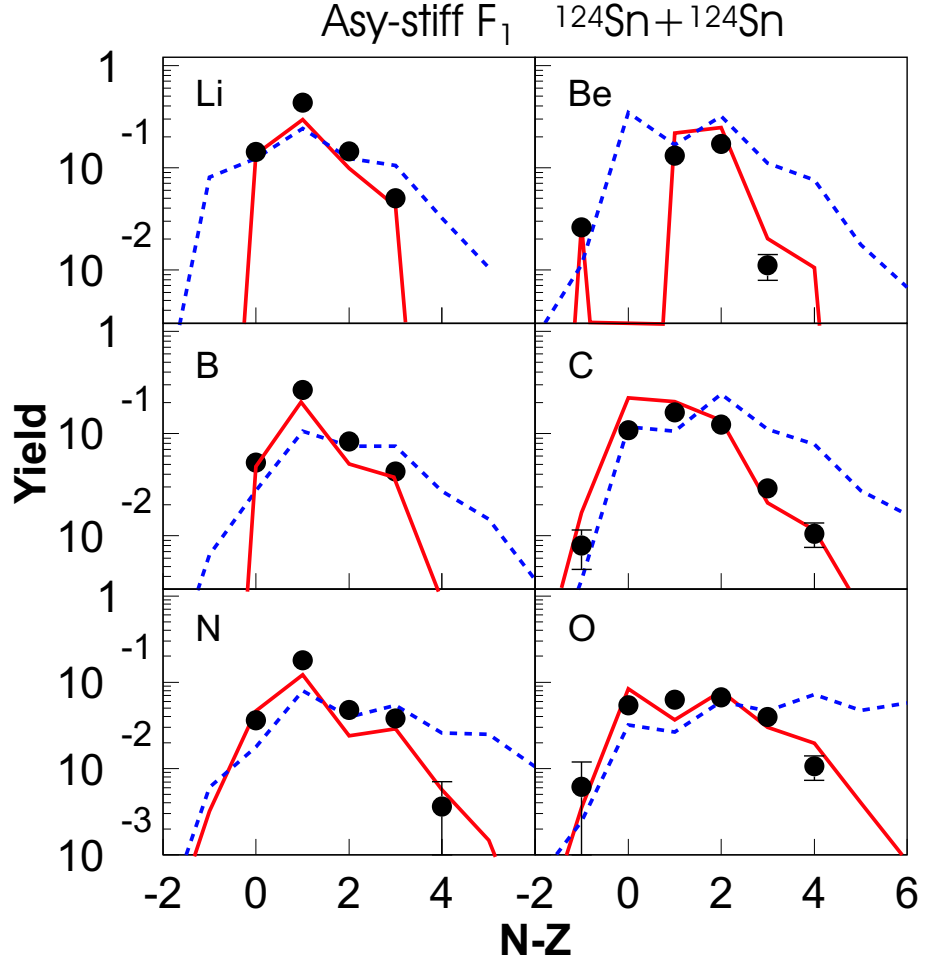


Figure 7.2: Isotopic distributions from Li to O are shown for central collisions of $^{124}\text{Sn}+^{124}\text{Sn}$. The full circles are experimental data while the solid (dashed) lines denote the final (primary) calculations from the hybrid model using the density dependence asy-stiff F_1 (Eq. 7.4) for the asymmetry term of the EOS.

excitation energy per nucleon of $E^*/A = 4-6$ MeV was therefore assumed in the subsequent SMM calculations to estimate the range of possible values consistent with the present approach.

7.3 Isotopic Composition and Isospin Dependence

Isotopic distributions calculated with the asy-stiff and asy-soft EOS's are compared with those measured for central collisions of $^{124}\text{Sn}+^{124}\text{Sn}$ at 50A MeV [41, 113]. Ac-

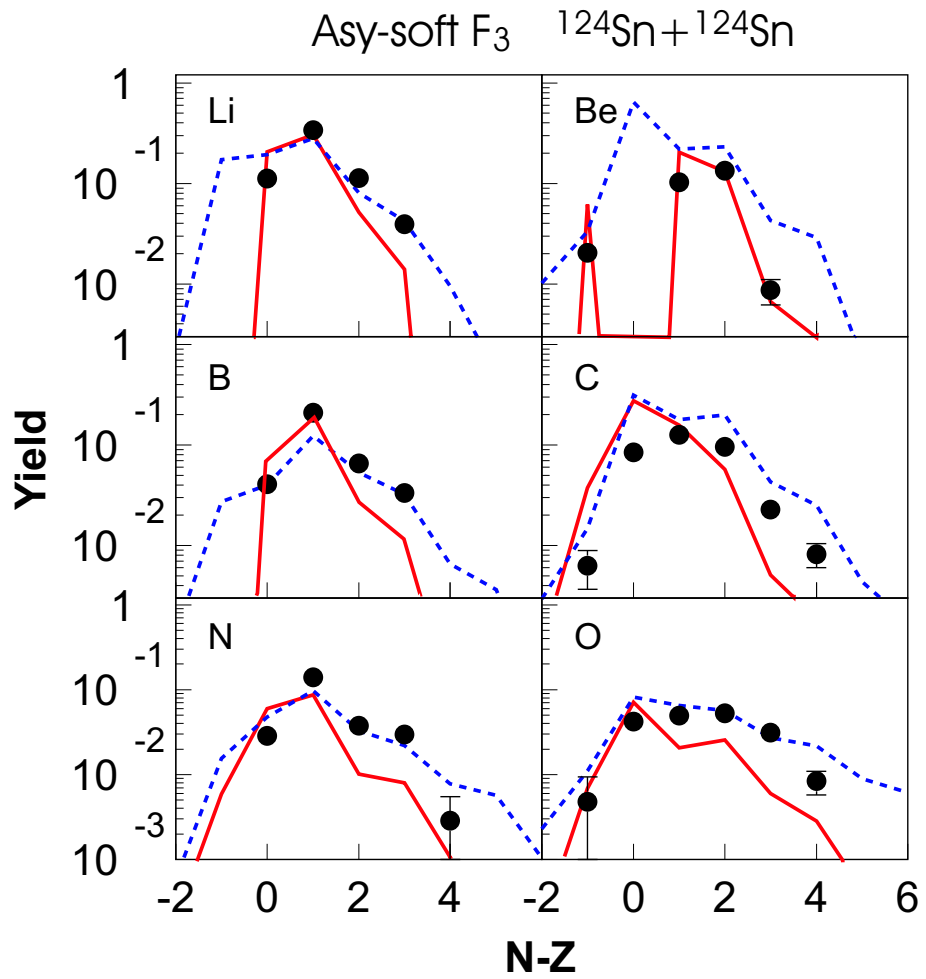


Figure 7.3: Isotopic distributions from Li to O are shown for central collisions of $^{124}\text{Sn}+^{124}\text{Sn}$. The full circles are experimental data while the solid (dashed) lines denote the final (primary) calculations from the hybrid model using the density dependence asy-soft F_3 (Eq. 7.4) for the asymmetry term of the EOS.

curate calculations for isotopic yields from the multifragment decay of the excited prefragment within the SMM approach require a careful accounting of the structure and branching ratios of the excited fragments. Using an SMM code (see the previous chapter) that carefully addresses such effects, the isotopic distributions in Figs. 7.2 and 7.3 were calculated for the prefragment source parameters in Table 7.1.

In Figure 7.2, the final isotopic distributions (solid lines) for the asy-stiff EOS agree well with the experimental data while in Figure 7.3 the final distributions (solid lines) for the asy-soft EOS are relatively narrower. From the comparisons of isotopic distributions the asy-stiff density dependence of asymmetry term of the EOS is likely favored. However, in both figures, the primary isotopic distributions (dashed lines) are enormously modified by secondary decay, which could easily overshadow the signals of the density dependence of asymmetry energy. In the following, we will show observables that are not as sensitive to secondary decay to distinguish the different isospin dependences of the EOS.

7.3.1 Relative Free n/p Densities and Mirror Nuclei Ratios

Unfortunately, the observed isotopic distributions are also influenced by secondary decay, making it very important to identify observables that are insensitive to sequential decay. Statistical calculations have identified certain ratios of isotopic multiplicities as being robust with respect to the secondary decay [41, 39]. For example, the ratio of the multiplicities $R_{21}(N_i, Z_i) = M_2(N_i, Z_i)/M_1(N_i, Z_i)$ of an isotope with neutron number N_i and proton number Z_i from two reactions 1 and 2 is relatively insensitive to the distortions from sequential decay. For multifragmentation, compound nuclear evaporation, and selected strongly damped collisions, such ratios as functions of N_i

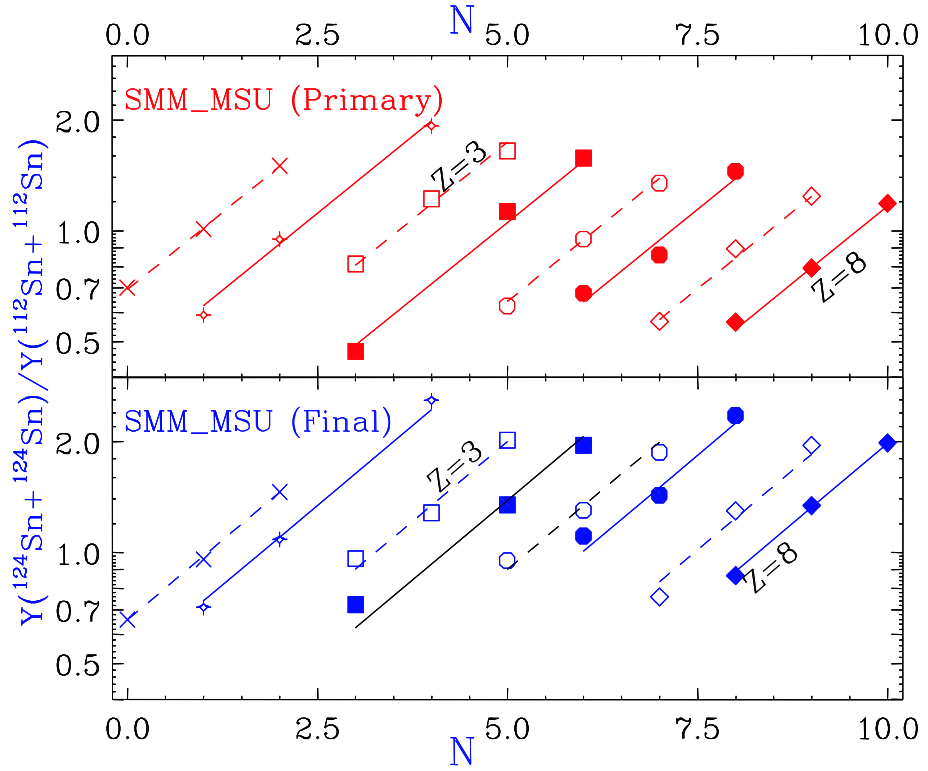


Figure 7.4: Relative isotope ratios, R_{21} , of two reactions $^{124}\text{Sn}+^{124}\text{Sn}$ and $^{112}\text{Sn}+^{112}\text{Sn}$ are shown as a function of neutron number. The upper panel presents the primary calculations using the hybrid model while the final isotope ratios after secondary decay are plotted in the lower panel. The lines denote the best fits through the symbols with the same slope.

and Z_i have been experimentally shown [64] to satisfy a power law relationship:

$$R_{21}(N_i, Z_i) = M_2(N_i, Z_i)/M_1(N_i, Z_i) = C (\hat{\rho}_p)^{Z_i} (\hat{\rho}_n)^{N_i} \quad (7.5)$$

where $\hat{\rho}_p$ and $\hat{\rho}_n$ are empirical parameters that have the interpretation, in the grand canonical approximation, of being the ratios of the free proton and free neutron densities in the two systems, $\hat{\rho}_p = \rho_{p2}/\rho_{p1}$; $\hat{\rho}_n = \rho_{n2}/\rho_{n1}$ [41].

Before we use this technique to test the density dependence of the asymmetry term, the relative isotope ratios calculated from the model are shown in Fig. 7.4 to verify if the calculations have the same behavior as the experimental data. In the upper panel of Fig. 7.4, the ratios of primary isotope yields are plotted as symbols

which lie along the dashed and solid Z lines with the same slope. Clearly one see that the calculations are in agreement with the parametrization in Eq. (7.5) and similar to the experimental data in ref. [41]. More importantly, in the lower panel of Fig. 7.4, the slopes of these ratios after secondary decay are very similar to the primary calculations. Therefore, this secondary decay insensitive observable is used below for probing the isospin dependence.

The solid circles and squares in Fig. 7.5 show values for ρ_p and ρ_n , respectively, obtained from fragments with $3 \leq Z_i \leq 8$ detected in central $^{112}\text{Sn}+^{112}\text{Sn}$, $^{112}\text{Sn}+^{124}\text{Sn}$ and $^{124}\text{Sn}+^{124}\text{Sn}$ collisions at $E/A=50$ MeV [41]. The $^{112}\text{Sn}+^{112}\text{Sn}$ reaction was labeled as 1 in Eq. 7.5; the different data points correspond to the three choices for reaction 2 and are plotted in both left and right panels as a function of $N_{\text{tot}}/Z_{\text{tot}}$ where N_{tot} and Z_{tot} are the total numbers of neutrons and protons involved in reaction 2. To indicate the sensitivity of these ratios to the secondary decay of heavier particle unstable nuclei, the open rectangles indicate the ratios obtained from the yields of primary fragments and the cross-hatched rectangles indicate the ratios obtained from the yields of the final fragments after secondary decay. The vertical height of each rectangle reflects the range of values for each quantity as the assumed excitation energy is varied over the range of $E^*/A = 4-6$ MeV.

The left and right panels in Fig. 7.5 provide values calculated for prefragments obtained with the asy-stiff and asy-soft EOS's, respectively. In both panels, it can be seen that the ratios calculated from the primary yields (open rectangles) and those calculated from the secondary yields (cross-hatched rectangles) are similar, indicating that values for $R_{21}(N,Z)$ are relatively insensitive to secondary decay. With the exception of the value of $\langle \hat{\rho}_p \rangle$ for the $^{124}\text{Sn}+^{124}\text{Sn}$ reaction, $N_{\text{tot}}/Z_{\text{tot}} = 1.48$, the ratios calculated from the final yields with the asy-stiff EOS (left panel) overlap the data. In comparison, the calculations using the asy-soft EOS (right panels) show

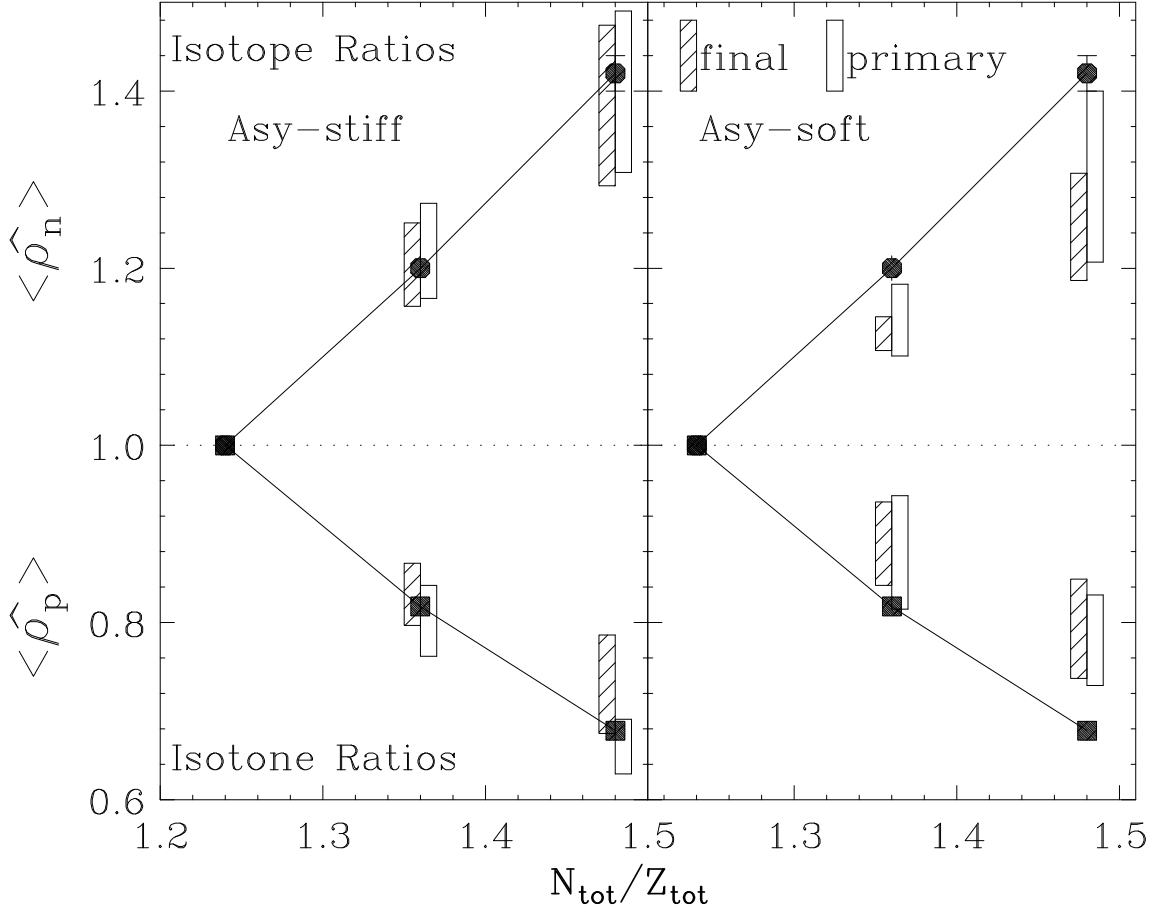


Figure 7.5: Both panels: The solid circles and solid squares show values for $\hat{\rho}_p$ and $\hat{\rho}_n$, respectively; measured in central $^{112}\text{Sn}+^{112}\text{Sn}$, $^{112}\text{Sn}+^{124}\text{Sn}$ and $^{124}\text{Sn}+^{124}\text{Sn}$ collisions at $E/A=50$ MeV. Left panel: the open and cross-hatched rectangles show corresponding hybrid calculations for R_{21} calculated from the primary and final fragment yields, respectively, predicted by the hybrid calculations using the Asy-stiff EOS. Right panel: the open and cross-hatched rectangles show corresponding hybrid calculations for R_{21} calculated from the primary and final fragment yields, respectively, predicted by the hybrid calculations using the Asy-soft EOS.

a significantly weaker dependence on $N_{\text{tot}}/Z_{\text{tot}}$ than do the data.

7.3.2 Mirror Nuclei Ratios

One can also reduce the influence of secondary decay by taking ratios of the multiplicities of mirror nuclei $M(N_i, Z_i)/M(Z_i, N_i)$ measured in a single reaction [41, 39], but the reduction of secondary decay effects may be less effective in this case.

The solid and open points in Fig. 7.6 show the experimental values for the mirror nuclei ratios constructed from the multiplicities of ${}^7\text{Li}$, ${}^7\text{Be}$, ${}^{11}\text{B}$ and ${}^{11}\text{C}$ fragments [41]. The upper and lower panels are for ${}^{124}\text{Sn}+{}^{124}\text{Sn}$ and ${}^{112}\text{Sn}+{}^{112}\text{Sn}$ collisions, respectively.

The left and right panels in Fig. 7.6 provide values for the mirror nuclei ratios calculated with the asy-stiff and asy-soft EOS's, respectively. For these ratios, the sensitivity to the density dependence of the symmetry energy and to the secondary decay corrections are more significant. Ratios of mirror nuclei calculated with the asy-stiff EOS exceed those calculated with the asy-soft EOS by about a factor of two and overlap with the experimental values for three of the four ratios measured.

7.4 Remarks

In the present simplified approach, the sensitivity of isotope and the mirror nuclei ratios to the asymmetry term arises from the different (N/Z) ratios of the prefragments that are predicted by BUU calculations. There is little sensitivity to the total mass of the prefragment, but additional sensitivity to its excitation energy per nucleon. Within the present model dependent analysis, this uncertainty in excitation energy is the limiting factor that prevents a more quantitative constraint on $S(\rho)$.

Light cluster emission during the early compression and expansion stages of the

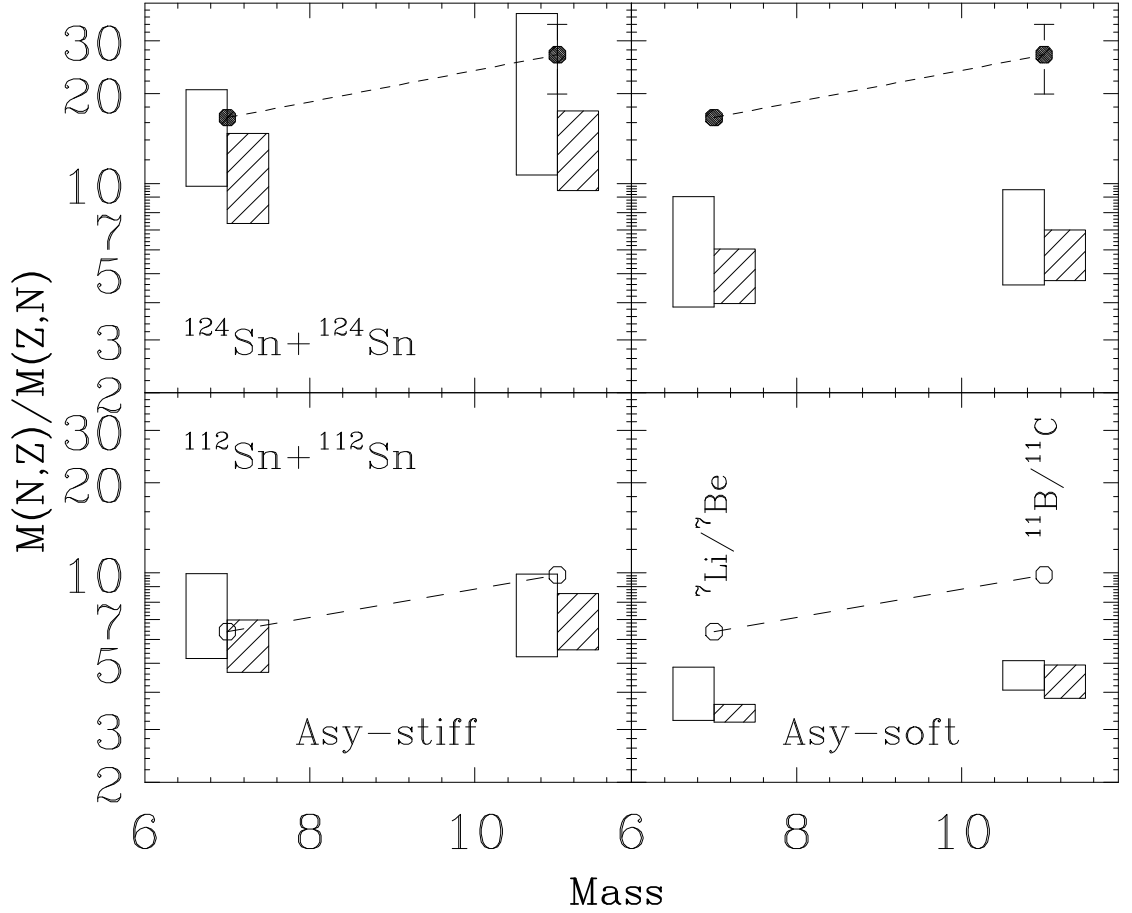


Figure 7.6: The solid and open points in the upper and lower panels show the mirror nuclei ratios measured for $^{124}\text{Sn} + ^{124}\text{Sn}$ and $^{112}\text{Sn} + ^{112}\text{Sn}$ collisions, respectively. Left panels: The open and cross-hatched rectangles show corresponding hybrid calculations of the mirror nuclei ratios calculated from the primary and final fragment yields, respectively, predicted by the hybrid calculations using the Asy-stiff EOS. Right panel: The open and cross-hatched rectangles show corresponding hybrid calculations of the mirror nuclei ratios calculated from the primary and final fragment yields, respectively, predicted by the hybrid calculations using the Asy-soft EOS.

collision can influence the N/Z ratio and excitation energy of the prefragment. Incorporating the emission of light particles up to $A=4$ within transport model calculations will help address this issue [133, 134]. While the present hybrid model approach demonstrates a sensitivity of the isotopic fragment yields to the asymmetry term of the EOS, the detailed nature of this sensitivity is model dependent. For example, the hybrid model predicts that an asy-stiff EOS leads to fragments that are more neutron-rich than those produced when the EOS is asy-soft. On the other hand, recent calculations with the Expanding Evaporating Source (EES) model, which assumes the fragments originate from surface emission and not from the equilibrium decay of the residue, predict the opposite trend [64]. It is therefore highly desirable to explore the connection between the fragment isotopic distributions and the EOS within other statistical and dynamical fragment production models currently in use and under development. These long-term goals require significant future theoretical efforts.

Chapter 8

Summary

Multifragmentation is main reaction mechanism for central nucleus-nucleus collisions at incident energies in excess of $E/A = 35\text{MeV}$. The assumption of local thermal equilibrium is often invoked by model descriptions of this process. In such descriptions, copious fragment production occurs when the system undergoes a low density phase transition conceptually similar to the liquid-gas phase transition of nuclear matter. The fragment observables in such models are assumed to reflect the temperatures and densities at freezeout, after which the interacting system decouples and fragments propagate to the detectors.

In order to study this freezeout stage, a Large Area Silicon-Strip/CsI detector Array (LASSA) was developed. The LASSA consists of nine identical telescopes, each of which is composed of two silicon-strip detectors and four CsI(Tl) crystals and provides excellent energy, angular and mass resolution for the detection of charged particles. Using LASSA and the Miniball/Miniwall 4π fragment detection array, central collisions of $^{129}\text{Xe}+^{197}\text{Au}$ at 50A MeV were measured with high energy and angular resolution.

These high quality measurements allowed the study of correlation functions for particles emitted from the central $^{129}\text{Xe}+^{197}\text{Au}$ collisions. An imaging technique was

used to analyze p-p correlation functions by numerically inverting the correlation function in the Koonin-Pratt formalism to obtain the source function. Both the inclusive and c.m. energy gated correlation functions were studied by this technique and the energy dependence of the source distribution was observed. The main observed trend was that sources of less energetic protons are more extended.

The d- α correlations were also studied in the Koonin-Pratt formalism, using a simple Gaussian source parametrization instead of the imaging approach which has not yet provided reliable source information for d- α correlations. However, the d- α correlation functions could not be fitted well, and especially the second resonance peak at excitation energy 4.31 MeV was overpredicted and displayed an incorrect shape. Simulations indicated this could be the effect of collective motion and that the phenomenon could be modelled by an effective temperature correction. The origin of this effect is that the mixed event yield has a broader relative energy distribution than the resonant yield when a significant collective flow occurs. After taking into account this effect, we fitted the d- α correlation functions with the Gaussian source parametrization. We found that the d- α source displayed an energy dependence that was similar to that observed for the p-p correlations.

This collective motion also led to a reduction in the detectable source due to the competition between the collective velocity field and the thermal or random velocity of the particles. The size reduction factor of the sources probed by the two particle correlations in LASSA is more significant for heavier particles. After taking this source reduction into account, we calculated the breakup density for both p-p and d- α correlations. As the energy of the particles is reduced, the extracted values of the density become smaller, indicating that the lower energy particles are emitted later after the system is expanded.

An equilibrium approach is developed for permitting the extension of these techniques to heavier particles for which the kernel of the conventional Koonin-Pratt approach has not yet been calculated. With this equilibrium assumption and taking collective effects into account, we fitted the d- α , t- α , ^3He - α and α - α correlations and extracted the detected free volume of the total source. After corrections for secondary decay and collective motion, we calculated the values of the density which are around $1/5$ - $1/3\rho_0$. When the collective and secondary decay effects are applied in the same way for both the equilibrium and Koonin-Pratt approaches, the extracted density values for the d- α correlation function are very similar for the two approaches. However, the uncertainties of this approach are still somewhat difficult to presently estimate. Additional information about the secondary decay and collective motion corrections to these data are needed to improve our understanding of the uncertainties in the extracted breakup density.

The equilibrium approach was also used to determine the spins of particle unstable states. The sensitivity to spin determination of this procedure is illustrated in the p- ^7Li correlation function where three groups of resonances are fitted. The spin of the first excited state of ^8B at 0.774 MeV has not been measured although the spin of the analog states of ^8Be and ^8Li indicates a 1^+ assignment for this state. By fitting the p- ^7Be correlation function, the spin value of this 0.774 MeV state is determined to be 0.98 ± 0.29 if there is no other state between the two known 0.774 MeV and 2.32 MeV states, or 0.95 ± 0.33 if a 1^+ state at 1.4 MeV is considered. In either of the cases, we confirm the spin of the 0.774 MeV state of ^8B is one. We also analyze the α - ^6Li correlation function in the similar way where more resonances of ^{10}B are involved in the fitting. Though the resolution and statistics are limited, it seems that a spin of $J = 2$ is favored for the 6.56 MeV state if the branching ratio of this state decaying through the α - ^6Li channel is 100%. If this state also decays to the d- α - α

channel, the spin could be higher. Some strength near threshold is observed in this channel, but we currently cannot say whether it is sufficient to influence this spin assignment. Besides the $d-\alpha-\alpha$ correlation, other stronger three particle correlations ($\alpha-\alpha-\alpha$, $p-p-\alpha$, and $p-\alpha-\alpha$) are also shown; some exhibit huge enhancements for the peaks near the threshold due to the small three body phase space near threshold. Such high sensitivity near threshold may prove interesting for future studies.

In order to test the thermal properties of multifragmenting systems, we develop an improved Statistical Multifragmentation Model (SMM). In this improved SMM, we incorporate experimental values of binding energies if possible or otherwise use the smoothly extrapolated values from an improved LDM if such experimental information is not available. The free energies used for calculating the primary populations of the fragments are also modified by taking into account the experimental level densities at low energy. To apply a consistent calculation, we model the secondary decay process with the same empirically modified level density scheme, which adopts all the experimental levels up to where the information seems complete and thereafter is smoothly interpolated from the empirical extension to the SMM limit of the level density at high energy. For all the experimentally known states, we also adopted the experimental values of excitation energies, spins, isospins, parities and branching ratios if possible. Before sequential decay starts, hot fragments from the primary breakup are populated according to the primary temperature over the sampled levels in the constructed 'table'. In the end, all the fragments will decay to their final stable states from top to bottom throughout the 'table' by use of the known branching ratios or the values calculated from the Hauser-Feshbach formula.

Before comparing this model to experimental data, we examined the caloric curves calculated from the improved SMM to check that they show similar behavior as those obtained from the standard (original) SMM. We point out that the caloric curve also

shows an important density dependence, which manifests the significance of finding and measuring observables that can constrain the freezeout density. In comparisons of the charge and mass distributions, the standard SMM overpredicts the yields of heavy fragments due to the fact that the binding energies calculated in the standard SMM for heavy fragments consistently exceed the empirical values used in the improved SMM. We have shown that the Albergo formula for extracting the isotopic temperatures from the double ratios of the isotopic yields is valid in this semi-microcanonical SMM even though the formula itself is derived from the grand canonical limit.

Secondary decay corrections are calculated with this model to provide corrections to the correlation functions and enable the determination of the breakup density. In addition, the final isotopic temperatures are extracted by this approach from a set of IMF thermometers with $3 \leq Z \leq 8$ and $\Delta B > 10$ MeV to limit the effects of non-equilibrium emission and reduce the calculation fluctuations. We obtained a very good agreement between the qualitative trends of the experimental data and the calculated values using the improved SMM, thanks to the incorporated empirical nuclear structure information in the model, especially in the later stages of the breakup, even though we did not try to adjust the input parameters of the model to optimize the agreement between experiment and theory. In contrast, calculations from the Botvina's version of the SMM which neglects the experimental structure details can not reproduce the experimental data. However, these final temperatures for the IMF's, either from the data or from this improved model, are significantly lower than the primary values calculated in the model, which shows that these observables are modified extensively by secondary decay. Furthermore, these IMF thermometers follow a decreasing trend as a function of the total mass number of the four involved isotopes, indicating that the heavier fragments are more strongly influenced by secondary decay.

The accuracy of this statistical approach allowed us to explore the sensitivity of the fragment isotope distributions to the isospin dynamics of the initial stage and to the isospin dependence of the nuclear equation of state (EOS). Hybrid model calculations are performed with the improved SMM and an isospin dependent BUU model for exploring the isospin dependence of the EOS. Two forms (one stiffer, the other softer) of the density dependence of the asymmetric terms in the EOS are tested for central collisions of $^{112}\text{Sn}+^{112}\text{Sn}$, $^{112}\text{Sn}+^{124}\text{Sn}$, and $^{124}\text{Sn}+^{124}\text{Sn}$ at $E/A=50$ MeV. Since the observed isotopic distributions are enormously modified by secondary decay, we need to identify observables insensitive to sequential decay in order to distinguish the different density dependences of the asymmetry term. The scaling parameters (α , β), which factorize the isotope ratios from two reactions into a simple parametrization, $R_{21}(N, Z) = C \exp(\alpha N + \beta Z)$, and are discovered in studying the isoscaling and isospin fractionation phenomena in multifragmentation, are found very robust with respect to secondary decay. By comparing the Sn+Sn data to the calculations with the hybrid model for the isoscaling parameters, the stiffer density dependence of the EOS is favored. Another test on the mirror nuclei ratios of $^7\text{Li}/^7\text{Be}$ and $^{11}\text{B}/^{11}\text{C}$ also shows a better agreement between the data and the calculations with the stiffer isospin dependence though the reduction of secondary decay effects may be less effective in this case.

While the present hybrid model approach demonstrates a sensitivity of the isotopic yields to the asymmetry term of the EOS, the detailed nature of this sensitivity is model dependent. For example, calculations with the EES model, which has a different emission mechanism from the SMM, predict the opposite trend. Therefore, it is highly desirable to explore this sensitivity of isotopic yields to the asymmetry terms of the EOS within other statistical and dynamical models. Experimental efforts are also in great need to produce larger isospin signals with more asymmetric systems,

which is becoming the focus of nuclear reaction studies with the available or proposed high intensity radioactive beam facilities.

After these extensive explorations of the multifragmentation process, it is somewhat surprising that we find few aspects that are well outside of the realm of description by equilibrium models. To be certain there are problems. For example, the freezeout density definitely depends on the energy of the emitted particle, consisting with the lower energy particles being emitted after the system has cooled and expanded to low density. On the other hand, the populations of excited states and isotopic distributions are remarkably well described by the equilibrium approach. The picture that appears to be emerging is the one where particles are emitted as a function of time from the bulk of the expanding system. While more time to digest these results is needed, this picture does not appear to correspond to any existing model.

Bibliography

- [1] L.D. Landau, JETP **30**, 1058 (1956).
- [2] G. Baym and Ch. Pethick, *Landau-Fermi Liquid Theory*, Wiley, New York (1991).
- [3] D.Q. Lamb *et al.*, Phys. Rev. Lett. **41**, 1623 (1978).
- [4] P. Danielewicz Nucl. Phys. **A314**, 465 (1979).
- [5] H. Jaqaman, A.Z. Mekjian, L. Zamick, Phys. Rev. **C27**, 2782 (1983).
- [6] M.W. Curtin, H. Toki, D.K. Scott, Phys. Lett. **B123** 289 (1983).
- [7] D. Teaney, J. Lauret, E. V. Shuryak, Phys. Rev. Lett. **86**, 4783 (2001).
- [8] Sven Soff, Steffen A. Bass, Adrian Dumitru, Phys. Rev. Lett. **86**, 3981 (2001).
- [9] J.P. Bondorf, A.S. Botvina, A.S. Iljinov, I.N. Mishustin, K. Sneppen, Phys. Rep. **257**, 133 (1995).
- [10] W.A. Friedman, Phys. Rev. **C42**, 667 (1990).
- [11] D.H.E. Gross, Phys. Rep. **279**, 119 (1997).
- [12] W.G. Lynch, Nucl. Phys. **A545**, 199c (1992).
- [13] J. Richert and P. Wagner, Phys. Rep. **350**, 1 (2001).
- [14] Multifragmentation, Proceedings of International Workshop 27 on Gross Properties of Nuclei and Nuclear Excitations, Hirschegg, Austria, 1999, edited by H. Feldmeier, J. Knoll, W. Noeremberg, and J. Wambach, GSI, Darmstadt, (1999).
- [15] K. Hagel *et al.*, Phys. Rev. **C50**, 2017 (1994).
- [16] P. Danielewicz, Phys. Rev. **C51**, 716 (1995).
- [17] G. Bertsch, P.J. Siemens, Phys. Lett. **B126**, 9 (1983).
- [18] P. Kreutz, J.C. Adloff, M. Begemann-Blaich, P. Bouissou, J. Hubele, G. Imme, I. Iori, G.J. Kunde, S. Leray, V. Lindenstruth, Z. Liu, U. Lynen, R.J. Meijer, U. Milkai, A. Moroni, W.F.J. Muller, C. Ngo, C.A. Ogilvie, J. Pochodzalla, G. Raciti, G. Rudolf, H. Sann, A. Schuttauf, W. Seidel, L. Stuttge, W. Trautmann, A. Tucholski, Nucl. Phys. **A556**, 672 (1993).

- [19] A. Schuttauf, W.D. Kunze, A. Worner, M. Begemann-Blaich, Th. Blaich, D.R. Bowman, R.J. Charity, A. Cosmo, A. Ferrero, C.K. Gelbke, C. Gross, W.C. Hsi, J. Hubele, G. Imme, I. Iori, J. Kempter, P. Kreutz, G.J. Kunde, V. Lindenstruth, M.A. Lisa, W.G. Lynch, U. Lynen, M. Mang, T. Mohlenkamp, A. Moroni, W.F.J. Muller, M. Neumann, B. Ocker, C.A. Ogilvie, G.F. Peaslee, J. Pochodzalla, G. Raciti, F. Rosenberger, Th. Rubehn, H. Sann, C. Schwarz, W. Seidel, V. Serfling, L.G. Sobotka, J. Stroth, L. Stuttge, S. Tomasevic, W. Trautmann, A. Trzcinski, M.B. Tsang, A. Tucholski, G. Verde, C.W. Williams, E. Zude, B. Zwieglinski, Nucl. Phys. **A607**, 457 (1996).
- [20] A. Insolia *et al.*, Phys. Rev. **C61**, 044902 (2000).
- [21] W.-c. Hsi, K. Kwiatkowski, G. Wang, D.S. Bracken, E. Cornell, D.S. Ginger, V.E. Viola, N.R. Yoder, R.G. Korteling, F. Gimeno-Nogures, E. Ramakrishnan, D. Rowland, S.J. Yennello, M.J. Huang, W.G. Lynch, M.B. Tsang, H. Xi, Y.Y. Chu, S. Gushue, L.P. Remsberg, K.B. Morley, and H. Breuer, Phys. Rev. Lett. **79**, 617 (1997).
- [22] V. Weisskopf, Phys. Rev. **52**, 295 (1937).
- [23] W. Hauser, H. Feshbach, Phys. Rev. **87**, 366 (1952).
- [24] P.J. Siemens, A.S. Jensen, *Elements of Nuclei*, Addison Wesley, (1987).
- [25] D.H.E. Gross, E.V. Votyakov, Eur. Phys. J. **B15**, 115 (2000).
- [26] S.R. Souza, W.P. Tan, R. Donangelo, C.K. Gelbke, W.G. Lynch, M.B. Tsang, Phys. Rev. **C62**, 064607 (2000).
- [27] J. Pochodzalla *et al.*, Phys. Lett. **B174** 275 (1986).
- [28] Y.D. Kim, R.T. de Souza, C.K. Gelbke, W.G. Gong, S. Pratt, Phys. Rev. **C45**, 387 (1992).
- [29] J.Pochodzalla *et al.*, Phys. Rev. Lett. **75**, 1040 (1995).
- [30] M.J. Huang *et al.*, Phys. Rev. Lett. **78**, 1648 (1997).
- [31] M.B. Tsang, W.G. Lynch, H. Xi, W.A. Friedman, Phys. Rev. Lett. **78**, 3836 (1997).
- [32] H.F. Xi *et al.*, Phys. Rev. **C58**, R2636 (1998).
- [33] J. Pochodzalla *et al.*, Phys. Rev. Lett. **55**, 177 (1985).
- [34] T.K. Nayak, T. Murakami, W.G. Lynch, K. Swartz, D.J. Fields, C.K. Gelbke, Y.D. Kim, J. Pochodzalla, M.B. Tsang, H.M. Xu, F. Zhu, K. Kwiatkowski, Phys. Rev. **C45**, 132 (1992).
- [35] H.M. Xu, P. Danielewicz, W.G. Lynch, Phys. Lett. **B299**, 199 (1993).
- [36] J.P. Bondorf, R.Donangelo, I.N. Mishustin, C.J. Pethick, H. Schulz, and K. Sneppen, Nucl. Phys. **A443**, 321 (1985); *ibid* **A444**, 460 (1985); *ibid* **A448**, 753 (1986).

- [37] R.W. Minich, S. Agarwal, A. Bujak, J. Chuang, J.E. Finn, L.J. Gutay, A.S. Hirsch, N.T. Porile, R.P. Scharenberg, B.C. Stringfellow, F. Turkot, Phys. Lett. **B118**, 458 (1982).
- [38] J.B. Elliott *et al.*, Phys. Rev. Lett. **88**, 042701 (2002).
- [39] M.B. Tsang, C.K. Gelbke, X.D. Liu, W.G. Lynch, W.P. Tan, G. Verde, H.S. Xu, W. A. Friedman, R. Donangelo, S. R. Souza, C.B. Das, S. Das Gupta, D. Zhabinsky, Phys. Rev. **C64**, 54615 (2001).
- [40] M.E. Fisher, Physics **3**, 255 (1967).
- [41] H.S. Xu, M.B. Tsang, T.X. Liu, X.D. Liu, W.G. Lynch, W.P. Tan, A. Vander Molen, G. Verde, A. Wagner, H.F. Xi, C.K. Gelbke, L. Beaulieu, B. Davin, Y. Larochelle, T. Lefort, R.T. de Souza, R. Yanez, V.E. Viola, R.J. Charity, L.G. Sobotka, Phys. Rev. Lett. **85**, 716 (2000).
- [42] W.P. Tan, B.-A. Li, R. Donangelo, C.K. Gelbke, M.-J. van Goethem, X.D. Liu, W.G. Lynch, S. Souza, M.B. Tsang, G. Verde, A. Wagner, H.S. Xu, Phys. Rev. **C64**, 051901R (2001).
- [43] W. A. Friedman and W. G. Lynch, Phys. Rev. **C28**, 950 (1983).
- [44] G. Bertsch and S. Das Gupta, Phys. Rep. **160**, 189 (1988) and refs. therein.
- [45] C. Williams, W. G. Lynch, C. Schwarz, M. B. Tsang, W. C. Hsi, M. J. Huang, D. R. Bowman, J. Dinius, C. K. Gelbke, D. O. Handzy, G. J. Kunde, M. A. Lisa, G. F. Peaslee, L. Phair, A. Botvina, M-C. Lemaire and S. R. Souza, G. Van Buren, R. J. Charity, and L. G. Sobotka, U. Lynen, J. Pochodzalla, H. Sann, and W. Trautmann, D. Fox and R. T. de Souza, N. Carlin, Phys. Rev. **C55**, R2132 (1997).
- [46] W.P. Tan *et al.*, to be published.
- [47] D.H.E.Gross, Rep. Prog. Phys. **53**, 605 (1990).
- [48] W. Bauer, D.R. Dean, U. Mosel, U. Post, Phys. Lett. **B150**, 53 (1985); W. Bauer, U. Post, D.R. Dean, U. Mosel, Nucl. Phys. **A452**, 699 (1986).
- [49] J. Pan, S. Das Gupta, Phys. Lett. **B344**, 29 (1995); J. Pan, S. Das Gupta, Phys. Rev. **C51**, 1384 (1995); S. Das Gupta, J. Pan, Phys. Rev. **C53**, 1319 (1996).
- [50] M.L. Miller, O. Bjarki, D.J. Magestro, R. Pak, N.T.B. Stone, M.B. Tonjes, A.M. Vander Molen, G.D. Westfall, W.A. Friedman, Phys. Rev. Lett. **82**, 1399 (1999).
- [51] G. Wang, K. Kwiatkowski, D.S. Bracken, E. Renshaw Foxford, W.-c. Hsi, K.B. Morley, V.E. Viola, N.R. Yoder, C. Volant, R. Legrain, E.C. Pollacco, R.G. Korteling, W.A. Friedman, A. Botvina, J. Brzychczyk, H. Breuer, Phys. Rev. **C60**, 014603 (1999).
- [52] M. Colonna, M. Di Toro, G. Fabbri, and S. Maccarone, Phys. Rev. **C57**, 1410 (1998) and refs. therein.

- [53] H. Horiuchi, Nucl. Phys. **A522**, 257c (1991); A. Ono, H. Horiuchi, T. Maruyama, A. Onishi, Prog. Theor. Phys. **87**, 1185 (1992).
- [54] S. Albergo, S. Costa, E. Costanza, A. Rubbino, Nuovo Cimento **89**, 1 (1985).
- [55] M. D'Agostino *et al.*, Phys. Lett. **B371**, 175 (1996).
- [56] T. Glasmacher *et al.*, Phys. Rev. **C50**, 952 (1994).
- [57] S. Fritz, C. Schwarz, R. Bassini, M. Begemann-Blaich, S.J. Gaff-Ejakov, D. Gourio, C. Gro, G. Imm, Phys. Lett. **B461**, 315 (1999).
- [58] R. Hanbury-Brown, R.Q. Twiss, Philos. Mag. **45**, 663 (1954); Nature **177**, 27 (1956); Nature **178**, 1046 (1956).
- [59] S.E. Koonin, Phys. Lett. **B70**, 43 (1977).
- [60] S.Pratt, T. Csrgo, J. Zimnyi, Phys. Rev. **C42**, 2646 (1990).
- [61] D.H. Boal, C.K. Gelbke, B.K. Jennings, Rev. Mod. Phys. **62**, 553 (1990).
- [62] W. Bauer, C.K. Gelbke, S. Pratt, Annu. Rev. Nucl. Part. Sci. **42**, 77 (1992)
- [63] G. Verde, D.A. Brown, P. Danielewicz, C.K. Gelbke, W.G. Lynch, M.B. Tsang, Phys. Rev. **C65**, 054609 (2002).
- [64] M.B. Tsang, W.A. Friedman, C.K. Gelbke, W.G. Lynch, G. Verde, H. Xu, Phys. Rev. Lett. **86**, 5023 (2001).
- [65] H.A. Bethe, Rev. Mod. Phys. **62**, 801 (1990).
- [66] C.J. Pethick and D.G. Ravenhall, Ann. Rev. Nucl. Part. Sci. **45**, 429 (1995).
- [67] J.M. Lattimer and M. Prakash, Ap. J. **550**, 426 (2001); J.M. Lattimer and M. Prakash, Phys. Rep. **333**, 121 (2000).
- [68] D. H. Youngblood, H. L. Clark, and Y.-W. Lui, Phys. Rev. Lett. **82**, 691 (1999); H. L. Clark, Y.-W. Lui, and D. H. Youngblood, Phys. Rev. **C63**, 031301(R) (2001).
- [69] P. Danielewicz, Nucl. Phys. **A685**, 368C (2001).
- [70] R.T. de Souza *et al.*, Nucl. Instr. Meth. Phys. Res. **A295**, 109 (1990); D.W. Stracener *et al.*, Nucl. Instr. Meth. Phys. Res. **A294**, 485 (1990).
- [71] A. Wagner, W.P. Tan, K. Chalut, R.J. Charity, B. Davin, Y. Larochelle, M.D. Lennek, T.X. Liu, X.D. Liu, W.G. Lynch, A.M. Ramos, R. Shomin, L.G. Sobotka, R.T. de Souza, M.B. Tsang, G. Verde, H.S. Xu, Nucl. Instr. Meth. Phys. Res. **A456**, 290 (2001).
- [72] B. Davin, R.T. de Souza, R. Yanez, Y. Larochelle, R. Alfaro, H.S. Xu, A. Alexander, K. Bastin, L. Beaulieu, J. Dorsett, G. Fleener, L. Gelovani, T. Lefort, J. Poehlman, R.J. Charity, L.G. Sobotka, J. Elson, A. Wagner, T.X. Liu, X.D. Liu, W.G. Lynch, L. Morris, R. Shomin, W.P. Tan, M.B. Tsang, G. Verde, J. Yurkon, Nucl. Instr. Meth. Phys. Res. **A473**, 302 (2001).

- [73] Micron Superconductor LTD, 1 Royal Buildings, Marlborough Road, Lancing, Sussex BN158UN, England.
- [74] Scionix Holland BV, P.O. Box 143, 3980 CC Bunnik, The Netherlands.
- [75] Bicron, 12345 Kinsman Road, Newbury, Ohio 44065.
- [76] General Electric, Silicone Products Department, Waterford, New York 12188
- [77] Y. Larochelle *et al.*, Nucl. Instr. Meth. Phys. Res. **A348**, 167 (1994).
- [78] J.B. Birks, Proc. Phys. Soc. **A64**, 874 (1951).
- [79] D.O. Handzy, Ph.D. Thesis, Department of Physics and Astronomy, Michigan State University (1995).
- [80] G. Goldhaber *et al.*, Phys. Rev. Lett. **3**, 181 (1959); G. Goldhaber *et al.*, Phys. Rev. **120**, 300 (1960).
- [81] J. Pochodzalla *et al.*, Phys. Rev. **C35**, 1695 (1987).
- [82] Z. Chen *et al.*, Phys. Rev. **C36**, 2297 (1987).
- [83] T. Murakami, T.K. Nayak, W.G. Lynch, K. Swartz, Z. Chen, D.J. Fields, C.K. Gelbke, Y.D. Kim, M.R. Maier, J. Pochodzalla, M.B. Tsang, H.M. Xu, F. Zhu, Nucl. Instr. Meth. Phys. Res. **A275**, 112 (1989).
- [84] Y.D. Kim, R.T. de Souza, D.R. Bowman, N. Carlin, C.K. Gelbke, W.G. Gong, W.G. Lynch, L. Phair, M.B. Tsang, F. Zhu, Phys. Rev. **C45**, 338 (1992).
- [85] W.G. Gong, C.K. Gelbke, W. Bauer, N. Carlin, R.T. de Souza, Y.D. Kim, W.G. Lynch, T. Murakami, G. Poggi, D.P. Sanderson, M. B. Tsang, H.M. Xu, D.E. Fields, K. Kwiatkowski, R. Planeta, V. E. Viola, S.J. Yennello, S. Pratt, Phys. Rev. **C43**, 1804 (1991).
- [86] D.A. Brown, P. Danielewicz, Phys. Lett. **B398**, 252 (1997).
- [87] D.A. Brown, P. Danielewicz, Phys. Rev. **C57**, 2474 (1998).
- [88] D.A. Brown, P. Danielewicz, Phys. Rev. **C64**, 014902 (2001).
- [89] A. Andronic *et al.*, Phys. Rev. **C64**, 041604 (2001).
- [90] G. Verde, private communication (2002).
- [91] C.B. Chitwood, D.J. Fields, C.K. Gelbke, D.R. Klesch, W.G. Lynch, M.B. Tsang, T.C. Awes, R.L. Ferguson, F.E. Obenshain, F. Plasil, R.L. Robinson, G. R. Young, Phys. Rev. **C34**, 858 (1986).
- [92] G. Verde *et al.*, to be published
- [93] L.D. Landau, E.M. Lifshitz, *Statistical Physics*, Pergamon Press, Oxford (1980).
- [94] D.H. Boal, J.C. Shillcock, Phys. Rev. **C33**, 549 (1986).

- [95] B.K. Jennings, D.H. Boal, J.C. Shillcock, Phys. Rev. **C33**, 1303 (1986).
- [96] K. Wildermuth, Y.C. Tang, *A Unified Theory of the Nucleus*, Academic Press, New York (1977).
- [97] W.C. Hsi et al., Phys. Rev. Lett. **73**, 3367 (1994).
- [98] F. Ajzenberg-Selove, Nucl. Phys. **A490**, 1 (1988).
- [99] John Kelley, private communication (2002).
- [100] A. Csoto, Phys. Rev. **C61**, 024311 (2000).
- [101] E.K. Warburton, B.A. Brown, Phys. Rev. **C46**, 923 (1992).
- [102] F. Ajzenberg-Selove, Nucl. Phys. **A506**, 1 (1990).
- [103] K. Sneppen, Nucl. Phys. **A470**, 213 (1987).
- [104] G. Audi and A.H. Wapstra, Nucl. Phys. **A595**, 409 (1995).
- [105] S.R. Souza, M.B. Tsang, P. Danielewicz, to be published.
- [106] M.A. Preston and R.K. Bhaduri, *Structure of the Nucleus*, Addison-Wesley publishing company, Massachusetts (1975).
- [107] R.B. Firestone, V.S. Shirley, C.M. Baglin, S.Y.F. Chu, and J. Zipkin, *Table of Isotopes*, John Wiley & Sons, Inc., (1996); Evaluated Nuclear Structure Data File (ENSDF), maintained by the National Nuclear Data Center (NNDC), Brookhaven National Laboratory.
- [108] A. Gilbert and A.G.W. Cameron, Can. J. Phys. **43**, 1446 (1965).
- [109] Z. Chen and C.K. Gelbke, Phys. Rev. **C38**, 2630 (1988).
- [110] R.J. Charity, M.A. McMahan, G.J. Wozniak, R.J. McDonald, L.G. Moretto, D.G. Sarantites, L.G. Sobotka, G. Guarino, A. Panteleo, L. Fiore, A. Gobbi and K. Hildenbrand, Nucl. Phys. **A483**, 371 (1988); R.J. Charity, M. Korolija, D.G. Sarantites, and L.G. Sobotka, Phys. Rev. **C56**, 873 (1997); R.J. Charity, Phys. Rev. **C58**, 1073 (1998).
- [111] J. Borg, I.N. Mishustin, J.P. Bondorf, Phys. Lett. **B470**, 13 (1999).
- [112] A.S. Botvina, A.S. Iljinov, I.N. Mishustin, J.P. Bondorf, R. Donangelo, and K. Sneppen, Nucl. Phys. A **475**, 663 (1987).
- [113] T.X. Liu *et al.*, to be published.
- [114] M. Prakash, T.L. Ainsworth and J.M. Lattimer, Phys. Rev. Lett. **61**, 2518 (1988).
- [115] I. Bombaci, in "Isospin Physics in Heavy-Ion Collisions at Intermediate Energies", Eds. Bao-An Li and W. Udo Schroeder, NOVA Science Publishers, Inc. (New York), (2001) in press and refs. therein.

- [116] Bao-An Li, Phys. Rev. Lett. **85**, 4221, (2000).
- [117] Bao-An Li, C.M. Ko, Zhongshou Ren, Phys. Rev. Lett. **78**, 1644 (1997).
- [118] V. Baran, M. Colonna, M. Di Toro, A.B. Larionov, Nucl. Phys. **A632**, 287 (1998).
- [119] L. Scalone, M. Colonna and M. Di Toro, Phys. Lett. **B461**, 9 (1999).
- [120] N. Marie *et al.*, Phys. Rev. **C58**, 256 (1998).
- [121] B. Borderie *et al.*, Phys. Rev. Lett. **86**, 3252 (2001).
- [122] D.R. Bowman *et al.*, Phys. Rev. Lett. **67**, 1527 (1991).
- [123] R. Popescu *et al.*, Phys. Rev. **C58**, 270 (1998).
- [124] L. Beaulieu *et al.*, Phys. Rev. Lett. **84**, 5971 (2000).
- [125] D.H.E. Gross, G. Klotz-Engmann, and H. Oeschler, Phys. Lett. **B224**, 29 (1989).
- [126] A.B. Larionov, A.S. Botvina, M. Colonna, and M Di Toro, Nucl. Phys. **A658**, 375 (1999).
- [127] R. Wada *et al.*, Phys. Rev. **C62**, 034601 (2000) and refs. therein.
- [128] B.-A. Li, A.R. De Angelis, and D.H.E. Gross, Phys. Lett. **B303**, 225 (1993).
- [129] A.S. Botvina *et al.*, Nucl. Phys. **A584**, 737 (1995).
- [130] K. Kwiatkowski *et al.*, Phys. Lett. **B423**, 21 (1998).
- [131] W. Reisdorf *et al.*, Nucl. Phys. **A612**, 493 (1997).
- [132] The N/Z of the residue is independent of the choice for the incompressibility of the symmetric matter part of the EOS and independent of the choice of in-medium nucleon-nucleon cross section [117]. The mass of the residue is influenced by the latter two choices but is immaterial to the main issues of the present work.
- [133] L.G. Sobotka, J.F. Dempsey, and R.J. Charity, Phys. Rev. **C55**, 2109 (1997).
- [134] M.B. Tsang *et al.*, Phys. Lett. **B297**, 243 (1992).